Synthesis, Self-Assembly and Photophysical Properties of Multichromophoric Systems

D I S S E R T A T I O N

zur Erlangung des akademischen Grades

eines Doktors der Naturwissenschaften (Dr. rer. nat.)

im Promotionsprogramm

„Fotophysik synthetischer und biologischer multichromophorer Systeme“

der Bayreuther Graduiertenschule für

Mathematik und Naturwissenschaften

vorgelegt von

Andreas Thomas Haedler

geboren in Naila, Deutschland

Bayreuth, 2014

Die vorliegende Arbeit wurde in der Zeit von Oktober 2009 bis März 2014 am Lehrstuhl Makromolekulare Chemie I der Universität Bayreuth unter der Betreuung von Prof. Dr. Hans-Werner Schmidt angefertigt.

Direktor der BayNAT:	Prof. Dr. Franz X. Schmid
Tag des Einreichens der Dissertation:	18. Juli 2014
Tag des wissenschaftlichen Kolloquiums:	23. Januar 2015

Prüfungsausschuss:

Prof. Dr. Hans-Werner Schmidt	(Erstgutachter)
Dr. Richard Hildner	(Zweitgutachter)
Prof. Dr. Stephan Förster	(Vorsitz)
Prof. Dr. Peter Strohriegl	

"...a scientist must also be absolutely like a child. If he sees a thing, he must say that he sees it, whether it was what he thought he was going to see or not. See first, think later, then test. But always see first. Otherwise you will only see what you were expecting."

(Douglas Adams, So Long, and Thanks for All the Fish)

Table of content

Table of content

Summary

Nature's story of success is vastly based on the elegant utilization of a variety of non-covalent interactions, demonstrating the power of supramolecular concepts. Some of the most prominent examples are the self-assembled architectures of light harvesting complexes, which enabl the conversion of sunlight into a storable energy resource. In order to understand and mimic these biological systems as well as their underlying processes, further fundamental knowledge of the interplay between different intermolecular interactions of chromophoric systems is needed. Equally important are the resulting influences of the supramolecular arrangement on the photophysical properties of the constituents, respectively, the supramolecular aggregates. One major scientific question is how can we design chromophoric and multichromophoric supramolecular building blocks to achieve an improvement of the crucial processes (*e*.*g*. transport of excitation energy) for efficient light harvesting? This thesis contributes to this challenging task dealing with the synthesis, the self-assembly and the investigations of photophysical properties of novel multichromophoric systems. The content covers state-of-the-art synthetic procedures and contemporary methods to study self-assembly and explore photophysical properties of the supramolecular aggregates. To exploit the full potential of supramolecular chemistry and supramolecular materials and to precisely construct architectures tailored for a particular application, an improved fundamental understanding concerning the governing influences of different intermolecular interactions on the self-assembly process and the resulting supramolecular architectures is necessary.

The first part of this thesis contributes to this complex issue of *the influences of steric effects and hydrogen-bonding on the self-assembly, the stacking behavior and the optical properties of pyrene derivatives*. The changing photophysical properties of the pyrene compounds were investigated in (i) highly diluted solutions in organic solvents, (ii) at increased concentrations in an intermediate self-assembly regime, and (iii) in the dry crystalline solid state, utilizing steady-state and time-resolved optical spectroscopy. For the investigated compounds, the π-stacking of the pyrene moieties into weakly coupling H-aggregates – i.e. cofacially arranged chromophores with in an optical forbidden lowest energy transition – turned out to be the governing driving force initiating self-assembly in solution. In this regime, the

ground state H-aggregates of the pyrene moieties give rise to excimer formation – i.e. an excited dimer. While, hydrogen-bonding and steric effects have almost no influence on the self-assembly process, they do however determine the excimer formation rate within the supramolecular aggregates. Upon transition to the crystalline state the influence of the different intermolecular interactions becomes more striking as the excimer fluorescence vanishes with increasing order in the crystalline state. This order is promoted by the formation of hydrogen-bonds and is decreased with the introduction of bulky groups. This study illustrates the delicate interplay of different non-covalent interactions influencing the supramolecular architecture and as a result the macroscopic photophysical properties. The results obtained from these fundamental studies were used to design and investigate more complex multichromophoric systems.

The second part of this thesis deals therefore with the *synthesis and the photophysical properties of two novel carbonyl-bridged triarylamine derivatives*. The central C_3 symmetric chromophore was connected in 2, 6, and 10 position via an amide linker and a short alkyl spacer with either naphthalimides or 4-(5-hexyl-2,2'-bithiophene)-naphthalimides. The used synthetic route represents a universal way allowing for a versatile functionalization of carbonyl-bridged triarylamines. Three reference compounds were additionally synthesized to study the individual optical properties of the chromophore moieties separately. In the multichromophoric compounds efficient energy transfer was investigated and proved by steady-state and time-resolved spectroscopic investigations. In the multichromophoric compound bearing naphthalimides in the periphery, the energy is funneled from the periphery to the carbonyl-bridged triarylamine core. In the second multichromophoric compound energy transfer proceeds in the opposite direction, from the central carbonyl-bridged triarylamine to the lateral 4-(5-hexyl-2,2'-bithiophene)-naphthalimide units. Furthermore, this compound forms transparent fluorescent gels in organic solvents at very low concentration while retaining the optical and energy transfer properties. The obtained results prove multichromophoric carbonyl-bridged triarylamines as interesting and supramolecular functional materials.

The last part of this thesis is concerned with the *self-assembly of multichromophoric systems*. The study was performed with the carbonyl-bridged triarylamine with 4-(5-hexyl-

2,2'-bithiophene)-naphthalimide substituents *which froms supramolecular nanofibers of molecular diameter*. A striking feature of these aggregates is the outstanding *excitation energy transport* along these fibers *at ambient conditions*. The above mentioned efficient gelation of this compound at very low concentrations demonstrates a pronounced self-assembly behavior. Electron and atomic force microscopy techniques revealed one-dimensional nanofibers with molecular diameter and several micrometers in length. Spectroscopic investigations demonstrate that hydrogen-bonding of the amide linkers together with strong π-stacking of the carbonyl-bridged triarylamine are responsible for the strong uniaxial self-assembly. The threefold-symmetric nature of the hydrogen-bonds enforces a cofacial H-aggregation of the carbonyl-bridged triarylamine cores with a nearest neighbor coupling as strong as in natural light harvesting systems. The high level of order in combination with the coupling of the carbonyl-bridged triarylamine cores along the supramolecular nanofibers result in long-range energy transport over at least 4 μm, which corresponds to more than 10.000 molecules. This was verified for individual nanofibers using a custom-built confocal fluorescence microscope. This long-range transport of excitation energy cannot be explained solely by classical diffusion controlled hopping processes. Instead, for this supramolecular system the energy transport is most likely explained by quantum coherent effects that allow for a wavelike transport and a distribution of the exciton over several chromophores. The self-assembly of this compound is an excellent example to demonstrate the enormous potential of supramolecular chemistry towards highly ordered non-covalently bonded architectures with remarkable properties and functionality.

Zusammenfassung

Die Erfolgsgeschichte der Natur beruht insbesondere auf der eleganten Nutzung von nichtkovalenten Wechselwirkungen und verdeutlicht damit eindrucksvoll das Leistungsvermögen supramolekularer Konzepte. Zu den bedeutendsten Beispielen gehören selbstaggregierte Strukturen von Lichtsammelkomplexen, welche Sonnenlicht in eine lagerbare Form der Energie umwandeln. Um diese biologischen Systeme und deren fundamentale Prozesse zu verstehen und nachzuahmen ist ein grundlegendes Verständnis der zwischenmolekularen Wechselwirkungen von farbstoffhaltigen Molekülen unabdingbar. Ebenso wichtig sind die Auswirkungen der Aggregation auf die fotophysikalischen Eigenschaften der Verbindungen, beziehungsweise der resultierenden supramolekularen Strukturen. Wie können farbstoffhaltige supramolekulare Bausteine gezielt entwickelt werden, um die essentiellen Prozesse und die effiziente Nutzung von Sonnenenergie (z. B. Transport von Anregungsenergie) nachzuahmen? Um zur Beantwortung dieser Frage beizutragen, behandelt diese Arbeit die Synthese, die Selbstaggregation und die Untersuchung fotophysikalischer Eigenschaften neuer farbstoffhaltiger Verbindung. Der Inhalt dieser Arbeit umfasst moderne Synthesemethoden und aktuelle Techniken zur Untersuchung der Eigenschaften der Selbstaggregation und der Fotophysik. Um das ganze Potential supramolekularer Chemie und supramolekularer Materialien auszunutzen und um Architekturen für eine bestimmte Anwendung gezielt aufzubauen, müssen die Einflüsse unterschiedlicher zwischenmolekularen Wechselwirkungen auf den Prozess der Selbstaggregation besser verstanden werden.

Der erste Teil dieser Arbeit befasst sich daher mit dieser komplexen Aufgabe. Der *Einfluss von sterischen Effekten und Wasserstoffbrücken auf die Selbstaggregation, das Stackingverhalten und die optischen Eigenschaften von Pyrenderivaten wird untersucht*. Die Änderungen der fotophysikalischen Eigenschaften der Pyrenverbindungen wurden in verschiedenen Zuständen studiert: (i) in hochverdünnten organischen Lösungen, (ii) bei erhöhter Konzentration in dem intermediärem Bereich der Selbstaggregation und (iii) im trockenen, kristallinen Feststoff. Hierzu wurden stationäre (unter Dauerbelichtung) und zeitaufgelöste Spektroskopiemethoden eingesetzt. Bei den untersuchten Verbindungen ist die Wechselwirkung (π-stacking) der Pyrenchromophore die Triebkraft zur Aggregation in

Lösung. Dabei kommt es zur Ausbildung von schwach gekoppelten H-Aggregaten (parallele Anordnung der Chromophore, welche den energieärmsten elektronischen Übergang optisch verbietet). Diese im Grundzustand vorliegenden H-Aggregate ermöglichen die Ausbildung von Excimeren (Dimere im angeregten Zustand). Wasserstoffbrücken und sterische Effekte spielen beim Prozess der Selbstaggregation nur eine untergeordnete Rolle. Sie bestimmen jedoch maßgeblich die Excimerbildungsgeschwindigkeiten innerhalb der supramolekularen Aggregate. Ein deutlicher Einfluss der unterschiedlichen nichtkovalenten Wechselwirkungen zeigt sich erst beim Übergang in den kristallinen Zustand. Die kristalline Ordnung wird durch Wasserstoffbrücken erhöht und durch sterische anspruchsvolle Gruppe erniedrigt wird. Dabei nimmt mit zunehmender Ordnung die Excimerfluoreszenz ab. Diese grundlegende Arbeit zeigt wie das empfindliche Wechselspiel verschiedener zwischenmolekularer Wechselwirkungen die supramolekulare Struktur und damit die makroskopischen fotophysikalischen Eigenschaften beeinflusst. Die Ergebnisse dieses Projekts dienten dem Design komplexerer Systeme, welche aus mehr als einer Farbstoffeinheit bestehen.

Der zweite Teil dieser Arbeit befasst sich folglich mit der *Synthese und den fotophysikalischen Eigenschaften von zwei neuartigen carbonylverbrückten Triarylaminderivaten*. Der zentrale C_3-symmetrische Farbstoff wurde in 2, 6 und 10 Position über Amide und kurze Alkylspacer entweder mit Naphthalimiden oder mit 4-(5-Hexyl-2,2‘-bithiophen)-naphthalimiden ausgestattet. Die hierfür verwendete Syntheseroute stellt eine universelle Methode zur vielfältigen Funktionalisierung von carbonylverbrückten Triarylaminen dar. Zusätzlich wurden drei Referenzverbindungen hergestellt, um die optischen Eigenschaften der einzelnen Farbstoffe unabhängig von einander zu untersuchen. Durch stationäre und zeitaufgelöste Spektroskopie konnte an den Triarylaminderivaten mit zusätzlichen peripheren Farbstoffen Energietransfer beobachtet und nachgewiesen werden. Bei den carbonylverbrückten Triarylaminen mit Naphthalimiden, wird die Energie von der Peripherie absorbiert und dann im Kern gesammelt. Im zweiten Fall wird die Energie in die andere Richtung übertragen, vom carbonylverbrückten Triarylaminkern zu den peripheren 4-(5-Hexyl-2,2‘-bithiophen)-naphthalimiden. Diese Verbindung ist des Weiteren in der Lage bereits bei sehr geringen Konzentrationen organische Lösungsmittel zu gellieren, wobei die fotophysikalischen und Energietransfer-Eigenschaften im Gelzustand erhalten bleiben. Die

erhaltenen Ergebnisse zeigen, dass carbonylverbrückte Triarylamine mit zusätzlichen Farbstoffen ausgestattet vielversprechende funktionelle Materialien sind.

Der letzte Teil dieser Dissertation befasst sich mit der *Selbstaggregation* des carbonylverbrückten Triarylamins mit 4-(5-Hexyl-2,2‘-bithiophen)-naphthalimiden in der Peripherie, welches *supramolekulare Nanofasern mit molekularem Durchmesser* ausbildet. Eine fazinierende Eigenschaft dieser Aggregate ist der *außergewöhnlich langweitreichige Transport von Anregungsenergie entlang der Fasern bei Raumtemperatur*. Die oben erwähnten effizienten Gelbildungseigenschaften bei geringen Konzentrationen verdeutlichen ein ausgeprägtes Selbstaggregationsverhalten. Elektronen- und rasterkraftmikroskopische Aufnahmen zeigen ausgedehnte, ein-dimensionale Nanofasern mit molekularem Durchmesser und Längen von mehreren Mikrometern. Durch spektroskopische Untersuchungen konnte nachgewiesen werden, dass starke Wasserstoffbrücken der Amide zusammen mit chromophoren Wechselwirkungen zwischen den carbonylverbrückten Triarylaminen für die ausgeprochen starke 1-dimenstionale Aggregation verantwortlich sind. Auf Grund der C_3-Symmetrie der Wasserstoffbrücken werden die zentralen carbonylverbrückten Triarylamine in eine parallele coplanare Anordnung gezwungen. Die entstehenden H-Aggregate weisen eine elektronische Kopplung auf, die in ihrer Stärke der Kopplung gleicht, wie sie von natürlichen Lichtsammelkomplexen vorkommt. Die hohe Ordnung zusammen mit der starkten Kopplung zwischen den carbonylverbrückten Triarylaminkernen entlang der Fasern ermöglicht einen langreichweitigen Energietransport über mindestens 4 µm, was mehr als 10000 Molekülen entspricht. Dies konnte mit einem selbstgebauten Fluoreszenzmikroskop an einzelnen Nanofasern nachgewiesen werden. Dieser langweitreichige Transport von Anregungsenergie kann nicht durch das klassische Hüpfen von Exitonen beschrieben werden. Stattdessen sind in diesen supramolekularen Aggregaten höchstwahrscheinlich quantenkohärente Effekte für den Energietransport verantwortlich, welche einen wellenartigen Energietransport ermöglichen, bei dem die Anregungsenergie über mehrere Chromophore verteilt wird. Die Selbstaggregation und die resultierenden Energietransproteigenschaften dieser Verbindung zeigt auf beeindruckende Art und Weise das enorme Potential der supramolekularen Chemie im Hinblick auf hochgeordnete, nicht-kovalente supramolekulare Architekturen mit bemerkenswerten Eigenschaften und Funktionen.

1. Introduction

1.1. Supramolecular Chemistry – Inspired by Nature

Supramolecular chemistry exploits non-covalent interactions to control the three-dimensional superstructure of individual (macro)molecules and the architecture of their assemblies in a bottom-up approach. Although non-covalent interactions, which are governed by local surface potentials, are in general weaker than covalent bonds their impact on the molecular functions as well as material properties can be just as striking. In this context the macroscopic properties do not arise from the sum of the individual parts but result from the supramolecular aggregates. As a consequence, complex architectures and functionality can be achieved with comparatively simple and well defined molecular building blocks.

Supramolecular Chemistry in Nature

During thousands of million years of evolution nature managed to perfect the use of intermolecular interactions to create life out of a handful of available and simple molecules.[1–3] The key part in every living cell is the ribosome, which is in charge of biological protein synthesis.[4–6] The large and the small ribosomal subunits - each consisting of a number of ribosomal ribonucleic acid (rRNA) and proteins - read out the encoded information of the messenger RNA (mRNA) to generate a peptide chain of precise length and sequence using transfer RNA (tRNA) (Figure 1).[7,8] In this biological factory, all of the individual molecular building blocks arrange themselves intra- and intermolecularly by non-covalent bonds.[9–11] Hence, the ribosome is a perfect example for supramolecular chemistry with exceptional functionality demonstrating the achievable potential. In 2009 Venkatraman Ramakrishnan, Thomas A. Steitz, and Ada E. Yonath were awarded the Nobel Prize in Chemistry for their "*studies of the structure and function of the ribosom*".[12] Further examples for supramolecular chemistry in nature are the distinct folding and intermolecular interactions of proteins,[13,14] the one-to-one recognition in DNA (deoxyribonucleic acid) double helices,[15,16] the supramolecular architecture of the tobacco mosaic virus[17,18] or the lipid bilayer in cell membranes[19,20] among others.[21,22]

Figure 1. The ribosome. Three dimensional representation including the small subunit (purple), the large subunit (blue), the messenger RNA (grey), and three transfer RNAs (green, pink, and red) at their respective binding sites.[12]

Fundamentals of Supramolecular Chemistry

Nowadays, scientists working in the field of supramolecular chemistry try to adopt and explore the principles used by nature to specifically employ them for manifold purposes.[23,24] The pioneering work of Donald J. Cram, Jean-Marie Lehn, and Charles J. Pedersen was honored with the Nobel Prize in chemistry in 1987 "*for their development and use of molecules with structure-specific interactions of high selectivity*".[25–27] These intermolecular

interactions constitute the toolbox of supramolecular chemists and include among others, salt bridges, organometallic complexation, hydrogen bonding (e.g. of amides, ureas, nucleotide base pairs), electrostatic interactions of dipoles, aromatic π-stacking, and hydrophilic and hydrophobic interactions. Those interactions highly differ in their *strength, directionality and selectivity*. The driving forces responsible for the aggregation need to be strong enough to overcome thermodynamic barriers like entropic losses due to constrained mobility and reduced flexibility of the involved molecules in the supramolecular structure. Hence, the covalent molecular structure is equally important to ensure the desired supramolecular aggregation and achieve the desired properties. In contrast to covalent synthesis, however, the dynamic nature of non-covalent bonding is an important factor. Inherent reversibility can be utilized and offers appealing auto-correcting properties diminishing the probability of structural errors in the non-equilibrium supramolecular framework.[28–37]

Development of Artificial Supramolecular Systems

The first research on supramolecular concepts dates back to the end of the 19th century, when Alfred Werner investigated the non-covalent coordination of metal-ions by suitable ligands.[38] He was 1913 awarded the Nobel Prize in chemistry for his work.[39] Jean-Marie Lehn further exploited the idea of non-covalent interactions and used the coordination properties of oligo-bipyridines in combination with metal-ions to construct helical architectures. Depending on the linker between the bipyridine units and the nature of the metallic ion (favoring tetrahedral or octahedral coordination) double or triple helices were achieved.[37,40] Extending this concept by introducing further bipyridine ligands and different metal ions led to a great variety of grid-type metal ion architectures in some cases templated by the respective counterion.[41] In other early work on the topic of supramolecular chemistry the group of George M. Whitesides applied complementary H-bonding motifs between melamine and cyanuric acid derivatives yielding two dimensional supramolecular architectures upon mixing. By clever covalent connection of melamine units and cyanuric acid units upon each other even three dimensional aggregates of precise size could be achieved.[30,42]

More recently, the one-to-one recognition in DNA base pairs was used to create two- and three-dimensional architectures of distinct shape and size.[43,44] This so called "DNA origami" exploits the powerful driving force of DNA strands with a certain nucleotide sequence to exclusively find its perfect match forming a double helical structure.[45] Smart sequencing of nucleic acids can lead by implication to formation of double helices including the interpenetration of multiple helices by individual strands. Subsequently, a precise construction of supramolecular architectures from a number of different strands is possible.

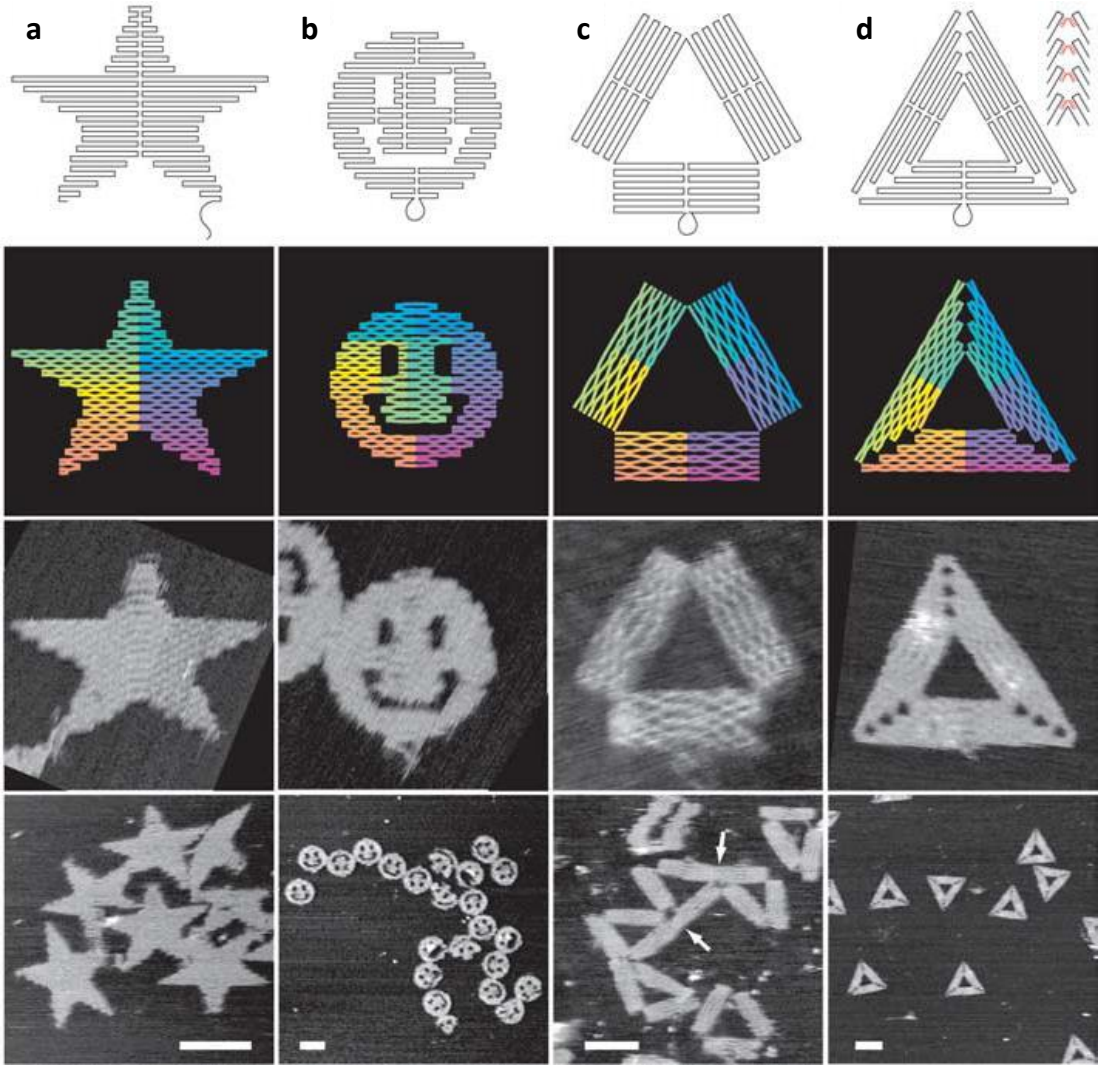

Figure 2. DNA Origami. First row: Folding paths towards different shapes: **a** star, **b** smile, **c** triangle with rectangular domains, **d** sharp triangle with trapezoidal domains; Second row: Diagrams showing the folding pattern of the DNA strand from the 1st (red) to the 7000th (purple) base pair.; Third row: AFM magnification images of the same size (165 nm x 165 nm); Fourth row: AFM overview images (scale bars are 100 nm).[43]

More importantly, the correct nucleic acid sequence, which is necessary to achieve the desired shape, can be calculated in advance. Consequently, different individual DNA strands need to be synthesized, mixed together and given enough time to self-assemble into the thermodynamically most favorable geometry. Some complex shapes, which can be achieved from this method, are presented in figure 2. The potential of DNA-origami for future applications and use is now to be explored.[46–48] In this particular case nature provided a powerful one-to-one recognition code which could be translated into a combined natural and artificial approach.

Unlike in the unique example of DNA origami, it is not yet possible to predict the final supramolecular architecture directly from the molecular structure of the individual building blocks. Even more challenging is the prediction of macroscopic functionalities or properties of supramolecular aggregates. Although knowledge in supramolecular chemistry increases rapidly, there is still a great work to be done by chemists, biologists, and physicists to obtain a comprehensive understanding of this complex matter. On the other hand nature displays great capabilities of supramolecular chemistry and some marvelous applications based on artificial supramolecular systems have already evolved.[49–51]

1.2. Supramolecular Chemistry – A Closer Look

The self-assembly of molecular building blocks into supramolecular aggregates is a complex and delicate process. This bottom-up approach is driven by intermolecular interactions leading to the formation of non-covalent bonds. Self-assembly is in general a dynamic process as non-covalent bonds, unlike their covalent counterparts, can be easily formed and broken. This reversibility of the non-covalent bond formation might at first be considered as a drawback, which is not the case. Nature specifically utilizes the reversibility of supramolecular architectures as build-in control system to repair damaged or ill-defined structures.[30] This self-healing ability is especially important in reproduction processes as it diminishes the probability of defects in supramolecular structures or even the genetic code.[12,16] Simultaneously, the dynamic state implies a great demand on the self-assembly process.

The self-assembly or disassembly of a certain supramolecular building block can be initiated by different triggers *i.e.* changes of the temperature, the concentration, the solvent polarity, the pH-value, or the molecular geometry.[52–58] These triggers can also drive the aggregation processes in a specific direction. However, to deliberately achieve and precisely control the outcome of the self-assembly, the factors that govern the aggregation process need to be better understood and adjusted carefully. According to Maggini et al. these factors can be divided into three groups, namely (i) thermodynamic and kinetic considerations, (ii) the internal, and (iii) the external factors (Figure 3).[59] The three groups, which will be discussed in the following, are not independent, but influence each other. Consequently, the final supramolecular architectures and morphologies that are formed are delicately determined by the interplay of these factors.

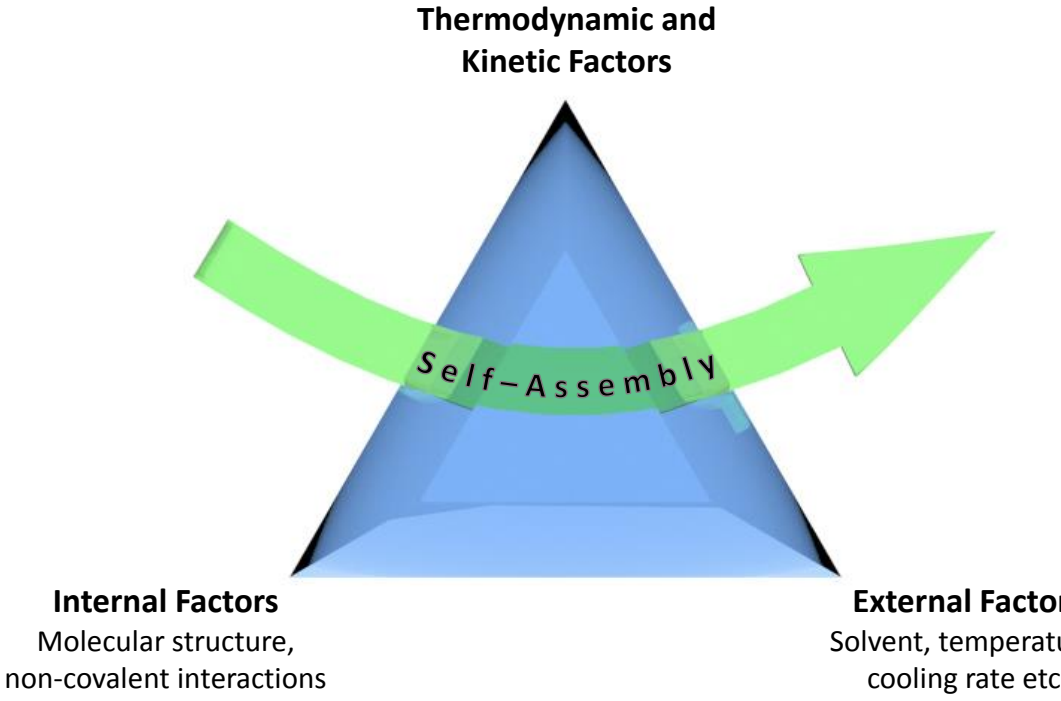

Figure 3. Factors governing self-assembly. The process of self-assembly and the morphology of the final supramolecular architecture are governed by thermodynamic and kinetic factors, internal factors and external factors.

Thermodynamic and Kinetic Considerations

Thermodynamics and kinetics are extremely important not only in covalent synthesis but also in supramolecular aggregation. In the course of self-assembly the enthalpic gain (ΔH_{SA}) has to compensate for the entropic penalty ($T\Delta S_{SA}$) associated with the organization *i.e*. $\Delta G_{SA} = \Delta H_{SA} - T\Delta S_{SA} < 0$.[30] In this context, the entropic consideration can also include the fixation of solvent molecules either in the non-aggregated as well as in the aggregated state. Dynamic self-assembly processes will adopt to a change in the conditions until the energetically most favored configuration is reached. Hence, the system can follow different pathways to approach its final state depending on the applied trigger and conditions. From a kinetic point of view, these processes may be extremely fast or too slow to be observed. Depending on the supramolecular system different self-assembly mechanisms can be distinguished, *e.g*. isodesmic, cooperative or anti-cooperative self-assembly (Figure 9).[60–62] The self-assembly process can be illustrated as the reversible non-covalent bonding of molecular building blocks to yield larger aggregates. For a theoretical description one might

consider individual, consecutive attachments of monomeric species to a growing aggregate. Here, each reversible step is described by an equilibrium constant *K* which is determined by the ratio of the forward and backward rate constants and the thermodynamic parameter of this addition step. In the case of *isodesmic self-assembly*, each equilibrium constant has the same value, *i.e*. every monomer addition step is equally favored (Figure 4 left).[63–67] Consequently, the distribution of the sizes of the supramolecular aggregates is rather broad and usually does not yield very large aggregates. In *cooperative self-assembly* two regimes of the self-assembly process are distinguished: nucleation and elongation, each with its own equilibrium constant K_n and K_e, respectively (Figure 4 right).[68–71] As the supramolecular aggregate reaches a certain nucleation size the aggregation process switches from nucleation to elongation. The degree of cooperativity σ is described by the ratio K_e/K_n. For σ > 1 the addition of monomer in the elongation is more favored than in the nucleation regime, which results in the formation of larger aggregates. *Anti-cooperative self-assembly* is described by σ < 1 which results in the termination of the supramolecular aggregation after a certain size or aggregate-state is reached.

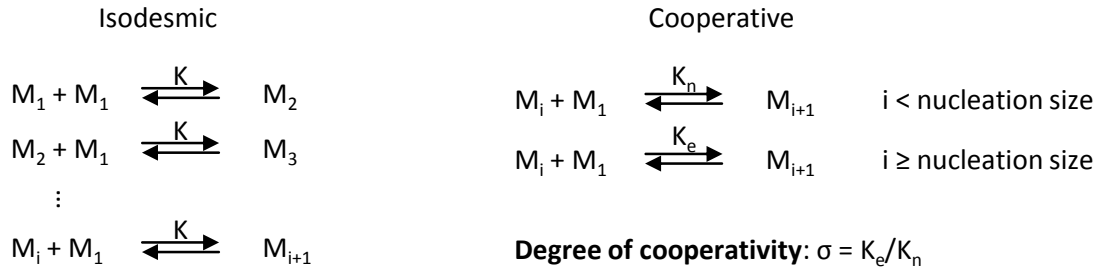

Figure 4. Kinetics of self-assembly mechanisms. Left: Model describing isodesmic or "equal K" self-assembly; Right: Model describing cooperative self-assembly.[60]

Depending on the kinetics of the self-assembly, the aggregating system can run into kinetic traps and might not reach the state of the global energy minimum.[59,72,73] Like in covalent synthesis, where different products can be obtained depending on the reaction conditions (*i.e*. thermodynamic or kinetic control), in supramolecular chemistry the final state can vary depending on the self-assembly conditions.[61,74]

Internal and External Factors

In the following the influences of the internal and external factors on the self-assembly will be discussed on selected examples comprising mainly naphthalenediimide derivatives as chromophore representatives. The *internal factors* refer to the molecular structure and the associated surface potential, which are closely connected to the intermolecular interactions implemented in the compounds *e.g*. coordination interaction, hydrogen bonds, dipole-dipole interactions and van der Waals interactions.[28,29,75–77] A prominent example is the one-to-one recognition in DNA double-helices, which are built up by only four different nucleotides stringed together. However, only with a proper sequence, recognition of two nucleic acid strands can successfully lead to a double helical self-assembly.[15,16]

Some interesting work by the group of Suhrit Ghosh on artificial systems demonstrates that even small changes in the molecular structure can have a great influence on the supramolecular architecture.[78–80] The system comprises two isomeric naphthalenediimide derivatives bearing two amide groups. These hydrogen bonding motifs were either positioned symmetrically to both sides of the chromophore or both on the same side (Figure 5).[81] Both compounds show a high tendency to self-assemble into fibrillar structures. However, despite their isomeric structures, they yield self-sorted aggregation upon cooling of a mixed solution.

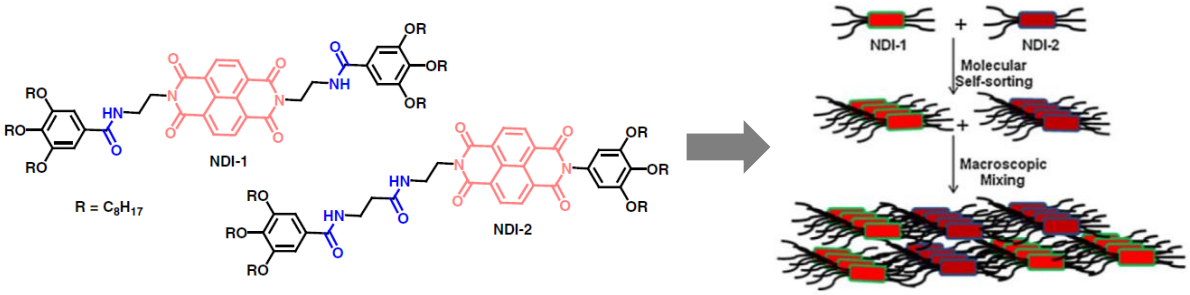

Figure 5. Internal factors: Influence of molecular structre. Self-sorted aggregation of two isomeric naphthalenediimide compounds comprising two hydrogen bonding amide groups.[81]

These studies were extended towards a donor-acceptor self-assembly using bisamide derivatives of naphthalenediimide (acceptor) and of dialkoxynaphthalenes (donor) with slight variations in the molecular structure.[82] Upon mixing the electron-poor

naphthalenediimides with the electron rich dialkoxynaphthalenes either self-sorted or alternating self-assembly was observed, depending on a match or mismatch between the incorporated hydrogen-bonding amide moieties of the respective donor and acceptor derivatives.

Another example from the group of Suhrit Ghosh comprises naphthalene diimide amphiphiles, which self-assemble due to a combination of π-π stacking of the chromophore and hydrogen bonding of an acid moiety[80]. It is shown that marginal changes in the spacer between the naphthalene diimide and the carboxylic acid influence the π-stacking behavior and consequently the macroscopic properties of the supramolecular aggregates *i.e*. the color of the photoluminescence (Figure 6).

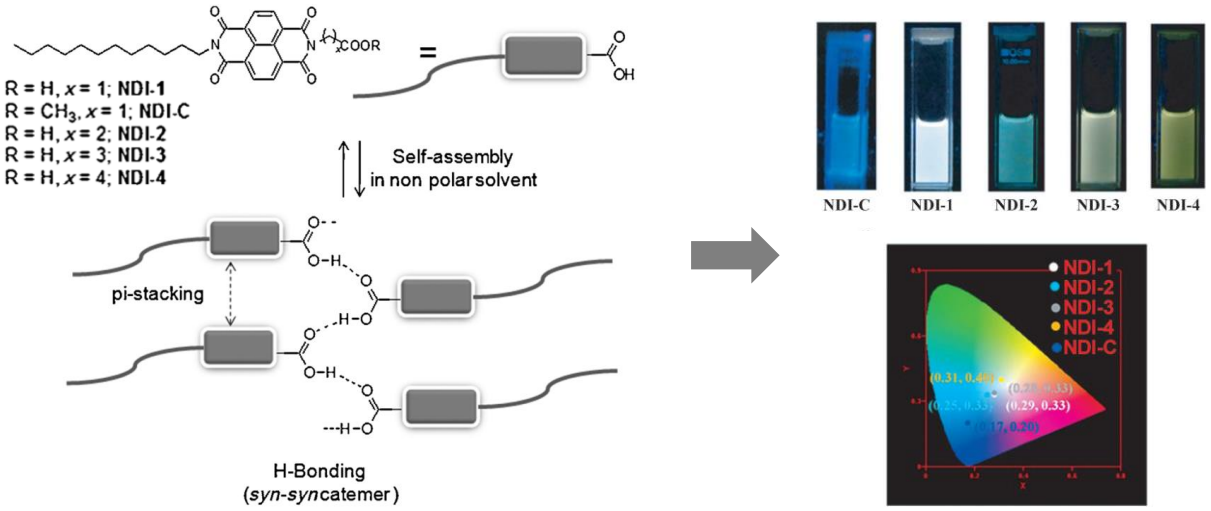

Figure 6. Internal factors: Influence of subtle changes in the molecular structure. Self-assembly of amphiphilic naphthalenediimide derivatives with slight changes in the molecular structure having a major influence on the π-stacking and consequently on the macroscopic photoluminescence properties.[80]

The *external factors* i.e. the experimental conditions include the trigger that is used to initiate self-assembly. But also all other processing parameters like the medium, the mass-concentration, the temperature window or the cooling rate have an influence on the outcome of the self-assembly process.[83] Some systems form different supramolecular architectures from the same initial state depending on the parameter that is changed.[84–90] If kinetic traps appear on the self-assembly pathway of a system, it is not only important which parameter is changed but also at which rate. It was shown in our group that the cooling rate

can have a significant influence on the supramolecular morphology of a thermo-responsive system (Figure 7).[91] Upon cooling the investigated benzene trisamide derivative (see also chapter 1.3) self-assembles into one-dimensional fibers. The fiber diameter depends strongly on the cooling rate, while the concentration, the solvent and the temperature window were kept the same. Faster cooling results in thinner fibers with a narrower distribution of the fiber diameter.

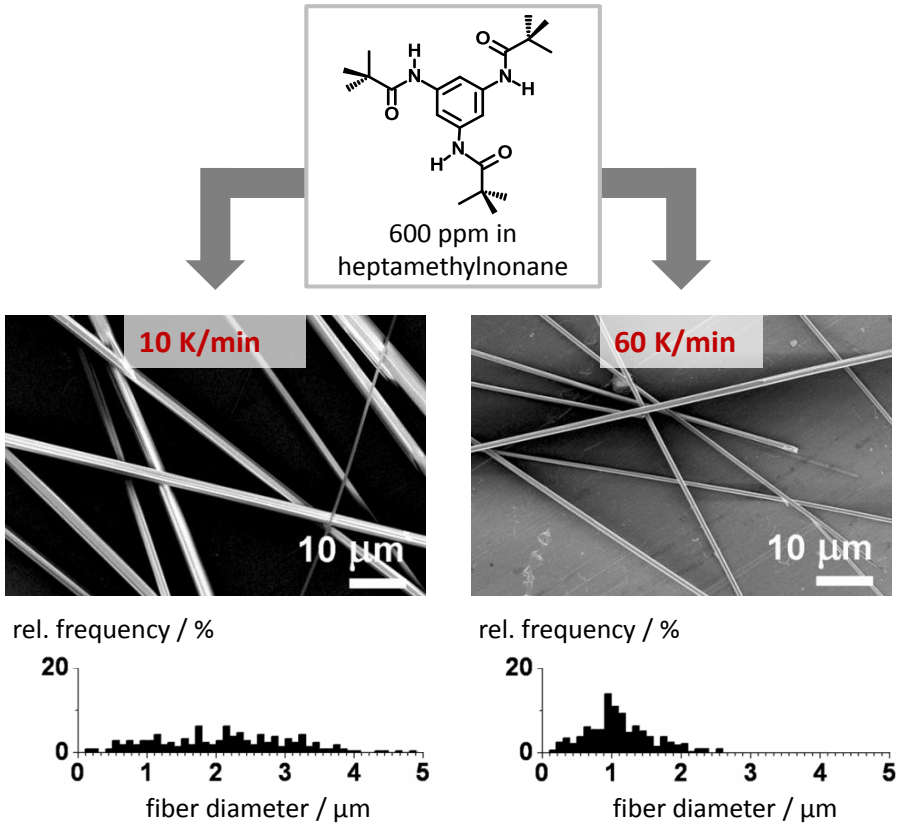

Figure 7. External factors: Influence of the cooling rate. Self-assembly of a 1,3,5-benzenetrisamide derivative from heptamethylnonane (600 ppm) into one-dimensional aggregates illustrating the influence of the cooling rate on the fiber diameter distribution.[91]

Next to the trigger, i.e. a change in the conditions of the self-assembly system, the *external factors* include also constant factors, that are not changed during the aggregation process. These unaltered parameters can be the solvent - more precisely the medium - in which the self-assembly takes place.[92] Fundamental investigations demonstrate the influence of the solvent on the final supramolecular architecture of 1,3,5-benzenetrisamide derivatives with halogene substituents.[93] Other groups present the possibility to form either vesicular or reverse-vesicular structures from the same amphiphilic building block depending on the used solvent (Figure 8).[94] The naphthalenediimide derivative self-assembles due to a

combination of an hydrogen-bonding amide moiety and the π-stacking of the chromophore into vesicular structures. However, depending on the polarity of the solvent i.e. water or toluene, the amphiphilic molecule interacts with the solvent either with the hydrophilic or the hydrophobic sidechains. Consequently, this compound forms vesicles in water and reverse vesicles in toluene.

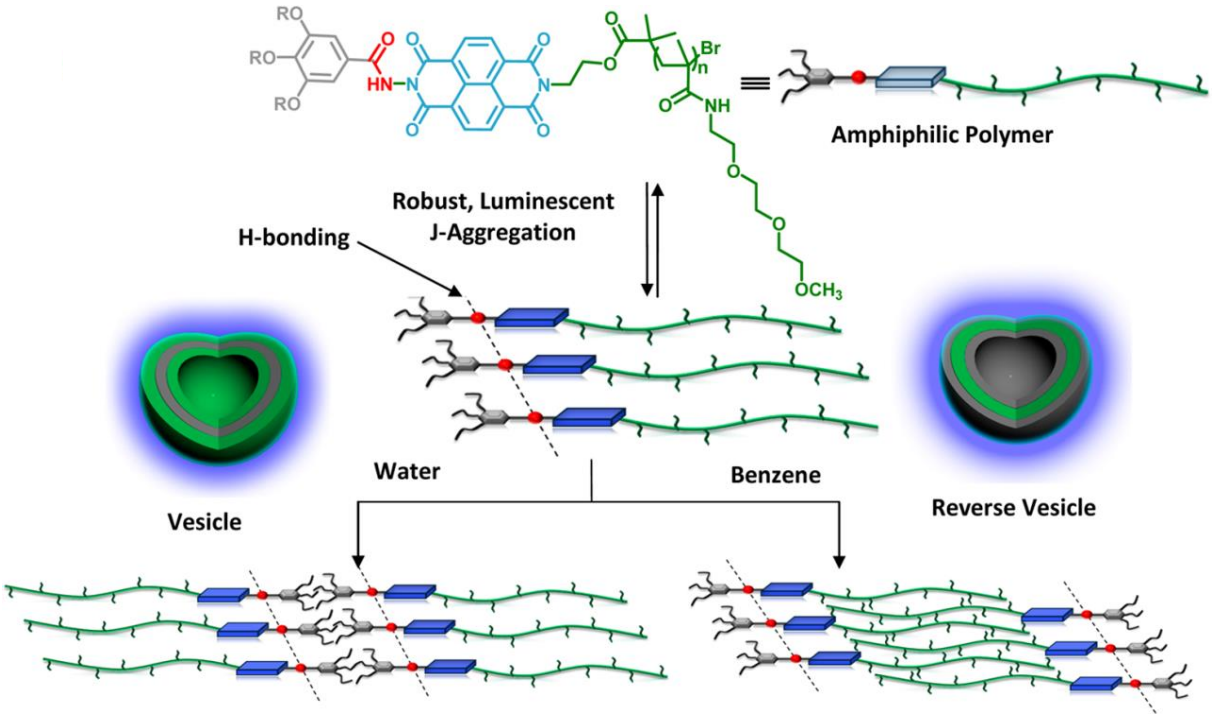

Figure 8. External factors: Influence of solvents. Self-assembly of an amphiphilic naphthalene diimide derivative into either vesicles or reverse vesicles depending on the solvent polarity.[94]

Furthermore, it has been shown that other external influences, like sonication during a self-assembly process upon cooling can also have an influence on the resulting supramolecular morphology.[95,96]

Owing to the delicate interactions of the three factors (thermodynamics and kinetics, internal, and external factors) it is not an easy task for scientists to understand and precisely control supramolecular chemistry. Nature gives us some astonishing examples of what is achievable utilizing the powerful tools of intermolecular interactions. To successfully imitate or even improve the highly functional and efficient biological systems a lot of fundamental work is still necessary. Nevertheless, with DNA origami the first steps towards predictable supramolecular architectures have been taken.

1.3. Supramolecular Aggregation via Directional Hydrogen Bonds

1-Dimensional Aggregates

Supramolecular building blocks that grow preferentially in a single direction are capable to self-assemble into one-dimensional architectures.[97–100] The obtained objects usually exhibit a pronounced aspect-ratio of length to diameter resulting in remarkable length to thickness aspect-ratios.[101,102] For one dimensional supramolecular architectures the thickness ranges from nanometers up to a few micrometers whereas the length is several magnitudes higher.[103–105] The shape and the size of the cross-section of the one-dimensional architectures can differ depending on the molecular structure of the individual building blocks leading to a variety of supramolecular morphologies, like fibers, ribbons or belts, and single or double walled tubes.[23,106–109] All of these morphologies feature appealing intrinsic properties for a variety of applications.[110–113] Pronounced one-dimensional self-assembly into fibrillar aggregates of extraordinary length results often in aggregates allowing for the utilization of these compounds as efficient hydro- and organo-gelators. Here, small tailored supramolecular building blocks enable gelation upon different external stimuli *e.g.* temperature, pH, light, ultrasonic sound.[114–118] Furthermore, the unidirectional nature of the aggregates in combination with aromatic π-functional systems is highly interesting for directed charge or energy transport on the nano-scale. This topic will be discussed in more detail in chapter 1.4.

1,3,5-Benzenetrisamides

A prominent supramolecular building block which is well known to self-assemble into one-dimensional aggregates is the 1,3,5-benzenetrisamide (BTA).[119,120,121] The general structure of BTAs comprises three amide groups which are attached to a central benzene ring either with the nitrogen or the carbonyl unite and form three-fold symmetric hydrogen bonds (Figure 9).[122] Depending on the attached appropriate peripheral substituents, BTAs exhibit a pronounced unidirectional growth perpendicular to the plane of the benzene ring. In the course of the aggregation process the three amide groups twist out of the plane of the central benzene ring by roughly 40° to form three H-bonds to one BTA molecule above and three H-bonds to one BTA molecule below. As a result, the central rings of neighboring benzenetrisamides are stacked parallel to each other but rotated by 60°.[119] Around the central stack of benzene rings the three-fold H-bonds are formed in a helical way holding the aggregates together.[123,124] Besides the dominant unidirectional growth a much less pronounced lateral growth is also observed. The reason for this lateral expanse is assumed to be the formation of a macrodipol which is introduced during the unidirectional aggregation process due to the individual dipoles of the three amide groups. In order to compensate this macrodipole the one-dimensional stacks align in an anti-parallel manner.[122,125,126]

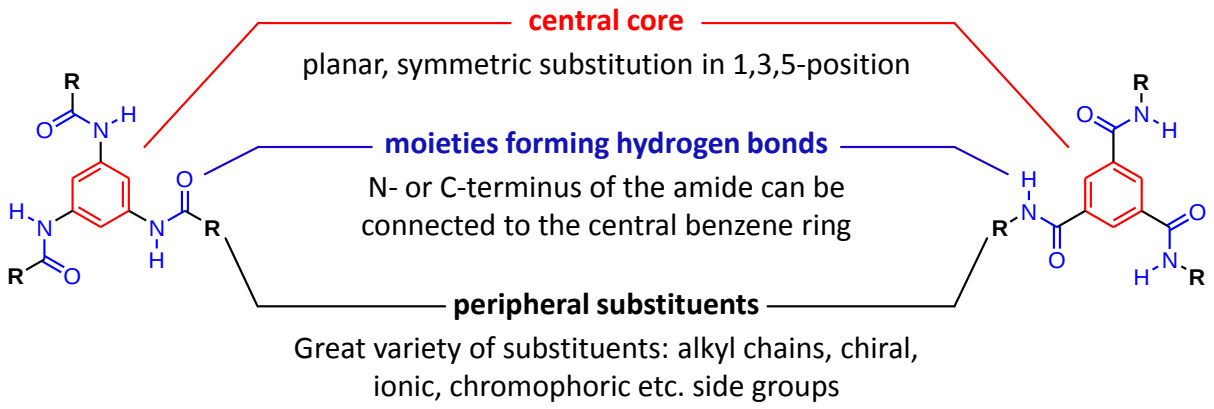

Figure 9. 1,3,5-Benzenetrisamides. Structural features of 1,3,5-benzenetrisamides including the central core, hydrogen bonds forming moieties and the peripheral substituents; left: 1,3,5-benzenetrisamide based on 1,3,5-triaminobenzene; right: 1,3,5-benzenetrisamide based on trimesic acid.

1,3,5-Benzenetrisamides are synthetically readily available and are excellently suited to study structure property relations concerning the self-assembly process. The self-assembly of the class of benzenetrisamides is most commonly described by a cooperative self-assembly mechanism.[127] However, depending on the peripheral substituents isodesmic or anti-cooperative behavior are also known.[60]

Besides their great value for supramolecular chemists to gather basic information and unravel the underlying processes during self-assembly, 1,3,5-benzenetrisamides already proved to be useful for a couple of applications. In this context, the good synthetic accessibility and the great variety of possible peripheral substituents is quite beneficial. Some benzenetrisamides which bear substituents of appropriate polarity were found to act as organo- or hydrogelator.[128–131] Incorporation of benzoic acids into the periphery yielded pH-responsive hydrogelators.[132,133] If equipped with azobenzene moieties, some benzenetrisamides show photo-responsive properties which render them highly appealing as materials for holographic data-storage.[134–136] On the other hand, benzenetrisamides with comparatively simple aliphatic side-chains exhibit great potential as filter media, if the self-assembly into long nanofibers is taking place inside a nonwoven scaffold, which supports the supramolecular network (Figure 10).[137]

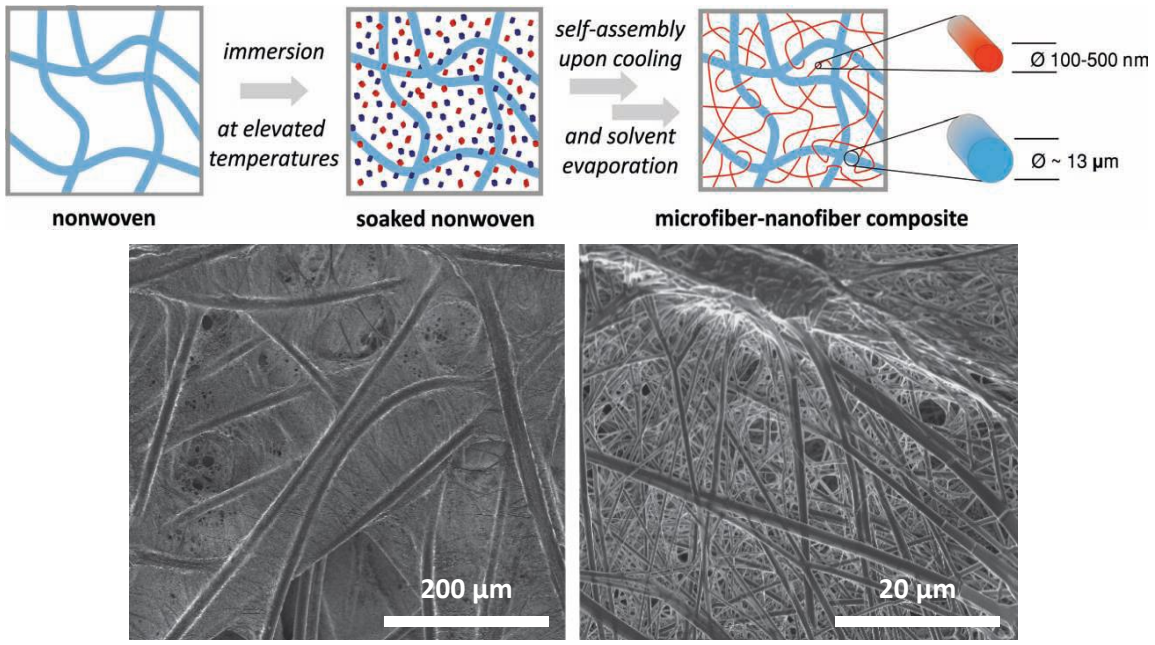

Figure 10. 1,3,5-Benzenetrisamides for filter applications. Self-assembly of supramolecular nanofibers inside a nonwoven scaffold as promising filtration media.[137]

Further applications make use of benzenetrisamides as polymer additives for example to yield electret materials with improved properties or as nucleation and clarification agent. This includes also the first commercially applied benzenetrisamide. Distributed by BASF, Irgaclear XT 386 used in small quantities increases the crystallization temperature of isotactic polypropylene and reduces the haze of the final material (Figure 11).[138,139] The reason for these properties, as revealed by X-ray structure analysis, is the ideal surface of the self-assembled architectures, which promotes epitaxial growth of the polymer.[140]

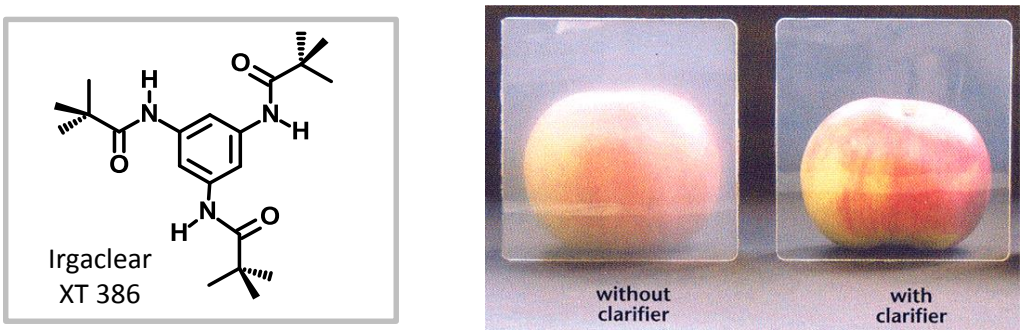

Figure 11. 1,3,5-Benzenetrisamides as polymer additives. Irgaclear XT 386 (left) as nucleation and clarification agent for *i*-PP (right).

Besides these applications in materials science, benzenetrisamides are also investigated in biomedical applications and for the coordination of metal ions.[141,142] In conclusion, 1,3,5-benzenetrisamides are easily accessible and tunable supramolecular building blocks with great potential for a variety of future applications.

1.4. Supramolecular Architectures Containing π-Conjugated Systems

Nature utilizes π-conjugated molecules for biological light harvesting in *e.g*. plants, algae and some classes of bacteria to convert sunlight into a storable energy resource.[143–147] These organisms absorb light in peripheral antenna systems which are self-assembled systems of chromophores within protein scaffolds highly tuned and adapted to the respective light conditions. After the absorption of light, excitons are generated and transferred via a cascade of chromophores from the peripheral antenna systems to the reaction center, where subsequently photosynthesis takes place.[148–151] The energy transport proceeds with remarkable quantum efficiencies of >95% involving more than 200 pigments, which corresponds to a distance of ~20-100 nm.[152] This process is not yet understood in full detail and could to date not be successfully copied in any artificial supramolecular system. However, it is believed that the spatial arrangement and the electronic coupling between the chromophores within the antenna complexes is connected to the high energy transport efficiency.[153–155]

H- and J-Aggregation

The π-stacking aggregation of chromophoric or multichromophoric systems crucially alters the optical properties in comparison to the monomeric species. This is reflected by the shift of the spectral position of absorption and photoluminescence bands and can also lead to distinct deviations of Lambert-Beer law.[156–158] Almost 80 years ago Scheibe and Jelly reported independently on a significant red-shift in the absorption of pseudoisocyanine chloride upon increasing concentration in water. This bathochromic shifted absorption band simultaneously became sharper and more intense, which was explained by the aggregation of the dye molecules in water.[159–163] Since then supramolecular aggregates exhibiting the aforementioned optical changes in the absorption spectra are denoted as Scheibe or J-aggregates, where J refers to Jelly.[164,165] On the other hand, supramolecular aggregates which exhibit a pronounced hypsochromic or blue-shift of the absorption maxima are labeled as H-aggregates. Here, H refers to hypsochromic.[166–168]

In the following a general classification of supramolecular chromophoric assemblies into H- or J-aggregates is given and connected to the respective geometrical and optical properties

as described by several research groups.[169–175] The self-assembly of π-conjugated systems into dimers or higher aggregates usually leads to a splitting of the excited states as depicted in Figure 12. This splitting depends on the number of involved chromophores as well as the coupling strength, and the respective orientation between them.

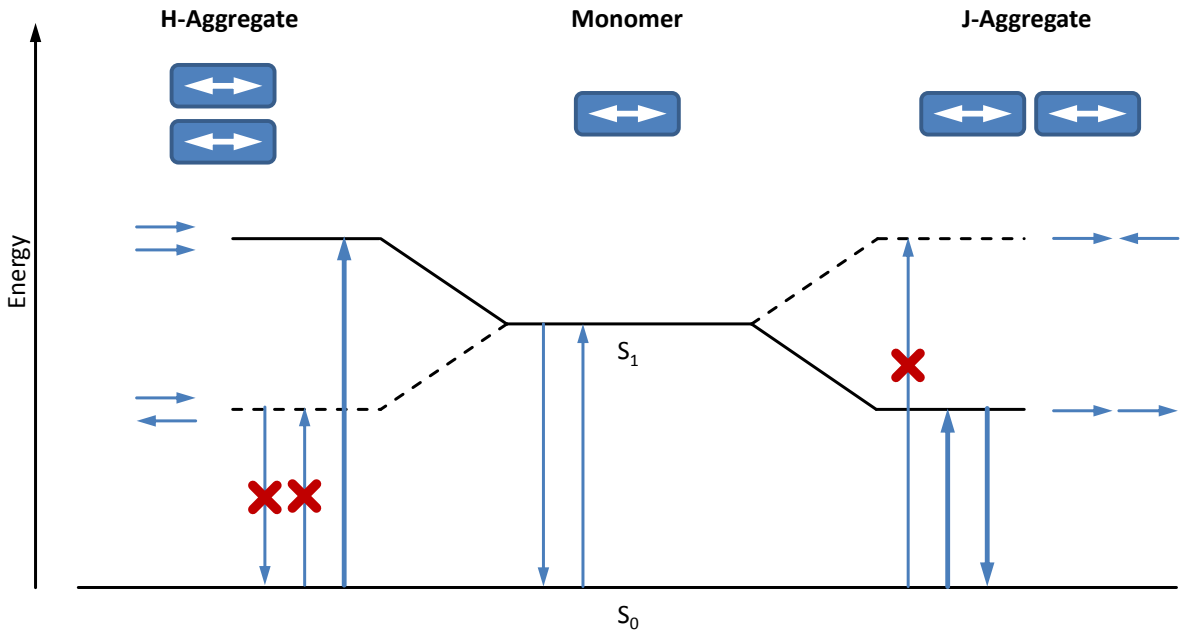

Figure 12. H- and J-aggregates. Simplified energy diagrams for the monomer and for H- and J-type aggregates. The respective geometrical orientations of the chromophores are depicted above the energy diagram and the individual dipole moments are shown next to their corresponding energy levels. In the H-aggregated case the optical transitions between the ground state and the lower energy excited state are forbidden, while in the J-aggregated case the same happens for the higher energy excited state. S_0 and S_1: electronic ground state and first electronically excited state of the monomer.

Using the point dipole approximation Kasha et al. described the splitting theoretically and distinguishes between two limiting cases. If the chromophores are stacked parallel on top of each other in a sandwich type manner, perfect H-aggregation is achieved. In this case the highest-energy excited state results from the case, when both dipole moments are pointing in the same direction, whereas, the lowest-energy excited state results from an antiparallel orientation of the two dipole moments. In this latter case the antiparallel orientation cancels out the overall transition dipole moment, hence, rendering a transition into the lower-energy excited state forbidden. On the other hand, in perfect J-aggregates i.e. a head-to-tail orientation, the first excited state is again splitted due to the coupling of the chromophores.

Here, by a similar line of argumentation, the transition to the highest-energy state is, however, forbidden, while the transition to the lowest-energy state is allowed. As a consequence, a blue-shifted (H-type) or a red-shifted (J-type) absorption is observed (Figure 12). In both cases, after excitation, a rapid relaxation to the lowest-energy excited state occurs from which the subsequent relaxation to the ground state takes place. As radiant transitions between the lower-energy excited state and the ground state are forbidden in H-aggregates, these species are hardly fluorescent. J-aggregates on the other hand are superradiant due to the enhanced transition dipole moment. Furthermore, for H- or J-aggregates a large, respectively, a small Stokes' shift is to be expected (Figure 12).

An extension of Kasha's theory describing the spectral effects of H- and J-aggregation, was done by Frank Spano, who includes the consideration of vibrational states.[170,174] Spano demonstrates the possibility to determine the nearest neighbor coupling of the aggregates from their absorption spectra. For that, he takes into account the intensity ratios of transitions from the ground state to the first and second (or higher) vibrational states in the exciton states. In all theoretic considerations further effects like the polarity of the environment, which also influence the optical properties of the chromophoric systems, are usually neglected. As a consequence of these additional effects an assignment of a supramolecular chromophoric system to the classes of H- or J-aggregates is not always straightforward and needs thorough investigation.

Supramolecular π-Conjugated Materials

Artificial π-conjugated aromatic systems are promising candidates to serve as active materials in a number of advanced optoelectronic and electronic applications *e.g.* sensors, field effect transistors, photovoltaic devices or logical gates.[50,99,165,176–178] In this bulk implementations not only the properties of the isolated π-conjugated systems but of the whole ensemble is crucial, which makes it important to precisely orient and position the chromophores to each other.[179,180] Supramolecular chromophoric building blocks are perfectly suited to meet this task, yielding new materials with tunable optical and electronic properties.[181,182] Furthermore, they combine the advantages of controlled structural definition and monodispersity with the ease of processing known from polymers.[183] In this context the self-assembly is driven either exclusively by π-stacking[184,185] of the chromophores or in combination with second intermolecular interactions.[186]

The group of Klaus Müllen exploits the strong π-stacking of hexabenzocoronenes as discotic aromatic systems to obtain self-assembled helical columnar structures.[187,188] In the group of Takuzo Aida the π-stacking of hexabenzocoronenes was further supported by weak and non-directional hydrophilic-hydrophobic interactions. As a result, this amphiphilic system self-assembles into defined nanotubes with a homogenous diameter of only a couple of nanometers and an aspect ratio of greater than 1000 (Figure 13). Other derivatives of this supramolecular building block show promising results as organic semiconductor[189,190] and energy transport material[191].

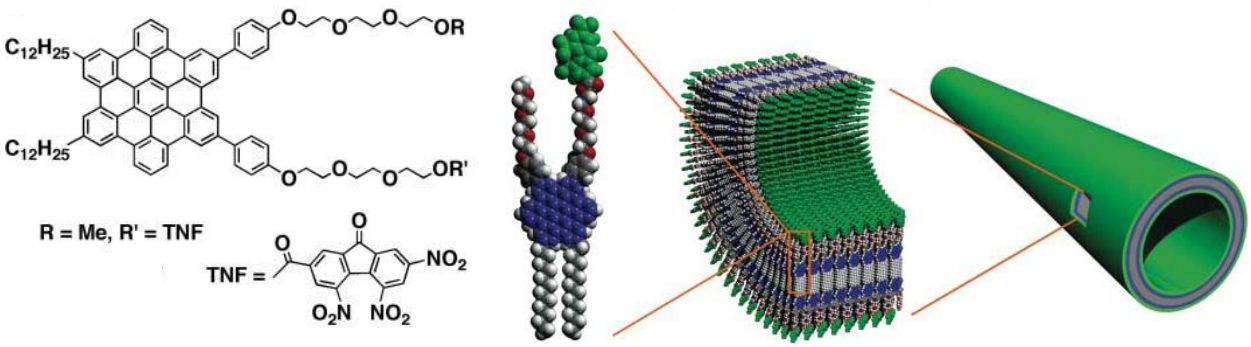

Figure 13. Self-assembly driven mainly by π-stacking. Self-assembly of an amphiphilic hexa-peri-hexabenzocoronene into double-walled nanotubes, mainly driven by strong π-stacking. The lateral electron poor trinitrofluorenones enable spatial charge separation accompanied by a quick photoconductive response with large on/off ratio.[190]

In many cases, the supramolecular assemblies of π-conjugated aromatic systems are supported by additional H-bonding moieties due to the favorable properties of this second intermolecular interaction *i.e*. high selectivity and directionality. Those supramolecular assemblies can be further distinguished, depending on whether the H-bonds point along or perpendicular to the π-stacking axis.[70,111,192] In the first case H-bonds can help to stabilize the resulting supramolecular structure and precisely control the stacking position of the chromophoric moieties. This was illustrated by the group of Würthner using perylene bisimides. Depending on the fashion of the H-bonding substituents the chromophores form either H-type or J-type aggregates and consequently exhibit quite different optical properties.[193] In other examples, the supramolecular motif of 1,3,5-benzenetrisamides, equipped with lateral triphenylenes, was used to obtain one-dimensional aggregates with improved charge carrier mobility.[194,195] In a joint attempt of the groups of Würthner, Schenning and Meijer the strong recognition of imides and diaminotriazines was used to couple oligophenylenevinylenes as p-type moiety with perylenebisimides as n-type moiety. The obtained p-n-p type junction was formed by triple H-bonding perpendicular to the π-stacking axis of the involved chromophores (Figure 14).[196,197] This orthogonal self-assembly resulted in supramolecular nano-fibers envisioned for antiparallel transport of charges and holes.

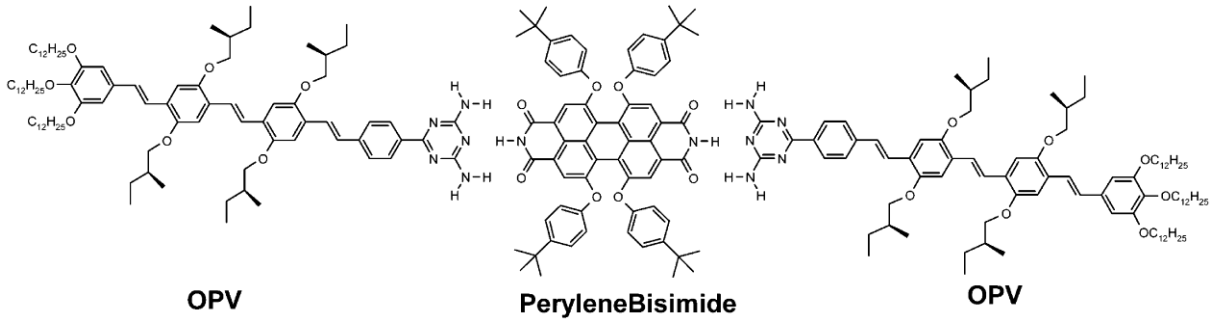

Figure 14. Self-assembly driven by π-stacking in combination with H-bonding. Aggregation of an oligo(*p*-phenylenevinylene) derivative and a perylene bisimide into a p-n-p type junction.[111]

A different approach, which recently got increasing attention, employs “mixed stack charge transfer” assemblies to obtain supramolecular architectures with increased conducting properties due to inherent, uniform doping.[67,198] This is achieved by alternating assembly of π-conjugated donor and acceptor compounds.[199,200] In order to ensure an alternate stacking of donor and acceptor moieties many design strategies are pursued involving the use of H-bonds, supramolecular amphiphiles and bolaamphiphiles.[201–204] The group of Subi J. George used a non-covalent, amphiphilic design employing a coronene salt in combination with a viologene derivative yielding cylindrical nano-fibers with good p-type conductor properties and record field effect mobility values (Figure 15).[205]

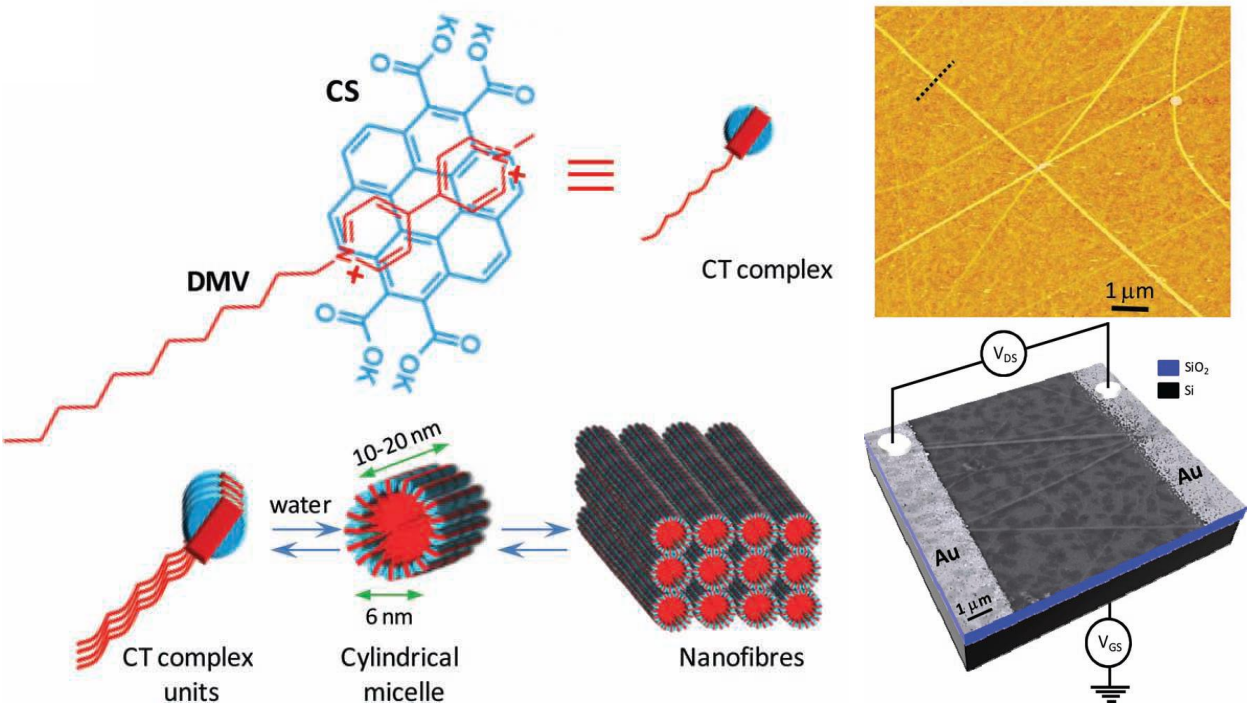

Figure 15. Self-assembly driven by donor acceptor π-stacking. Alternated self-assembly of electron rich coronene salts (CS, donor) with electron poor viologene derivatives (DMV, acceptor) into cylindrical micelles and nanofibers with remarkable field effect mobility.[205]

An ambitious goal is pursued by the group of Stefan Matile, who wants to achieve self-assembled organic solar cells with precise architecture and functionality.[206,207] In this concept, a layer-by-layer assembly is used to generate solar cells with fine-tuned morphology exhibiting a broad absorption range, large n/p heterojunction interfaces in combination with continuous pathways for electrons and holes along a directing redox-

gradient. These self-assembled heterojunction devices with “oriented multichromophoric antiparallel redox gradients” represent an ideal morphology for organic solar cells. To achieve this goal *p*-oligophenyls or *p*-oligophenylethynyls acting as electron-donor backbone were equipped with electron accepting naphthalenediimides of suitable HOMO and LUMO levels and band gaps. The naphthalimides were, furthermore, functionalized either with cationic or anionic side chains allowing for layer-by-layer zipper self-assembly as shown in figure 16. The complex design of these supramolecular building blocks makes use of π,π-stacking, intrastack hydrogen bonding and interstack ion pairing. Although currently the organic solar cell characteristics of these systems are not among the best performing devices, they achieved promising results and illustrate the power of intermolecular interactions to precisely control the architecture of supramolecular assemblies.

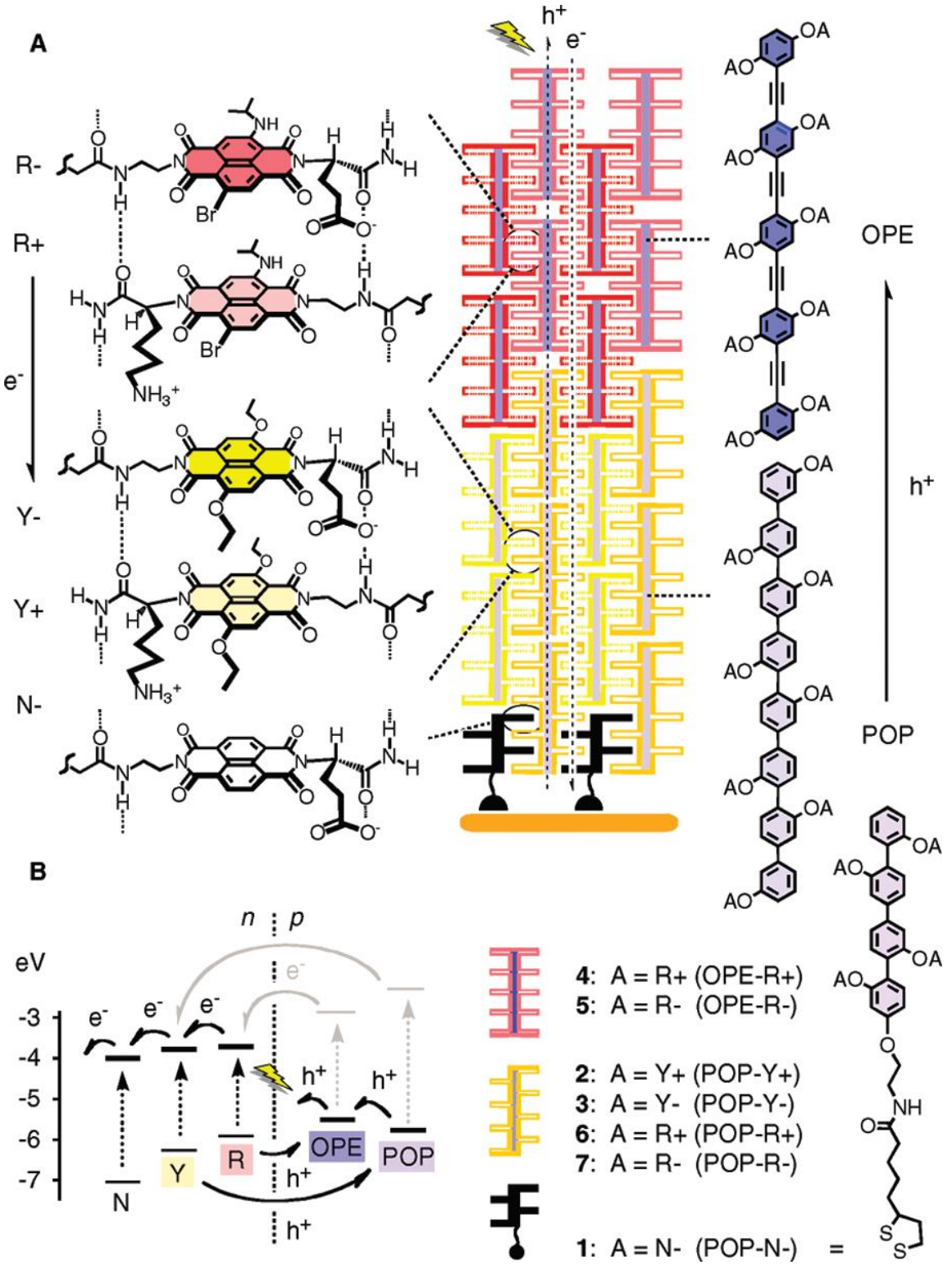

Figure 16. **A**: Molecular structures and suggested architecture of a oriented multichromophoric antiparallel redox gradients supramolecular n/p heterojunction of *p*-oligophenyl POP-N initiator (**1**) and *p*-oligophenyl POP-Y (**2**, **3**) and *p*-oligophenylethynyl POE-R (**4**, **5**) propagators on gold. **B**: HOMO and LUMO levels show photo-induced (dashed arrows) e^- (gray) and h^+ (black) injection into e^- (n)- and h^+ (p)-transportation pathways (bold).[207]

Planarized Triarylamines - an Emerging π-System

Planarized triarylamines so called heterotriangulenes[208,209] are chromophoric building blocks, which are recently getting increasing attention due to their optical and self-assembly properties (Figure 17).[210–212] For example, some of these chromophores were already investigated as active materials in opto-electronic devices like organic solar cells or organic light emitting diodes.[213–217] Equipped with suitable substituents, planarized triarylamines are able to self-assemble in solution, on surfaces and in the bulk.[218,219] For these compounds efficient π-stacking is the main driving force leading to the formation of supramolecular aggregates. Noteworthy representatives from the class of heterotriangulenes are the perfectly planar carbonyl-bridged triarylamines, which possess a high tendency to self-assemble into columnar structures.[220,221] These particular chromophores are comparatively electron deficient due to the three bridging carbonyl moieties.

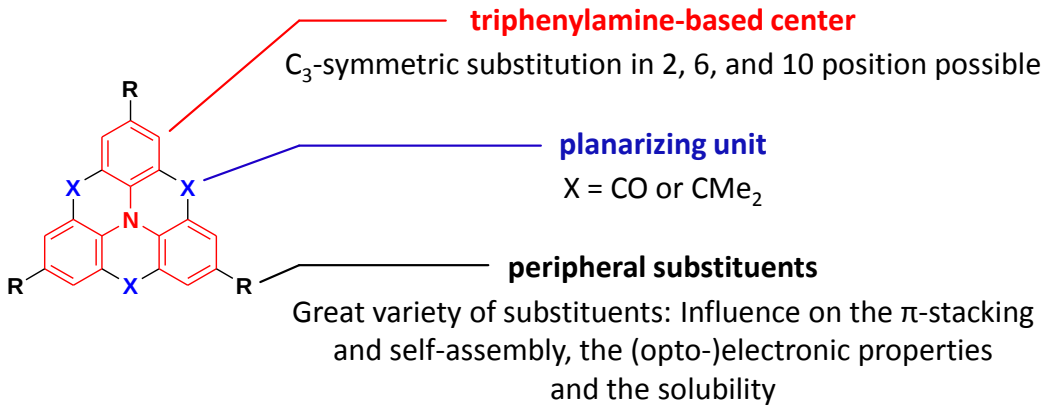

Figure 17. Planarized triarylamines. Structural features of planarized triarylamines so called heterotriangulenes including the planarized triphenylamine, bridging unit and the peripheral substituents.

1.5. References

1. G. F. Joyce; RNA evolution and the origins of life, *Nature* **1989**, *338,* 217–224.
2. O. Leslie E.; Prebiotic Chemistry and the Origin of the RNA World, *Critical Reviews in Biochemistry and Molecular Biology* **2004**, *39,* 99–123.
3. P. Reichard; From RNA to DNA, why so many ribonucleotide reductases?, *Science* **1993**, *260,* 1773–1777.
4. M. Kozak; The scanning model for translation: an update, *The Journal of Cell Biology* **1989**, *108,* 229–241.
5. V. Ramakrishnan; Ribosome Structure and the Mechanism of Translation, *Cell* **2002**, *108,* 557–572.
6. T. A. Steitz; A structural understanding of the dynamic ribosome machine, *Nat Rev Mol Cell Biol* **2008**, *9,* 242–253.
7. F. Schluenzen, A. Tocilj, R. Zarivach, J. Harms, M. Gluehmann, D. Janell, A. Bashan, H. Bartels, I. Agmon, F. Franceschi, A. Yonath; Structure of Functionally Activated Small Ribosomal Subunit at 3.3 Å Resolution, *Cell* **2000**, *102,* 615–623.
8. P. B. Moore, T. A. Steitz; The involvement of RNA in ribosome function, *Nature* **2002**, *418,* 229–235.
9. J. Venema, D. Tollervey; Ribosome Synthesis in Saccharomyces Cerevisiae, *Annu. Rev. Genet.* **1999**, *33,* 261–311.
10. A. Fatica, D. Tollervey; Making ribosomes, *Current Opinion in Cell Biology* **2002**, *14,* 313–318.
11. A. Bashan, I. Agmon, R. Zarivach, F. Schluenzen, J. Harms, R. Berisio, H. Bartels, F. Franceschi, T. Auerbach, H. A. Hansen, E. Kossoy, M. Kessler, A. Yonath; Structural Basis of the Ribosomal Machinery for Peptide Bond Formation, Translocation, and Nascent Chain Progression, *Molecular Cell* **2003**, *11,* 91–102.
12. A. Yonath; Hibernating Bears, Antibiotics, and the Evolving Ribosome, *Angew. Chem. Int. Ed.* **2010**, *49,* 4340–4354.
13. C. B. Anfinsen; Principles that Govern the Folding of Protein Chains, *Science* **1973**, *181,* 223–230.
14. C. M. Dobson; Protein folding and misfolding, *Nature* **2003**, *426,* 884–890.
15. S. Neidle. *Nucleic acid structure and recognition* (Oxford University Press, Oxford, New York, 2002).
16. J. M. Berg, J. L. Tymoczko, L. Stryer, N. D. Clarke. *Biochemistry.* 5th ed. (Freeman and Company, New York, op. 2002).
17. S. Casjens, J. King; Virus Assembly, *Annu. Rev. Biochem.* **1975**, *44,* 555–611.

18. A. Klug; The tobacco mosaic virus particle: structure and assembly, *Philosophical Transactions of the Royal Society B: Biological Sciences* **1999**, *354,* 531–535.

19. P.-A. Monnard, D. W. Deamer; Membrane self-assembly processes: Steps toward the first cellular life, *Anat. Rec.* **2002**, *268,* 196–207.

20. A. Pohorille, D. Deamer; Self-assembly and function of primitive cell membranes, *Research in Microbiology* **2009**, *160,* 449–456.

21. P. Ball; Natural strategies for the molecular engineer, *Nanotechnology* **2002**, *13,* R15-R28.

22. D. Philp, J. F. Stoddart; Self-Assembly in Natural and Unnatural Systems, *Angew. Chem. Int. Ed. Engl.* **1996**, *35,* 1154–1196.

23. S. I. Stupp, L. C. Palmer; Supramolecular Chemistry and Self-Assembly in Organic Materials Design, *Chem. Mater.* **2014**, *26,* 507–518.

24. J. Tian; Supramolecular chemistry, *Annu. Rep. Prog. Chem. Sect. B: Org. Chem.* **2012**, *108,* 171-185.

25. D. J. Cram; The Design of Molecular Hosts, Guests, and Their Complexes, *Angew. Chem. Int. Ed. Engl.* **1988**, *27,* 1009–1020.

26. J.-M. Lehn; Supramolecular Chemistry—Scope and Perspectives Molecules, Supermolecules, and Molecular Devices, *Angew. Chem. Int. Ed. Engl.* **1988**, *27,* 89–112.

27. C. J. Pedersen; The Discovery of Crown Ethers, *Angew. Chem. Int. Ed. Engl.* **1988**, *27,* 1021–1027.

28. J. W. Steed, D. R. Turner, K. J. Wallace. *Core concepts in supramolecular chemistry and nanochemistry* (John Wiley, Chichester, England, Hoboken, NJ, 2007).

29. J. L. Atwood, J. W. Steed. *Supramolecular chemistry* (Wiley, Hoboken, N.J, 2013).

30. G. Whitesides, J. Mathias, C. Seto; Molecular self-assembly and nanochemistry: a chemical strategy for the synthesis of nanostructures, *Science* **1991**, *254,* 1312–1319.

31. G. M. Whitesides, M. Boncheva; Beyond molecules: Self-assembly of mesoscopic and macroscopic components, *Proceedings of the National Academy of Sciences* **2002**, *99,* 4769–4774.

32. G. M. Whitesides; Self-Assembly at All Scales, *Science* **2002**, *295,* 2418–2421.

33. P. J. Cragg. *Supramolecular chemistry. From biological inspiration to biomedical applications* (Springer, Dordrecht, New York, 2010).

34. M. C. T. Fyfe, J. F. Stoddart; Synthetic Supramolecular Chemistry, *Acc. Chem. Res.* **1997**, *30,* 393–401.

35. J. Lehn; Supramolecular chemistry, *Science* **1993**, *260,* 1762–1763.

36. J.-M. Lehn; Supramolecular polymer chemistry-scope and perspectives, *Polym. Int.* **2002**, *51,* 825–839.

37. J.-M. Lehn; Toward Self-Organization and Complex Matter, *Science* **2002**, *295,* 2400–2403.

38. A. Werner; Zur Kenntnis des asymmetrischen Kobaltatoms. I, *Ber. Dtsch. Chem. Ges.* **1911**, *44,* 1887–1898.

39. A. Werner; über die Konstitution und Konfiguration von Verbindungen höherer Ordnung, *Naturwissenschaften* **1914**, *2,* 1–7.

40. J.-M. Lehn; Dynamic Combinatorial Chemistry and Virtual Combinatorial Libraries, *Chem. Eur. J.* **1999**, *5,* 2455–2463.

41. M. Ruben, J. Rojo, F. J. Romero-Salguero, L. H. Uppadine, J.-M. Lehn; Grid-Type Metal Ion Architectures: Functional Metallosupramolecular Arrays, *Angew. Chem. Int. Ed.* **2004**, *43,* 3644–3662.

42. G. M. Whitesides, E. E. Simanek, J. P. Mathias, C. T. Seto, D. Chin, M. Mammen, D. M. Gordon; Noncovalent Synthesis: Using Physical-Organic Chemistry To Make Aggregates, *Acc. Chem. Res.* **1995**, *28,* 37–44.

43. P. W. K. Rothemund; Folding DNA to create nanoscale shapes and patterns, *Nature* **2006**, *440,* 297–302.

44. D. Han, S. Pal, J. Nangreave, Z. Deng, Y. Liu, H. Yan; DNA Origami with Complex Curvatures in Three-Dimensional Space, *Science* **2011**, *332,* 342–346.

45. B. Saccà, C. M. Niemeyer; DNA Origami: The Art of Folding DNA, *Angew. Chem. Int. Ed.* **2012**, *51,* 58–66.

46. K. Sanderson; Bioengineering: What to make with DNA origami, *Nature* **2010**, *464,* 158–159.

47. B. Ding, Z. Deng, H. Yan, S. Cabrini, R. N. Zuckermann, J. Bokor; Gold Nanoparticle Self-Similar Chain Structure Organized by DNA Origami, *J. Am. Chem. Soc.* **2010**, *132,* 3248–3249.

48. E. S. Andersen, M. Dong, M. M. Nielsen, K. Jahn, R. Subramani, W. Mamdouh, M. M. Golas, B. Sander, H. Stark, C. L. P. Oliveira, J. S. Pedersen, V. Birkedal, F. Besenbacher, K. V. Gothelf, J. Kjems; Self-assembly of a nanoscale DNA box with a controllable lid, *Nature* **2009**, *459,* 73–76.

49. M.-C. Daniel, D. Astruc; Gold Nanoparticles: Assembly, Supramolecular Chemistry, Quantum-Size-Related Properties, and Applications toward Biology, Catalysis, and Nanotechnology, *Chem. Rev.* **2004**, *104,* 293–346.

50. A. R. Hirst, B. Escuder, J. F. Miravet, D. K. Smith; High-Tech Applications of Self-Assembling Supramolecular Nanostructured Gel-Phase Materials: From Regenerative Medicine to Electronic Devices, *Angew. Chem. Int. Ed.* **2008**, *47,* 8002–8018.

51. J. W. Steed; Anion-tuned supramolecular gels: a natural evolution from urea supramolecular chemistry, *Chem. Soc. Rev.* **2010**, *39,* 3686-3699.

52. M. Barboiu, J.-M. Lehn; Dynamic chemical devices: Modulation of contraction/extension molecular motion by coupled-ion binding/pH change-induced structural switching, *Proceedings of the National Academy of Sciences* **2002**, *99,* 5201–5206.

53. K. K. Cotí, M. E. Belowich, M. Liong, M. W. Ambrogio, Y. A. Lau, H. A. Khatib, J. I. Zink, N. M. Khashab, J. F. Stoddart; Mechanised nanoparticles for drug delivery, *Nanoscale* **2009**, *1,* 16-39.

54. F. Ercole, T. P. Davis, R. A. Evans; Photo-responsive systems and biomaterials: photochromic polymers, light-triggered self-assembly, surface modification, fluorescence modulation and beyond, *Polym. Chem.* **2010**, *1,* 37-54.

55. H.-J. Kim, T. Kim, M. Lee; Responsive Nanostructures from Aqueous Assembly of Rigid−Flexible Block Molecules, *Acc. Chem. Res.* **2011**, *44,* 72–82.

56. H.-J. Schneider, R. M. Strongin; Supramolecular Interactions in Chemomechanical Polymers, *Acc. Chem. Res.* **2009**, *42,* 1489–1500.

57. C. Tsitsilianis; Responsive reversible hydrogels from associative "smart" macromolecules, *Soft Matter* **2010**, *6,* 2372-2388.

58. Y. Wang, H. Xu, X. Zhang; Tuning the Amphiphilicity of Building Blocks: Controlled Self-Assembly and Disassembly for Functional Supramolecular Materials, *Adv. Mater.* **2009**, *21,* 2849–2864.

59. L. Maggini, D. Bonifazi; Hierarchised luminescent organic architectures: design, synthesis, self-assembly, self-organisation and functions, *Chem. Soc. Rev.* **2011**, *41,* 211-241.

60. T. F. A. de Greef, M. M. J. Smulders, M. Wolffs, A. P. H. J. Schenning, R. P. Sijbesma, E. W. Meijer; Supramolecular Polymerization, *Chem. Rev.* **2009**, *109,* 5687–5754.

61. P. A. Korevaar, T. F. A. de Greef, E. W. Meijer; Pathway Complexity in π-Conjugated Materials, *Chem. Mater.* **2014**, *26,* 576–586.

62. M. A. J. Gillissen, T. T. Hoeben, A. J. H. Spiering, J. A. J. M. Vekemans, A. R. A. Palmans, E. W. Meijer; Supramolecular Chirality Using Both Cooperative and Isodesmic Self-Assembly: hierarchical growth through competition, *Isr. J. Chem.* **2011**, *51,* 1118–1127.

63. T. Metzroth, A. Hoffmann, R. Martín-Rapún, M. M. J. Smulders, K. Pieterse, A. R. A. Palmans, J. A. J. M. Vekemans, E. W. Meijer, H. W. Spiess, J. Gauss; Unravelling the fine structure of stacked bipyridine diamine-derived C3-discotics as determined by X-ray diffraction, quantum-chemical calculations, Fast-MAS NMR and CD spectroscopy, *Chem. Sci.* **2010**, *2,* 69-76.

64. M. M. J. Smulders, M. M. L. Nieuwenhuizen, T. F. A. de Greef, P. van der Schoot, A. P. H. J. Schenning, E. W. Meijer; How to Distinguish Isodesmic from Cooperative Supramolecular Polymerisation, *Chem. Eur. J.* **2010**, *16,* 362–367.

65. C. Kulkarni, R. Munirathinam, S. J. George; Self-Assembly of Coronene Bisimides: Mechanistic Insight and Chiral Amplification, *Chem. Eur. J.* **2013**, *19,* 11270–11278.

66. B. Narayan, C. Kulkarni, S. J. George; Synthesis and self-assembly of a C3-symmetric benzene-1,3,5-tricarboxamide (BTA) anchored naphthalene diimide disc, *J. Mater. Chem. C* **2012**, *1,* 626-629.

67. K. Tambara, J.-C. Olsen, D. E. Hansen, G. D. Pantoş; The thermodynamics of the self-assembly of covalently linked oligomeric naphthalenediimides into helical organic nanotubes, *Org. Biomol. Chem.* **2013**, *12,* 607-614.

68. I. A. W. Filot, A. R. A. Palmans, P. A. J. Hilbers, R. A. van Santen, E. A. Pidko, T. F. A. de Greef; Understanding Cooperativity in Hydrogen-Bond-Induced Supramolecular Polymerization: A Density Functional Theory Study, *J. Phys. Chem. B* **2010**, *114,* 13667–13674.

69. C. A. Hunter, H. L. Anderson; What is Cooperativity?, *Angew. Chem. Int. Ed.* **2009**, *48,* 7488–7499.

70. P. Jonkheijm; Probing the Solvent-Assisted Nucleation Pathway in Chemical Self-Assembly, *Science* **2006**, *313,* 80–83.

71. S. Cantekin, H. M. M. ten Eikelder, A. J. Markvoort, M. A. J. Veld, P. A. Korevaar, M. M. Green, A. R. A. Palmans, E. W. Meijer; Consequences of Cooperativity in Racemizing Supramolecular Systems, *Angew. Chem. Int. Ed.* **2012**, *51,* 6426–6431.

72. C.-A. Palma, M. Cecchini, P. Samorì; Predicting self-assembly: from empirism to determinism, *Chem. Soc. Rev.* **2012**, *41,* 3713-3730.

73. C. Piguet; Five thermodynamic describers for addressing serendipity in the self-assembly of polynuclear complexes in solution, *Chem. Commun.* **2010**, *46,* 6209-6231.

74. S. Ogi, K. Sugiyasu, S. Manna, S. Samitsu, M. Takeuchi; Living supramolecular polymerization realized through a biomimetic approach, *Nature Chem* **2014**, *6,* 188–195.

75. P. Dastidar; Supramolecular gelling agents: can they be designed?, *Chem. Soc. Rev.* **2008**, *37,* 2699-2715.

76. J. R. Nitschke; Construction, Substitution, and Sorting of Metallo-organic Structures via Subcomponent Self-Assembly, *Acc. Chem. Res.* **2007**, *40,* 103–112.

77. M. Shimomura, T. Sawadaishi; Bottom-up strategy of materials fabrication: a new trend in nanotechnology of soft materials, *Current Opinion in Colloid & Interface Science* **2001**, *6,* 11–16.

78. H. Kar, S. Ghosh; Three component assemblies by orthogonal H-bonding and donor–acceptor charge–transfer interaction, *Chem. Commun.* **2013**, *50,* 1064-1066.

79. H. Kar, M. R. Molla, S. Ghosh; Two-component gelation and morphology-dependent conductivity of a naphthalene-diimide (NDI) π-system by orthogonal hydrogen bonding, *Chem. Commun.* **2013**, *49,* 4220-4222.

80. M. R. Molla, D. Gehrig, L. Roy, V. Kamm, A. Paul, F. Laquai, S. Ghosh; Self-Assembly of Carboxylic Acid Appended Naphthalene Diimide Derivatives with Tunable Luminescent Color and Electrical Conductivity, *Chem. Eur. J.* **2014**, *20,* 760–771.

81. A. Das, M. R. Molla, S. Ghosh; Comparative self-assembly studies and self-sorting of two structurally isomeric naphthalene-diimide (NDI)-gelators, *J Chem Sci* **2011**, *123,* 963–973.

82. A. Das, M. R. Molla, B. Maity, D. Koley, S. Ghosh; Hydrogen-Bonding Induced Alternate Stacking of Donor (D) and Acceptor (A) Chromophores and their Supramolecular Switching to Segregated States, *Chem. Eur. J.* **2012**, *18,* 9849–9859.

83. J. Lee, K. Baek, M. Kim, G. Yun, Y. H. Ko, N.-S. Lee, I. Hwang, J. Kim, R. Natarajan, C. G. Park, W. Sung, K. Kim; Hollow nanotubular toroidal polymer microrings, *Nature Chem* **2014**, *6,* 97–103.

84. P. Duan, Y. Li, L. Li, J. Deng, M. Liu; Multiresponsive Chiroptical Switch of an Azobenzene-Containing Lipid: Solvent, Temperature, and Photoregulated Supramolecular Chirality, *J. Phys. Chem. B* **2011**, *115,* 3322–3329.

85. D. S. Kim, V. M. Lynch, J. S. Park, J. L. Sessler; Three Distinct Equilibrium States via Self-Assembly: Simple Access to a Supramolecular Ion-Controlled NAND Logic Gate, *J. Am. Chem. Soc.* **2013**, *135,* 14889–14894.

86. T. T. H. Pham, J. Wang, M. W. T. Werten, F. Snijkers, F. A. de Wolf, M. A. Cohen Stuart, J. van der Gucht; Multi-responsive physical gels formed by a biosynthetic asymmetric triblock protein polymer and a polyanion, *Soft Matter* **2013**, *9,* 8923-8930.

87. M. Xu, L. Chen, Y. Zhou, T. Yi, F. Li, C. Huang; Multiresponsive self-assembled liquid crystals with azobenzene groups, *Journal of Colloid and Interface Science* **2008**, *326,* 496–502.

88. X. Yan, D. Xu, X. Chi, J. Chen, S. Dong, X. Ding, Y. Yu, F. Huang; A Multiresponsive, Shape-Persistent, and Elastic Supramolecular Polymer Network Gel Constructed by Orthogonal Self-Assembly, *Adv. Mater.* **2012**, *24,* 362–369.

89. A. Das, S. Ghosh; Stimuli-Responsive Self-Assembly of a Naphthalene Diimide by Orthogonal Hydrogen Bonding and Its Coassembly with a Pyrene Derivative by a Pseudo-Intramolecular Charge-Transfer Interaction, *Angew. Chem. Int. Ed.* **2014**, *53,* 1092–1097.

90. S. Yagai, Y. Nakano, S. Seki, A. Asano, T. Okubo, T. Isoshima, T. Karatsu, A. Kitamura, Y. Kikkawa; Supramolecularly Engineered Aggregation of a Dipolar Dye: Vesicular and Ribbonlike Architectures, *Angew. Chem. Int. Ed.* **2010**, *49,* 9990–9994.

91 F. Abraham; Synthesis and structure-property relations of 1,3,5-benzenetrisamides as nucleating agents for isotactic polypropylene and poly(vinylidene fluoride), *Dissertation Universität Bayreuth* **2009**.

92. M. A. J. Gillissen, M. M. E. Koenigs, J. J. H. Spiering, J. A. J. M. Vekemans, A. R. A. Palmans, I. K. Voets, E. W. Meijer; Triple Helix Formation in Amphiphilic Discotics: Demystifying Solvent Effects in Supramolecular Self-Assembly, *J. Am. Chem. Soc.* **2014**, *136,* 336–343.

93. L. Rajput, G. Mukherjee, K. Biradha; Influence of Solvents in Assembling Tris(4-halophenyl)benzene-1,3,5-tricarboxamides: Interplay of N–H···O and Halogen···Halogen Interactions, *Crystal Growth & Design* **2012**, *12,* 5773–5782.

94. A. Das, S. Ghosh; Luminescent Invertible Polymersome by Remarkably Stable Supramolecular Assembly of Naphthalene Diimide (NDI) π-System, *Macromolecules* **2013**, *46,* 3939–3949.

95. J. Wu, T. Yi, Q. Xia, Y. Zou, F. Liu, J. Dong, T. Shu, F. Li, C. Huang; Tunable Gel Formation by Both Sonication and Thermal Processing in a Cholesterol-Based Self-Assembly System, *Chem. Eur. J.* **2009**, *15,* 6234–6243.

96. X. Yu, Q. Liu, J. Wu, M. Zhang, X. Cao, S. Zhang, Q. Wang, L. Chen, T. Yi; Sonication-Triggered Instantaneous Gel-to-Gel Transformation, *Chem. Eur. J.* **2010**, *16,* 9099–9106.

97. L. C. Palmer, S. I. Stupp; Molecular Self-Assembly into One-Dimensional Nanostructures, *Acc. Chem. Res.* **2008**, *41,* 1674–1684.

98. S. Scanlon, A. Aggeli; Self-assembling peptide nanotubes, *Nano Today* **2008**, *3,* 22–30.

99. M. Hasegawa, M. Iyoda; Conducting supramolecular nanofibers and nanorods, *Chem. Soc. Rev.* **2010**, *39,* 2420-2427.

100. M. E. Salmon, P. E. Russell, E. B. Troughton; Growth and Characterization of Self-assembled Nanofibers, *MAM* **2005**, *11,* 372-373.

101. C. C. Lee, C. Grenier, E. W. Meijer, A. P. H. J. Schenning; Preparation and characterization of helical self-assembled nanofibers, *Chem. Soc. Rev.* **2009**, *38,* 671-683.

102. J. Schneider, H. Cui, M. J. Webber, S. I. Stupp; Self-assembly of peptide amphiphiles: From molecules to nanostructures to biomaterials, *Biopolymers* **2010**, *94,* 1–18.

103. C. M. A. Leenders, T. Mes, M. B. Baker, M. M. E. Koenigs, P. Besenius, A. R. A. Palmans, E. W. Meijer; From supramolecular polymers to hydrogel materials, *Mater. Horiz.* **2013**, *1,* 116-120.

104. M. Shirakawa, N. Fujita, S. Shinkai; A Stable Single Piece of Unimolecularly π-Stacked Porphyrin Aggregate in a Thixotropic Low Molecular Weight Gel: A One-Dimensional Molecular Template for Polydiacetylene Wiring up to Several Tens of Micrometers in Length, *J. Am. Chem. Soc.* **2005**, *127,* 4164–4165.

105. J. Boekhoven, A. M. Brizard, P. van Rijn, M. C. A. Stuart, R. Eelkema, J. H. van Esch; Programmed Morphological Transitions of Multisegment Assemblies by Molecular Chaperone Analogues, *Angew. Chem. Int. Ed.* **2011**, *50,* 12285–12289.

106. L. C. Palmer, Y. S. Velichko, M. de La Olvera Cruz, S. I. Stupp; Supramolecular self-assembly codes for functional structures, *Philosophical Transactions of the Royal Society A: Mathematical, Physical and Engineering Sciences* **2007**, *365,* 1417–1433.

107. T. Aida, E. W. Meijer, S. I. Stupp; Functional Supramolecular Polymers, *Science* **2012**, *335,* 813–817.

108. F. García, J. Buendía, L. Sánchez; Supramolecular Ribbons from Amphiphilic Trisamides Self-Assembly, *J. Org. Chem.* **2011**, *76,* 6271–6276.

109. M. Yamauchi, S. Kubota, T. Karatsu, A. Kitamura, A. Ajayaghosh, S. Yagai; Guided supramolecular polymerization of oligo(p-phenylenevinylene) functionalized bismelamines, *Chem. Commun.* **2013**, *49,* 4941-4943.

110. H. Shao, T. Nguyen, N. C. Romano, D. A. Modarelli, J. R. Parquette; Self-Assembly of 1-D n -Type Nanostructures Based on Naphthalene Diimide-Appended Dipeptides, *J. Am. Chem. Soc.* **2009**, *131,* 16374–16376.

111. A. P. H. J. Schenning, E. W. Meijer; Supramolecular electronics; nanowires from self-assembled π-conjugated systems, *Chem. Commun.* **2005,** 3245-3258.

112. I. Danila, F. Riobé, J. Puigmartí-Luis, Á. Pérez del Pino, J. D. Wallis, D. B. Amabilino, N. Avarvari; Supramolecular electroactive organogel and conducting nanofibers with C3-symmetrical architectures, *J. Mater. Chem.* **2009**, *19,* 4495-4504.

113. A. Ajayaghosh, V. K. Praveen, C. Vijayakumar, S. J. George; Molecular Wire Encapsulated into π Organogels: Efficient Supramolecular Light-Harvesting Antennae with Color-Tunable Emission, *Angew. Chem. Int. Ed.* **2007**, *46,* 6260–6265.

114. B. Xu; Gels as Functional Nanomaterials for Biology and Medicine, *Langmuir* **2009**, *25,* 8375–8377.

115. J. Boekhoven, J. M. Poolman, C. Maity, F. Li, L. van der Mee, C. B. Minkenberg, E. Mendes, J. H. van Esch, R. Eelkema; Catalytic control over supramolecular gel formation, *Nature Chem* **2013**, *5,* 433–437.

116. X. Yan, S. Li, T. R. Cook, X. Ji, Y. Yao, J. B. Pollock, Y. Shi, G. Yu, J. Li, F. Huang, P. J. Stang; Hierarchical Self-Assembly: Well-Defined Supramolecular Nanostructures and Metallohydrogels via Amphiphilic Discrete Organoplatinum(II) Metallacycles, *J. Am. Chem. Soc.* **2013**, *135,* 14036–14039.

117. M. de Loos, J. H. van Esch, R. M. Kellogg, B. L. Feringa; C3-Symmetric, amino acid based organogelators and thickeners: a systematic study of structure–property relations, *Tetrahedron* **2007**, *63,* 7285–7301.

118. G. O. Lloyd, J. W. Steed; Anion-tuning of supramolecular gel properties, *Nature Chem* **2009**, *1,* 437–442.

119. M. P. Lightfoot, F. S. Mair, R. G. Pritchard, J. E. Warren; New supramolecular packing motifs: π-stacked rods encased in triply-helical hydrogen bonded amide strands, *Chem. Commun.* **1999,** 1945–1946.

120. S. Cantekin, T. F. A. de Greef, A. R. A. Palmans; Benzene-1,3,5-tricarboxamide: a versatile ordering moiety for supramolecular chemistry, *Chem. Soc. Rev.* **2012**, *41,* 6125-6137.

121. A. J. Markvoort, H. M. ten Eikelder, P. A. Hilbers, T. F. de Greef, E. Meijer; Theoretical models of nonlinear effects in two-component cooperative supramolecular copolymerizations, *Nat Comms* **2011**, *2,* 509.

122. M. Wegner, D. Dudenko, D. Sebastiani, A. R. A. Palmans, T. F. A. de Greef, R. Graf, H. W. Spiess; The impact of the amide connectivity on the assembly and dynamics of benzene-1,3,5-tricarboxamides in the solid state, *Chem. Sci.* **2011**, *2,* 2040-2049.

123. A. R. A. Palmans, E. W. Meijer; Amplification of Chirality in Dynamic Supramolecular Aggregates, *Angew. Chem. Int. Ed.* **2007**, *46,* 8948–8968.

124. M. M. J. Smulders, I. A. W. Filot, J. M. A. Leenders, P. van der Schoot, A. R. A. Palmans, A. P. H. J. Schenning, E. W. Meijer; Tuning the Extent of Chiral Amplification by Temperature in a Dynamic Supramolecular Polymer, *J. Am. Chem. Soc.* **2010**, *132,* 611–619.

125. C. F. C. Fitié, W. S. C. Roelofs, M. Kemerink, R. P. Sijbesma; Remnant Polarization in Thin Films from a Columnar Liquid Crystal, *J. Am. Chem. Soc.* **2010**, *132,* 6892–6893.

126. R. Q. Albuquerque, A. Timme, R. Kress, J. Senker, H.-W. Schmidt; Theoretical Investigation of Macrodipoles in Supramolecular Columnar Stackings, *Chem. Eur. J.* **2013**, *19,* 1647–1657.

127. F. García, P. A. Korevaar, A. Verlee, E. W. Meijer, A. R. A. Palmans, L. Sánchez; The influence of π-conjugated moieties on the thermodynamics of cooperatively self-assembling tricarboxamides, *Chem. Commun.* **2013**, *49,* 8674-8676.

128. S. Y. Ryu, S. Kim, J. Seo, Y.-W. Kim, O.-H. Kwon, D.-J. Jang, S. Y. Park; Strong fluorescence emission induced by supramolecular assembly and gelation: luminescent organogel from nonemissive oxadiazole-based benzene-1,3,5-tricarboxamide gelator, *Chem. Commun.* **2004,** 70-71.

129. Y. Zhou, M. Xu, T. Yi, S. Xiao, Z. Zhou, F. Li, C. Huang; Morphology-Tunable and Photoresponsive Properties in a Self-Assembled Two-Component Gel System, *Langmuir* **2007**, *23,* 202–208.

130. F. Camerel, C. F. J. Faul; Combination of ionic self-assembly and hydrogen bonding as a tool for the synthesis of liquid-crystalline materials and organogelators from a simple building block, *Chem. Commun.* **2003,** 1958-1959.

131. J. J. van Gorp, J. A. J. M. Vekemans, E. W. Meijer; C3, *J. Am. Chem. Soc.* **2002**, *124,* 14759–14769.

132. R. C. T. Howe, A. P. Smalley, A. P. M. Guttenplan, M. W. R. Doggett, M. D. Eddleston, J. C. Tan, G. O. Lloyd; A family of simple benzene 1,3,5-tricarboxamide (BTA) aromatic carboxylic acid hydrogels, *Chem. Commun.* **2013**, *49,* 4268-4270.

133. A. Bernet, R. Q. Albuquerque, M. Behr, S. T. Hoffmann, H.-W. Schmidt; Formation of a supramolecular chromophore: a spectroscopic and theoretical study, *Soft Matter* **2011**, *8,* 66-69.

134. Y.-W. Hao, H.-Y. Wang, Y.-J. Huang, B.-R. Gao, Q.-D. Chen, L.-B. Li, H.-B. Sun; Evidence of concerted inversion for the photon-induced molecular switching of azobenzene using rotation-free azobenzene derivatives, *J. Mater. Chem. C* **2013**, *1,* 5244-5249.

135. K. Kreger, P. Wolfer, H. Audorff, L. Kador, N. Stingelin-Stutzmann, P. Smith, H.-W. Schmidt; Stable Holographic Gratings with Small-Molecular Trisazobenzene Derivatives, *J. Am. Chem. Soc.* **2010**, *132,* 509–516.

136. S. Lee, S. Oh, J. Lee, Y. Malpani, Y.-S. Jung, B. Kang, J. Y. Lee, K. Ozasa, T. Isoshima, S. Y. Lee, M. Hara, D. Hashizume, J.-M. Kim; Stimulus-Responsive Azobenzene Supramolecules: Fibers, Gels, and Hollow Spheres, *Langmuir* **2013**, *29,* 5869–5877.

137. H. Misslitz, K. Kreger, H.-W. Schmidt; Supramolecular Nanofiber Webs in Nonwoven Scaffolds as Potential Filter Media, *Small* **2013**, *9,* 2053–2058.

138. M. Blomenhofer, S. Ganzleben, D. Hanft, H.-W. Schmidt, M. Kristiansen, P. Smith, K. Stoll, D. Mäder, K. Hoffmann; "Designer" Nucleating Agents for Polypropylene, *Macromolecules* **2005**, *38,* 3688–3695.

139. F. Abraham, S. Ganzleben, D. Hanft, P. Smith, H.-W. Schmidt; Synthesis and Structure-Efficiency Relations of 1,3,5-Benzenetrisamides as Nucleating Agents and Clarifiers for Isotactic Poly(propylene), *Macromol. Chem. Phys.* **2010**, *211,* 171–181.

140. M. Kristiansen, P. Smith, H. Chanzy, C. Baerlocher, V. Gramlich, L. McCusker, T. Weber, P. Pattison, M. Blomenhofer, H.-W. Schmidt; Structural Aspects of 1,3,5-Benzenetrisamides−A New Family of Nucleating Agents, *Crystal Growth & Design* **2009**, *9,* 2556–2558.

141. H. Kubas, M. Schäfer, U. Bauder-Wüst, M. Eder, D. Oltmanns, U. Haberkorn, W. Mier, M. Eisenhut; Multivalent cyclic RGD ligands: influence of linker lengths on receptor binding, *Nuclear Medicine and Biology* **2010**, *37,* 885–891.

142. J. Lee, O. K. Farha, J. Roberts, K. A. Scheidt, S. T. Nguyen, J. T. Hupp; Metal–organic framework materials as catalysts, *Chem. Soc. Rev.* **2009**, *38,* 1450-1459.

143. H. Kurreck, M. Huber; Model Reactions for Photosynthesis—Photoinduced Charge and Energy Transfer between Covalently Linked Porphyrin and Quinone Units, *Angew. Chem. Int. Ed. Engl.* **1995**, *34,* 849–866.

144. C. J. Brabec, N. S. Sariciftci, J. C. Hummelen; Plastic Solar Cells, *Adv. Funct. Mater.* **2001**, *11,* 15–26.

145. G. H. Krause, E. Weis; Chlorophyll Fluorescence and Photosynthesis: The Basics, *Annu. Rev. Plant. Physiol. Plant. Mol. Biol.* **1991**, *42,* 313–349.

146. G. D. Scholes, G. R. Fleming, A. Olaya-Castro, R. van Grondelle; Lessons from nature about solar light harvesting, *Nature Chem* **2011**, *3,* 763–774.

147. M.-S. Choi, T. Yamazaki, I. Yamazaki, T. Aida; Bioinspired Molecular Design of Light-Harvesting Multiporphyrin Arrays, *Angew. Chem. Int. Ed.* **2004**, *43,* 150–158.

148. R. K. Clayton. *Photosynthesis. Physical mechanisms and chemical patterns* (Cambridge University Press, Cambridge [Eng.], New York, 1980).

149. E-M. Aro, I. Virgin, B. Andersson; Photoinhibition of Photosystem II. Inactivation, protein damage and turnover, *Biochimica et Biophysica Acta (BBA) - Bioenergetics* **1993**, *1143,* 113–134.

150. D. O. Hall, K. K. Rao. *Photosynthesis.* 6th ed. (Cambridge University Press, Cambridge, UK, New York, 1999).

151. S. P. Long, S. Humphries, P. G. Falkowski; Photoinhibition of Photosynthesis in Nature, *Annu. Rev. Plant. Physiol. Plant. Mol. Biol.* **1994**, *45,* 633–662.

152. G. D. Scholes; Quantum-Coherent Electronic Energy Transfer: Did Nature Think of It First?, *J. Phys. Chem. Lett.* **2010**, *1,* 2–8.

153. G. D. Scholes, G. Rumbles; Excitons in nanoscale systems, *Nat Mater* **2006**, *5,* 683–696.

154. G. S. Engel, T. R. Calhoun, E. L. Read, T.-K. Ahn, T. Mančal, Y.-C. Cheng, R. E. Blankenship, G. R. Fleming; Evidence for wavelike energy transfer through quantum coherence in photosynthetic systems, *Nature* **2007**, *446,* 782–786.

155. G. D. Scholes, T. Mirkovic, D. B. Turner, F. Fassioli, A. Buchleitner; Solar light harvesting by energy transfer: from ecology to coherence, *Energy Environ. Sci.* **2012**, *5,* 9374-9393.

156. M. Baghgar, J. A. Labastide, F. Bokel, R. C. Hayward, M. D. Barnes; Effect of Polymer Chain Folding on the Transition from H- to J-Aggregate Behavior in P3HT Nanofibers, *J. Phys. Chem. C* **2014**, *118,* 2229–2235.

157. Z. Chen, A. Lohr, C. R. Saha-Möller, F. Würthner; Self-assembled π-stacks of functional dyes in solution: structural and thermodynamic features, *Chem. Soc. Rev.* **2009**, *38,* 564-584.

158. D. Görl, X. Zhang, F. Würthner; Molecular Assemblies of Perylene Bisimide Dyes in Water, *Angew. Chem. Int. Ed.* **2012**, *51,* 6328–6348.

159. H. Fromherz; Münchener Chemische Gesellschaft, *Angew. Chem.* **1937**, *50,* 51–52.

160. G. Scheibe; Über die Veränderlichkeit der Absorptionsspektren in Lösungen und die Nebenvalenzen als ihre Ursache, *Angew. Chem.* **1937**, *50,* 212–219.

161. G. Scheibe, L. Kandler, H. Ecker; Polymerisation und polymere Adsorption als Ursache neuartiger Absorptionsbanden von organischen Farbstoffen, *Naturwissenschaften* **1937**, *25,* 75.

162. E. E. Jelley; Spectral Absorption and Fluorescence of Dyes in the Molecular State, *Nature* **1936**, *138,* 1009–1010.

163. E. E. Jelley; Molecular, Nematic and Crystal States of I:I'-Diethyl-Ψ-Cyanine Chloride, *Nature* **1937**, *139,* 631-632.

164. D. Möbius; Scheibe Aggregates, *Adv. Mater.* **1995**, *7,* 437–444.

165. S. Sengupta, F. Würthner; Chlorophyll J-Aggregates: From Bioinspired Dye Stacks to Nanotubes, Liquid Crystals, and Biosupramolecular Electronics, *Acc. Chem. Res.* **2013**, *46,* 2498–2512.

166. A. Herz; Aggregation of sensitizing dyes in solution and their adsorption onto silver halides, *Advances in Colloid and Interface Science* **1977**, *8,* 237–298.

167. F. Meinardi, M. Cerminara, A. Sassella, R. Bonifacio, R. Tubino; Superradiance in Molecular H Aggregates, *Phys. Rev. Lett.* **2003**, *91,* 247401.

168. U. Rösch, S. Yao, R. Wortmann, F. Würthner; Fluorescent H-Aggregates of Merocyanine Dyes, *Angew. Chem. Int. Ed.* **2006**, *45,* 7026–7030.

169. M. Kasha, H. R. Rawls, M. Ashraf El-Bayoumi; The exciton model in molecular spectroscopy, *Pure and Applied Chemistry* **1965**, *11,* 371-392.

170. F. C. Spano; Modeling disorder in polymer aggregates: The optical spectroscopy of regioregular poly(3-hexylthiophene) thin films, *J. Chem. Phys.* **2005**, *122,* 234701.

171. A. Eisfeld, J. Briggs; The J- and H-bands of organic dye aggregates, *Chemical Physics* **2006**, *324,* 376–384.

172. M. Sauer, J. Hofkens, J. Enderlein. *Handbook of fluorescence spectroscopy and imaging. From single molecules to ensembles* (Wiley-VCH, Weinheim, Germany, op. 2011).

173. M. Shirakawa, S.-i. Kawano, N. Fujita, K. Sada, S. Shinkai; Hydrogen-Bond-Assisted Control of H versus J Aggregation Mode of Porphyrins Stacks in an Organogel System, *J. Org. Chem.* **2003**, *68,* 5037–5044.

174. F. C. Spano; The Spectral Signatures of Frenkel Polarons in H- and J-Aggregates, *Acc. Chem. Res.* **2010**, *43,* 429–439.

175. F. Würthner, T. E. Kaiser, C. R. Saha-Möller; J-Aggregates: From Serendipitous Discovery to Supramolecular Engineering of Functional Dye Materials, *Angew. Chem. Int. Ed.* **2011**, *50,* 3376–3410.

176. F. J. M. Hoeben, P. Jonkheijm, E. W. Meijer, A. P. H. J. Schenning; About Supramolecular Assemblies of π-Conjugated Systems, *Chem. Rev.* **2005**, *105,* 1491–1546.

177. M. R. Wasielewski; Self-Assembly Strategies for Integrating Light Harvesting and Charge Separation in Artificial Photosynthetic Systems, *Acc. Chem. Res.* **2009**, *42,* 1910–1921.

178. A. Adronov, J. M. J. Fréchet; Light-harvesting dendrimers, *Chem. Commun.* **2000,** 1701–1710.

179. J. A. A. W. Elemans, R. van Hameren, R. J. M. Nolte, A. E. Rowan; Molecular Materials by Self-Assembly of Porphyrins, Phthalocyanines, and Perylenes, *Adv. Mater.* **2006**, *18,* 1251–1266.

180. F. Würthner; Perylene bisimide dyes as versatile building blocks for functional supramolecular architectures, *Chem. Commun.* **2004,** 1564-1579.

181. P. M. Beaujuge, J. M. J. Fréchet; Molecular Design and Ordering Effects in π-Functional Materials for Transistor and Solar Cell Applications, *J. Am. Chem. Soc.* **2011**, *133,* 20009–20029.

182. V. K. Praveen, C. Ranjith, N. Armaroli; White-Light-Emitting Supramolecular Gels, *Angew. Chem. Int. Ed.* **2014**, *53,* 365–368.

183. A. Ajayaghosh, V. K. Praveen, C. Vijayakumar; Organogels as scaffolds for excitation energy transfer and light harvesting, *Chem. Soc. Rev.* **2007**, *37,* 109-122.

184. A. Miura, Z. Chen, H. Uji-i, S. de Feyter, M. Zdanowska, P. Jonkheijm, A. P. H. J. Schenning, E. W. Meijer, F. Würthner, F. C. de Schryver; Bias-Dependent Visualization of Electron Donor (D) and Electron Acceptor (A) Moieties in a Chiral DAD Triad Molecule, *J. Am. Chem. Soc.* **2003**, *125,* 14968–14969.

185. L. F. Dössel, V. Kamm, I. A. Howard, F. Laquai, W. Pisula, X. Feng, C. Li, M. Takase, T. Kudernac, S. de Feyter, K. Müllen; Synthesis and Controlled Self-Assembly of Covalently Linked Hexa- peri -hexabenzocoronene/Perylene Diimide Dyads as Models To Study Fundamental Energy and Electron Transfer Processes, *J. Am. Chem. Soc.* **2012**, *134,* 5876–5886.

186. D. González-Rodríguez, A. P. H. J. Schenning; Hydrogen-bonded Supramolecular π-Functional Materials, *Chem. Mater.* **2011**, *23,* 310–325.

187. X. Feng, W. Pisula, M. Takase, X. Dou, V. Enkelmann, M. Wagner, N. Ding, K. Müllen; Synthesis, Helical Organization, and Fibrous Formation of C3 Symmetric Methoxy-Substituted Discotic Hexa- peri -hexabenzocoronene, *Chem. Mater.* **2008**, *20,* 2872–2874.

188. G. de Luca, A. Liscio, F. Nolde, L. M. Scolaro, V. Palermo, K. Müllen, P. Samorì; Self-assembly of discotic molecules into mesoscopic crystals by solvent-vapour annealing, *Soft Matter* **2008**, *4,* 2064-2070.

189. J. P. Hill; Self-Assembled Hexa-peri-hexabenzocoronene Graphitic Nanotube, *Science* **2004**, *304,* 1481–1483.

190. Y. Yamamoto, T. Fukushima, Y. Suna, N. Ishii, A. Saeki, S. Seki, S. Tagawa, M. Taniguchi, T. Kawai, T. Aida; Photoconductive Coaxial Nanotubes of Molecularly Connected Electron Donor and Acceptor Layers, *Science* **2006**, *314,* 1761–1764.

191. W. Zhang, W. Jin, T. Fukushima, A. Saeki, S. Seki, T. Aida; Supramolecular Linear Heterojunction Composed of Graphite-Like Semiconducting Nanotubular Segments, *Science* **2011**, *334,* 340–343.

192. T. E. Kaiser, H. Wang, V. Stepanenko, F. Würthner; Supramolecular Construction of Fluorescent J-Aggregates Based on Hydrogen-Bonded Perylene Dyes, *Angew. Chem. Int. Ed.* **2007**, *46,* 5541–5544.

193. S. Ghosh, X.-Q. Li, V. Stepanenko, F. Würthner; Control of H- and J-Type π Stacking by Peripheral Alkyl Chains and Self-Sorting Phenomena in Perylene Bisimide Homo- and Heteroaggregates, *Chem. Eur. J.* **2008**, *14,* 11343–11357.

194. I. Paraschiv, M. Giesbers, B. van Lagen, F. C. Grozema, R. D. Abellon, L. D. A. Siebbeles, A. T. M. Marcelis, H. Zuilhof, E. J. R. Sudhölter; H-Bond-Stabilized Triphenylene-Based Columnar Discotic Liquid Crystals, *Chem. Mater.* **2006**, *18,* 968–974.

195. I. Paraschiv, K. de Lange, M. Giesbers, B. van Lagen, F. C. Grozema, R. D. Abellon, L. D. A. Siebbeles, E. J. R. Sudhölter, H. Zuilhof, A. T. M. Marcelis; Hydrogen-bond stabilized columnar discotic benzenetrisamides with pendant triphenylene groups, *J. Mater. Chem.* **2008**, *18,* 5475-5481.

196. F. Würthner, Z. Chen, F. J. M. Hoeben, P. Osswald, C.-C. You, P. Jonkheijm, J. v. Herrikhuyzen, A. P. H. J. Schenning, P. P. A. M. van der Schoot, E. W. Meijer, E. H. A. Beckers, S. C. J. Meskers, R. A. J. Janssen; Supramolecular p−n-Heterojunctions by Co-Self-Organization of Oligo(p -phenylene Vinylene) and Perylene Bisimide Dyes, *J. Am. Chem. Soc.* **2004**, *126,* 10611–10618.

197. A. P. H. J. Schenning, J. v. Herrikhuyzen, P. Jonkheijm, Z. Chen, F. Würthner, E. W. Meijer; Photoinduced Electron Transfer in Hydrogen-Bonded Oligo(p -phenylene vinylene)−Perylene Bisimide Chiral Assemblies, *J. Am. Chem. Soc.* **2002**, *124,* 10252–10253.

198. M. Kumar, K. Venkata Rao, S. J. George; Supramolecular charge transfer nanostructures, *Phys. Chem. Chem. Phys.* **2013**, *16,* 1300-1313.

199. K. V. Rao, S. J. George; Supramolecular Alternate Co-Assembly through a Non-Covalent Amphiphilic Design: Conducting Nanotubes with a Mixed D-A Structure, *Chem. Eur. J.* **2012**, *18,* 14286–14291.

200. T. Ishi-i, R. Iguchi, E. Snip, M. Ikeda, S. Shinkai, *Langmuir* **2001**, *17,* 5825–5833.

201. M. R. Molla, A. Das, S. Ghosh; Chiral induction by helical neighbour: spectroscopic visualization of macroscopic-interaction among self-sorted donor and acceptor π-stacks, *Chem. Commun.* **2011**, *47,* 8934-8936.

202. C. Wang, S. Yin, S. Chen, H. Xu, Z. Wang, X. Zhang; Controlled Self-Assembly Manipulated by Charge-Transfer Interactions: From Tubes to Vesicles, *Angew. Chem. Int. Ed.* **2008**, *47,* 9049–9052.

203. K. Jalani, M. Kumar, S. J. George; Mixed donor–acceptor charge-transfer stacks formed via hierarchical self-assembly of a non-covalent amphiphilic foldamer, *Chem. Commun.* **2013**, *49,* 5174-5176.

204. A. Das, S. Ghosh; A generalized supramolecular strategy for self-sorted assembly between donor and acceptor gelators, *Chem. Commun.* **2011**, *47,* 8922-8924.

205. A. A. Sagade, K. V. Rao, U. Mogera, S. J. George, A. Datta, G. U. Kulkarni; High-Mobility Field Effect Transistors Based on Supramolecular Charge Transfer Nanofibres, *Adv. Mater.* **2013**, *25,* 559–564.

206. R. Bhosale, J. Míšek, N. Sakai, S. Matile; Supramolecular n/p-heterojunction photosystems with oriented multicolored antiparallel redox gradients (OMARG-SHJs), *Chem. Soc. Rev.* **2009**, *39,* 138-149.

207. N. Sakai, R. Bhosale, D. Emery, J. Mareda, S. Matile; Supramolecular n/p-Heterojunction Photosystems with Antiparallel Redox Gradients in Electron- and Hole-Transporting Pathways, *J. Am. Chem. Soc.* **2010**, *132,* 6923–6925.

208. D. Hellwinkel, M. Melan; Heteropolycyclen vom Triangulen-Typ, I. 8.12-Dihydro-4H-benzo[1.9]chinolizino[3.4.5.6.7-defg]acridin-trion-(4.8.12) und 5.9-Dihydro-chino[3.2.1-de]acridin-dion-(5.9), *Chem. Ber.* **1971**, *104,* 1001–1016.

209. D. Hellwinkel, M. Melan; Heteropolycyclen vom Triangulen-Typ, II. Zur Stereochemie verbrückter Triarylamine, *Chem. Ber.* **1974**, *107,* 616–626.

210. M. Bieri, S. Blankenburg, M. Kivala, C. A. Pignedoli, P. Ruffieux, K. Müllen, R. Fasel; Surface-supported 2D heterotriangulene polymers, *Chem. Commun.* **2011**, *47,* 10239-10241.

211. J. E. Field, D. Venkataraman; Heterotriangulenes-Structure and Properties, *Chem. Mater.* **2002**, *14,* 962–964.

212. N. S. Makarov, S. Mukhopadhyay, K. Yesudas, J.-L. Brédas, J. W. Perry, A. Pron, M. Kivala, K. Müllen; Impact of Electronic Coupling, Symmetry, and Planarization on One- and Two-Photon Properties of Triarylamines with One, Two, or Three Diarylboryl Acceptors, *J. Phys. Chem. A* **2012**, *116,* 3781–3793.

213. K. Do, D. Kim, N. Cho, S. Paek, K. Song, J. Ko; New Type of Organic Sensitizers with a Planar Amine Unit for Efficient Dye-Sensitized Solar Cells, *Org. Lett.* **2012**, *14,* 222–225.

214. S. Paek, N. Cho, S. Cho, J. K. Lee, J. Ko; Planar Star-Shaped Organic Semiconductor with Fused Triphenylamine Core for Solution-Processed Small-Molecule Organic Solar Cells and Field-Effect Transistors, *Org. Lett.* **2012**, *14,* 6326–6329.

215. Z. Fang, V. Chellappan, R. D. Webster, L. Ke, T. Zhang, B. Liu, Y.-H. Lai; Bridged-triarylamine starburst oligomers as hole transporting materials for electroluminescent devices, *J. Mater. Chem.* **2012**, *22,* 15397-15404.

216. C. Liu, Y. Li, Y. Zhang, C. Yang, H. Wu, J. Qin, Y. Cao; Solution-Processed Undoped Deep-Blue Organic Light-Emitting Diodes Based on Starburst Oligofluorenes with a Planar Triphenylamine Core, *Chem. Eur. J.* **2012,** *18,* 6928-6934.

217. H. Zhang, S. Wang, Y. Li, B. Zhang, C. Du, X. Wan, Y. Chen; Synthesis, characterization, and electroluminescent properties of star shaped donor–acceptor dendrimers with carbazole dendrons as peripheral branches and heterotriangulene as central core, *Tetrahedron* **2009**, *65,* 4455–4463.

218. X. Wan, H. Zhang, Y. Li, Y. Chen; Self-assembly based on heterotriangulene derivatives: from nanowires to microrods, *New J. Chem.* **2010**, *34,* 661-666.

219. H. Zhang, Y. Li, X. Wan, Y. Chen; Two-level self-assembly from nanowires to microrods based on a heterotriangulene derivative, *Chem. Phys. Lett.* **2009**, *479,* 117–119.

220. M. Kivala, W. Pisula, S. Wang, A. Mavrinskiy, J.-P. Gisselbrecht, X. Feng, K. Müllen; Columnar Self-Assembly in Electron-Deficient Heterotriangulenes, *Chem. Eur. J.* **2013**, *19,* 8117–8128.

221. S. Wang, M. Kivala, I. Lieberwirth, K. Kirchhoff, X. Feng, W. Pisula, K. Müllen; Dip-Coating-Induced Fiber Growth of a Soluble Heterotriangulene, *ChemPhysChem* **2011**, *12,* 1648–1651.

2. Overview of the Thesis

This thesis focuses on the synthesis, the self-assembly, and the photophysical properties of multichromophoric systems. It contributes to a fundamental understanding on the influence of the interplay of intermolecular interactions to *control the π-stacking* and subsequently the photophysical properties of chromophoric systems. Furthermore, the *energy transfer* and self-assembly properties of selected multichromophoric carbonyl-bridged triarylamines are revealed. The highlight of this thesis is the achievement of long-range excitation energy transport along individual supramolecular nanofibers of molecular diameter due to a precise arrangement of multichromophoric building blocks within a supramolecular scaffold. The most important results that were obtained in the course of this thesis are condensed in 3 publications. One is published in *ChemPhysChem*, one is accepted in *Chemistry a European Journal* and one is intended for submission to *Nature*. An outline of the conducted research is presented in Figure 1.

Nature uses the powerful tools of supramolecular chemistry to construct multifunctional architectures in a bottom-up approach. Precisely mastering these possibilities can have a great impact on future technologies. Due to the great variety of factors, that crucially influence the outcome of self-assembly processes, the formation of supramolecular architectures is highly complex and non-trivial. This issue is addressed in the first part of this thesis. To shed light on the complex interplay of different intermolecular interactions two sets of relatively simple supramolecular building blocks were compared. It is shown, how hydrogen-bonding and steric effects can be used to *control the π-stacking* and subsequently the optical properties of a pyrene chromophore. For that, four different derivatives were synthesized and studied in solution, the aggregated state, and in bulk. The chromophoric compounds comprise amide or ester linkers in combination either with or without the sterically demanding *tert*-butyl group. Hence, they differ in their capability to form H-bonds and in their steric demand. The influences of both effects on the self-assembly, the crystalline order and the stacking behavior of the aromatic pyrene system in the different states is shown and unraveled. While monomer fluorescence is observed in the molecularly dissolved state, the supramolecular aggregates show excimer fluorescence, which changes back to monomer fluorescence upon crystallization (Figure 1 top).

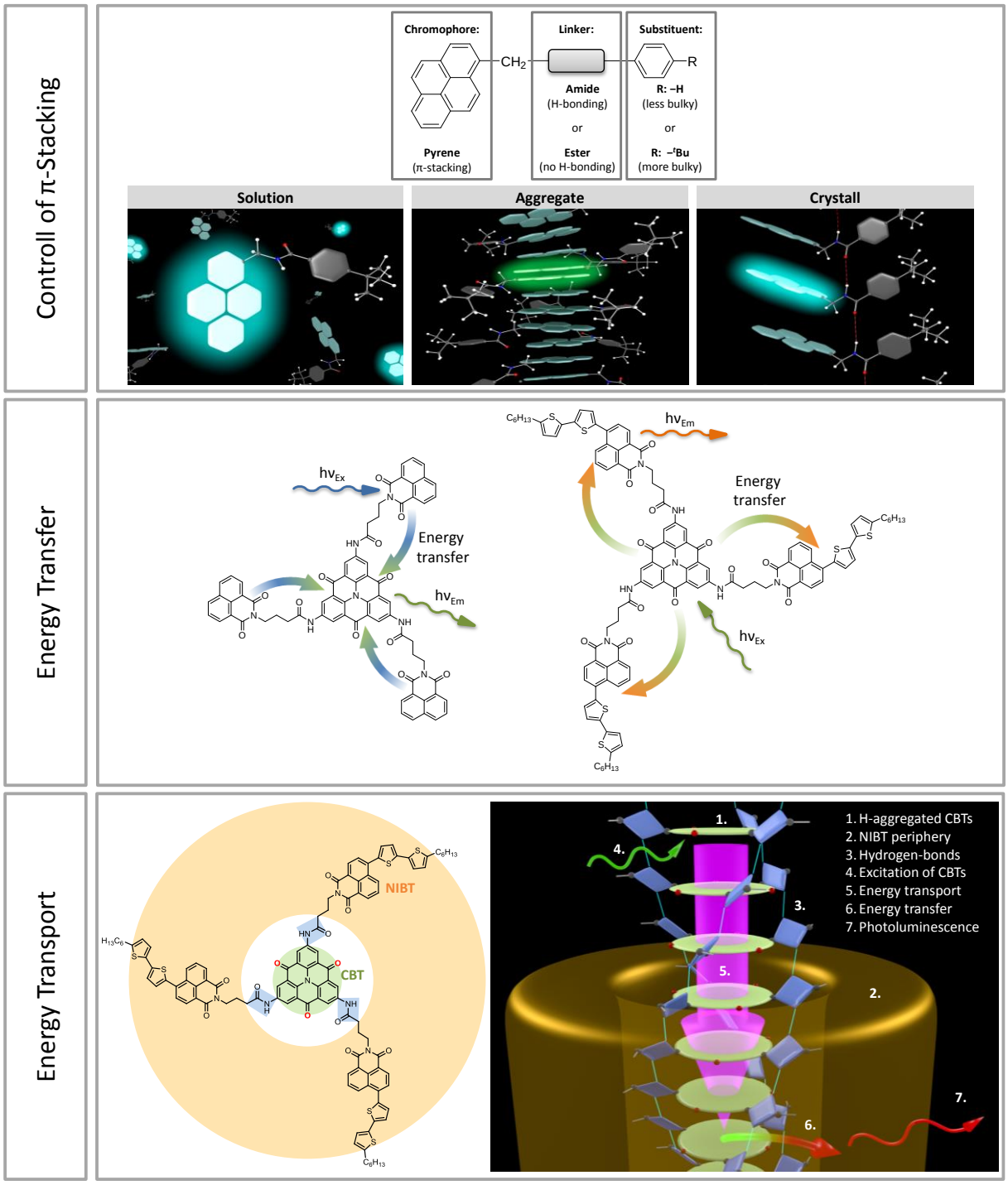

Figure 1. Top: Fundamental investigations on the photopyhsical properties of four pyrene derivatives with varying H-bonding capabilities and steric demand in different states of aggregation. Middle: Synthesis and efficient energy transfer properties in two multichromophoric carbonyl-bridged triarylamines. Bottom: Self-assembly and energy transport properties of a multichromophoric 2,6,10-(carbonyl-bridged triarylamine)-trisamide along single strands of individual supramolecular nanofibers.

The results from the fundamental investigations led to the design of multichromophoric systems of higher complexity and functionality. For these compounds a carbonyl-bridged triarylamine core was chosen as central building block due to its appealing optical and self-assembly properties. This planarized C_3-symmetric chromophore was equipped via amide linkers with naphthalimide or 4-bithiophene-naphthalimide chromophores. The multichromophoric compounds were studied by means of comprehensive steady-state and time-resolved spectroscopic investigations in diluted solution *i.e*. the chromophores are molecularly dissolved. Together with three reference compounds efficient *energy transfer* was demonstrated in both compounds. Excitation energy can be funneled from the lateral naphthalimides acting as antenna chromophores into the carbonyl-bridged triaraylamine core; or energy transfer proceeds *vice versa* from the core to the 4-bithiophene-naphthalimides in the periphery (Figure 1 middle). The latter compound forms gels in *ortho*-dichlorobenzene at very low concentrations of 0.7 mM, while the photophysical and energy transfer properties are retained.

The pronounced gelation properties of the carbonyl-bridged triarylamine bearing the lateral 4-(bithiophene)-naphthalimides lead to thorough investigations of the self-assembly behavior. Electronic and atomic force microscopy reveals supramolecular nanofibers with molecular diameter. Combined analytical investigations demonstrate strong H-aggregation of the carbonyl-bridged triarylamine core and three-fold symmetric hydrogen-bonds of the amide groups. Micrometer-long nanofibers were studied individually with a custom build fluorescence microscope. Confocal excitation at one end of the fiber results in a photoluminescent response over the entire fiber. This observation is attributed to quantum coherent *energy transport* through the strongly coupled carbonyl-bridged triarylamine cores (Figure 1 bottom). It is the first time that such remarkable energy transport, which proceeds over more than 4 µm is observed on individual supramolecular nanofibers at room temperature. These results show the potential of supramolecular ordering of chromophoric building blocks and opens new pathways to future quantum information technologies.

The key results of the three publications are summarized in the following sections and incorporated in the overall context. Details on the synthesis, the characterization and investigation methods, and the thorough discussions are presented in the chapters 3-5.

2.1. Controlling the π-Stacking Behavior of Pyrene Derivatives: Influence of H-Bonding and Steric Effects in Different States of Aggregation

In this first topic tailored model systems were synthesized and investigated to study the influence of H-bonding and steric effects on the π-stacking and the photophysical properties of pyrenes as model chromophores. The optical properties of this π-functional moiety are well known, which facilitates the interpretation of the acquired optical data with a focus on the influence of the different intermolecular interactions. The pyrene system was attached via a methylene bridge and a linker moiety to a *para*-substituted benzene ring. The linker moiety is either an amide moiety, which allows for hydrogen bonding, or an ester group. The *para*-substitution at the benzene ring determines the sterical demand as it is either hydrogen or a bulky *tert*-butyl group. The four pyrene derivatives which arise from the possible combinations of linker moiety and *para*-substituent are shown in Figure 2.

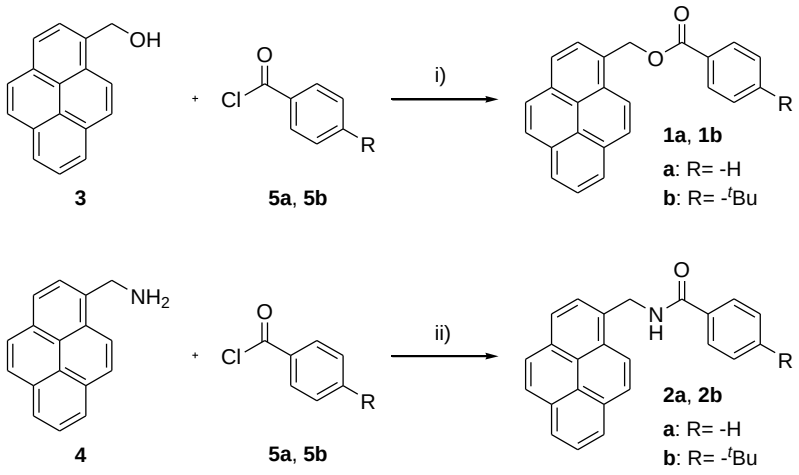

Figure 2. Synthesis and chemical structures of the four pyrene derivatives; i) chloroform, triethylamine, DMAP, 60°C; ii) NMP, pyridine, 80°C.

Below 10^{-5} molL^{-1} in THF the compounds are molecularly dissolved as proven by UV/vis and photoluminescence spectroscopy. In an intermediate concentration regime they form a non-emissive species after excitation of an unaltered ground state. For concentrations exceeding $3 \cdot 10^{-4}$ molL^{-1} the UV/vis absorption spectra provide clear evidence for weakly interacting H-aggregation of the pyrene chromophores in the ground state. This conclusion could be drawn from the observed deviations from Lambert-Beers Law and by thorough analysis of

the oscillator strengths of the 0-0 and 0-1 transitions from the ground state to the second and third excited state (Figure 3). Simultaneous to the stabilization of the ground state by H-aggregation excimer formation is observed in the respective photoluminescence spectra. It is noteworthy that the described changes are observed equally for all four compounds without any major influence of the linker moiety (amide or ester) and the streric demand of the *para*-substituent. Only slight differences could be observed in the excimer formation rate, when the chromophores need to approach each other very closely. Hence, the main driving force for the self-assembly in THF solution is the H-aggregation of the pyrene chromophores independent of the variable groups.

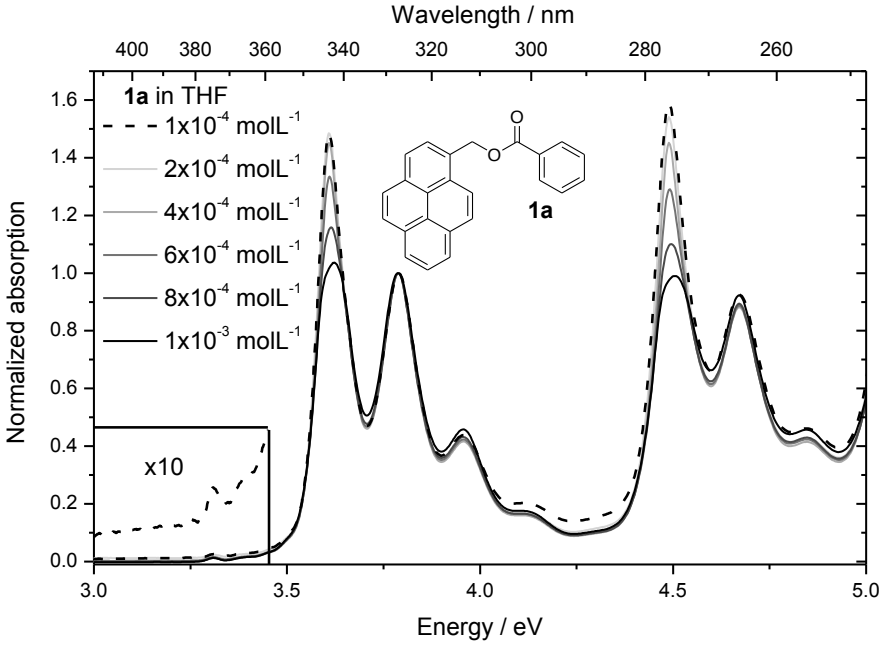

Figure 3. Concentration dependent UV/vis absorption of compound **1a** as representative example normalized at 326 nm. The vibrational fine-structures of the first (10 times enlarged inlay), second, and third electronic excitation are shown. With increasing concentration the intensity of the 0-0 transition is reduced compared to the 0-1 and higher transitions.

The supramolecular aggregates were successfully transferred on a solid support by spin-coating. This yielded optically transparent thin films which show the same photophysical behavior as the aggregates in solution. By subsequent annealing or aging at room temperature crystallization of the thin films was induced. For the amide compounds it was shown by FT-IR spectroscopy that H-bonds were not present in the initial supramolecular

aggregates but were formed during the crystallization process. For all compounds, except for the *tert*-butyl substituted ester compound, the excimer fluorescence, which was observed in the supramolecular aggregates, vanishes with increasing crystallinity. Finally, in the crystalline state an influence of the variable groups on the π-stacking behavior was demonstrated by photoluminescence spectroscopy at low temperature (down to 5 K), which was additionally supported by molecular modeling. With reducing temperature the excimer fluorescence is further quenched while the monomer fluorescence rises accordingly. The observed quenching of the excimer fluorescence depends on the order of the crystalline state, which can be increased by H-bonding amide groups and decreased by bulky *tert*-butyl groups. An exception is the *tert*-butyl substituted ester derivative, which shows exclusively excimer fluorescence, even at 5 K. Hence, this compound needs almost no activation energy for excimer formation, which is only possible if preorientation in the ground state is present.

In summary, for the used model systems the dependence of the π-stacking of the pyrene chromophores on H-bonding and steric effects was unraveled in different states of aggregation. Intriguingly, prior to crystallization the variable groups have only little influence on the π-stacking of the pyrene chromophores and no H-bonds are formed. The gathered knowledge and the developed investigation methods successfully paved the way to study more complex systems.

2.2. Synthesis and Photophysical Properties of Multichromophoric Carbonyl-Bridged Triarylamines

The encouraging fundamental work on the influence of different intermolecular interactions on the self-assembly led to the design of more complex supramolecular building blocks. In this approach a C_3-symmetric planarized triarylamine was used as a chromophoric core building block. This emerging chromophore, which is lately getting increasing attention due to its appealing photophysical properties, was equipped via amide groups in 2, 6, and 10 positions with peripheral chromophores. Thus novel multichromophoric compounds with a threefold symmetric hydrogen-bonding motif were obtained. In the following two sections these first trisamide compounds based on a 2,6,10-carbonyl-bridged triarylamine core are presented. This first part deals with the synthesis and the fundamental photophysical properties of two multichromophoric compounds as well as three reference compounds representing the individual chromophoric subunits (Figure 4). The following part presents the self-assembly of one of the two multichromophoric compounds into supramolecular nanofibers with molecular diameter and the outstanding energy transport properties along these fibers.

Two novel multichromophoric systems were synthesized comprising a carbonyl-bridged triarylamine core which was equipped in 2, 6, and 10 positions via an amide linker and a short decoupling alkyl-spacer with a second chromophore in the periphery. This lateral chromophore was either a 1,8-naphthalimide or a 4-(5-hexyl-2,2'bithiophene)-naphthalimide (Figure 4 top). The chosen synthetic routes follow a construction-kit principle and describe a straightforward strategy suitable for the functionalization of carbonyl-bridged triarylamines. Three additional reference compounds were prepared representing the individual chromophores *i.e*. the carbonyl-bridged triarylamine, the naphthalimide and the 4-(5-hexyl-2,2'bithiophene)-naphthalimide (Figure 4 bottom). The molecular structures of the reference compounds were kept very similar to the respective parts of the multichromophoric systems in order to ensure comparable electronic structures in the chromophore moieties. Consequently, the reference compounds were perfectly suited to assign the individual optical and electronic contributions of the different chromophores within the multichromophoric systems.

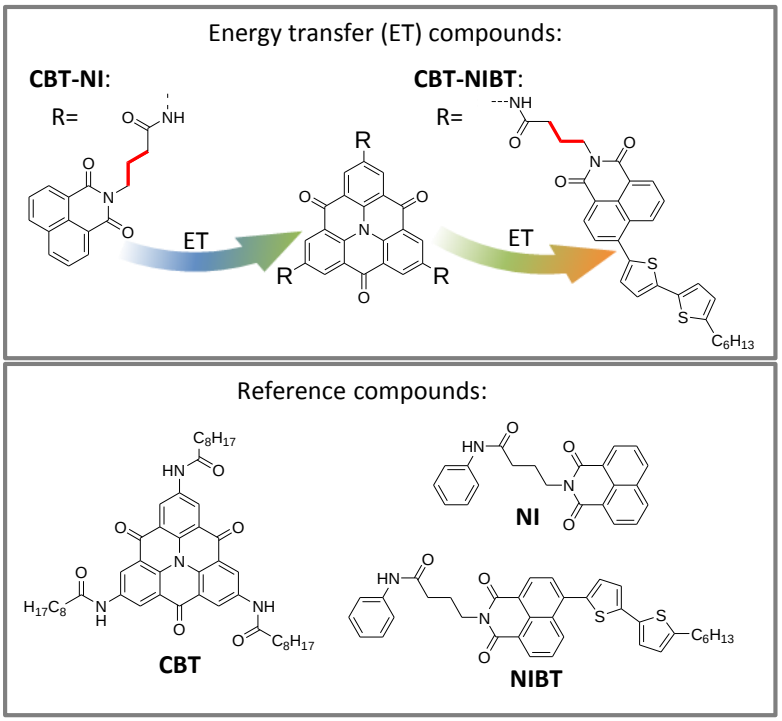

Figure 4. Top: Molecular structures of the multichromophoric compounds **CBT-NI** and **CBT-NIBT** including the direction of the energy transfer; electronically decoupling alkyl spacers are marked in red; CBT: carbonyl-bridged triarylamine; Bottom: Molecular structures of the reference compounds **CBT**, **NI**, and **NIBT**.

Absorption, steady-state and time-resolved photoluminescence (PL) spectroscopy including PL emission maps were recorded on µM solutions of all five compounds in 1,1,2,2-tetrachloroethane (TCE). Additionally, PL emission maps were recorded on mixed solutions of the respective reference compounds for comparison with the multichromophoric compounds. To complete the studies, the photoluminescence quantum yields were determined and cyclic voltammetry measurement were performed.

Investigation of the reference compounds revealed a spectral overlap between the photoluminescence of the **NI** and the absorption of the **CBT** as well as between the photoluminescence of the **CBT** and the absorption of the **NIBT**. This is an important prerequisite for efficient energy transfer between the chromophoric subunits within the multichromophoric compounds **CBT-NI** and **CBT-NIBT**.

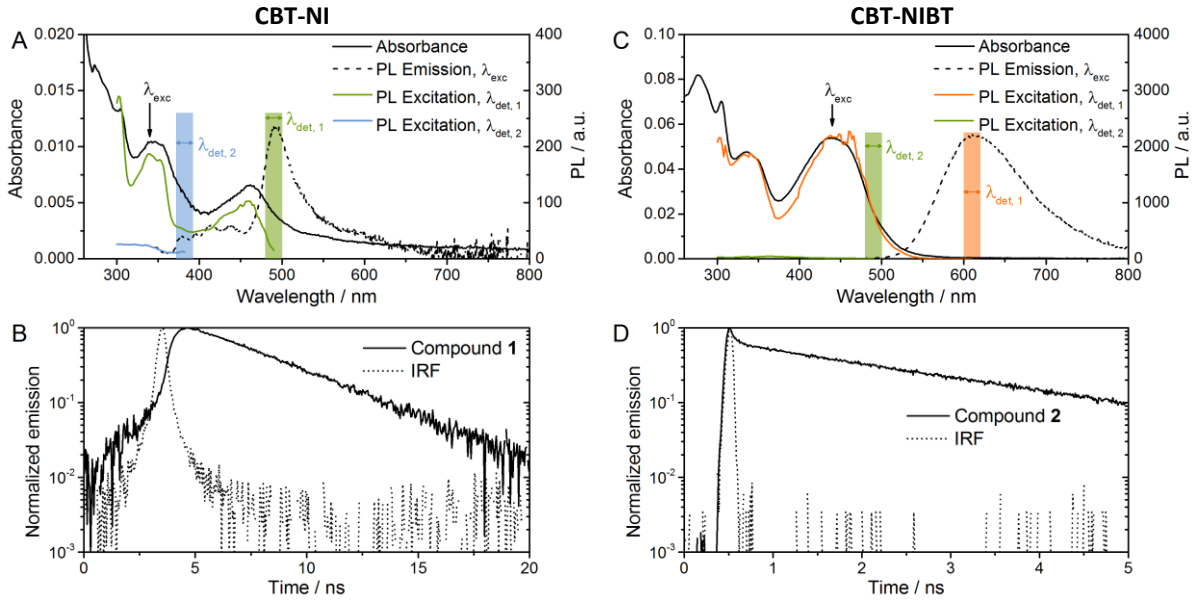

Figure 5. Photophysical properties of **CBT-NI** (A and B) and **CBT-NIBT** (C and D). A and C: Absorption (black solid line), photoluminescence (PL) emission (dotted line) and PL excitation detected at the spectral signatures of the respective chromophoric subunits (colored lines). B and D: Time-resolved PL emission (λ_{exc} = 360 nm for CBT-NI and 440 nm for CBT-NIBT, solid line) and Instrumental Response Function (IRF, dashed line).

The absorption of the first multichromophoric compound **CBT-NI** is a superposition of the absorption of the two chromophoric subunits, which hardly influence each other. Excitation of the naphthalimides in the periphery of the **CBT-NI** results in an exclusive photoluminescence from the carbonyl-bridged triarylamine core and the time-resolved transient of this emission shows a clear rise component (Figure 5 A and B). Both results verify an efficient energy transfer from the peripheral naphthalimides to the carbonyl-bridged triarylamine core. Using a standard kinetic model, the quantum yield for the energy transfer was determined to be 0.38. In the second multichromophoric system **CBT-NIBT** neither of the two chromophoric subunits could be excited individually. Nevertheless, using a similar line of argumentation, energy transfer in the opposite direction from the carbonyl-bridged triarylamine to the lateral 4-(bithiophene)-naphthalimide was demonstrated.

Interestingly, the second multichromophoric compound **CBT-NIBT** forms transparent, fluorescent gels in *ortho*-dichlorobenzene at very low concentrations of 0.7 mM. In this gel state the above mentioned photophysical and energy transfer properties are retained.

2.3. Long-Range Energy Transport through Individual Self-Assembled Nanofibres of Molecular Diameter

The capability of the multichromophoric compound **CBT-NIBT** (s. above Figure 4 top) to form transparent gels in *o*-DCB at sub-mmolar concentrations demonstrates the pronounced self-assembly of this compound into supramolecular networks of thin fibers. This is confirmed by tunneling electron microscopy images, revealing extremely long nanofibers with a homogenous diameter of only 5 nm (Figure 6 A, B). This value corresponds very well to the ideal diameter of a **CBT-NIBT** molecule, as determines by force field calculations (6 nm, Figure 6 C), illustrating the single stranded nature of those nanofibers. AFM studies, further, show the strong tendency of **CBT-NIBT** to self-assemble even at strongly reduced concentrations (10 ppm) into individual µm-long nanofibers (Figure 6 D). Spectroscopic techniques were used to shed light on the supramolecular interactions between the molecular units with respect to the amide linkers and the π-conjugated chromophores. FT-IR confirms the formation of strong hydrogen-bonds upon the self-assembly process. The photoluminescence spectra show due to the quenching of the carbonyl-bridged triarylamin core by energy transfer (s. chapter 2.2) only the emission of the lateral 4-(bithiophene)-naphthalimides, which give no sign of an aggregation into ordered structures. In the UV/vis absorption spectra, on the other, hand the rise of a blue-shifted band indicates the formation of H-aggregates of the central chromophore. This was confirmed by the **CBT**-reference compound from the previous chapter (Figure 4 bottom). According to theoretical models a coupling constant between the carbonyl-bridged triarylamines of at least $W = 350\ cm^{-1}$ was determined, which is in the coupling range observed in natural light harvesting systems. Conclusively, the molecular design of **CBT-NIBT** favors the formation of three-fold symmetric hydrogen bonds, which enforces a perfect cofacial stacking of the central triarylamine into strongly coupling H-aggregates.

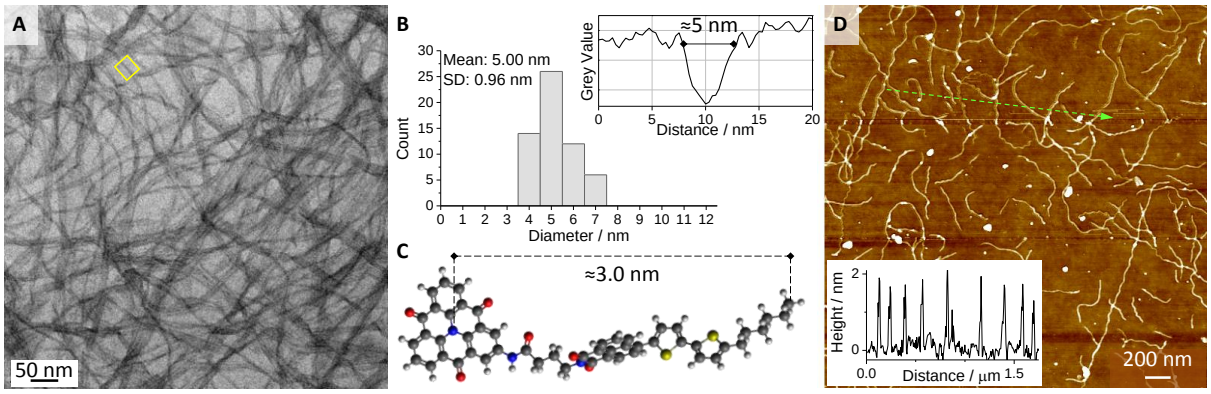

Figure 6. Self-assembly of **CBT-NIBT** into nanofibres with molecular diameter. A: TEM micrograph of a gelled sample (o-DCB at 1000 ppm, 0.1 wt.%, 0.7 mM); B: Statistic presentation of diameters from single fibres determined by grey value integration as exemplarily shown in the inlay which corresponds to the yellow boxed area in A. C: Energy minimized, elongated model of the CBT moiety with a single arm as part of the structure of **CBT-NIBT**. D: AFM micrograph of a self-assembled and spin-cast sample (10 ppm, o-DCB) of **CBT-NIBT**; Inset: height profile along the green arrow.

The prolonged lifetime of the excited state in H-aggregated chromophores should facilitate long-range energy transport. Consequently, spin-casted samples were investigated using a custom-build fluorescence microscope, revealing individual nanofibers with lengths of up to 4 µm (Figure 7 A). Intriguingly, confocal excitation of those fibers, under ambient conditions, exclusively at one end results in an emission from the entire fiber (Figure 7 B). This observation can only be explained by efficient long-range energy transport along the fibers, which corresponds to over more than 10000 molecules and is in this case only limited by the length of the fiber. Although the observed photoluminescence stems clearly from the lateral 4-(bithiophene)-naphthalimides (Figure 7 C, D), the mentioned lack of order between these chromophores suggests that the energy transport does not proceed through the periphery. Instead, the energy is transported through the strongly coupling H-aggregated carbonyl-bridged triarylamines in the core of the fiber. This transport is only hampered where the order of the central chromophores is slightly disturbed. At these sites the energy transfer from the core to the photoluminescent periphery becomes competitive, which is in accordance with the inhomogeneous emission-intensity-profile along the fibers (Figure 7 B bottom). Such long-range energy transport cannot be rationalized by diffusive Förster-type exciton migration. More likely is a wave-like transport induced by the strongly coupled H-aggregation, which distributes the excitation coherently over several chromophores.

According to theoretical models, which describe exciton motions in molecular crystals, the exciton diffusion constant in supramolecular nanofibers of **CBT-NIBT** can be determined to *D* = 0.04 cm^2/s. This value as well as the distance of the energy transport over 4 µm along individual supramolecular nanofibers of molecular diameter at ambient conditions is remarkable.

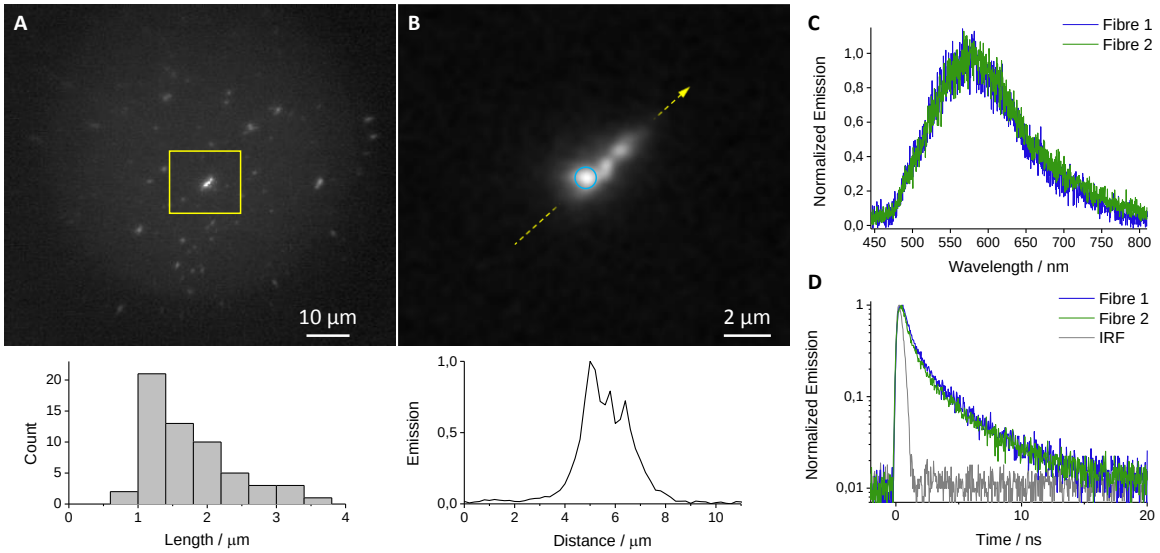

Figure 7. Long range excitation energy transfer along supramolecular nanofibers. A: Photoluminescence overview image of a spin-coated sample of aggregated **CBT-NIBT**. Bottom: Distribution of the fibre lengths. B: Photoluminescence image of the nanofibre in the yellow boxed region (A) upon confocal excitation exclusively within the blue circled area. Bottom: Intensity profile of the nanofibre along the dashed arrow. C: Photoluminescence spectra of two supramolecular fibres (blue, green). D: Time-resolved photoluminescence transients of two supramolecular fibres (blue, green). The instrument response function (IRF) is show in grey.

The obtained results bear promising perspectives for novel technologies *e.g.* in the fields of energy harvesting or quantum information technology. Furthermore, this study shows the great potential of highly ordered chromophoric or multichromophoric compounds, which are assembled employing the tools of supramolecular chemistry using precise molecular design.

2.4. Individual Contributions to Joint Publications

As part of the research training group 1640 on "*Photophysics of Synthetic and Biological Multichromophoric Systems*" I conducted the work on this thesis under the supervision of Prof. Dr. Hans-Werner Schmidt (Macromolecular Chemistry I, University of Bayreuth). The first topic of this thesis was carried out in cooperation with the chair of Prof. Dr. Anna Köhler (Experimental Physics II, University of Bayreuth). For the second and third part I worked closely together with Prof. Dr. Jürgen Köhler and Dr. Richard Hildner (Experimental Physics IV, University of Bayreuth) as well as Dr. Milan Kivala (Organic Chemistry I, University of Erlangen-Nürnberg). In the following, individual contributions of each author are presented.

Controlling the π-Stacking Behavior of Pyrene Derivatives: Influence of H-Bonding and Steric Effects in Different States of Aggregation

ChemPhysChem, **2013**, *14*, 1818

Andreas T. Haedler, Holger Misslitz, Christian Buehlmeyer, Rodrigo Q. Albuquerque, Anna Köhler, and Hans-Werner Schmidt

The first two authors of this manuscript contributed equally to this work.

I conducted the concentration dependent UV/vis absorption measurements that were essential for the understanding of the self-assembly of the compounds and are a major contribution to the paper. I interpreted most of the acquired data, which finally led to the publication. I steadily improved the data to the final form.

Holger Misslitz synthesized and characterized the compounds and conducted the concentration dependent photoluminescence measurements. He wrote a preliminary draft of the manuscript.

Christian Buehlmeyer (Experimental Physics II, University of Bayreuth) conducted the time-dependent and low temperature spectroscopy.

Rodrigo Albuquerque (Experimental Physics II, University of Bayreuth) did the molecular modeling and helped with the finalization of the manuscript.

Anna Köhler and Hans-Werner Schmidt supervised the project and were involved in discussions, the finalization of the manuscript, and the reviewing process.

Synthesis and Photophysical Properties of Multichromophoric Carbonyl-Bridged Triarylamines

Chemistry a European Journal, **2014**, *20*, 11708-11718

Andreas T. Haedler, Sebastian R. Beyer, Richard Hildner, Natalie Hammer, Milan Kivala, Jürgen Köhler, and Hans-Werner Schmidt

The first two authors of this manuscript contributed equally to this work.

I developed a synthetic route towards a versatile functionalization of carbonyl-bridged triarylamines. Following this route, I prepared in a multistep synthesis two multichromophoric carbonyl-bridged triarylamines. Furthermore, I synthesized three reference compounds including the majority of the involved intermediate products. I characterized the products with respect to their chemical structure. I studied the thermal, photophysical and electronic properties of the obtained compounds. Finally, I revealed for the first time the ability of carbonyl-bridged triarylamines to form organogels at surprisingly low concentrations.

Sebastian Beyer (Experimental Physics IV, University of Bayreuth) was in charge of the time resolved spectroscopic investigations that were conducted on the two multichromophoric systems and the reference compounds.

Sebastian Beyer and I discussed and interpreted the data and we wrote the majority of the final manuscript together.

Richard Hildner was involved in the discussion and the finalization of the manuscript.

Natalie Hammer (Organic Chemistry I, University of Erlangen-Nürnberg) synthesized the 2,6,10-trinitro-carbonyl-bridged triaraylamine, which served as starting material for the carbonyl-bridged triarylamine compounds.

Milan Kivala provided the trinitro CBT derivative and was involved in the finalization of the manuscript.

Jürgen Köhler and Hans-Werner Schmidt supervised the project and were involved in discussions, the finalization of the manuscript, the finalization of the manuscript, and the reviewing process.

Long-Range Energy Transport through Individual Self-Assembled Nanofibres of Molecular Diameter

Accepted in *Nature*

Andreas T. Haedler, Klaus Kreger, Abey Issac, Bernd Wittmann, Milan Kivala, Jürgen Köhler, Hans-Werner Schmidt, and Richard Hildner

I conducted the study of the gel and the investigations on the self-assembly of the multichromophoric compound. I studied the supramolecular aggregates with electronic and atomic force microscopy techniques, demonstrating the formation of extremely long nanofibers with molecular diameter. Using optical and FT-IR spectroscopy, I revealed that hydrogen-bonding of the amide moieties and H-aggregation of the carbonyl-bridged triarylamines are the reasons for the pronounced self-assembly. I interpreted the experimental data on the self-assembly and I was involved in the discussions concerning the energy transport properties. Together with Richard Hildner I wrote the majority of the manuscript.

Richard Hildner conducted the time-dependent spectroscopic measurements and he did the calculations on the nearest neighbor coupling and the exciton diffusion constant. With the support of Abbey Isaac and Bernd Wittmann he investigated the energy transport using a custom-built confocal fluorescence spectroscopy. Furthermore, he was involved in the discussion and interpretation of the data as well as the preparation of the manuscript.

Klaus Kreger and Milan Kivala were involved in discussions and the preparation of the manuscript.

Jürgen Köhler and Hans-Werner Schmidt supervised the project and were involved in discussions and the finalization of the manuscript.

3. Controlling the π-Stacking Behavior of Pyrene Derivatives: Influence of H-Bonding and Steric Effects in Different States of Aggregation

Andreas T. Haedler,[#1] Holger Misslitz,[#1] Christian Buehlmeyer,[2] Rodrigo Q. Albuquerque,[3] Anna Köhler,[2] and Hans-Werner Schmidt[1]*

[1] Macromolecular Chemistry I and Bayreuther Institut für Makromolekülforschung (BIMF) and Bayreuth Zentrum für Kolloide und Grenzflächen (BZKG) University of Bayreuth, 95440 Bayreuth (Germany)

[2] Experimental Physics II and Bayreuther Institut für Makromolekülforschung (BIMF) University of Bayreuth, 95440 Bayreuth (Germany)

[3] Experimental Physics II University of Bayreuth, 95447 Bayreuth (Germany) Current address: Institute of Chemistry of São Carlos University of São Paulo (USP), 13560-970 São Carlos-SP (Brazil)

[#] Both authors contributed equally to this contribution

* E-mail corresponding author: hans-werner.schmidt@uni-bayreuth.de

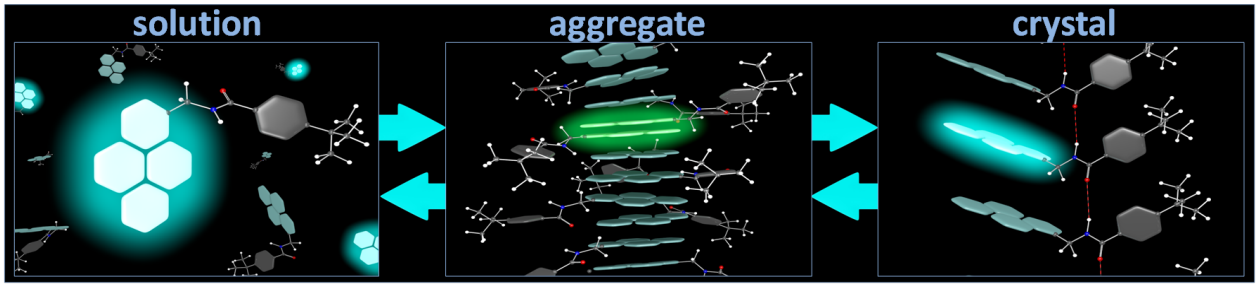

Published in *ChemPhysChem*, **2013**, *14*, 1818 – 1829

Abstract: The performance of opto-electronic devices built from low molecular weight dye molecules depends crucially on the stacking properties and the resulting coupling of the chromophoric systems. In this paper we investigate the influence of H-bonding amide and bulky substituents on the π-stacking of pyrene-containing small molecules in dilute solution, as supramoleuclar aggregates, and in the solid state. A set of four pyrene derivatives was synthesized in which benzene or 4-tert-butyl benzene was linked to the pyrene unit either via an ester or an amide. All four molecules form supramolecular H-aggregates in THF solution at concentrations above $1 \cdot 10^{-4}$ molL^{-1}. These aggregates were transferred on a solid support and crystallized. We investigate: the excimer formation rates within supramolecular aggregates; the formation of H-bonds as well as the optical changes during the transition from the amorphous to the crystalline state and; the excimer to monomer fluorescence ratio in crystalline films at low temperatures. We reveal that in solution supramolecular aggregation depends predominantly on the pyrene chromophores. In the crystalline state, however, the pyrene stacking can be controlled gradually by H-bonding and steric effects. These results are further confirmed by molecular modeling. This work bears fundamental information for tailoring the solid state of functional optoelectronic materials.

Keywords: self-assembly • kinetics • photophysics • fluorescence • molecular modeling

Introduction

Supramolecular chromophoric or multichromophoric systems are envisioned to serve as active materials in opto-electronic devices, in particular for organic photovoltaics (OPVs).[1] For those applications π-conjugated aromatic systems are promising candidates. They can transfer charge and energy, and their absorption and photoluminescence wavelength can be tuned comparatively easily.[2] Transport as well as the optical properties and thus the device performance depend largely on the electronic coupling of the π-conjugated systems.[3] Therefore, the distance between and the relative orientation of the chromophores are crucial and need to be adjusted thoroughly by fine-tuning the molecular structure.[4] To solve this difficult task, tools and concepts of supramolecular chemistry are utilized. However, a good understanding of the interplay of non-covalent intermolecular interactions like ionic-,

dipole- or Van-der-Waals interactions and combinations thereof is needed.[5] Especially H-bonding, hydrophilic-hydrophobic interactions and, steric repulsion are widely used in this context.[6] Furthermore, the influence of those intermolecular interactions on the π-π stacking of the active chromophoric system depends also on the state of matter and aggregation.

A well-established chromophore is needed to investigate the complex relationship between the molecular structure, the relative orientation of the π-conjugated systems and the resulting optic and electronic properties. Pyrene is a suitable candidate as its optical behavior is well understood in solution, the aggregated and the solid state.[7] Förster assigned the quenching of fluorescence in pyrenes to the formation of excimers already in 1955, and Birks later investigated this excimer formation in detail.[8] An excimer may be considered as a pair of molecules that, in the ground state, are bound together only weakly (e.g. in the solid) or not at all (e.g. in solution), and that absorb light as monomers, but that reorient in the excited state and then fluoresce as dimers. [9,10] The excited dimer (= excimer) fluorescence is broad, unstructured and bathochromically shifted from the monomer fluorescence, and it leads to the two monomers in their ground state.[11–13] The strong tendency of pyrene to form excimers prevails both in solution and in condensed matter such as amorphous films, liquid crystals and crystals.[9,14] Note that in the condensed phase, the pyrene chromophores are usually already in close proximity and often, e.g. in the crystal, arranged in sandwich-type pairs. However, for the excimer formation, a displacement leading to closer and/or differently oriented arrangement is still needed. This excimer emission can also be indirectly used to detect the aggregation process of pyrene derivatives.[10,15] These characteristic properties have been employed in the investigation of pyrene-based tweezer molecules[16] and multimolecular aggregates of micelles and membranes[17], the gelation detection of organic low-molecular weight compounds[18], the inspection of the active sites of enzymes[19], the molecular recognition process of artificial receptors[20] and DNA sequences[21] and, in the detection of nitroaromatic explosives.[22]

Herein, we use pyrene derivatives to study the influence of H-bonding and steric effects on the coupling behaviour of the chromophores in different phases. For that purpose a set of four compounds was synthesized comprising of a benzene or a 4-*tert*-butyl benzene group

connected to the pyrene via a methylene-ester or -amide linker (Figure 1). The methylene group breaks the conjugation between the dye and the rest of the molecule, hence, the optical properties of the pyrene is not directly influenced by the linker and the benzene substituent. However, indirect influence is possible due to the potential formation of H-bonds in the case of the amide compounds and due to steric effects arising from the additional *tert*-butyl group.

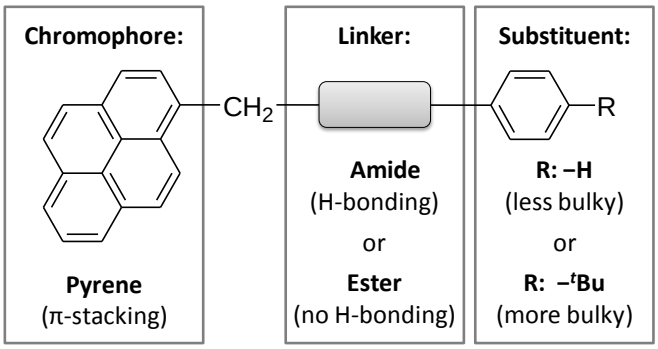

Figure 1. Pyrene derivatives consisting of different linker and substituents separated by a methylene group from the chromophore.

Results and Discussion

Synthesis and Thermal Properties

The synthetic routes to pyrenyl-based ester derivatives **1a-b** and their corresponding amide derivatives **2a-b** are shown in Scheme 1. (1-Pyrenyl) methanol was reacted with benzoic acid chloride or *p*-(*tert*-butyl) benzoic acid chloride in chloroform and triethylamine as base to obtain the two ester compounds **1a-b**. For the amide compounds **2a-b** the same acid chlorides were reacted with (1-pyrenyl) methylamine in dry *N*-methyl-2-pyrrolidone (NMP) and pyridine as base. All products are insoluble in apolar solvents and show moderate solubility in THF, chloroform, dioxane and DMSO.

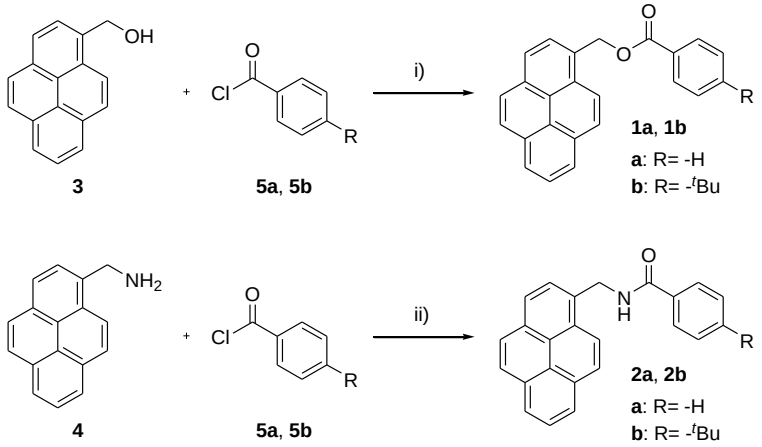

Scheme 1. Synthesis of pyrene derivatives with ester linker **1a-b** and amide linker **2a-b**. i) chloroform, triethylamine, DMAP, 60°C; ii) NMP, pyridine, 80°C.

The thermal properties of compounds **1a-b** and **2a-b** were determined by differential scanning calorimetry (DSC). Upon first heating, the ester compounds **1a** and **1b** exhibit melting points (T_m) at 133°C and 140°C, respectively. Both compounds do not crystallize upon cooling forming a vitrified supercooled liquid. Consequently, upon second heating **1a** and **1b** feature glass transitions with temperatures (T_g) at 4°C and 23°C. On further heating, only **1a** recrystallizes at 70°C and subsequently melts at 130°C. As expected, the glass transition temperature is shifted to higher temperatures for compound **1b** due to the bulky *tert*-butyl-group. In contrast, the amide compounds **2a** and **2b** possess a more pronounced crystalline behavior. Upon first heating the melting points were detected at 199°C and 248°C, respectively; while upon cooling both compounds crystallize at 123°C and 178°C. Upon second heating **2a** features a glass transition at 54°C and recrystallize at 114°C indicating incomplete crystallization upon cooling. In contrast, compound **2b** exhibits complete crystallization upon cooling. Hence, to determine its glass transition temperature, an amorphous sample was prepared by rapid quenching from the molten state. The first heating curve reveals the T_g at 77°C. Similar to the ester compounds, the T_g and the T_m increase with the introduction of the *tert*-butyl-group. A significant difference between the ester and the amide compounds are higher T_m (70°C to 100°C) and T_g (50°C) values for the latter. This result is a consequence of the formation of intermolecular H-bonds by the amide units. A similar shift of T_g and T_m to higher temperatures by substituting ester with amide linkages was recently also reported for trisazobenzene derivatives.[23]

Table 1. Thermal properties of amide and ester compounds determined from DSC measurements (Heating and cooling rate: 20 °Cmin^{-1} under N_2)

	T_m / °C (first/second heating)	T_{cryst} / °C (cooling)	$T_{recryst}$ / °C (second heating)	T_g / °C (on heating)
1a	133/130	-	70	4[a]
1b	140/ -	-	-	23[a]
2a	199/196	123	114	54[a]
2b	248/245	178	-	77[b]

[a] Determined from second heating.

[b] Determined upon first heating of a previously quenched sample.

Structural Influences on the Pyrene Interaction in Diluted to Concentrated THF Solution

In this section we first focus on discussing the photophysical properties inherent to all four pyrene-derivative before then considering the differences resulting from the substitutents. *The UV-Vis absorption spectra* were recorded at different concentrations in THF solution and are shown in Fig. 2 exemplary for **1a** and for all compounds in the supporting information Figure S1. For all absorption measurements 1 mm cuvettes were used to account for the high concentrations at which the measurements were performed keeping the maximum OD values below 3. All four compounds show almost identical absorption characteristics (**1a-b**, **2a-b**), which proofs the electronic decoupling of the chromophore from the substituent by the methylene spacer. The absorption closely resembles that of pyrene. It shows a very weak feature at about 375 nm and two intense bands, one in the 350-300 nm range and one from 280-240 nm. By comparison with the pyrene spectrum these features can be readily assigned. The weak 375nm feature is the symmetry-forbidden $S_0 \rightarrow S_1$ transition in pyrene, the first intense band with a (0-0) peak at 344 nm and vibronic replicas at 326 nm, 313 nm and 301 nm corresponds to the the pyrene $S_0 \rightarrow S_2$ transition and the peak at 278 nm is due

to the pyrene $S_0 \rightarrow S_3$ (0-0) transition, with vibronic replicas at shorter wavelength.[24]Those characteristics are likewise reported in literature for similar pyrene derivatives.[25]

An interesting detail concerns the relative intensities of the vibrational peaks at different concentrations. The curves in figure 2 are normalized to the peak maximum of the (0-1) transition of S_2 at 326 nm, which enables a comparison of the absorption intensities originating from the different vibrational transitions $A_{(0-0)}$, $A_{(0-1)}$, $A_{(0-2)}$, etc.. With increasing concentration, $A_{(0-0)}/A_{(0-1)}$ decreases while the ratio of the (0-1) transition to higher transitions is almost identical. A similar behavior is also seen for the vibrational structure of the third electronic excitation. This is unusual. A relative reduction of the 0-0 peak intensity compared to the 0-1 has been reported for the S_1 state of perylene bisimide dyes and of the polymer P3HT. In both cases, it has been taken as indication for the formation of weakly interacting H-aggregates.[26,27] Higher electronic excitations have not been considered explicitly so far in this framework. For the best of our knowledge, this is the first experimental report explicitly describing such behavior in the excitation of two higher electronic states. We note, though, that Winnik, in a review article, also noticed a reduction in relative 0-0 peak height with increasing degree of pyrene association.[10] Winnik assessed this by considering the 0-0 peak height and comparing it to the intensity of the minimum between the 0-0 and the 0-1 vibrational peak. In view of todays knowledge on electronic interactions between molecules,[26,28] we consider that the reduction of the 0-0 peak in S_2 and S_3 in the pyrene derivatives may be taken to indicate the formation of such a weakly interacting H-aggregate, i.e. associations of pyrene molecules that electronically interact already in the ground state.

In the same concentration range ($1 \cdot 10^{-4}$ molL^{-1} - $1 \cdot 10^{-3}$ molL^{-1}), *dynamic light scattering (DLS) measurement*s were conducted to obtain an indication for the size of the aggregates. We used a laser beam of 632.8 nm wavelength to avoid the excitation of the pyrene units during the measurements. For all compounds (**1a-b**, **2a-b**) the obtained scattering signal implies that at a concentration of $1 \cdot 10^{-4}$ molL^{-1} in THF, the size of any supramolecular aggregates is below the detection threshhold, whereas particles of at least a few tens of nm in size are detected at concentrations above $1 \cdot 10^{-3}$ molL^{-1}. From the DLS measurements we cannot give a reliable size-distribution of the particles as the supramolecular aggregates are

non-spherical in all cases. The morphology of the supramolecular aggregates at concentrations of $1 \cdot 10^{-2}$ molL^{-1} was visualized by (SEM) using freeze-dried samples from dioxane (Figure S2.1 and S2.2).

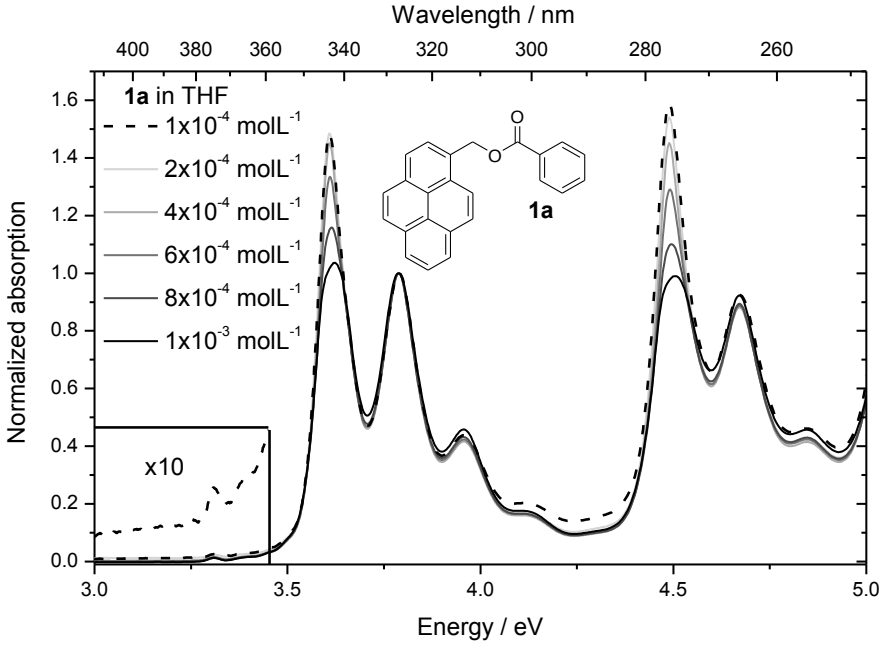

Figure 2. UV-Vis absorption spectra of compound **1a** at different concentrations from $1 \cdot 10^{-4}$ to $1 \cdot 10^{-3}$ molL^{-1} in THF normalized to the (0-1) transition at 326 nm; the enlargement shows the 10 times magnified transition to the first electronically excited state for the concentration of $1 \cdot 10^{-4}$ molL^{-1}.

The steady state photoluminescence (PL) spectra of the compounds in THF were investigated at different concentrations ranging from $6 \cdot 10^{-6}$ to $6 \cdot 10^{-2}$ molL^{-1}. The spectra are displayed in figure 3. The evolution of the monomer fluorescence intensity and the relative $A_{(0\text{-}0)}/A_{(0\text{-}1)}$ absorption peak height with concentration is shown in figure 4. All compounds (**1a-b**, **2a-b**) show the same concentration-dependent PL properties. At low concentrations, the PL spectrum shows a vibrational structure that is characteristic for the $S_1 \rightarrow S_0$ fluorescence of molecularly dissolved pyrenes.[29] With increasing concentration, a broad unstructured emission appears, centered at around 470 nm, that is typical for the excimer fluorescence of pyrene. All four compounds (**1a-b**, **2a-b**) show an identical excimer fluorescence at a concentration of $6 \cdot 10^{-2}$ molL^{-1}, which confirms the formation of the same excimer species in all cases (Figure S3). This excimer fluorescence is first barely discernible at a concentration of $6 \cdot 10^{-4}$ molL^{-1} (and more clearly visible at $1 \cdot 10^{-3}$ molL^{-1}) and then increases in intensity with concentration. In contrast, when considering the intensity of the monomer fluorescence, the

intensity increases with concentration until, at $2 \cdot 10^{-5}$ molL^{-1}, it reaches its maximum and then reduces drastically. The ratio of $A_{(0-0)}/A_{(0-1)}$ in absorption remains constant up to a concentration of $3 \cdot 10^{-4}$ molL^{-1} and then drops steeply.

For the interpretation of this data it is important to recall that the three spectroscopic signatures, i.e. the monomer fluorescence, the excimer fluorescence and the $A_{(0-0)}/A_{(0-1)}$ absorption peak height indicate distinct photophysical processes. (i) The sudden decrease of the $A_{(0-0)}/A_{(0-1)}$ ratio in absorption gives the concentration at which ground state association begins to occur. In Fig. 4, this is highlighted by a grey shading. In contrast, (ii) the fluorescence quenching at a much lower concentration marks the regime where some interaction takes place in the excited state of the molecule, leading to a non-emissive species. This species cannot be the sandwich-type pyrene excimer identified by Birks[11] for the following reason. The quantum yield of emission of the pyrene monomer and the pyrene excimer observed by Birks are comparable, e.g. in cyclohexane solution being 0.65 for the monomer and 0.75 for the excimer and in toluene solution being 0.52 and 0.55, respectively.[24] If the excited monomer were to result in an excimer, according to the reaction M+M*→E* (E* denotes the excimer (M+M)*), the reduction of monomer fluorescence should be accompanied by a concomitant growth of excimer fluorescence. In the experiment, this is, however, not the case. We therefore come to the conclusion that the quenching of monomer fluorescence in the intermediate concentration regime ($1 \cdot 10^{-5}$ molL^{-1}-$3 \cdot 10^{-4}$ molL^{-1}) indicates the formation of a non-emissive precursor-type species. At this stage, we can only speculate on the nature of this species. It is conceivable that the molecular approach and orientation required for the formation of an emissive excimer is impeded in compounds **1** and **2** by the substituents, so that only a non-emissive precursor can be formed. (iii) We now focus our attention on the experimental observation that excimer fluorescence is only observable at concentrations in excess of $6 \cdot 10^{-4}$ molL^{-1}, yet not at lower concentration. From the $A_{(0-0)}/A_{(0-1)}$ ratio we know that ground-state associates prevail in this regime, and the DSL measurements tell us these evolve into supramolecular aggregates of a few tens of nm for concentrations above $1 \cdot 10^{-4}$ molL^{-1}. This implies that for the pyrene-derivatives **1** and **2**, the formation of emissive excimers requires a kind of ground state stabilization that is onlv available in the environement provided by supramolecular aggregates.

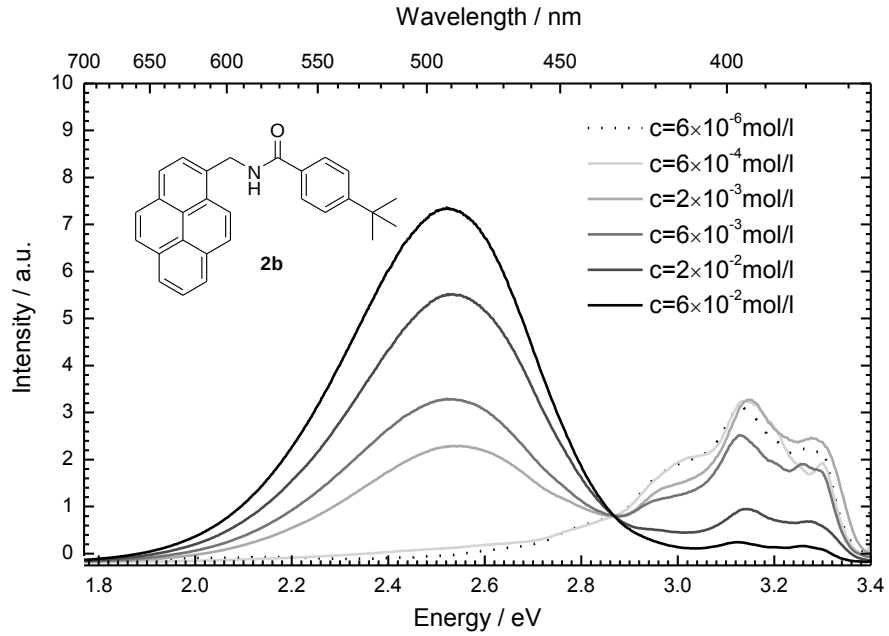

Figure 3. Photoluminescence spectra of compound **2b** at different concentrations from $6 \cdot 10^{-6}$ to $6 \cdot 10^{-2}$ molL^{-1} normalized at 434 nm.

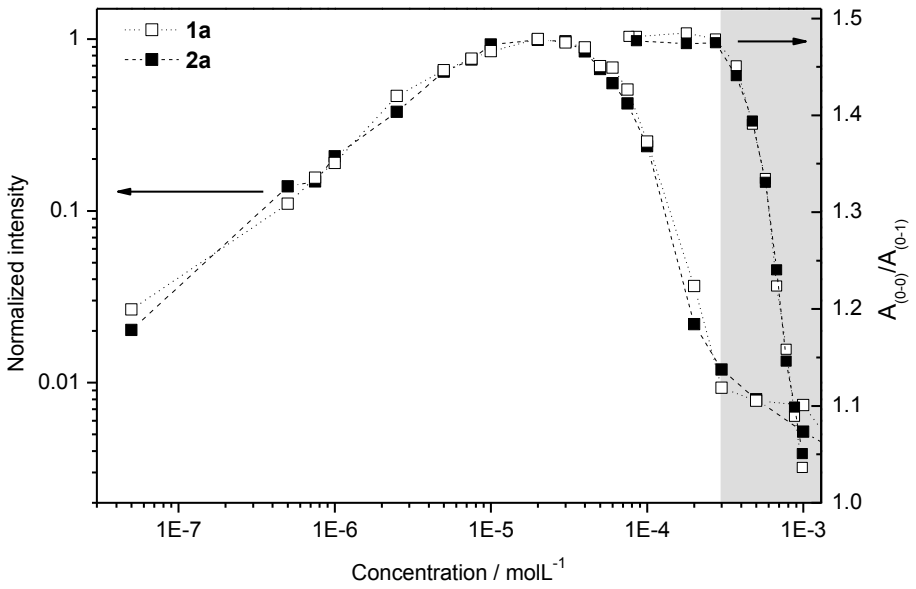

Figure 4. Photoluminescence intensities of the (0-0) transition at 375 nm (left) and the ratio of $A_{(0-0)}/A_{(1-0)}$ (right) of compounds **1a** and **2a** at different concentrations. The shaded area depicts the concentration range in which the formation of aggregates starts to occur.

While the decay of the monomer fluorescence with increasing concentration is almost identical for all compounds, a small variation in the ratio of monomer to excimer fluorescence intensity can be observed for the different substituents. In order to evaluate how the excimer formation is affected by chemical modification, we have determined the excimer formation rates using *time-resolved photoluminescence* measurements and analyzing the associated rate equations analogous to the approach taken by Birks et al. in 1963. Birks and coworkers described excimer formation as a process of the type $M+M^* \rightleftharpoons E^*$that takes place with a concentration-dependent rate $k_{FM}[M]$ for the forward reaction (excimer formation) and a concentration-independent rate k_{ME} for the back reaction (excimer dissociation).[12] Here, [M] is the concentration of monomers. In addition, the deactivation processes $M^* \rightarrow M$ and $E^* \rightarrow M+M$ are considered with rates k_M and k_E, respectively. After pulsed excitation, the decay of M* and E* is then described by the rate equations $d[M^*]/dt=-(k_M+k_{EM}[M])[M^*]+k_{ME}[E^*]$ and $d[E^*]/dt=-(k_E+k_{ME})[E^*]+k_{EM}[M^*]$. These two coupled differential equations can be solved to give two concentration-dependent decay constants λ_1 and λ_2 from which the excimer formation rate k_{EM} can be extracted by a linear fit to the concentration-dependence since $\lambda_{1+}\lambda_2=k_M+k_E+k_{ME}+k_{EM}[M]$.[12]

For the pyrene derivatives investigated here, we need to consider that the excimer is evidently not formed by the association of two monomers but that it is preceeded by the formation of ground-state associates. As we have no experimental information on the number of electronically interacting molecules in these associates, we take the heuristic approach of considering dimers. The excimer formation is then described as $D+D^* \rightleftharpoons E^*+D$ with $k_{ED}[D]$ and k_{DE} being the forward and back reaction rate. The deactivation processes are $D^* \rightarrow D$ and $(E^*+D) \rightarrow (D+D)$ with rates k_D and k_E, respectively. The decay rates can be formulated and analyzed analogously to the Birks-1963 model, $d[D^*]/dt=-(k_D+k_{ED}[D])[D^*]+k_E[(E^*+D)]$ and $d[(E^*+D)]/dt=-(k_E+k_{DE})[(E^*+D)]+k_E[D^*]$. The signals to monitor as function of concentration are then the fluorescence of the (dimer stabilized) excimer (E*+D) at 470 nm and the fluorescence of the excited dimer D*. What is the spectral signature of the dimer fluorescence? Since the dimer is of a weakly interacting H-aggregate type, as suggested by the absorption spectra, the emission is at the same spectral position than the monomer emission, albeit of a different, i.e. weaker oscillator strength. The signal to monitor is therefore the emission at 400 nm.

We have thus measured the photoluminescence decay of the compounds in THF at different concentrations ranging from $2 \cdot 10^{-4}$ molL^{-1} to $6 \cdot 10^{-2}$ molL^{-1} using a time-correlated single photon counting (TCSPC) set up. The chromophores were excited with a 375 nm laser and the time-dependent spectra were recorded at 400 nm and at 485 nm. The typical change in the fluorescence decays with increasing concentration is shown in Figures 5 for compound **2a**, along with the concentration-dependence obtained for the decay constants λ_1 and λ_2. The decay curves show a build-up of the excimer emission (grey curve) at short times, e.g. below 50 ns at $5.7 \cdot 10^{-4}$ molL^{-1} and below 10 ns at $6 \cdot 10^{-2}$ molL^{-1}, followed by a mono-exponential decay. The dimer emission at 400 nm (black curve) also decays mono-exponentially. The decay of the dimer fluorescence (black curve) becomes faster with increasing concentration as the formation of excimers gets more likely. The excimer fluorescence (grey curve) increases in the beginning due to the time-delayed formation of the excimer species after the initial excitation of the monomer. The excimer fluorescence reaches, as expected, its maximum faster with increasing concentration. From those curves, the decay constants λ_1 and λ_2 can be determined and can be plotted against the concentration of monomers (= twice the dimer concentration) (Figure 5). The dependence of their sum on the concentration agrees well with the linear relationship suggested by the kinetic model and gives, a posteriori, further support to the heuristic approach taken. Fitting the data with the equations from Birks et al. yields the relevant values of k_{ED} (Table 2). The entire approach is portrayed in more detail in the supporting information (Figure S4, S5).[12]

The excimer formation rates (k_{ED}) found in this way for all four compounds (**1a-b**, **2a-b**) for the formation of excimers from pre-exisisting dimers are between $6.9 \cdot 10^9$ and $3.9 \cdot 10^9$ Ls^{-1}mol^{-1}. This agrees well with the value of $6.7 \cdot 10^9$ Ls^{-1}mol^{-1} determined by Birks et al. for the formation of excimers from individual monomers in the unaltered pyrene[12]. Within the four compounds the ones with the bulky *tert*-butyl group **1b** and **2b** show the lowest excimer formation rates of approximately $3.9 \cdot 10^9$ Ls^{-1}mol^{-1}. We attribute this to sterical hindrance. For both, the –H and –^{t}Bu substituted compounds the one with the ester linker **1a** and **1b** show higher excimer formation rates than the corresponding amide compound **2a** or **2b**. Hence, the amide linker does not favor the formation of an excimer but hinders it.

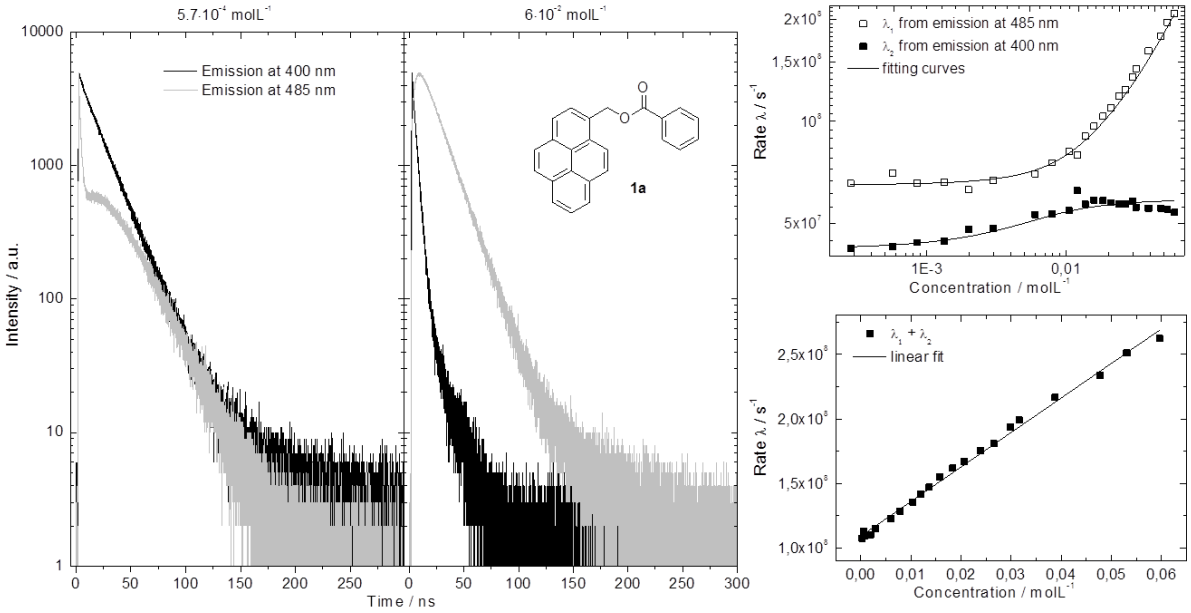

Figure 5. Time-resolved photoluminescence transients of compound **2a** at $5.7 \cdot 10^{-4}$ molL^{-1} (left) and $6 \cdot 10^{-2}$ molL^{-1} (middle) showing the fall-off of the emission at 400 nm (black) and at 485 nm (grey). Right top: Decay rates λ_1 and λ_2 of the emission at 485 nm (□) and at 400 nm (■) at different concentrations for compound **1a** fitted according to Birks.[12] Right bottom: Sum of λ_1 and λ_2 plotted against the concentration yielding the expected linear dependency.

Table 2. The excimer formation rates for pyrene and the four compounds **1a-b** and **2a-b** determined from the TCSPC measurements.

	Pyrene[a]	**1a**	**2a**	**1b**
k_{ED} [10^9 Ls^{-1}mol^{-1}]	6.7	6.88 ± 0.7	5.34 ± 0.5	3.96 ± 0.4

[a] Value was determined by Birks et al.[12]

We now summarize the insight gained from the spectroscopic investigations in solution. At low concentrations, i.e. below $1 \cdot 10^{-5}$ molL^{-1}, the four compounds (**1a-b**, **2a-b**) are molecularly dissolved in THF. In an intermediate concentration range (about $1 \cdot 10^{-5}$ molL^{-1}- $3 \cdot 10^{-4}$ molL^{-1}), non-emissive intermediate species are formed. They quench the monomer fluorescence yet do not impinge on the absorption spectra, implying that they may be viewed as a non-emissive precursor to an excimer state. At increased concentrations, i.e. above $3 \cdot 10^{-4}$ molL^{-1} weakly interacting ground state H-aggregates are formed. In contrast to unaltered pyrene, in

the compounds (**1a-b**, **2a-b**) with the comparatively large sidechains, the formation of emissive excimers requires a stabilization evidently provided by the aggregate. A significant influence of the structural variations, namely the linker moiety (ester or amide) and the sterical hindrance of the substituted benzene unit on the optical and aggregation properties in THF cannot be observed. Therefore, we conclude that the pyrene chromophores, which are coherently present in all compounds, are the crucial and determining part of the compounds in this concentration regime. Only a closer look at the excimer fluorescence and the excimer formation rates reveal the influence of the variable substitutions on the pyrene chromophore. The ester compound **1a** is most feasible to form excimers. The introduction of the *tert*-butyl group strongly hinders the excimer formation. The same effect is observed much weaker when the ester group is replaced with an amide linker. The influence of the linker and the bulky *tert*-butyl group on the pyrene chromophore is just secondary and only observable at concentrations where supramolecular aggregates are present.

Structural Influences on the Pyrene Interaction in Thin Films

Thin films were prepared as detailed below and investigated in two morphologies, an optically isotropic one and a crystalline one, by using *polarized optical microscopy* (POM), *absorption and fluorescence spectroscopy*, and in the case of the amide compounds also by *FT-IR spectroscopy*. The POM images of the crystalline films are presented in the supporting information (Figure S7).

Optically isotropic films: All compounds (**1a**-**b, 2a**-**b**) were spin coated from THF solution at a concentration of $5 \cdot 10^{-2}$ molL^{-1}. At this concentration supramolecular aggregates are present in solution as previously demonstrated in DLS experiments. The fresh films were optically transparent and no crystalline structure could be observed by POM. The absorption spectra are similar for all compounds (Figure S6) and closely resemble that observed in concentrated solution, except for a slight red-shift. Interestingly, the $A_{(0\text{-}0)}/A_{(0\text{-}1)}$ ratio is slightly lower in concentrated solution (about 1.0 for concentrations of $1 \cdot 10^{-3}$ molL^{-1} and above) than in the thin film (about 1.1). This implies that electronic coupling within aggregates is slightly stronger in solution than in the film, presumably because the local geometry can be optimized more in solution as compared to film. The room-temperature photoluminescence

spectra of the fresh films of all investigated compounds do not show any monomer fluorescence. Instead, they show only the same excimer fluorescence that was already observed in concentrated solution, except that the center wavelength shifts from 470 nm in solution to 500 nm in the film due to the different dielectric constant (Figure S8).

From the solution measurements we know that, in contrast to unsubsitituted pyrene, the substituted derivatives (**1a**-**b, 2a**-**b**) only show excimer emission when the excimer geometry is stabilized within a ground state associate. Thus we can interpret the thin film PL data such as to indicate the presence of aggregates in the film. This is not surprising. For example, for the polymers poly(9,9'-dioctyl-fluorene) (PFO) and poly(3-hexylthiophene) (P3HT), it is well known that aggregate formation is enhanced in thin films upon spin-coating when aggregates already existed in the solution used. [30] The absence of any monomer fluorescence suggests that either no monomers are present, or, any excited monomer state is quenched by energy transfer either to non-emissive states such as the states observed in solution at intermediate concentration or to emissive excimers.

Crystalline films: The PL spectra are different when the films are processed such as to obtain a crystalline structure. To induce crystallization, the fresh films of amide **2a** and amide **2b** were annealed above T_g at 80°C and 130°C. The observation of light transmission under crossed polarizers in an optical microcope confirms the presence of crystalline structures in the film (Figure S7). To obtain further insight into the structural changes associated with the crystallization process, FT-IR studies were performed on the films of the amide compounds (**2a**-**b**) in the isotropic and crystalline state. For both compounds, a shift of the N-H and the carbonyl stretching vibration to lower wave numbers as well as an increase in the IR absorption intensity is observed during the crystallization process. Both changes in the FT-IR spectra strongly indicate the formation of strong hydrogen-bonds.[31] The shift of the N-H and carbonyl stretching vibration from 3312 cm^{-1} to 3281 cm^{-1} and from 1637 cm^{-1} to 1629 cm^{-1}, respectively, is shown exemplarily for compound **2a** in Figure 6. Amide **2b** exhibits the same trend but much less pronounced. This indicates weaker hydrogen-bonds due to the steric hindrance of the *tert*-butyl group (Figure S10).

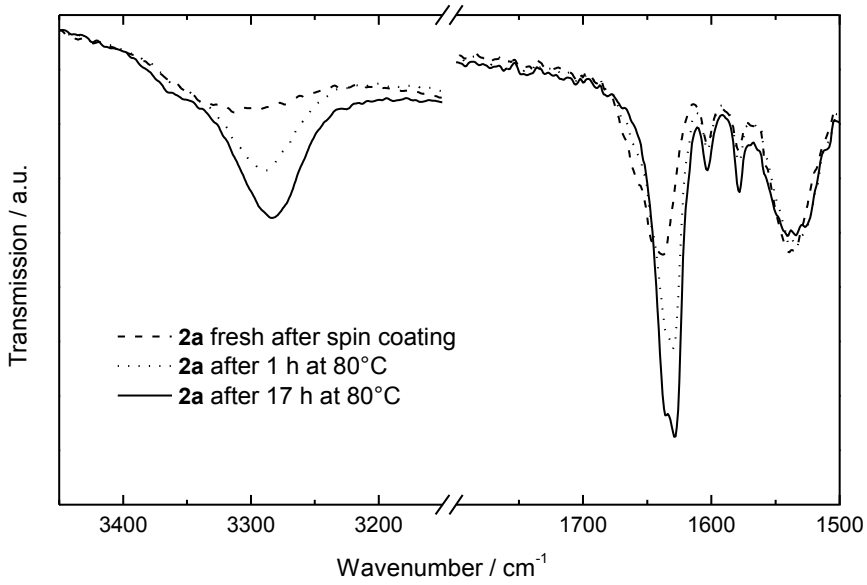

Figure 6. Enlargements of the relevant parts of the FT-IR spectra of a thin film of compound **2a** during the aging process resembling different degrees of crystallization; the N-H stretching vibration (left: around 3300 cm^{-1}) and the carbonyl stretching vibration (right: around 1630 cm^{-1}) are represented.

For the ester compounds, a different approach needed to be taken to obtain crystalline films. Unlike the amide compounds, the fresh films of the ester compounds exhibited dewetting at elevated temperatures. Therefore, they were aged at room temperature in the dark for several months to induce crystallization, as confirmed by POM. Hence, in all cases we were able to convert the optically isotropic fresh film into one containing crystallites. The aging and annealing processes were conducted until a stable state was achieved and no further changes could be observed in the POM, FT-IR and photoluminescence spectra at room temperature.

For all compounds except **1b**, the photoluminescence spectra change upon crystallization. During this process, the excimer emission is reduced and simultaneously a structured higher-energy emission rises. This is exemplarily shown in Figure 7 for ester **1a**.

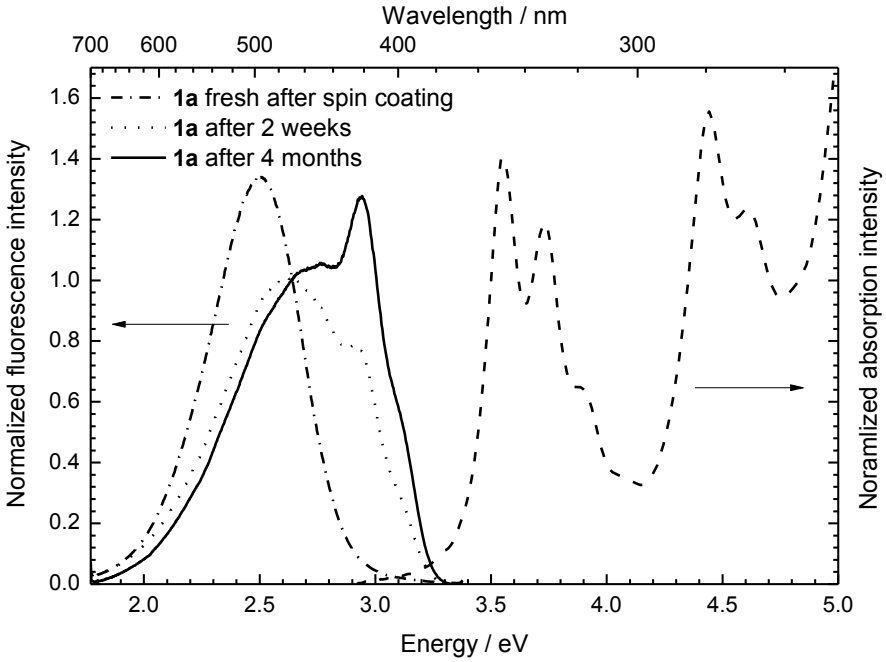

Figure 7. Absorption (right) of an amorphous thin film of compound 1a directly after spin coating and photoluminsecence spectra (left) of a thin film of compound 1a during the aging process resembling different degrees of crystallization.

For a clearer understanding of the molecular behavior in the crystalline state, the thin film photoluminescence was investigated as a function of temperature upon heating from 5 K to 295 K. The spectra at selected temperatures are shown in Fig.8. For all compounds except **1b**, the excimer fluorescence vanishes gradually upon decreasing the temperature, while simultaneously the structured higher energy fluorescence intensity rises. At 5 K, only the structured higher energy emission prevails. In contrast, compound **1b** shows exclusively excimer fluorescence even at 5 K. In general, the relative fraction of excimer emission compared to the higher energy emission is higher in compounds **1b** and **2b** containing the sterically demanding *tert*-butyl group compared to compounds **1a** and **1b**, that only contain a –H atom instead. The relative amount of excimer emission is also higher in the ester-containing compounds (**1a** and **1b**) compared to the amide-containing compounds (**2a** and **2b**).

To understand the changes that take place in the electronic structure upon crystallization, let us first recall that compound **2a** allows for the most ordered structure due to the effect of the H-bonding amide moieties. On the other hand, the sterically demanding *tert*-butyl

group and the absence of the stabilizing amide group implies that compound **1b** is likely to have the least ordered structure. This correlates with the fact that compound **2a** shows the lowest relative amount of excimer emission while **1b** exhibits purely excimer emission. Evidently, excimer formation is prevented upon crystallization, while it is promoted by aggregates. This is different to the situation in unsubstituted pyrene, where excimers form in the crystalline state. In fact, in pyrene crystals, the basis of the unit cell is formed by sandwich-type dimer pairs of pyrene-molecules that slip horizontally upon photoexcitation to form an excimer.[9,24]

How can we understand the absence of excimer emission in crystallites of the substituted pyrene-derivatives? The aggregates prevailing in the optically isotropic film and the crystallites in the films evidenced by the POM patterns differ in the degree of structural order. We propose that the aggregates that are formed in solution or in the non-equilibrium structure of a spin-cast film will be subject to a certain amount of structural variation with regard to molecular orientation or distance. Further, intermolecular distance between two pyrenes may vary at the interface between the ends of two aggregates. Some of these local geometries may be suitable for excimer formation after photoexcitation. As mentioned above, the fact that in freshly spun films only excimer fluorescence is observed implies that there is an excimer-site within the exciton diffusion range of any photoexcited chromophore. In contrast, the structure within the crystallites is, by definition, more regular and, as experiment tells us, of a kind that does not allow for excimer formation. It seems that the horizontal slip movement that results in excimers in unsubstituted crystalline pyrene is impeded by the large sidechain in substituted crystallized pyrene. Thus, upon crystallization, the number of sites that allow for excimer formation therefore reduces, as manifested in figure 7.

In this framework, we can interpret the results of figure 8. For compound **1b**, which is structurally most disordered, excimer emission is observed at all temperatures even when the light transmission in the POM indicates that crystallites have been formed. This leads to two conclusions. First, in this compound, the remaining structural inhomogeneity is sufficient to result in sites for excimer formation and / or monomer quenching within the exciton diffusion range of each chromophore. Second, since excimer emission occurs at 5 K,

it does not require any activation energy. This confirms that sites with molecules already in the excimer geometries must be pre-exisiting. In passing we point out that the increasing blue-shift of the high-energy emission tail with increasing temperature is an exceptionally nice example for the increase in thermal equilibrium energy in a Gaussian density of states.[32] We now turn to compounds **1a**, **2a** and **2b**. At 5 K, these compounds show a structured emission with a 0-0 peak at 400 nm and a 0-1 peak at about 425 nm. The relative intensity of the vibrational peaks varies between the compounds. This emission can be attributed to the pyrene monomer unit, possibly slightly modified by weak H-type interaction. (Since the $S_1 \rightarrow S_0$ transition in pyrene is symmetry-forbidden, one cannot distinguish whether the 0-0 peak height is modified due to symmetry-selection rules or due to weak H-type interaction). At 5 K, spectral diffusion of singlet excitons is reduced. Evidently, structural order in the crystalline compounds **1a**, **2a** and **2b** is increased such there are no sites with excimer geometry within reach at 5 K. At elevated temperatures, the exciton diffusion range increases so that some excimer sites can be populated and a spectrum showing both, monomer and excimer fluorescence results.

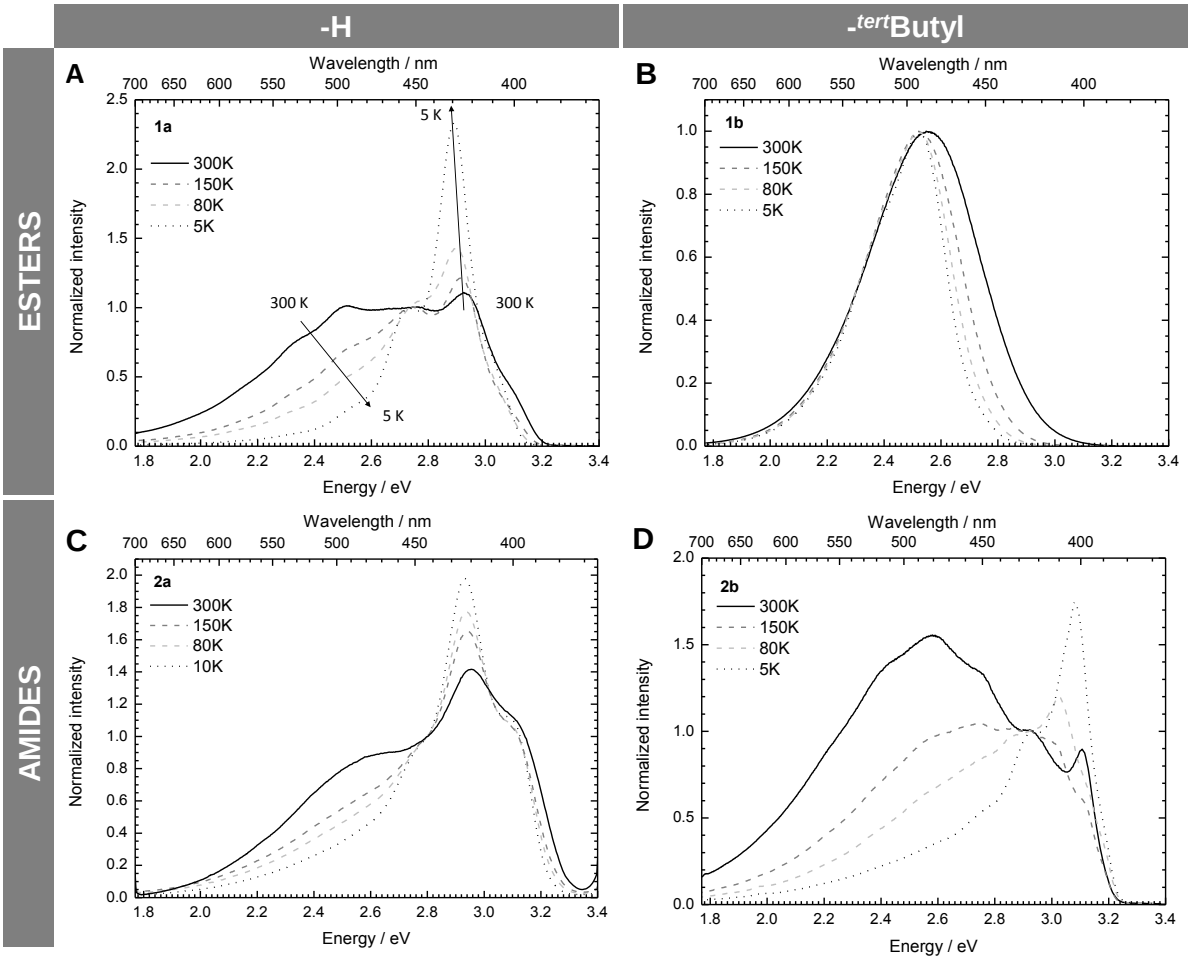

Figure 8. Photoluminescence spectra at different temperatures from room temperature to 5 K of the four compounds **1a** (A), **1b,** (B), **2a** (C) and, **2b** (D) in crystallized thin films. For a comprehensive representation, graph A was normalized at 2.73 eV, graph B at the maximum intensity, graph C at 2.78 eV and, graph D at 2.93 eV. For compound **1a** the decrease of the excimer fluorescence and the increase in monomer fluorescence with reduced temperature are indicated with arrows. This is also commonly observed for compounds **2a** and **2b**.

Structural Influences on the Pyrene Interaction – Molecular Modeling

The conclusings drawn so far on the basis of spectroscopic data are well supported by molecular modeling of the crystallite structure. In order to assess, how the molecules pack, **t**he geometry of the monomers of the esters **1a, 1b** and the amides **2a, 2b** were optimized using the B3LYP functional and basis set 6-31G. The optimized structures, together with the predicted partial charges, were used to build and optimize the structure of the aggregates by

means of Molecular Mechanics (MM), from which qualitative results could be obtained (Figure 9).

As expected, the π-π stacking of the pyrene moieties is the dominant driving force towards self-aggregation. This can be seen from the almost parallel orientation of the chromophores in all cases. The distance between the pyrene units is approximately 3.50 Å in the calculated hexamer aggregates, which is in good agreement with crystal structure data of stacked pyrenes featuring a distance of 3.53 Å.[29] In the case of the amide compounds **2a** and **2b** additional H-bonds are observed in the MM calculations with O-H distances of 1.92 Å and 2.17 Å, respectively. The longer O-H distance of compound **2b** indicates weaker H-bonds than in the case of compound **2a** which can be attributed to the additional bulky *tert*-butyl group. This is in perfect agreement with the previous results from the FT-IR measurements. Furthermore, the sterically demanding *tert*-butyl group of compound **2b** enforces a slight twist in the molecular structure within the calculated hexamer aggregate.

Although in general π-π stacking of the pyrene moieties is present in all calculated hexamer aggregates, slight differences can be observed in the relative orientation of the chromophores. While ester compound **1a** features an almost perfect π-π stacking of the pyrene units an increasing parallel offset is observed for compound **2a** and **2b**. Additionally, in the hexamer aggregate of compound **1b** a rotational twist of adjacent pyrene units is present (yellow lines Figure 9). In compound **1a** the π-π stacking of the pyrene chromophores is the only intermolecular interaction. The columnar stacking is increasingly disturbed by the introduction of the amide and the *tert*-butyl moiety. The results from the molecular modeling calculations are in good agreement with the previous discussion on thin film properties, whereas the solution properties differ. In the film the steric demand and disorder introduced by the *tert*-butyl group (s. figure 9B and D) correlates well with the enhanced propensity to form excimers which was already observed in the low temperature photoluminescence measurements (s. figure 8B and D). Compound **1b**, which has, as already assumed previously, the least ordered structure is unique in two ways - it exhibits a strong rotational twist of adjacent pyrene chromophores and shows exclusively excimer fluorescence even after crystallization and at very low temperatures. On the other hand, H-bonding amide groups as well as the lack of the sterically demanding *tert*-butyl group

promote a more ordered structure reducing the propensity to form excimers in the crystalline state. Note that in the crystalline state, unlike the unchanged pyrene, the investigated molecules (**1a-b**, **2a-b**) do not arrange in a sandwich-type structure but seem to exhibit equidistance.

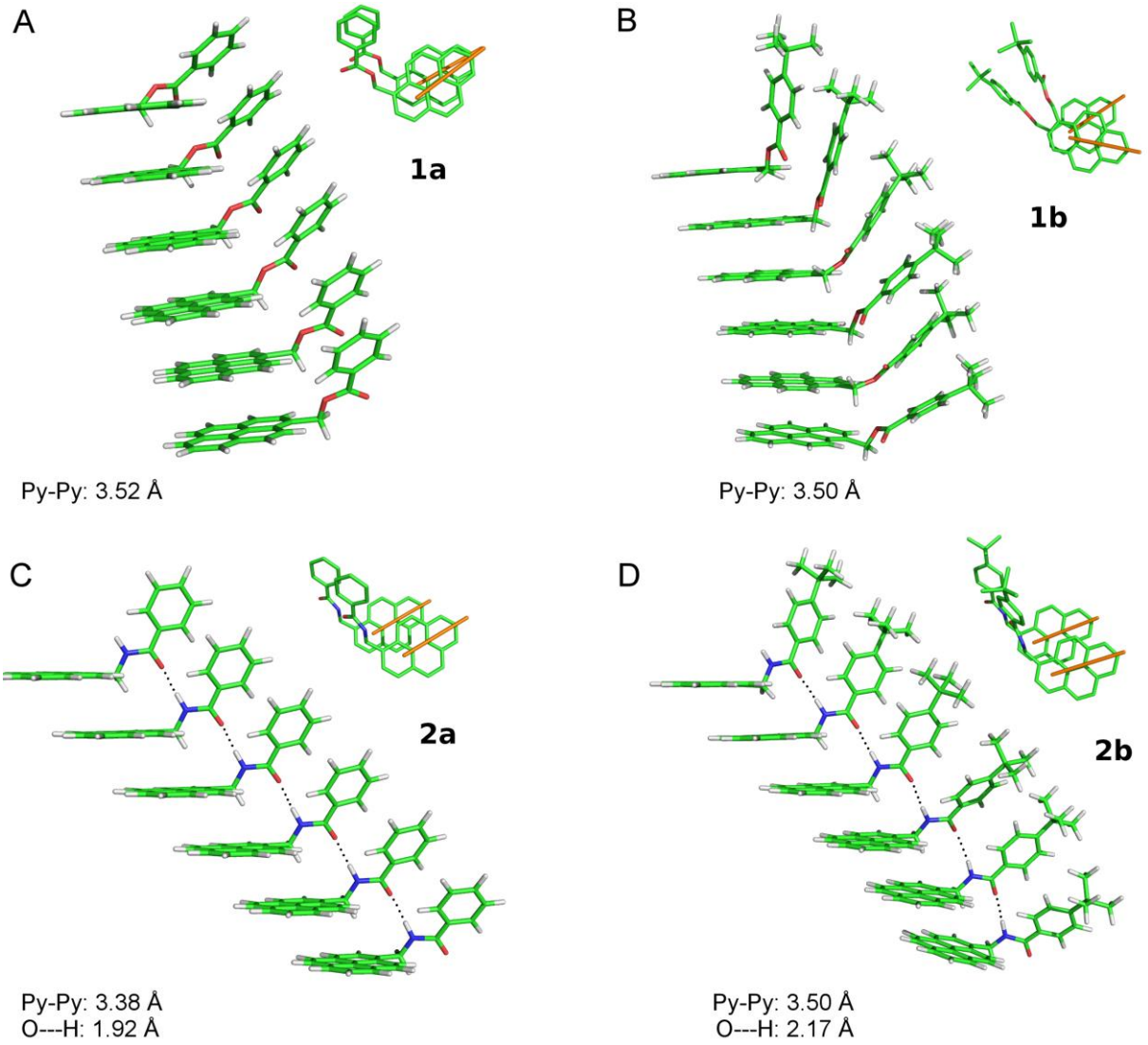

Figure 9. Molecular mechanics geometry optimization of hexamer aggregates of the esters **1a** (A) and **1b** (B) and the amides **2a** (C) and **2b** (D) with the corresponding top views of two stacked molecules. The two orange lines represent the twist of two adjacent pyrene chromophores. Additionally, the distance between two pyrene chromophores and in the case of the amide compounds **2a-b** the O-H distance of the H-bonding amide moieties are stated. The geometry of the monomers was optimized with DFT.

Conclusion

In conclusion, we were able to understand the influence of H-bonding amide linkers and sterically demanding *tert*-butyl groups on the π-stacking of pyrene chromophores in different states of matter. This was achieved by carefully studying a set of four pyrene derivatives exhibiting either an ester or amide linker and with or without a bulky *tert*-butyl substituent. The four compounds were investigated from molecularly dissolved solutions up to concentrations where supramolecular aggregates are formed, as well as in spin-cast films in a virgin and in a crstallized state.

The influence of the linker and the steric hindrance on the pyrene stacking gets more significant the closer the molecules are forced together. In dilute solution up to the threshold concentrations for the formation of aggregates the molecular behavior is independent of the variable groups, as all four compounds show identical spectra and behavior. The four compounds differ, however, from unsubsituted pyrene. Whereas unsubstituted pyrene readily forms excimer in solution from monomers, in the substituted derivatives excimer formation requires additional stabilization within aggregates. The rate of excimer formation depends on the nature of the sidechain. While the excimer formation rate in the ester compound **1a** is comparable to that of unsubstituted pyrene, excimer formation proceeds slower with the amide linker of compound **2a**, and is reduced even more by the bulky substituents of **1b** and **2b**.

In thin films we find that excimers are readily formed within the supramolecular aggregates present in freshly spin-cast films, yet that excimer formation becomes suppressed by crystallization. Such crystallization can be induced by heating the amide-containing compounds, which develop intermolecular H-bonds, as well as by aging at room temperature in the case of the ester compounds. The amount of structural order in the crystalline state is strongly dependent on the variable groups. H-bonding amide groups in contrast to ester groups promote a more ordered structure, while the sterically demanding *tert*-butyl substituent hinders a highly ordered packing of the molecules. In the case of compound **1b** this leads to a strong rotational twist of adjacent pyrene moieties and an enhanced propensity to form excimers in the crystalline structure. Compound **2a** on the

other hand favors a highly ordered packing resulting in the least amount of excimer fluorescence of all compounds.

With this variety of experiments we were able to understand the molecular behavior and the influence of the variable groups on the pyrene stacking in different states of matter in great detail. This study clearly points out how crucially the molecular design can affect the performance of chromophoric systems.

Experimental Section

Materials and Methods: Solvents were distilled and when necessary dried according to standard procedures. All starting materials were obtained from Aldrich, Alfa Aesar, Fluka or Riedel-de Haën and used without further purification. ^{1}H-NMR spectra were recorded on a Bruker Avance 300 spectrometer. Mass spectra were recorded on a Finnigan MAT 8500 apparatus (EI, 70 eV) using direct injection mode. Elemental analysis (C, H, N) was carried out with an EA 3000 instrument (HEKAtech).

General Synthetic Route to Pyrenyl Substituted Esters 1a-b: 1-Pyrenyl-methanol (2.5 g, 10.8 mmol) were disolved in chloroform in a schlenk tube under inert gas. Triethylamine (1.8 mL) and 4-dimethylaminopyridine (DMAP) (50 mg) were added. The solution was cooled to 0°C and benzoic acid chloride (12.0 mmol) was added dropwise. The reaction mixture was boiled for 15 h. After cooling to room temperature, the yellow mixture was filtered (Alox N) and washed with chloroform. The solvent was evaporated and the raw product was dissolved in dichloromethane and extracted subsequently with aqueous HCl (2N), aqueous $NaHCO_3$ (5 %) and water. The solution was dried over Na_2SO_4 and the solvent was evaporated in vacuum.

1a: Yield 2.9 g of a yellow powder (92 %, 8.9 mmol); Rf=0.76 (Hexane/THF 2:1); m.p. 133°C; 1H NMR (300 MHz, [D_6]DMSO, 25°C, TMS): δ=6.11 (s, 2H), 7.50 (m, 1H), 7.64 (m, 1H), 7.98 (m, 1H), 8.08-8.49 ppm (m, 9H); IR: ν˜=1709 cm-1 (C=O); UV/Vis (THF): λmax (ε)=344 nm (31924 $mol^{-1}dm^{3}cm^{-1}$); elemental analysis calcd (%) for $C_{24}H_{16}O_2$ C 85.69, H 4.79, O 9.51; found: C 85.55, H 5.07, O 9.17.

1b: Compound **1b** was recristallized from toluene. Yield 1.8 g of a yellowish powder (43 %, 4.6 mmol); Rf=0.83 (Hexane/THF 2:1); m.p. 140°C; 1H NMR (300 MHz, [D_6]DMSO, 25°C, TMS): δ=1.52 (s, 9H), 6.09 (s, 2H), 7.50 (d, J=8.4 Hz, 1H), 7.90 (d, J=8.4 Hz, 1H), 8.08-8.46 ppm

(m, 9H); IR: ν̃=1717 cm-1 (C=O); UV/Vis (THF): λmax (ε)=344 nm (32819 $mol^{-1}dm^3cm^{-1}$); elemental analysis calc (%) for $C_{28}H_{24}O_2$: C 85.68, H 6.16, O 8.15; found: C 85.66, H 5.95, O 8.39.

General Synthetic Procedure to Pyrenyl Substituted Amides 2a-b: 1-Pyrenyl-methyl-amine-hydrochloride (2.5 g, 9.4 mmol) was suspended in *N*-methyl-2-pyrrolidone (NMP) in a schlenk tube under inert gas. Dry pyridine (20 mL) and LiCl (0.05 g) was added and the mixture was stirred for 30 min. The solution was cooled to 0°C and benzoic acid chloride (9.4 mmol) was added dropwise and the reaction mixture was stirred for 2 h at 70 °C to yield a yellowish solution. After cooling to room temperature, the mixture was precipitated in ice water (600 mL). The mixtures were filtered to retrieve the solid, which was washed with water and dried under vacuum at 80°C.

2a: Compound **2a** was recristallized from ethyl acetate/hexane mixture (1:1). Yield 3.1 g of a white powder (98 %, 9.2 mmol); Rf=0.22 (THF/Toluene 1:20); m.p. 199°C; 1H NMR (300 MHz, [D_6]DMSO, 25°C, TMS): δ=5.24 (d, J=5.6 Hz, 2H), 7.45-7.54 (m, 3H), 7.93-7.96 (m, 2H), 8.04-8.54 (m, 9H), 9.25 ppm (t, J=5.6Hz, 1H); IR: ν̃=1625 (C=O), 3266 cm-1 (N-H); UV/Vis (THF): λmax (ε)=344 nm (29098 $mol^{-1}dm^3cm^{-1}$); elemental analysis calcd (%) for $C_{24}H_{17}NO$: C 85.95, H 5.18, N 4.18, O 4.77; found: C 85.91, H 5.07, N 3.79, O 5.04.

2b: Compound **2b** was recrystallized from toluene. Yield 2.6 g of a white powder (71 %, 6.6 mmol); Rf=0.31 (THF/Toluene 1:20); m.p. 248°C; 1H NMR (300 MHz, [D_6]DMSO, 25°C, TMS): δ=1.29 (s, 9H), 5.24 (d, J=5.7 Hz, 2H), 7.49 (d, J=8.2 Hz, 2H), 7.89 (d, J=8.2 Hz, 2H), 8.06-8.53 (m, 9H), 9.18 ppm (t, J=5.7 Hz, 1H); IR: ν̃=1633 (C=O), 3311 cm-1 (N-H); UV/Vis (THF): λmax (ε)=344 nm (31324 $mol^{-1}dm^3cm^{-1}$); elemental analysis calcd (%) for $C_{28}H_{25}NO$: C 85.90, H 6.44, N 3.58, O 4.09; found: C 85.51, H 6.07, N 3.70, O 4.76.

Differential Scanning Calorimetry (DSC): The thermal properties were investigated by DSC measurements with a PERKIN-ELMER DSC7 (standard heating rate: 20 K/min) utilizing 10 mg of the compounds.

Dynamic Light Scattering (DLS): DLS was performed on an ALV DLS/SLS-SP 5022F compact goniometer system with an ALV 5000/E cross-correlator and a He-Ne laser (632.8 nm). All measurements were performed at concentrations of $1\cdot10^{-4}$ $molL^{-1}$, $1\cdot10^{-3}$ $molL^{-1}$, and $1\cdot10^{-2}$ $molL^{-1}$ of the four compounds **1a-b** and **2a-b** in THF.

Thin Film Preparation: THF solutions (concentration: $5 \cdot 10^{-2}$ molL^{-1}) of the four compounds were spin coated on spectrosil or silicon wafer substrates (30 s, 1020 rpm).

UV-Vis Spectroscopy: UV-Vis spectra on solution and thin film samples were recorded on a JASCO V-670 spectrophotometer. For the measurements in THF the path length of the cuvettes was 1 mm. The extinction coefficient of the 0-0 transition to the S2 state was for all compounds about $5 \cdot 10^{4}$ Lmol^{-1}cm^{-1} in the molecularly dissolved state at $1 \cdot 10^{-4}$ molL^{-1} which results in an OD of 0.5. The further increase of the concentration aggregation occurs and the extinction coefficient is substantially reduced so that the OD values are still below 3. Note also that only the extinction coefficients of the two 0-0 transitions to the S2 and S3 states are reduced due to aggregation at higher concentrations, while the others remain unchanged.

Photoluminescence Spectroscopy in Solution: For the photoluminescence study THF solutions of the compounds were prepared and investigated with a FluoroMax 3 spectrometer at an excitation wavelength of 344 nm.

Photoluminescence Spectroscopy on Thin Films: The photoluminescence measurements of the thin films were performed on a home-built setup. An argon laser (Coherent Innova 300C) with wavelengths of 354 nm and 361 nm was used for the excitation and a CCD-camera (Andor iDus DU420) was used as detector.

Time-Correlated Single Photon Counting (TCSPC) Measurements: The TCSPC measurements were conducted on a FluoTime 200 setup from PicoQuant. The samples were excited with 375 nm laser pulses and the resulting fluorescence was detected with a MCP-PMT detector from Hamatsu.

Optical Microscopy: The spin coated thin films were investigated between crossed polarizors on an optical microscope (Leica DMRX) equipped with a hot-stage (Mettler, model FP82TM).

Preparation of Freeze Dried Samples: Supramolecular aggregates of the four compounds were prepared in dioxane (concentration: $1 \cdot 10^{-2}$ molL^{-1}) by heating to dissolution and subsequent cooling to room temperature. One drop of the mixture was given on a DSC pan, frozen in liquid nitrogen/pentane mixture and subsequently dried at high vacuum (0.007 mbar).

Scanning Electron Microscopy (SEM): The samples were coated using platinum (about 1.4 nm) in a Cressington sputter coater 208HR. The SEM micrographs were recorded on a LEO 1530 FE-SEM (Zeiss, Jena) with Schottky-field-emission cathode and an in-lens detector.

FT-IR Spectroscopy: The infrared measurements were perfomed on a Perkin Elmer FTIR Spectrum 100 spectrometer. The solution measurements were conducted in THF solutions at $1 \cdot 10^{-2}$ molL^{-1} using a NaCl cell of 0.5 mm diameter. For the measurements on thin films, the films had to be spin coated on silica wavers (30 s, 1020 rpm). The resulting films were measured at the ATR unit of the spectrometer.

Modeling: Initially a conformational search was carried out to know the most probable conformation of the molecules **1a**, **1b**, **2a** and **2b**. DFT calculations were carried out for those compounds using the functional B3LYP and basis set 6-31G for all atoms and the program Gaussian03 was used. No constraints in the geometry optimizations were applied. The optimized geometries were checked by calculation of the vibrational spectra, where no negative frequencies were found. The optimized geometries and the partial charges obtained from the DFT calculations were used in order to build aggregates containing 6 monomers each. The geometries of the aggregates were then optimized using the Molecular Mechanics and considering explicitly the atomic charges (MM+ force field, Hyperchem 7.5 program).

Acknowledgements

We gratefully acknowledge financial support by the Deutsche Forschungsgemeinschaft within the DFG Research Training Group (GRK 1640) "*Photophysics of Synthetic and Biological Multichromophoric Systems*". ATH and HM would also like to thank the elite study program "Macromolecular Science" at the University of Bayreuth. "Elite Netzwerk Bayern" is acknowledged for a fellowship for ATH. We are indebted to Doris Hanft and Irene Bauer for synthetic support and Dr. Klaus Kreger for many fruitful discussions.

References

[1] a) T. Aida, E. W. Meijer, S. I. Stupp, *Science* **2012**, *335*, 813–817. b) V. Percec, M. Glodde, T. K. Bera, Y. Miura, I. Shiyanovskaya, K.D. Singer, V.S.K. Balagurusamy, P.A. Heiney, I. Schnell, A. Rapp, H.-W. Spiess, S. D. Hudson, H. Duan, *Nature* **2002**, *419*, 384-387. c) F. Würthner, K. Meerholz, *Chem. Eur. J.* **2010**, *16*, 9366–9373. d) B. Bodenant, F. Fages, M.-H. Delville, *J. Am. Chem. Soc.* **1998**, *120*, 7511–7519. e) Y. Sun, G. C. Welch, W. L. Leong, C. J. Takacs, G. C. Bazan, A. J. Heeger, *Nat Mater* **2011**, *11*, 44–48.

[2] a) K. R. Leight, B. E. Esarey, A. E. Murray, J. J. Reczek, *Chem. Mater.* **2012**, *24*, 3318–3328. b) L. F. Dössel, V. Kamm, I. A. Howard, F. Laquai, W. Pisula, X. Feng, C. Li, M. Takase, T. Kudernac, S. de Feyter et al., *J. Am. Chem. Soc.* **2012**, *134*, 5876–5886. c) Z. Chen, A. Lohr, C. R. Saha-Möller, F. Würthner, *Chem. Soc. Rev.* **2009**, *38*, 564-584.

[3] a) L. van Dijk, P. A. Bobbert, F. C. Spano, *J. Phys. Chem. B* **2009**, *113*, 9708–9717. b) L. van Dijk, F. C. Spano, P. A. Bobbert, *Chemical Physics Letters* **2012**, *529*, 69–73. c) A. A. Voityuk, *Phys. Chem. Chem. Phys.* **2012**, *14*, 13789-13793.

[4] a) M. R. Molla, S. Ghosh, *Chem. Mater.* **2011**, *23*, 95–105. b) F. Würthner, *Chem. Commun.* **2004**, 1564-1579.

[5] a) A. Ajayaghosh, S. J. George, A. P. Schenning in *Topics in Current Chemistry* (Ed.: F. Würthner), Springer-Verlag, Berlin/Heidelberg, **2005**. b) T. Metzroth, A. Hoffmann, R. Martín-Rapún, M. M. J. Smulders, K. Pieterse, A. R. A. Palmans, J. A. J. M. Vekemans, E. W. Meijer, H. W. Spiess, J. Gauss, *Chem. Sci.* **2010**, *2*, 69-76.

[6] a) D. González-Rodríguez, A. P. H. J. Schenning, *Chem. Mater.* **2011**, *23*, 310–325. b) T. Shu, J. Wu, M. Lu, L. Chen, T. Yi, F. Li, C. Huang, *J. Mater. Chem.* **2008**, *18*, 886-893. c) M. Blomenhofer, S. Ganzleben, D. Hanft, H.-W. Schmidt, M. Kristiansen, P. Smith, K. Stoll, D. Mäder, K. Hoffmann, *Macromolecules* **2005**, *38*, 3688–3695. d) J. B. Bodapati, H. Icil, *Photochem. Photobiol. Sci.* **2011**, *10*, 1283-1293.

[7] a) S. Sankararaman, G. Venkataramana, B. Varghese, *J. Org. Chem.* **2008**, *73*, 2404–2407. b) X. Zhang, S. Rehm, M. M. Safont-Sempere, F. Würthner, *Nature Chem* **2009**, *1*, 623–629.

[8] T. Förster, K. Kasper, *Zeitschrift für Elektrochemie Berichte der Bunsengesellschaft für physikalische Chemie*, **1955**, *59*, 976–980.

[9] M. Schwoerer, H. C. Wolf, *Organic molecular solids*, Wiley-VCH, Weinheim, **2007**.

[10] F. M. Winnik, *Chem. Rev.* **1993**, *93*,587-614.

[11] J. B. Birks, L. G. Christophorou, *Spectrochimica Acta*, **1963**, *19*, 401-410.

[12] J. B. Birks, D. J. Dyson, I. H. Munro, *Proceedings of the Royal Society A: Mathematical, Physical and Engineering Sciences* **1963**, *275*, 575–588.

[13] a) J. B. Birks, M. D. Lumb, I. H. Munro, *Proceedings of the Royal Society A: Mathematical, Physical and Engineering Sciences* **1964**, *280*, 289–297. b) J. B. Birks, A. A. Kazzaz, T. A. King, *Proceedings of the Royal Society A: Mathematical, Physical and*

Engineering Sciences **1966**, *291*, 556–569. c) J. B. Birks, A. A. Kazzaz, *Proceedings of the Royal Society A: Mathematical, Physical and Engineering Sciences* **1968**, *304*, 291–301.

[14] A. Hayer, V. de Halleux, A. Köhler, A. El-Garoughy, E. W. Meijer, J. Barberá, J. Tant, J. Levin, M. Lehmann, J. Gierschner et al., *J. Phys. Chem. B* **2006**, *110*, 7653–7659.

[15] a) L. You, G. W. Gokel, *Chem. Eur. J.* **2008**, *14*, 5861–5870. b) J. Xiao, Y. Li, Y. Song, L. Jiang, Y. Li, S. Wang, H. Liu, W. Xu, D. Zhu, *Tetrahedron Letters* **2007**, *48*, 7599–7604. c) F. D. Lewis, J.-S. Yang, C. L. Stern, *J. Am. Chem. Soc.*, **1996**, *118*, 12029-12037. d) M. Kimura, N. Miki, D. Suzuki, N. Adachi, Y. Tatewaki, H. Shirai, *Langmuir* **2009**, *25*, 776–780.

[16] a) H. M. Colquhoun, Z. Zhu, *Angew. Chem. Int. Ed.* **2004**, *43*, 5040–5045. b) B. W. Greenland, S. Burattini, W. Hayes, H. M. Colquhoun, *Tetrahedron* **2008**, *64*, 8346–8354.

[17] M. S. Becherer, B. Schade, C. Böttcher, A. Hirsch, *Chem. Eur. J.* **2009**, *15*, 1637–1648.

[18] B. Adhikari, J. Nanda, A. Banerjee, *Chem. Eur. J.* **2011**, *17*, 11488–11496.

[19] S. T. Caldwell, G. Cooke, S. G. Hewage, S. Mabruk, G. Rabani, V. Rotello, B. O. Smith, C. Subramani, P. Woisel, *Chem. Commun.* **2008**, 4126-4128.

[20] H. M. Colquhoun, Z. Zhu, D. J. Williams, M. G. B. Drew, C. J. Cardin, Y. Gan, A. G. Crawford, T. B. Marder, *Chem. Eur. J.* **2009**, *64*, 8346-8354.

[21] a) L. Hernandez-Folgado, D. Baretić, I. Piantanida, M. Marjanović, M. Kralj, T. Rehm, C. Schmuck, *Chem. Eur. J.* **2010**, *16*, 3036–3056. b) R. Häner, F. Samain, V. L. Malinovskii, *Chem. Eur. J.* **2009**, *15*, 5701–5708. c) R. Varghese, H.-A. Wagenknecht, *Chem. Commun.* **2009**, 2615-2624.

[22] a) Y. H. Lee, H. Liu, J. Y. Lee, S. H. Kim, S. K. Kim, J. L. Sessler, Y. Kim, J. S. Kim, *Chem. Eur. J.* **2010**, *16*, 5895-5901. b) A. D. Hughes, I. C. Glenn, A. D. Patrick, A. Ellington, E. V. Anslyn, *Chem. Eur. J.* **2008**, *14*, 1822–1827.

[23] K. Kreger, P. Wolfer, H. Audorff, L. Kador, N. Stingelin-Stutzmann, P. Smith, H.-W. Schmidt, *J. Am. Chem. Soc.* **2010**, *132*, 509–516.

[24] J. B. Birks, *Photophysics of aromatic molecules*, Wiley-Interscience, London, New York, **1970**.

[25] J. Xiao, Y. Li, Y. Song, L. Jiang, Y. Li, S. Wang, H. Liu, W. Xu, D. Zhu, *Tetrahedron Letters* **2007**, *48*, 7599–7604.

[26] D. Görl, X. Zhang, F. Würthner, *Angew. Chem. Int. Ed.* **2012**, *51*, 6328–6348.

[27] J. Clark, J.-F. Chang, F. C. Spano, R. H. Friend, C. Silva, *Appl. Phys. Lett.* **2009**, *94*, 163306.

[28] a) F. C. Spano, *Chemical Physics* **2006**, *325*, 22–35. b) S. Ghosh, X.-Q. Li, V. Stepanenko, F. Würthner, *Chem. Eur. J.* **2008**, *14*, 11343–11357.

[29] J. B. Birks, *Rep. Prog. Phys.* **1975**, *38*, 903–974.

[30] a) A. L. T. Khan, P. Sreearunothai, L. M. Herz, M. J. Banach, A. Köhler, *Phys. Rev. B* **2004**, *69*, 085201. b) C. Scharsich, R. H. Lohwasser, M. Sommer, U. Asawapirom, U. Scherf, M. Thelakkat, D. Neher, A. Köhler, *J. Polym. Sci. B Polym. Phys.* **2012**, *50*, 442–453.

[31] a) D. J. Skrovanek, S. E. Howe, P. C. Painter, M. M. Coleman, *Macromolecules* **1985**, *18*, 1676–1683. b) T. Mes, M. M. J. Smulders, A. R. A. Palmans, E. W. Meijer, *Macromolecules* **2010**, *43*, 1981–1991.

[32] H. Bässler, *phys. stat. sol. (b)* **1993**, *175*, 15–56.

Supporting Information to

Controlling the π-stacking behavior of pyrene derivatives: Influence of H-bonding and steric effects in different states of aggregation

Andreas T. Haedler,[#1] Holger Misslitz,[#1] Christian Buehlmeyer,[2] Rodrigo Q. Albuquerque,[3] Anna Köhler,[2] and Hans-Werner Schmidt[1]*

[1] Macromolecular Chemistry I and Bayreuther Institut für Makromolekülforschung (BIMF) and Bayreuth Zentrum für Kolloide und Grenzflächen (BZKG) University of Bayreuth, 95440 Bayreuth (Germany)

[2] Experimental Physics II and Bayreuther Institut für Makromolekülforschung (BIMF) University of Bayreuth, 95440 Bayreuth (Germany)

[3] Experimental Physics II University of Bayreuth, 95447 Bayreuth (Germany) Current address: Institute of Chemistry of São Carlos University of São Paulo (USP), 13560-970 São Carlos-SP (Brazil)

[#] Both authors contributed equally to this contribution

Table of Content

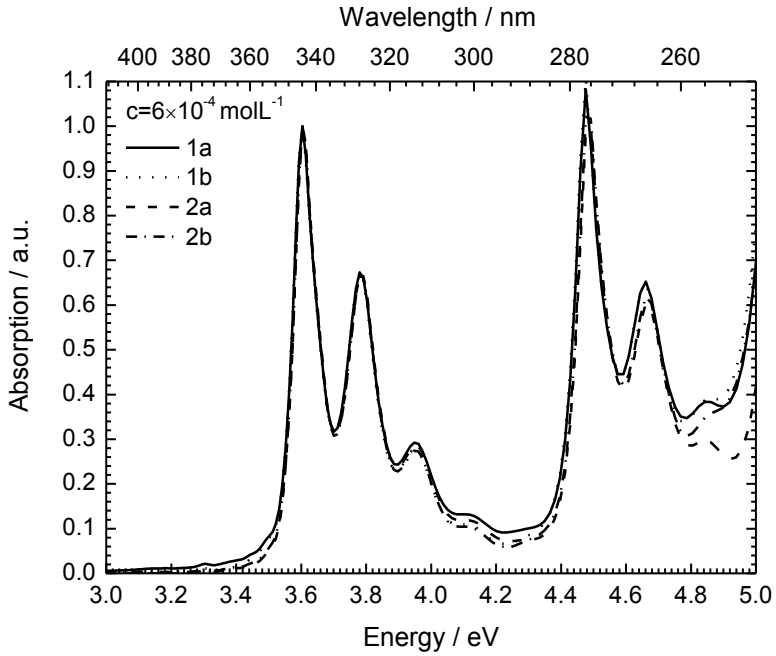

Figure S1. Absorption spectra of the four pyrene derivatives **1a-b** and **2a-b** in THF at $6 \cdot 10^{-4}$ molL^{-1} exhibiting the excitation from the electronic ground state to the 1st and 2nd excited state with respective vibrational fission.

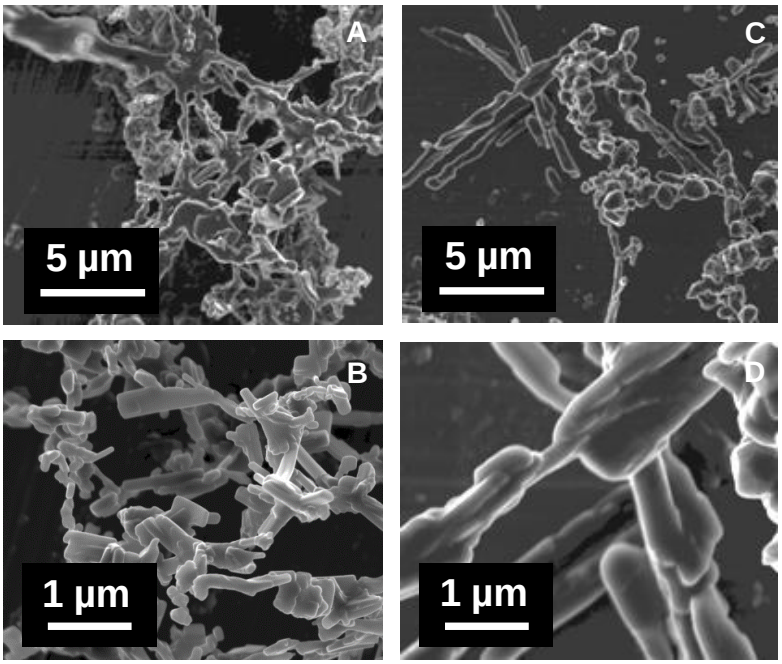

Figure S2.1. Scanning electron microscopy images of supramolecular structures from dioxane solutions after freeze-drying (concentration: $1 \cdot 10^{-2}$ molL^{-1}) of the esters **1a** (left: A, B) and **1b** (right: C, D); the bottom micrographs show a fivefold higher magnification.

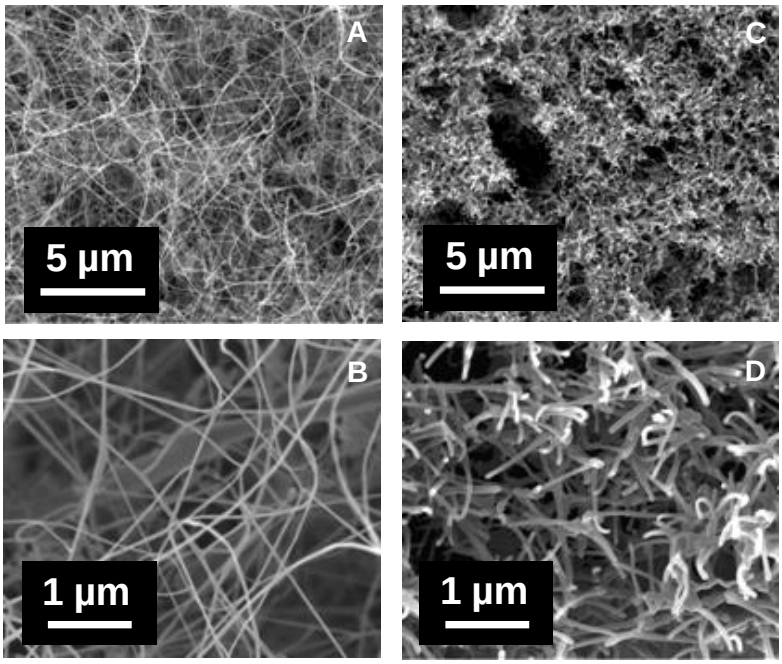

Figure S2.2. Scanning electron microscopy images of supramolecular structures of dioxane solutions after freeze-drying (concentration: $1 \cdot 10^{-2}$ molL^{-1}) of the amides **2a** (left: A, B) and **2b** (right: C, D); the bottom micrographs show a fivefold higher magnification.

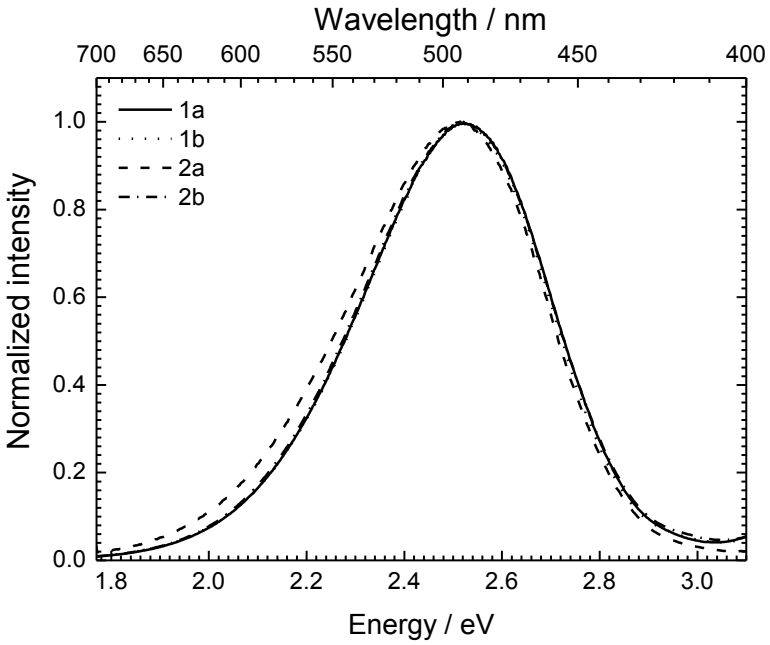

Figure S3. Excimer fluorescence spectra of the four compounds **1a-b** and **2a-b** at $6 \cdot 10^{-2}$ molL^{-1} in THF.

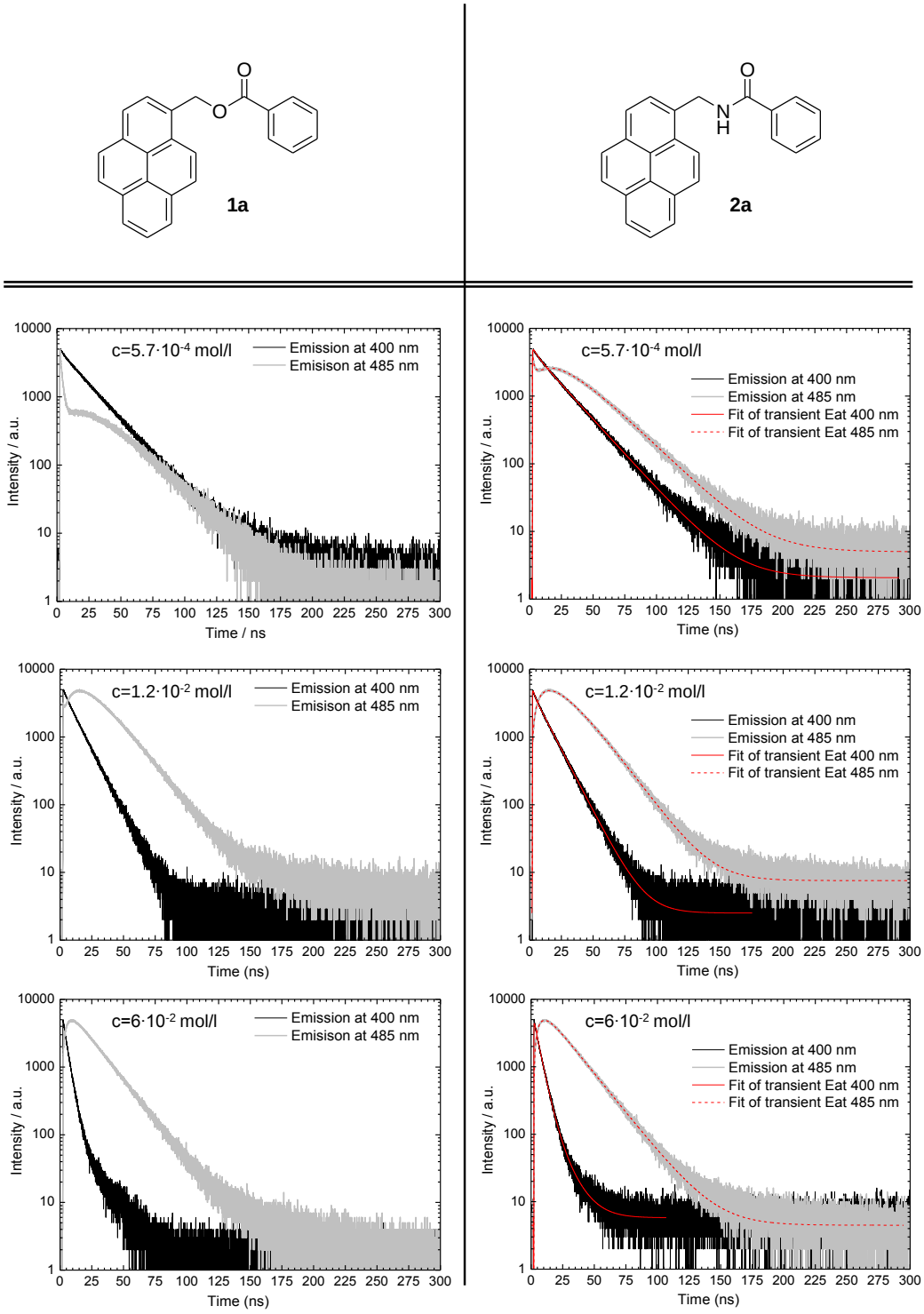

Figure S4. Time resolved photoluminescence transients of compound **1a** (left) and **2a** (right) at different concentrations $5.7 \cdot 10^{-4}$ molL^{-1} (top), $1.2 \cdot 10^{-2}$ molL^{-1} (middle) and, $6 \cdot 10^{-2}$ molL^{-1} (bottom) shown for the monomer (black) and the excimer fluorescence (grey). For compound **2a** the fits are shown from which λ_1 and λ_2 are derived.

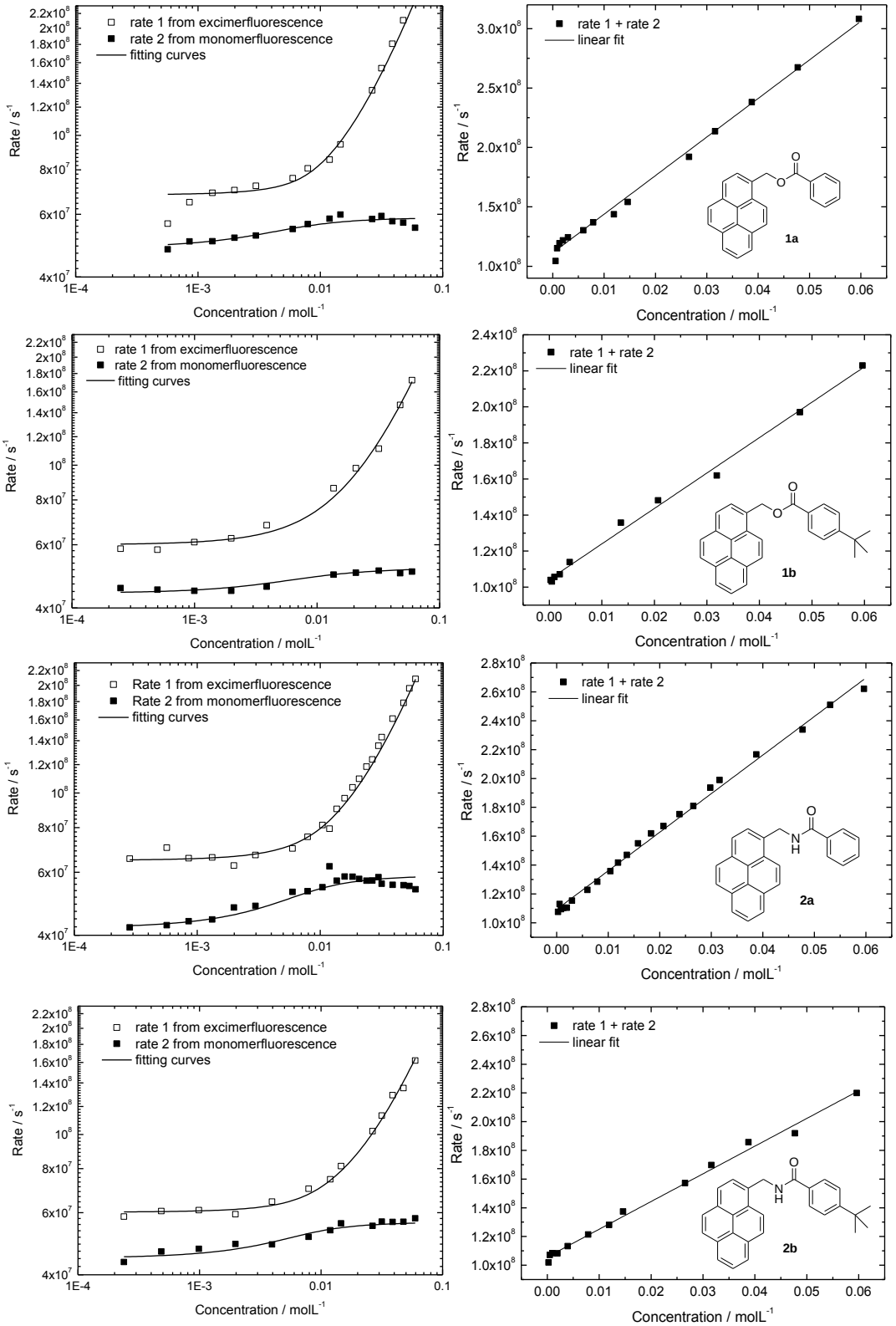

Figure S5. Left: Excimer (□) and monomer (■) fluorescence fall-off rates at different concentrations for compound **1a-b** and **2a-b** (from top to bottom) fitted according to Birks. Right: Sum of the two fall-off rates plotted against the concentration yielding the expected linear dependence.

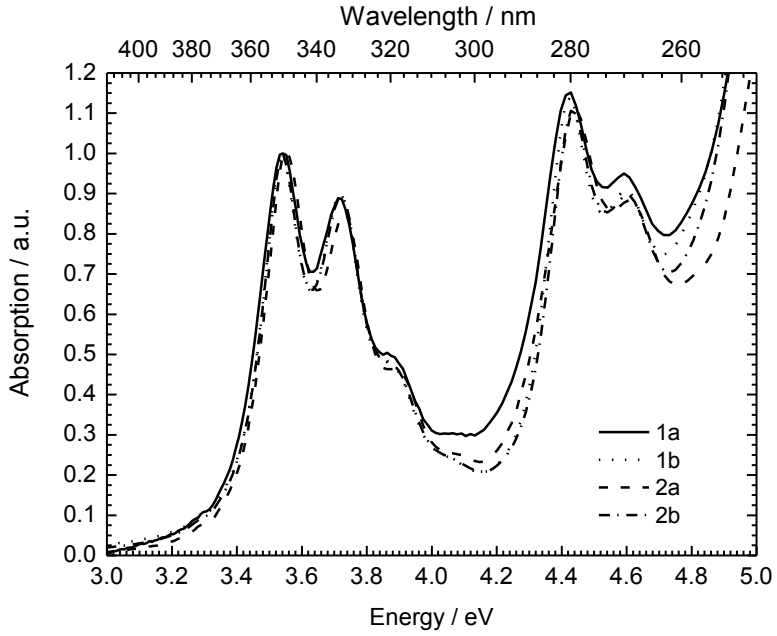

Figure S6. Absorption spectra of the four compounds **1a-b** and **2a-b** in optically transparent thin films.

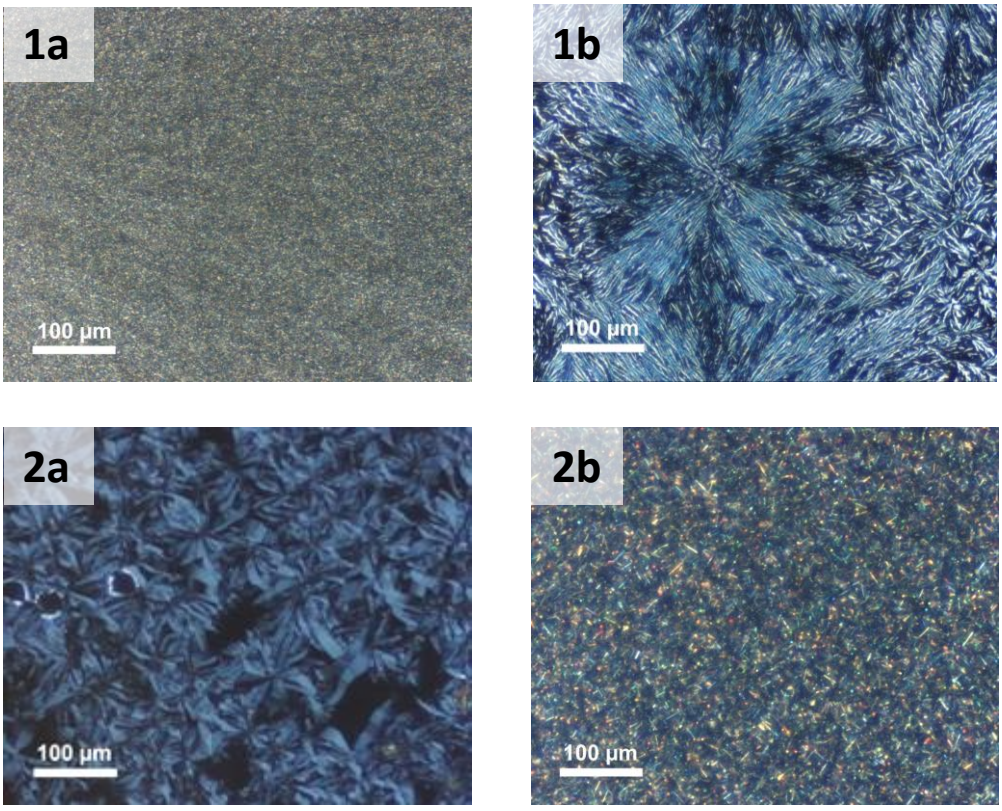

Figure S7. Optical micrographs taken between two crossed polarizers of the ester compounds **1a** and **1b** after aging at room temperature for two months (top) and the amide compounds **2a** and **2b** after annealing at 80°C and 130°C (bottom).

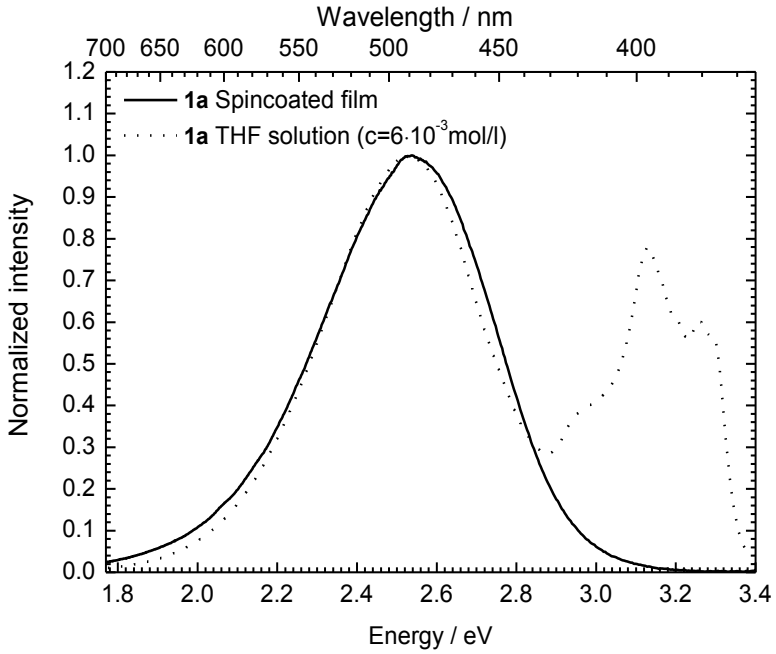

Figure S8. Excimer fluorescence of the fresh prepared thin films excemplarily shown for compound **1a** (—) compared with the corresponding fluorescence spectrum in THF at $6 \cdot 10^{-3}$ molL^{-1} (·····).

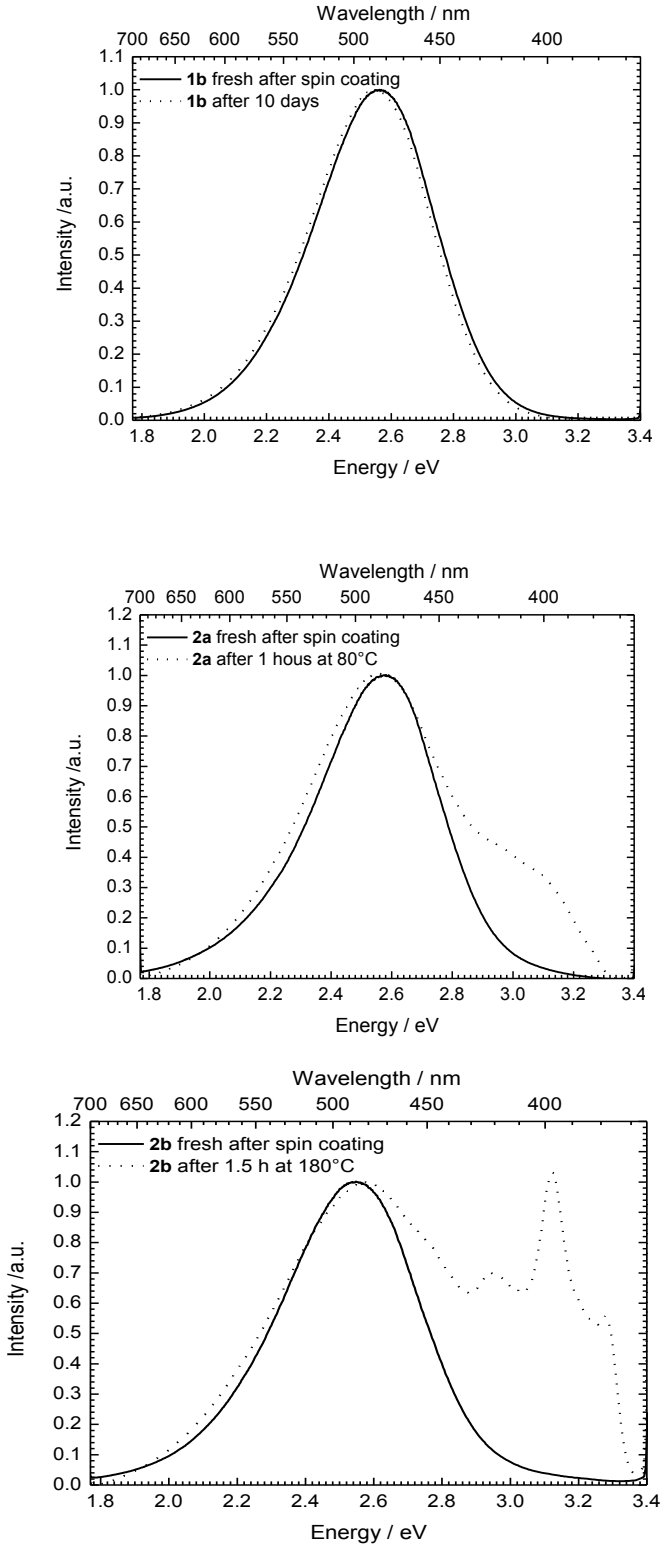

Figure S9. Photoluminsecence spectra of thin films of compound **1b** directly after processing and after 10 days at room temperature (top), of compound **2a** directly after processing and after 1 h at 80°C (middle), and of compound **2b** directly after processing and after 1.5 h at 180°C (bottom).

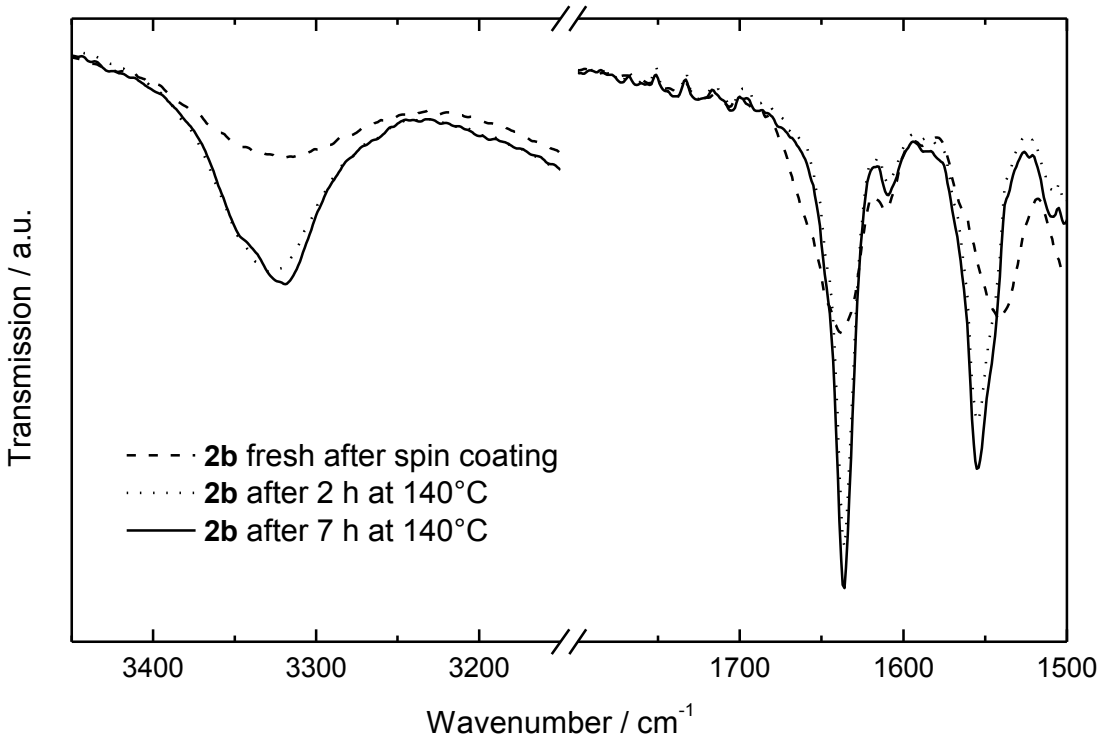

Figure S10. Enlargements of the relevant parts of the FT-IR spectra of a thin film of compound **2b** during the aging process directly after processing, after 2 h and, after 7 h at 140°C resembling different degrees of crystallization; the N-H stretching vibration (left: around 3300 cm^{-1}) and the carbonyl stretching vibration (right: around 1630 cm^{-1}) are represented.

4. Synthesis and Photophysical Properties of Multichromophoric Carbonyl-Bridged Triarylamines

Andreas T. Haedler,[#1] Sebastian R. Beyer,[#2] Natalie Hammer,[3] Richard Hildner,[2]* Milan Kivala,[3]* Jürgen Köhler,[2] and Hans-Werner Schmidt[1]*

[1] Macromolecular Chemistry I and Bayreuther Institut für Makromolekülforschung (BIMF) and Bayreuther Zentrum für Kolloide und Grenzflächen (BZKG) University of Bayreuth, 95440 Bayreuth (Germany)

[2] Experimental Physics IV and Bayreuther Institut für Makromolekülforschung (BIMF) University of Bayreuth, 95440 Bayreuth (Germany)

[3] Chair of Organic Chemistry I, Department of Chemistry and Pharmacy, University of Erlangen-Nürnberg, 91054 Erlangen (Germany)

[#] Both authors contributed equally to this contribution

* E-mail corresponding authors: hans-werner.schmidt@uni-bayreuth.de, richard.hildner@uni-bayreuth.de, milan.kivala@fau.de

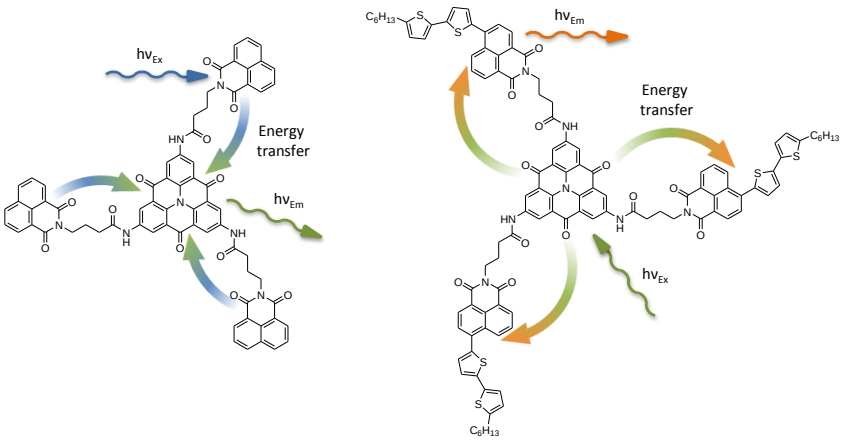

Synthesis and Photophysical Properties of Multichromophoric Carbonyl-Bridged Triarylamines

Published in *Chem. Eur. J.*,**2014**, *20*, 11708-11718.

Synthesis and Photophysical Properties of Multichromophoric Carbonyl-Bridged Triarylamines

Abstract: We report on the synthesis and photophysical properties of two novel multichromophoric compounds. Their molecular design comprises a carbonyl-bridged triarylamine core and either naphthalimides or 4-(5-hexyl-2,2′-bithiophene)-naphthalimides as second chromophore in the periphery. The lateral chromophores are attached to the core via an amide linkage and a short alkyl spacer. The synthetic approach demonstrates a straightforward functionalization strategy for carbonyl-bridged triarylamines. Steady-state and time-resolved spectroscopic investigations of these compounds, in combination with three reference compounds, provide clear evidence for energy transfer in both multichromophoric compounds. The direction of the energy transfer depends on the lateral chromophore used. In addition, the compound bearing the lateral 4-(bithiophene)-naphthalimides is capable of forming fluorescent gels at very low concentrations in the sub-mmol regime while retaining its energy transfer properties.

Keywords: Multichromophoric compounds • bridged triarylamines • energy transfer • donor-acceptor molecules • fluorescent gels

Introduction

Exploiting the unique properties of organic matter for electronic applications holds great promise. Not only does the production of organic materials and devices typically need less resources and energy than their inorganic counterparts, but organic materials also have the potential to open up new applications in light harvesting and solar energy conversion. In particular, functional π-conjugated systems are of key interest for such applications, because they possess appealing optoelectronic properties.[1] However, an order of magnitude estimate, based on the absorption cross section of a typical organic chromophore and the number of photons provided from the sun, yields that under optimum conditions an organic molecule would absorb only a few photons per second.[2] From this it becomes clear that employing organic matter for any kind of solar energy conversion requires an efficient light-harvesting apparatus - an antenna - for collecting as many photons as possible. This requirement is nicely illustrated by the setup of the natural light-harvesting machineries

where hundreds of light-absorbing chromophores, organized in protein complexes serve for the collection of sunlight, whose energy is transferred efficiently among these chromophores to a special pair of pigments, which initiates an electron transfer chain thereby acting as a transducer.[3] The attempt to mimic these biological systems led to a number of different approaches aiming for an excess of donor chromophores, which funnel the excitation energy into a small number of acceptor chromophores. Despite extensive research the structural diversity of the employed chromophoric systems remains rather narrow and comprises mostly rylene diimides,[4] fullerenes,[5] porphyrins and phthalocyanines,[6] potentially decorated with thiophene and triarylamine donors.[7] In addition, multichromophoric dendritic,[8] polymeric,[9] and supramolecular systems[10] were investigated.

Promising alternative building blocks are bridged C_3-symmetric triarylamines, so-called heterotriangulenes,[11] in particular with three electron-withdrawing carbonyl moieties. When suitably substituted, these compounds form columnar structures[12] and possess tuneable photophysical properties.[13,14] The carbonyl-bridged triarylamine (CBT) moiety acts as a moderate electron acceptor with appealing optoelectronic and materials characteristics for organic electronics applications.[15] For example, star-shaped CBT-derivatives, bearing directly connected lateral carbazole moieties, have been reported as electroluminescent materials in organic light emitting diodes.[16]

Synthetic procedures to obtain functionalized carbonyl-bridged triarylamines as well as basic studies of their photophysical properties are still rare. Herein, we present two three-armed multichromophoric compounds **1** and **2** comprising the carbonyl-bridged triarylamine core with either three naphthalimide (NI) or three 4-(5-hexyl-2,2′-bithiophene)-naphthalimide (NIBT) chromophores in the periphery (Fig. 1). The bridged triarylamine and the chromophores in the periphery are linked by an amide unit and a short alkyl spacer to break the conjugation between the chromophores. In order to understand the photophysical properties of the multichromphoric compounds **1** and **2**, three reference compounds **3**–**5** (Fig. 2) were synthesized. In the following we demonstrate that the energy transfer in **1** proceeds from the naphthalimide periphery to the CBT core and in **2** from the core to the 4-(5-hexyl-2,2-bithiophene)-naphthalimide.

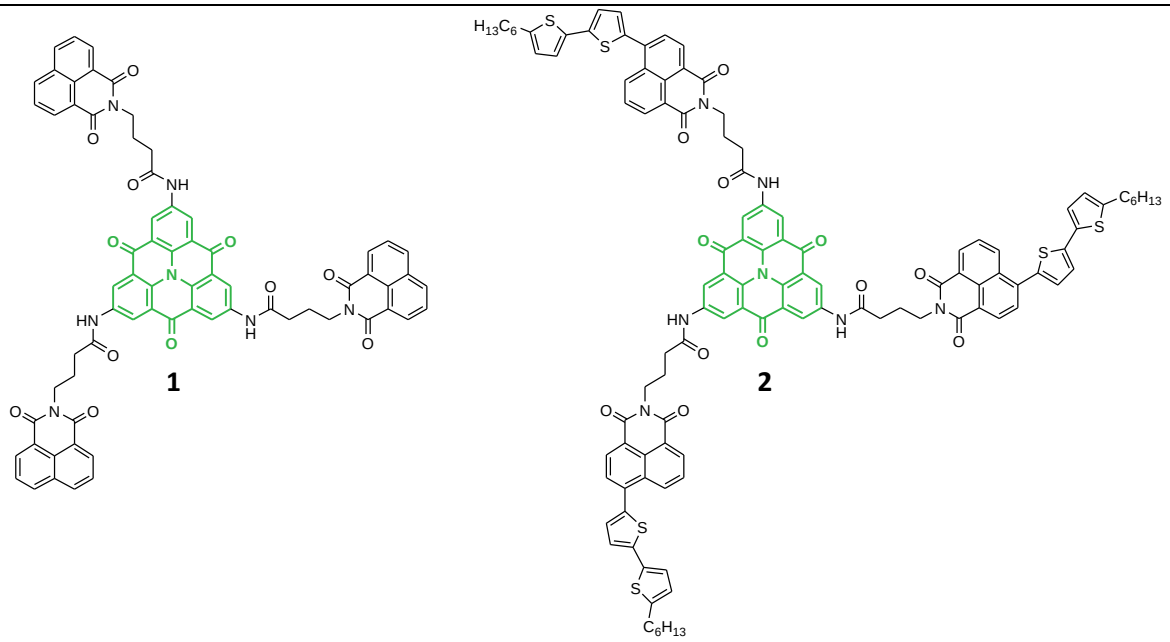

Figure 1. Molecular structures of the multichromophoric compounds **1** and **2** comprising a carbonyl-bridged triarylamine (CBT, highlighted in green) with peripheral naphthalimides (NI, left) and 4-(5-hexyl-2,2'-bithiophene)-naphthalimide (NIBT, right) chromophores, respectively.

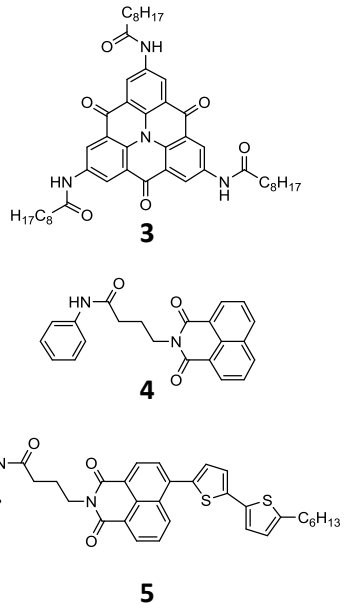

Figure 2. Chemical structures of the reference compounds **3**-**5** representing the CBT-core the naphthalimide (NI), and the 4-(5-hexyl-2,2'-bithiophene)-naphthalimide (NIBT) moiety, respectively.

Results and Discussion

Synthesis. The synthetic routes towards the multichromophoric compounds **1** and **2** are shown in Scheme 1. Starting from 1,8-naphthalic anhydride **6** via the carboxylic acid **7**, the first peripheral building block **8**, bearing the naphthalimide (NI), was readily accessible in two steps.[17] The second peripheral building block **13**, containing the 4-(5-hexyl-2,2'-bithiophene)-naphthalimide (NIBT) chromophore, was obtained by reacting 4-chloro-1,8-naphthalic anhydride **9** with 4-aminobutyric acid introducing the aliphatic spacer. To prevent substitution of the chlorine of the naphthalimide **9** by the amino group of the 4-aminobutyric acid, ethanol was used instead of N,N'-dimethylformamide as solvent. In addition, the carboxylic acid group was converted into the corresponding ethyl ester **10** in a two-step-one-pot reaction. We applied a Pd-catalyzed arylation to directly couple 5-hexyl-2,2'-bithiophene to the chlorinated naphthalimide to obtain **11** with 80% yield. After basic hydrolysis of the ethylester group, the carboxylic acid **12** was converted with oxalylchloride to the corresponding acid chloride **13**. 2,6,10-triamino-CBT **15** was obtained by Pd-catalyzed hydrogenation of 2,6,10-trinitro-CBT **14**, which was synthesized from methyl 2-aminobenzoate and methyl 2-iodobenzoate following literature procedures.[13,18] Reaction of 2,6,10-triamino-CBT core **15** with acid chlorides allows for the preparation of a great variety of different CBT derivatives.

From the CBT core **15** and the two peripheral building blocks **8** and **13** we obtained the multichromophoric molecules **1** and **2**. Both compounds were clearly identified by analytical techniques such as ^{1}H- NMR, ^{13}C-NMR, ^{1}H-^{1}H-COSY (SI Figs. S1 and S2), FT-IR spectroscopy, and matrix-assisted laser desorption ionization with time of flight detection mass spectrometry (MALDI-TOF MS).

The reference compound **3** was synthesized by conversion of nonanoyl chloride with the 2,6,10-triamino-CBT core **15**. The aliphatic substituent was chosen to provide sufficient solubility in common organic solvents. For the reference compounds **4** and **5**, aniline was reacted with the intermediates **8** and **13**, respectively.

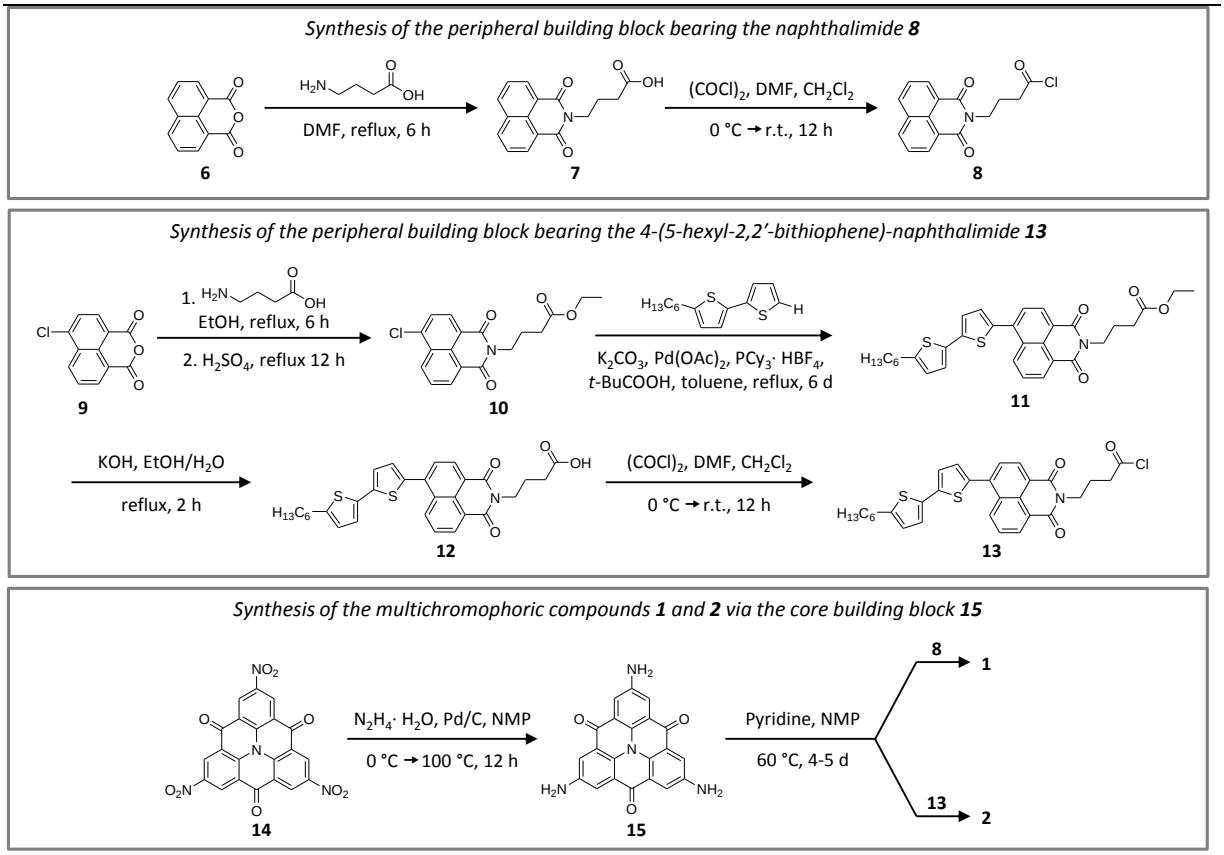

Scheme 1. Overview of the synthetic steps to the multichromophoric compounds **1** and **2**; NMP: N-methyl-2-pyrrolidone; DMF: N,N-dimethylformamide.

Photophysical and Electronic Characterization. The photophysical properties of the two multichromophoric compounds **1** and **2** were investigated in solution by UV/vis absorption, steady state, and time-resolved photoluminescence (PL) spectroscopy. To facilitate the interpretation of the data, we also studied the reference compounds **3**–**5** with molecular structures as close as possible to their respective π-conjugated subunits in the multichromophoric systems. Furthermore, the photoluminescence quantum yields (PL-QY) were determined for all five compounds using an integrating sphere. For all measurements, 1,1,2,2-tetrachloroethane (TCE) was used as it is a good solvent for these compounds. The concentration of the CBT derivatives **1**–**3** was adjusted to 1 µM, while for the naphthalimide and the 4-bithiophene-naphthalimide bearing reference compounds **4** and **5** the concentration was set to 3 µM, to account for the three-armed geometry of compounds **1** and **2**. Photoluminescence emission maps of all five compounds were recorded varying the excitation wavelength between 280 and 700 nm (SI Fig. S3). Two additional maps were

recorded from mixed solutions of compounds **3** + **4** and **3** + **5** for comparison with the multichromophoric systems **1** and **2**. From these maps, PL emission and PL excitation spectra could be extracted for different excitation and emission wavelengths. The time-resolved spectra were recorded on custom-built streak camera setups with pico-second time-resolution using excitation wavelengths of either 360 nm for compounds **1** and **4** or 440 nm for compounds **2**, **3**, and **5**. (s. Experimental section for more details) The relevant photophysical properties are summarized in Table 1.

Table 1. Optical and electronic data of compounds **1–5**.

Comp.	λ_{max}[a] / nm		PL-QY[b]	τ[c]	LUMO[d]	Opt. gap[e]
	Abs.	PL	/ %	/ ns	/ eV	/ eV
1	281 340 460	492	~ 10	0.307(**r**) 3.6	---	2.5
2	279 340 433	608	~ 10	0.041 2.4	---	2.3
3	278 459	489	~ 15	2.5	-3.22	2.5
4	338	382	~ 5	0.495	-3.06	3.4]
5	335 433	609	~ 25	0.017 2.5	-3.22	2.3

[a] Measured in TCE solution, c = 1–3 µM. [b] Photoluminescence quantum yield (PL-QY), averaged over 4 measurements. The excitation wavelength was 340 nm for compounds **1** and **4** and 440 nm for compounds **2**, **3** and **5**. [c] PL lifetime. Multiple values mark multiexponential behavior, **r** denotes rising component. [d] Determined by cyclic voltammetry in NMP with respect to ferrocene. [e] Determined from the absorption onset in UV/vis measurements.

Reference compounds. We start the discussion with the CBT reference compound **3**. The absorption spectrum shows two distinct peaks (Fig. 3 solid line) – an aromatic π–π^* transition at 278 nm with a shoulder at 300 nm and a weak bathochromically shifted absorption at 459 nm. An illustrative PL spectrum of compound **3** upon excitation of the

lowest energy absorption peak at 440 nm is shown in Figure 3 (dashed line), which was picked from the respective photoluminescence emission map (SI Fig. S3A).

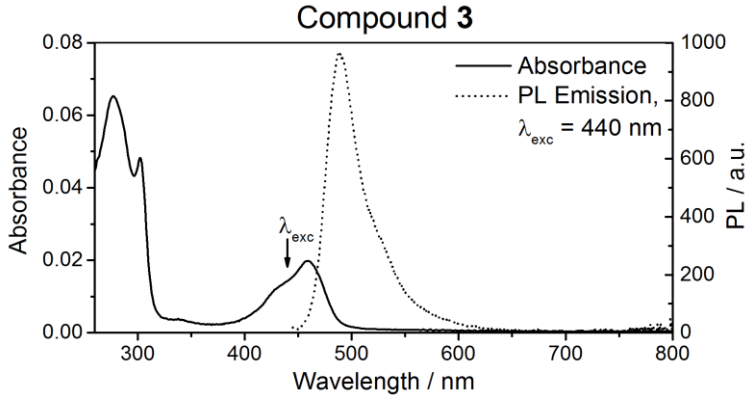

Figure 3. Absorbance (solid line) and PL emission (dashed line) spectrum of compound **3** at c = 1 µM in 1,1,2,2-tetrachloroethane (TCE). PL was excited at λ_{exc} = 440 nm.

A single fluorescence band is observed at 490 nm with a small vibronic shoulder around 520 nm. The PL emission map reveals, that the emission maximum is independent of the excitation wavelength. The PL decay curve of compound **3**, after excitation at 440 nm, shows a clear monoexponential behavior with a time constant of τ = 2.5 ns (SI Fig. S4) and the photoluminescence quantum yield (PL-QY) of the CBT reference compound was determined to be about 15 %.

The absorption spectrum of the second reference compound **4** comprising the naphthalimide exhibits a vibronically structured $S_0 \rightarrow S_1$ transition peaking at 338 nm (Fig. 4, solid line), which is typical for these chromophores. The photoluminescence spectrum upon excitation at 340 nm (Fig. 4, dashed line) reveals the expected vibronically structured naphthalimide fluorescence peaking around 382 nm, which is independent of the excitation wavelength as shown in the PL emission map (SI Fig. S3B).[17] The time-resolved PL decay features a monoexponential behaviour with a time constant of τ = 495 ps (SI Fig. S5) and the PL QY was determined to be about 5 %.

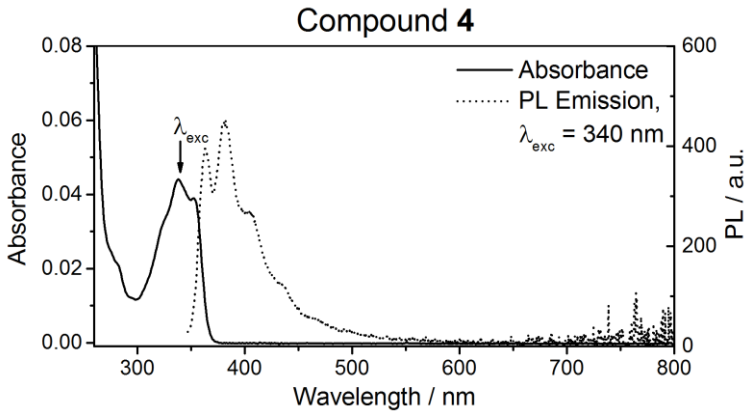

Figure 4. Absorbance (solid line) and PL emission (dashed line) spectrum of compound **4** at c = 3 µM in 1,1,2,2-tetrachloroethane (TCE). PL was excited at λ_{exc} = 340 nm.

The last reference compound **5** bearing the 4-bithiophene-napthalimide shows absorption over a broad range from 280 to almost 550 nm with two main peaks (Fig. 5, solid line). A higher energy peak is located at 335 nm and a broad and unstructured peak can be detected around 440 nm, which we attribute to a charge-transfer (CT) absorption between the covalently linked electron-deficient naphthalimide and the electron-rich bithiophene. This CT character is reflected in the broad and unstructured photoluminescence between 500 and 800 nm peaking at 609 nm (Fig. 5, dashed line), independent of the excitation wavelength (SI Fig. S3C). The PL transient of this compound exhibits a more complex, multiexponential decay that can best be described by two exponents with time constants of τ_1 = 17 ps and τ_2 = 2.5 ns and an amplitude ratio of A_1/A_2 = 1.57 (SI Fig. S6). Compound **5** possesses the highest PL-QY (~ 25 %) of the reference compounds, which is in accordance with the strong emission intensity of the illustrative spectrum shown in Figure 5.

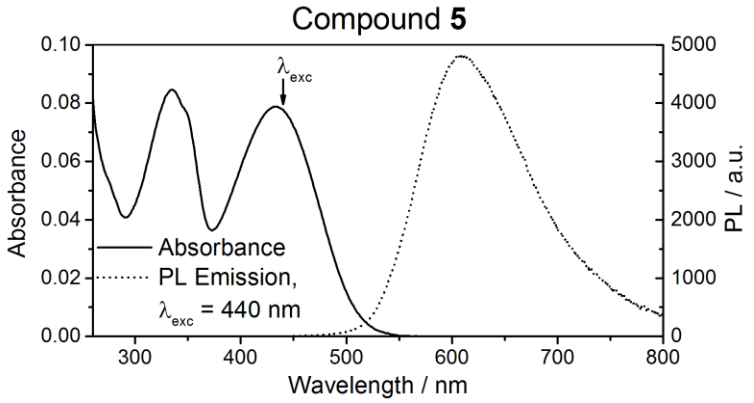

Figure 5. Absorbance (solid line) and PL emission (dashed line) spectrum of compound 5 at c = 3 μM in 1,1,2,2-tetrachloroethane (TCE). PL was excited at λ_{exc} = 440 nm.

From the spectra of the reference compounds **3**-**5** shown in Figs. 3-5 and in the SI Figs. S3A-C it is clear that the spectral shape of the photoluminescence of these substances is independent of the excitation wavelength. The peak maximum of the PL can be easily attributed to the naphthalimides (382 nm), the carbonyl-bridged triarylamine (489 nm), and the 4-bithiophene-naphthalimide (609 nm). The characterization of the individual chromophores shows a significant spectral overlap between the PL of the naphthalimide (NI) and the absorption of the carbonyl-bridged triarylamine (CBT) as well as between the PL of the CBT and the absorption of the 4-bithiophene-naphthalimide (NIBT). This is an important prerequisite for efficient energy transfer.

For a detailed characterization of organic molecules not only the photophysical but also the electronic properties are of interest. Hence, we performed cyclic voltammetry (CV) measurements using the reference compounds **3–5** in *N*-methyl-2-pyrrolidone (NMP). The three compounds representing the individual chromophores show reversible reductive peaks (SI Figs. S8–10), while meaningful oxidation potentials could not be determined due to inhibition of the electrode. Comparison of the reductive waves with a ferrocene standard revealed LUMO (lowest unoccupied molecular orbital)[20] levels of the carbonyl-bridged triarylamine derivative **3** and the 4-bithiophene-naphthalimide **5** to be identical at –3.22 eV, while the naphthalimide **4** exhibits a slightly higher value of –3.06 eV (Table 1). The optical gaps are 3.4 eV for compound **4**, 2.5 eV for compound **3**, and 2.3 eV for compound **5** (Table 1; SI Figs. S8–10).

Multichromophoric compounds. Having characterized the reference compounds, we now turn to the photophysical properties of the more complex multichromophoric systems **1** and **2**. In both compounds the CBT core is in close proximity of a few nanometers to the respective peripheral chromophore, which should facilitate energy transfer. The UV/vis absorption spectra of both multichromophoric systems are a superposition of the absorption of their respective chromophoric parts with only slight differences in the shape of the bands and in the position of their maxima (Figs. 6A and 7A, solid lines). For both compounds **1** and

2 neither strongly shifted nor additional absorption peaks are observed with respect to the reference materials, which evidences that the electronic coupling between the subunits is weak.

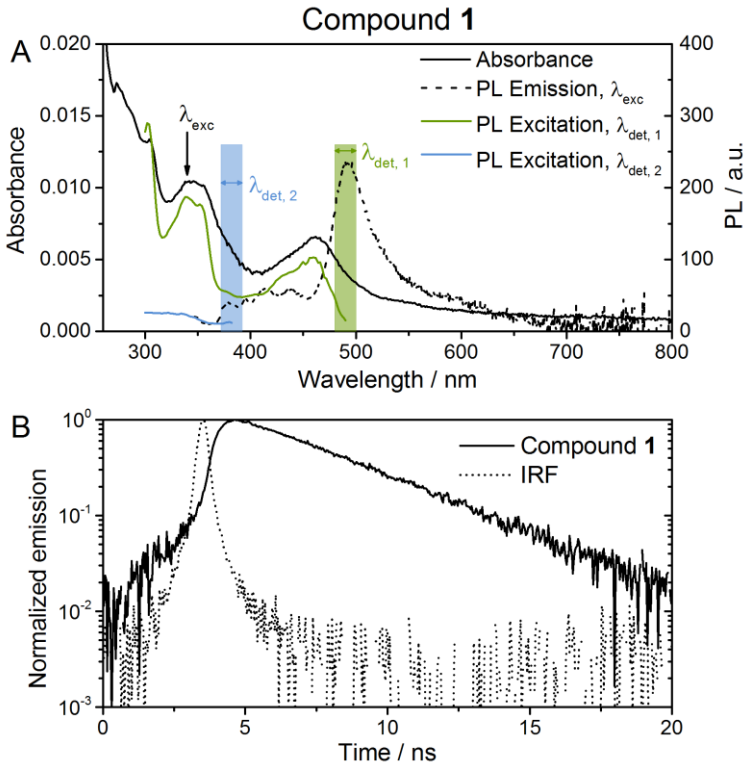

Figure 6. Photophysical properties of compound **1** in 1,1,2,2-tetrachloroethane (TCE) at c = 1 µM. **A**) Absorbance (black solid line) and PL emission spectrum at λ_{exc} = 340 nm (dashed line). The features observed in the PL emission spectrum between 370 and 450 nm are of instrumental origin and appear in all spectra at such low intensities. PL excitation spectra at the spectral signatures of the NI periphery (blue line, detected 372-392 nm) and the CBT core (green line, detected 480-500 nm). **B**) Time-resolved PL emission at λ_{exc} = 360 nm (solid line). The Instrument Response Function (IRF, dashed line) was measured with scattered excitation light. Fitting resulted in a multiexponential decay with τ_{decay} = 3.6 ns and τ_{rise} = 307 ps.

The PL response of compound **1** shows the characteristic emission signature of the CBT core upon excitation at 340 nm but no photoluminescence from the peripheral naphthalimide (Fig. 6A, dashed line). This behavior is independent of the excitation wavelength (SI Fig. S3F), throughout the whole absorption regime of compound **1**. From the PL emission map, we also extracted the PL excitation spectra of compound **1** for detection wavelengths that represent the characteristic PL signature of the naphthalimide (372 – 392 nm) and the CBT

core (480 – 500 nm). The PL excitation spectrum that was detected in the spectral signature of the CBT core (Fig. 6A, green box), follows the absorption spectrum of compound **1** closely without major deviations. Thus it incorporates the absorptive channels of the CBT core as well as those of the peripheral NI. The PL excitation spectrum that was detected in the spectral signature of the peripheral NI, on the other hand, shows no signal at all (Fig. 6A, blue box). This means that both the absorption of the CBT core and of the peripheral naphthalimides result in PL of the CBT core. In a control experiment with a mixed solution of reference compounds **3** and **4** (SI Fig. S3D) the chromophores are on average about 75 nm apart, which renders energy transfer highly unlikely. In this experiment photoluminescence stems either from the carbonyl-bridged triarylamine or from the naphthalimide chromophore, depending on which chromophore is addressed at the particular excitation wavelength. These findings suggest that in compound **1** the energy absorbed by the peripheral naphthalimide (energy donor) is funneled to the carbonyl-bridged triarylamine core (energy acceptor) by intramolecular energy transfer.

Time-resolved PL measurements provide direct evidence for energy transfer. For these experiments on compound **1** we excited at 360 nm where the absorption of the naphthalimide is prominent while that of the core is negligible, and integrated the PL spectrally from 450 to 580 nm. The resulting PL decay curve (Fig. 6B, solid line) features a clear rising component with a time constant of 307 ps followed by a monoexponential decay with a time constant of 3.6 ns. As we almost exclusively excite the NI periphery, the rising component in the PL transient from the CBT core clearly demonstrates energy transfer from the periphery to the core. We note that the time constant of the decay of compound **1** is longer with respect to reference compound **3**. Presumably, this reflects a change in the dielectric environment due to the different molecular structure. The quantum yield of the energy transfer can be estimated according to a standard kinetic model (SI pages S6-S7). The obtained rise time corresponds to the inverse sum of the rates that depopulate the NI exited state $\tau_{rise} = (\Gamma + k_{nr} + k_{trans})^{-1}$ with Γ being the radiative and k_{nr} the nonradiative rate of NI and k_{trans} the transfer rate from NI to CBT. Assuming that for the NI chromophore in reference compound **4** and in compound **1**, Γ and k_{nr} remain constant, we can estimate the energy transfer time to be $(k_{trans})^{-1}$ = 808 ps and the energy transfer quantum yield from NI to CBT to

be $k_{trans}/(k_{trans} + \Gamma + k_{nr}) = 0.38$, with $(\Gamma + k_{nr})^{-1} = 495$ ps being the observed lifetime of NI in compound **4**.

Compound **2** shows the characteristic PL signature of the peripheral 4-bithiophene-naphthalimide around 610 nm when excited at 440 nm (Fig. 7A, dashed line). The spectral signature of the CBT core around 492 nm, though, cannot be observed. The PL emission map (SI Fig. S3G) shows that this holds true for all employed excitation wavelengths from 280 to 600 nm. As the peripheral NIBT chromophore absorbs over a broad spectral range, it is not possible to exclusively excite the carbonyl-bridged triarylamine. However, the PL excitation spectrum detected in the emission range of the NIBT (600-620 nm, Fig. 7A orange box) reproduces the absorption spectrum of compound **2** very well. In contrast, the respective spectrum detected in the PL range of the CBT core (480-500 nm, Fig. 7B green box) shows no signal at all. Hence, it can be concluded that the absorption of both chromophores contribute to the emission of the NIBT. Furthermore, in a control experiment on a mixed solution of compounds **3** and **5** (SI Fig. S3E), where energy transfer can be excluded, an additional PL peak arises around 500 nm which can be clearly assigned to the central carbonyl-bridged triarylamine, after excitation in the absorption regime of that chromophore. This peak is not present in the spectra of the multichromophoric compound **2**. These results provide first evidence for an intramolecular energy transfer in compound **2** from the triarylamine core to the peripheral chromophores.

The time-resolved PL transient for compound **2** was recorded upon excitation at 440 nm and spectrally integrated from 480 -600 nm, according to the procedure employed for compound **1**. Interpretation of the time-resolved photoluminescence spectrum of compound **2** (Fig. 7B, solid line) is, however, more challenging. Just like for compound **5** we find a biexponential transient with decay times of $\tau_1 = 41$ ps and $\tau_2 = 2.4$ ns with an amplitude ratio of $A_1/A_2 = 1.55$. Within the experimental uncertainty the values for compounds **2** and **5** are identical. We could not identify a rise component in the transient of **2**. This is due to two factors: (i) the core distributes its energy to three peripheral molecules, which results in a shortening of the rise time, (ii) we simultaneously excite the core and the periphery, where the latter possesses a much larger absorption cross section. This is in agreement with a kinetic model (SI pages S6-S7) that predicts a 2 to 6-fold decrease in the amplitude of the rising component

of the acceptor chromophore relative to the amplitude of the decay of the donor. Therefore, we cannot determine the efficiency for the transfer from CBT to NIBT in compound **2**. Yet, from steady state spectroscopy, we have evidence that this transfer occurs.

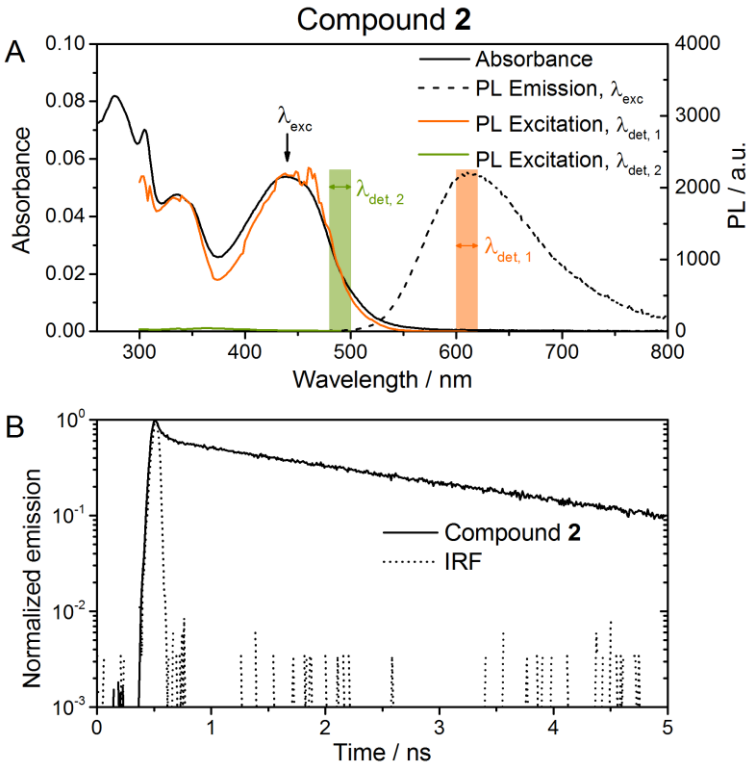

Figure 7. Photophysical properties of compound 2 in 1,1,2,2-tetrachloroethane (TCE) at c = 1 µM. A) Absorbance (black solid line) and PL emission spectrum at λ_{exc} = 440 nm (dashed line). PL excitation spectra at the spectral signatures of the NIBT periphery (orange line, detected 600-620 nm) and the CBT core (green line, detected 480-500 nm). B) Time-resolved PL emission at λ_{exc} = 440 nm (solid line). The Instrument Response Function (IRF, dashed line) was measured with scattered excitation light. Fitting resulted in a biexponential decay with τ_1 = 41 ps, τ_2 = 2.4 ns, and A_1/A_2 = 1.55.

A PL-QY of 10% was found for both mutlichromophoric compounds **1** and **2**. This is lower compared to the PL-QYs of the reference compounds **3** and **5** representing the respective acceptor chromophore and can be rationalized with the larger molecular structures of **1** and **2**, which enables additional non-radiative relaxation pathways due to structural distortion.

Cyclic voltammetry experiments on compounds **1** and **2** did not yield meaningful results due to electrode inhibition. However, in the multichromophoric compounds **1** and **2**, the building blocks are electronically decoupled by alkyl spacers, which efficiently break the conjugation.

Therefore, the positions of the energy levels and thus also the optical gaps are presumably very close to those of the structurally similar reference compounds **3**–**5**. The LUMO values and the optical gaps of the reference compounds **3–5** rationalize the direction of the energy transfer: from the peripheral naphthalimide to the central carbonyl-bridged triarylamine in compound **1** and from the carbonyl-bridged triarylamine to the 4-bithiophene-naphthalimide in the periphery of compound **2**.

An interesting feature of compound **2** is the formation of transparent fluorescent gels of orange colour in *ortho*-dichloro-benzene at very low concentrations down to 0.7 mM (Fig. 8A). The PL emission map of a gelled sample reveals that the photophysical properties are very similar in the gel state and in dilute solution (SI Fig. S11). In particular the emission of the CBT-core around 500 nm is still quenched by energy transfer to the periphery independent of the excitation wavelength (Fig. 8B). To the best of our knowledge, this is the first time that a supramolecular gel is obtained based on a CBT derivative. Detailed investigation of this phenomena and the characterization of the resulting gel is a part of ongoing work.

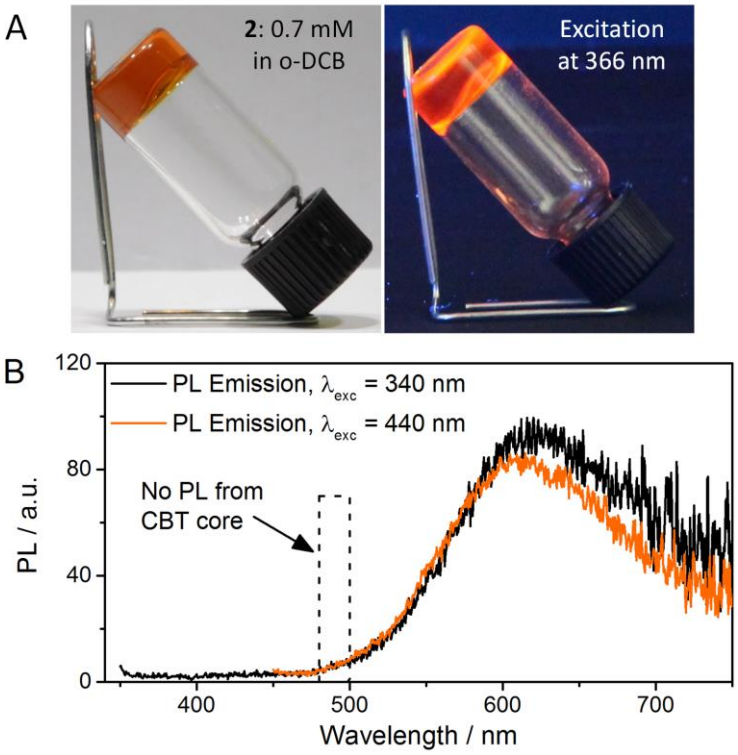

Figure 8. A) Photoluminescent gel of compound **2** in *ortho*-dichloro benzene (*o*-DCB; c = 0.7 mM); right: excitation at 366 nm; **B**) PL emission spectra of the gelled sample upon

excitation at 340 (black line) and 440 nm (orange line). The dashed box marks the spectral area where PL of the CBT core would be expected.

Conclusion

We presented a newly developed reliable synthetic route to functionalize the periphery of carbonyl-bridged triarylamines. The three-armed multichromophoric systems **1** and **2** comprise next to the carbonyl-bridged triarylamine core either naphthalimides or 4-(5-hexyl-2,2'-bithiophene)-naphthalimides as peripheral chromophores, respectively. Steady-state and time-resolved spectroscopy of **1** and **2** in comparison with three reference compounds **3**-**5** provide clear evidence for energy transfer in both multichromophoric compounds. For system **1** the energy is funnelled from the peripheral naphthalimides (energy donor) to the carbonyl-bridged triarylamine core (energy acceptor). In the second system (compound **2**) the energy transfer proceeds in the opposite direction *i.e.* from the carbonyl-bridged triarylamine core (energy donor) to the 4-(5-hexyl-2,2'-bithiophene)-naphthalimides (energy acceptor) in the periphery. Furthermore, the latter compound is an efficient gelator for *ortho*-dichlorobenzene (0.7 mM) and retains its energy transfer and photoluminescent properties in the gel state.

Experimental Section

1 Synthetic Materials and Methods

If not mentioned otherwise, all commercially available starting materials and solvents were used as received. N-Methyl-2-pyrrolidone (NMP) was stirred over CaH2 for 2 days, then fractionally distilled and stored under argon before use. All NMR data were recorded on a Bruker Avance 300 spectrometer at 300.1 MHz in deuterated solvents at 298 K. Gas chromatography with mass spectrometry was recorded on a Finnigan MAT 8500 GC/MS. Matrix assisted laser desorption ionization spectrometry with time of flight mass spectrometry (MALDI-TOF MS) measurements were performed on a Bruker Reflex III in reflection mode using trans-2-(3-(4-tert-butylphenyl)-2-methyl-2-propenylidene)malono-nitrile (DCTB) as matrix and silver trifluoroacetate (AgTFA) as cationizing salt. Solutions of the analyte (1 mg/200 µL), the matrix (1 mg/100 µL) and the cationizing salt (1 mg/100 µL) in chloroform with 1 vol% trifluoroacetic acid were mixed in the ratio 5:20:1 (v:v:v) and spotted

onto the MALDI target plate prior to the measurement. The laser intensity was set to around 25%. Thermogravimetric analysis was conducted on a TGA/DTA 851e from Mettler Toledo. Differential scanning calorimetry was conducted on a Diamond DSC from Perkin Elmer.

2 UV/vis Absorption Spectroscopy

All UV/vis spectra were recorded on a Perkin Elmer Lambda 750 Spectrophotometer with a scan speed of 274 nm/min, a spectral resolution of 2.0 nm and a data interval of 1 nm in the range of 250–1100 nm (for clarity we do not show the full range). The solutions were measured directly after preparation in 10 mm Hellma QS quartz-glass cuvettes at room temperature. As solvent 1,1,2,2-tetrachloroethane (TCE) was used as received.

3 Photoluminescence (PL) Spectroscopy

All PL spectra were recorded on a JASCO FP-8600 Spectrofluorometer with a scan speed of 200 nm/min and a data interval of 0.4 nm from 10 nm above the excitation wavelength to 800 nm. The excitation and emission bandwidth were set to 5 and 2 nm, respectively, with a 0.1 s response time. For the photoluminescence (PL) emission maps (s. SI Fig S4) the excitation wavelength was varied in 2 nm steps from 280 to 700 nm. The solutions were measured directly after preparation in 10 mm Hellma QS quartz-glass cuvettes at room temperature. As solvent 1,1,2,2-tetrachloroethane (TCE) was used as received. Compounds that contain 4-(5-hexyl-2,2'-)-naphthalimide (2 and 5) show strong photo-bleaching upon excitation in the high energy range of the spectrum. To avoid corruption of the PL emission maps by this effect, we had to replace solutions containing these compounds by unilluminated samples in distinct intervals. The excitation wavelengths at which the sample was replaced are marked by dashed horizontal lines in SI Fig. S3.

4 Time-Resolved Spectroscopy

Time-resolved measurements were performed with different custom-built setups. The excitation source was always a frequency-doubled, pulse-picked Ti:sapphire laser systems (Tsunami, Spectra Physics or Chameleon 2 Ultra, Coherent). The laser light was focussed onto the samples that were held in quartz-glass cuvettes. The emission signal was collected

in a right-angle geometry and directed to Streak-camera systems equipped with imaging spectrographs (Hamamatsu C5680 with spectrograph 250IS, Bruker, or Optronis SRU-BA with spectrograph Acton SP2300, Princeton Instruments).

Compounds **2**, **3** and **5** were excited at 440 nm with a repetition rate of 810 kHz, and a fluence of 10^{13} photons/pulse/cm². the instrument response function for these measurements was 78 ps (FWHM). Compounds **1** and **4** were excited at 360 nm with a repetition rate of 8 MHz and a fluence of $3.6 \cdot 10^{14}$ photons/pulse/cm². The FWHM of the instrument response function was 410 ps. As the repetition rates and fluences of the excitation light were kept as low as possible to avoid annihilation processes, we had to spectrally integrate the emission signal from all compounds. For data analysis we used home-written software to conduct a reconvolutive (multi-) exponential fit, taking into account the instrument response function of the system.

5 Cyclic Voltammetry, LUMO Values, and Optical Gaps

Cyclic voltammetry measurements were conducted on a Pt working electrode with 0.1 M $Ag/AgNO_3$ in acetonitrile reference electrode. We used 0.1 M tetrabutylammonium hexafluorophosphate in distilled NMP as solvent scanning the range from –2.5 to +0.5 V at 50 mV/s. Reduction potentials were determined by the half-wave potential of the reversible cathodic peak potential and anionic peak potential. Ferrocene (FC) was used as internal standard to calculate the (approximate) LUMO values of compounds 3–5 assuming a HOMO level of ferrocene in NMP at –4.8 eV.[20] In all cases at least 10 cycles were conducted to demonstrate the reversibility of the reduction and re-oxidation processes of the compounds. The optical gaps were determined from the UV/vis absorption onset of the respective chromophore (3–5) in TCE (s SI Figs. S8-S10).

6 Synthesis

Synthesis of compounds **7** and **14** were performed following literature procedures.[13,17,18]

Synthesis of the acid chlorides **8** and **13**: Under argon atmosphere the respective acid (1 eq.) was dissolved in dichloromethane (75 ml per 15 mmol acid) in a previously baked round-

bottom flask and a few drops of *N*,*N*-dimethylformamide were added. The mixture was cooled to 0 °C before 5 eq. of oxalylchloride were added. The reaction mixture was stirred at room temperature for 12 h. After the reaction was finished, the solvent and the remaining oxalylchloride were removed at high vacuum. The precipitated product was stored under argon and used without further purification.

Synthesis of compound **10**: In a round-bottom flask with a reflux condenser 26.9 g of 4-chloro-1,8-naphthalic anhydride **9** (1.0 eq., 115.7 mmol) and 11.9 g of 4-aminobutyric acid (1.0 eq., 115.7 mmol) were dissolved in 750 ml ethanol. The mixture was refluxed for 6 hours before 5 ml of H_2SO_4 (conc.) was added and then further refluxed for 12 h. The reaction mixture was cooled to room temperature and the precipitate was filtered off, washed 3 times with diethylether and dried. The product was obtained as light yellow powder in 81% yield (32.5 g).

^{1}H-NMR (300.1 MHz, $CDCl_3$): □ = 1.25 (t, 3H, OCH_2CH_3), 2.11 (quin, 2H, $CH_2CH_2CH_2$), 2.45 (t, 2H, CH_2CH_2CO), 4.12 (quart, 2H, OCH_2CH_3), 4.26 (t, 2H, NCH_2CH_2), 7.82–7.89 (t, 1H, CHCHCH, d, 1H, ClCCH), 8.51 (d, 1H, ClCCHCH), 8.61 (d, 1H, CHCHCH), 8.67 (d, 1H, CHCHCH) ppm.

Synthesis of compound **11**: 370 mg of K_2CO_3 (1.5 eq., 2.7 mmol) was added in a round-bottom flask equipped with a reflux condenser and baked and dried with the glassware. Under argon atmosphere 617 mg of compound **10** (1.0 eq., 1.8 mmol), 1.1 ml of 5-hexyl-2,2'-bithiophene (1.11 g, 2.5 eq., 4.5 mmol), 8 mg of $Pd(OAc)_2$ (0.02 eq., 0.04 mmol), 26 mg of $PCy_3{\cdot}HBF_4$ (0.04 eq., 0.1 mmol), 55 mg of pivalic acid (0.3 eq., 0.5 mmol), and 6 ml of toluene were added. The mixture was degased 3 times before it was refluxed for 6 days. The reaction mixture was filtered and the solvent was evaporated. The crude product was pre-purified by column chromatography (silica gel, toluene/THF, 15:1). The fractions containing the product were dried and recrystallized from acetone. The product was obtained as orange powder in 80% yield (800 mg).

^{1}H-NMR (300.1 MHz, $CDCl_3$): δ = 0.93 (t, 3H, CH_2 CH_2CH_3), 1.26 (t, 3H, OCH_2CH_3), 1.32–1.42 (m, 6H, $CH_2(CH_2)_3CH_2$), 1.73 (quin, 2H, CH_2CH_2CS), 2.14 (quin, 2H, $CH_2CH_2CH_2$), 2.45 (t, 2H, CH_2CH_2CO), 2.85 (t, 2H, CH_2CS), 4.13 (quart, 2H, OCH_2CH_3), 4.30 (t, 2H, NCH_2CH_2), 6.76 (d, 1H,

CH_2CCH), 7.11 (d, 1H, CH_2CCHCH), 7.24–7.28 (d, 2H, $CHCHCC$–NI), 7.80 (t, 1H, $CHCHCH$), 7.85 (d, 1H, BT–CCH), 8.62 (d, 1H, BT–$CCHCH$), 8.67 (d, 1H, $CHCHCH$), 8.74 (d, 1H, $CHCHCH$) ppm.

Synthesis of compound **12**: In a round-bottom flask equipped with a reflux condenser 1.19 g of compound **11** (1.0 eq., 2.7 mmol) was dissolved in 15 ml of ethanol before a 10 wt.% aqueous solution of KOH was added. The mixture was refluxed for 2 hours. The reaction mixture was precipitated in aqueous HCl solution, filtered off, washed with water and dried. The product was obtained as orange powder in 95% yield (1.07 g).

^{1}H-NMR (300.1 MHz, DMSO-d_6): $\delta = 0.87$ (t, 3H, CH_2 CH_2CH_3), 1.29–1.40 (m, 6H, $CH_2(CH_2)_3CH_2$), 1.63 (quin, 2H, CH_2CH_2CS), 1.91 (quin, 2H, $CH_2CH_2CH_2$), 2.32 (t, 2H, CH_2CH_2CO), 2.81 (t, 2H, CH_2CS), 4.11 (t, 2H, NCH_2CH_2), 6.86 (d, 1H, CH_2CCH), 7.25 (d, 1H, CH_2CCHCH), 7.41 (d, 1H, $CHCHCC$–NI), 7.48 (d, 1H, $CHCHCC$–NI), 7.91–7.95 (t, 1H, $CHCHCH$, d, 1H, $ClCCH$), 8.49 (d, 1H, BT–$CCHCH$), 8.55 (d, 1H, $CHCHCH$), 8.71 (d, 1H, $CHCHCH$), 12.03 (s, 1H, $COOH$) ppm.

Synthesis of compound **15**: In a round-bottom flask equipped with a reflux condenser 335 mg of compound **14** (1.0 eq., 0.7 mmol) was dissolved in 25 ml of NMP and cooled to 0 °C. 55 mg of Pd on activated charcoal (25 mg per mmol NO_2) and subsequently 0.32 ml of hydrazine monohydrate (9.0 eq., 6.6 mmol) was added slowly. The reaction mixture was stirred for 12 h at 100 °C and then cooled to room temperature. The suspension was filtered through silica gel and washed with concentrated H_2SO_4. The solution was then precipitated in an alkaline solution of aqueous NaOH and carefully filtered after the product agglomerated. The product was washed with water, ethanol, and diethyl ether and finally dried. The product was obtained as deep purple powder in 56% yield (150 mg).

^{1}H-NMR (300.1 MHz, DMSO-d_6): $\delta = 5.96$ (s, 6H, NH_2), 8.09 (s, 6H, $CCHC$) ppm.

General preparation method for the synthesis of the three armed triangulene trisamides **1**–**3**: The reactions of the triamino compound **15** with the acid chlorides **8**, **13**, and nonanoylchlorid were conducted under argon and in dry conditions. In a round-bottom flask compound **15** (1.0 eq.) was dissolved in NMP and the respective acid chloride (5.0 eq.) and pyridine (5.0 eq.) as base were added. The mixture was stirred at 60 °C for 4–5 days and then

poured into water. The precipitate was filtered off and washed with water, ethanol, and acetone.

Purification of compound **1**: The crude product was recrystallized from DMSO, filtered and washed with water, ethanol, and acetone. The product was obtained as dark red powder in 40% yield (128 mg).

^{1}H-NMR (300.1 MHz, $CDCl_3$/TFA-d_1): δ = 2.37 (quin, 6H, $CH_2CH_2CH_2$), 2.85 (t, 6H, CH_2CO), 4.47 (t, 6H, NCH_2CH_2), 7.88 (t, 6H, CHCHCH), 8.38 (d, 6H, CHCHCH), 8.73 (d, 6H, CHCHCH), 9.34 (s, 6H, CCHC) ppm; ^{13}C-NMR (75.5 MHz, $CDCl_3$/TFA-d_1): δ = 24.1, 34.7, 40.6, 121.1, 123.6, 127.8, 127.9, 128.4, 132.0, 133.5, 134.8, 136.2, 136.7, 167.1, 175.9, 177.9 ppm; IR (neat): $\tilde{\nu}$ = 3258 (m), 3066 (w), 1691 (s), 1647 (s), 1587 (s), 1547 (s), 1464 (s), 1438 (m), 1384 (m), 1342 (s), 1234 (m), 1167 (m), 1141 (m), 1045 (m), 893 (w), 846 (m), 802 cm^{-1} (s); MALDI-TOF-MS: *m/z* calcd for the Ag-adduct $C_{69}H_{45}AgN_7O_{12}$ $[M]^+$ 1272.22 g/mol, found 1272.06 g/mol; thermally stable up to 300 °C, melting was not observed below decomposition temperature.

Purification of compound **2**: The crude product was boiled in *N*,*N*-dimethylformamide for 2 hours, cooled, filtered and washed with water, ethanol, and acetone. The product was obtained as brown powder in 60% yield (300 mg).

^{1}H-NMR (300.1 MHz, $CDCl_3$/TFA-d_1): δ = 0.92 (t, 9H, $CH_2CH_2CH_3$), 1.32–1.43 (m, 18H, $CH_2(CH_2)_3CH_2$), 1.72 (quin, 6H, CH_2CH_2CS), 2.41 (quin, 6H, $CH_2CH_2CH_2$), 2.79–2.87 (t, 6H, CH_2CH_2CO, t, 6H, CH_2CS), 4.50 (t, 6H, NCH_2CH_2), 6.75 (d, 3H, CH_2CCH), 7.05 (d, 3H, CH_2CCHCH), 7.15 (d, 3H, CHCHCC–NI), 7.22 (d, 3H, CHCHCC–NI), 7.83–7.89 (t, 3H, CHCHCH, d, 3H, BT–CCH), 8.66 (d, 3H, BT–CCHCH), 8.76 (d, 3H, CHCHCH), 8.80 (d, 3H, CHCHCH), 9.17 (s, 6H, CCHC) ppm; ^{13}C-NMR (75.5 MHz, $CDCl_3$/TFA-d_1): δ = 14.0, 22.6, 28.8, 30.2, 31.6, 120.0, 121.0, 122.5, 123.8, 124.4, 125.1, 126.2, 127.6, 128.2, 128.2, 129.2, 130.4, 130.4, 132.1, 133.0, 133.5, 136.1, 136.8, 137.5, 140.4, 141.5, 147.0, 165.5, 165.8, 175.2, 178.3 ppm; IR (neat): $\tilde{\nu}$ = 3288 (w), 2925 (m), 2853 (m), 1695 (s), 1647 (s), 1585 (s), 1549 (m), 1463 (s), 1384 (m), 1348 (s), 1232 (m), 1156 (m), 1116 (m), 1051 (m), 857 (m), 801 cm^{-1} (s); MALDI-TOF-MS: *m/z* calcd for the Ag-adduct $C_{111}H_{93}AgN_7O_{12}S_6$ $[M]^+$ 2016.43 g/mol, found 2016.47 g/mol.

Purification of compound **3**: The crude product was boiled in dimethylformamide for 2 hours, cooled, filtered and washed with water and ethanol. The product was obtained as brown powder in 58% yield (250 mg).

^{1}H-NMR (300.1 MHz, $CDCl_3$/TFA-d_1): δ = 0.92 (t, 9H, CH_2 CH_2CH_3), 1.31–1.59 (m, 30H, $CH_2(CH_2)_5CH_2$), 1.94 (quin, 6H, $COCH_2$ CH_2), 2.73 (t, 6H, $COCH_2$), 8.99 (s, 6H, CCHC) ppm; ^{13}C–NMR (75.5 MHz, $CDCl_3$/TFA–d_1): δ = 13.8, 22.7, 26.6, 29.2, 29.2, 29.3, 31.9, 37.5, 122.5, 127.1, 132.7, 137.0, 175.8, 178.5 ppm; IR (neat): $\tilde{\nu}$ = 3334 (m), 2921 (s), 2852 (s), 1703 (m), 1660 (m), 1633 (s), 1598 (s), 1548 (s), 1521 (m), 1358 (m), 1285 (m), 1258 (m), 1199 (m), 1158 (m), 1106 (m), 1017 (w), 910 (s), 869 (w), 801 cm^{-1} (s); MS: *m/z* calcd for $C_{48}H_{60}N_4O_6$ $[M]^+$ 788.45 g/mol, found 788 g/mol; thermally stable up to 300 °C, melting was not observed below decomposition temperature.

General preparation method for the synthesis of the reference compounds **4** and **5**: The reactions of the acid chlorides **8** and **13** with aniline were conducted under argon and in dry conditions. In a round-bottom flask the respective acid chloride (1.0 eq.) was dissolved in NMP and aniline (2.5 eq.) was added as reactive amine and as base. The mixture was stirred at 60 °C for 2 days.

Purification of compound **4**: The reaction mixture was poured in acidic (HCl) water. The precipitate was filtered off, washed with water and dried. The crude product was recrystallized from ethanol at 4 °C. The product was obtained as white powder in 79% yield (930 mg).

^{1}H-NMR (300.1 MHz, DSMO-d_6): δ = 2.30 (quin, 2H, $CH_2CH_2CH_2$), 2.72 (t, 2H, CH_2CH_2CO), 4.40 (t, 2H, NCH_2CH_2), 7.20–7.39 (m, 5H, NH–C(C*H*)$_5$), 7.84 (t, 2H, CHC*H*CH), 8.35 (d, 2H, CHCHC*H*), 8.65 (d, 2H, C*H*CHCH) ppm; ^{13}C-NMR (75.5 MHz, $CDCl_3$/TFA-d_1): δ = 24.1, 33.9, 40.3, 121.0, 122.2, 127.2, 127.7, 128.2, 129.4, 131.8, 133.3, 135.1, 136.5, 166.8, 175.5 ppm; IR (neat): $\tilde{\nu}$ = 3279 (s), 3066 (w), 2959 (w), 1696 (s), 1654 (s), 1625 (m), 1590 (s), 1536 (s), 1499 (m), 1438 (s), 1386 (s), 1341 (s), 1246 (s), 1200 (m), 1168 (s), 1142 (m), 1047 (s), 971 (s), 894 (s), 846 cm^{-1} (s); MS: *m/z* calcd for $C_{22}H_{18}N_2O_3$ $[M]^+$ 358.13 g/mol, found 358 g/mol; thermally stable up to 300 °C, melting point: 208 °C.

Purification of compound **5**: The reaction mixture was poured in acidic (HCl) water. The precipitate was filtered off, washed with water and dried. The crude product was recrystallized from ethanol at 4 °C. The product was obtained as orange powder in 58% yield (290 mg).

^{1}H-NMR (300.1 MHz, DSMO-d_6): δ = 0.87 (t, 3H, CH_2 CH_2CH_3), 1.23–1.37 (m, 6H, $CH_2(CH_2)_3CH_2$), 1.64 (quin, 2H, CH_2CH_2CS), 2.02 (quin, 2H, $CH_2CH_2CH_2$), 2.40 (t, 2H, CH_2CH_2CO), 2.81 (t, 2H, CH_2CS), 4.17 (t, 2H, NCH_2CH_2), 6.88 (d, 1H, CH_2CCH), 6.96 (d, 1H, CH_2CCHCH), 7.19 (d, 1H, CHCHCC–NI), 7.27 (d, 1H, CHCHCC–NI), 7.46 (m, 5H, NH–C($CH)_5$), 7.92 (t, 1H, CHCHCH), 7.94 (d, 1H, BT–CCH), 8.50 (d, 1H, BT–CCHCH), 8.57 (d, 1H, CHCHCH), 8.71 (d, 1H, CHCHCH) ppm; ^{13}C-NMR (75.5 MHz, TCE-d_2): δ = 14.2, 22.5, 24.2, 28.7, 30.1, 31.4, 34.9, 39.5, 119.7, 121.0, 122.3, 123.7, 124.1, 124.2, 125.1, 127.3, 128.2, 128.8, 128.9, 129.4, 129.9, 131.0, 131.7, 133.6, 137.3, 138.0, 139.1, 140.5, 146.6, 164.3, 164.6, 170.7, ppm; IR (neat): $\tilde{\nu}$ = 3289 (m), 3062 (w), 2925 (s), 2854 (m), 1695 (s), 1652 (s), 1585 (s), 1534 (s), 1498 (m), 1438 (s), 1386 (s), 1350 (s), 1311 (w), 1249 (s), 1229 (s), 1174 (m), 1156 (m), 1119 (s), 1055 (s), 965 (m), 897 (s), 865 cm^{-1} (s); MS: *m/z* calcd for $C_{36}H_{34}N_2O_3S_2$ $[M]^+$ 606.20 g/mol, found 606 g/mol; thermally stable up to 300 °C, melting point: 165 °C.

Acknowledgements

Financial support by the Bavarian State Ministry of Science, Research, and the Arts for the Collaborative Research Network "*Solar Technologies go Hybrid*" is gratefully acknowledged. ATH, SRB, RH, JK, and HWS are thankful for support by the DFG within GRK 1640. ATH would like to thank the elite study program "*Macromolecular Science*" at the University of Bayreuth and the "*Elite Netzwerk Bayern*" for a fellowship. MK and NH gratefully acknowledge the support by the Deutsche Forschungsgemeinschaft (DFG) as part of SFB953 "Synthetic Carbon Allotropes". We are indebted to Doris Hanft for synthetic support and Dr. Klaus Kreger for many fruitful discussions. We thank Prof. Dr. Anna Köhler and Alexander Rudnick for help with parts of the time-resolved measurements.

References

[1] a) M. Hasegawa, M. Iyoda, *Chem. Soc. Rev.* **2010**, *39*, 2420-2427; b) A. A. Sagade, K. V. Rao, U. Mogera, S. J. George, A. Datta, G. U. Kulkarni, *Adv. Mater.* **2013**, *25*, 559–564.

[2] R. J. Cogdell, J. Köhler in *Semiconductors and Semimetals*, Elsevier, **2010**, pp. 77–94.

[3] R. J. Cogdell, A. Gall, J. Köhler, *Quart. Rev. Biophys.* **2006**, *39*, 227-324.

[4] a) X. Zhan, A. Facchetti, S. Barlow, T. J. Marks, M. A. Ratner, M. R. Wasielewski, S. R. Marder, *Adv. Mater.* **2011**, *23*, 268–284; b) F. Schlosser, J. Sung, P. Kim, D. Kim, F. Würthner, *Chem. Sci.* **2012**, *3*, 2778-2785; c) W. Yue, A. Lv, J. Gao, W. Jiang, L. Hao, C. Li, Y. Li, L. E. Polander, S. Barlow, W. Hu, S. Di Motta, F. Negri, S. R. Marder, Z. Wang, *J. Am. Chem. Soc.* **2012**, *134*, 5770–5773; d) L. F. Dössel, V. Kamm, I. A. Howard, F. Laquai, W. Pisula, X. Feng, C. Li, M. Takase, T. Kudernac, S. de Feyter, K. Müllen, *J. Am. Chem. Soc.* **2012**, *134*, 5876–5886; e) E. Lang, R. Hildner, H. Engelke, P. Osswald, F. Würthner, J. Köhler, *ChemPhysChem* **2007**, *8*, 1487–1496; f) A. Issac, R. Hildner, D. Ernst, C. Hippius, F. Würthner, J. Köhler, *Phys. Chem. Chem. Phys.* **2012**, *14*, 10789-10798; g) A. Issac, R. Hildner, C. Hippius, F. Würthner, J. Köhler, *ACS Nano* **2014**, *8*, 1708–1717.

[5] a) D. M. Guldi, *Chem. Commun.* **2000**, 321–327; b) F. Giacalone, N. Martín, *Adv. Mater.* **2010**, *22*, 4220–4248; c) H. C. Hesse, J. Weickert, C. Hundschell, X. Feng, K. Müllen, B. Nickel, A. J. Mozer, L. Schmidt-Mende, *Adv. Energy Mater.* **2011**, *1*, 861–869; d) L. Feng, M. Rudolf, S. Wolfrum, A. Troeger, Z. Slanina, T. Akasaka, S. Nagase, N. Martín, T. Ameri, C. J. Brabec, D. M. Guldi, *J. Am. Chem. Soc.* **2012**, *134*, 12190–12197; e) C. C. Hofmann, S. M. Lindner, M. Ruppert, A. Hirsch, S. A. Haque, M. Thelakkat, J. Köhler, *J. Phys. Chem. B* **2010**, *114*, 9148–9156; f) C. C. Hofmann, S. M. Lindner, M. Ruppert, A. Hirsch, S. A. Haque, M. Thelakkat, J. Köhler, *Phys. Chem. Chem. Phys.* **2010**, *12*, 14485-14491.

[6] a) H. Imahori, T. Umeyama, K. Kurotobi, Y. Takano, *Chem. Commun.* **2012**, *48*, 4032-4045; b) T. Hasobe, *J. Phys. Chem. Lett.* **2013**, *4*, 1771–1780; c) F. D'Souza, A. N. Amin, M. E. El-Khouly, N. K. Subbaiyan, M. E. Zandler, S. Fukuzumi, *J. Am. Chem. Soc.* **2012**, *134*, 654–664; d) Á. J. Jiménez, R. M. K. Calderón, M. S. Rodríguez-Morgade, D. M. Guldi, T. Torres, *Chem. Sci.* **2013**, *4*, 1064-1074.

[7] a) J. R. Pinzón, D. C. Gasca, S. G. Sankaranarayanan, G. Bottari, T. Torres, D. M. Guldi, L. Echegoyen, *J. Am. Chem. Soc.* **2009**, *131*, 7727–7734; b) J. L. Segura, H. Herrera, P. Bäuerle, *J. Mater. Chem.* **2012**, *22*, 8717-8733; c) C. A. Wijesinghe, M. E. El-Khouly, M. E. Zandler, S. Fukuzumi, F. D'Souza, *Chem. Eur. J.* **2013**, *19*, 9629–9638.

[8] a) E. Fron, L. Puhl, I. Oesterling, C. Li, K. Müllen, F. C. de Schryver, J. Hofkens, T. Vosch, *ChemPhysChem* **2011**, *12*, 595–608; b) M. A. Oar, W. R. Dichtel, J. M. Serin, Fréchet, Jean M. J, J. E. Rogers, J. E. Slagle, P. A. Fleitz, L.-S. Tan, T. Y. Ohulchanskyy, P. N. Prasad, *Chem. Mater.* **2006**, *18*, 3682–3692; c) W. R. Dichtel, S. Hecht, Fréchet, Jean M. J, *Org. Lett.* **2005**, *7*, 4451–4454.

[9] a) R. Hildner, U. Lemmer, U. Scherf, M. van Heel, J. Köhler, *Adv. Mater.* **2007**, *19*, 1978–1982; b) T. Adachi, G. Lakhwani, M. C. Traub, R. J. Ono, C. W. Bielawski, P. F. Barbara, Vanden Bout, David A, *J. Phys. Chem. B* **2012**, *116*, 9866–9872; c) J. Vogelsang, T. Adachi, J. Brazard, Vanden Bout, David A, P. F. Barbara, *Nat Mater* **2011**, *10*, 942–946; d) A. Thiessen, J. Vogelsang, T. Adachi, F. Steiner, D. Vanden Bout, J. M. Lupton, *Proc. Natl. Acad. Sci. U.S.A.* **2013**, *110*, E3550-E3556; e) E. Fron, A. Deres, S. Rocha, G. Zhou, K. Müllen, De Schryver, Frans C, M. Sliwa, H. Uji-i, J. Hofkens, T. Vosch, *J. Phys. Chem. B* **2010**, *114*, 1277–1286.

[10] a) E. Lang, A. Sorokin, M. Drechsler, Y. V. Malyukin, J. Köhler, *Nano Lett.* **2005**, *5*, 2635–2640; b) X. Zhang, D. Görl, F. Würthner, *Chem. Commun.* **2013**, *49*, 8178-8180; c) C. Röger, Y. Miloslavina, D. Brunner, A. R. Holzwarth, F. Würthner, *J. Am. Chem. Soc.* **2008**, *130*, 5929–5939; d) W. Zhang, W. Jin, T. Fukushima, A. Saeki, S. Seki, T. Aida, *Science* **2011**, *334*, 340–343.

[11] a) D. Hellwinkel, M. Melan, *Chem. Ber.* **1971**, *104*, 1001–1016; b) D. Hellwinkel, M. Melan, *Chem. Ber.* **1974**, *107*, 616–626.

[12] a) H. Zhang, Y. Li, X. Wan, Y. Chen, *Chem. Phys. Lett.* **2009**, *479*, 117–119; b) X. Wan, H. Zhang, Y. Li, Y. Chen, *New J. Chem.* **2010**, *34*, 661-666; c) S. Wang, M. Kivala, I. Lieberwirth, K. Kirchhoff, X. Feng, W. Pisula, K. Müllen, *ChemPhysChem* **2011**, *12*, 1648–1651; d) M. Kivala, W. Pisula, S. Wang, A. Mavrinskiy, J.-P. Gisselbrecht, X. Feng, K. Müllen, *Chem. Eur. J.* **2013**, *19*, 8117–8128.

[13] J. E. Field, D. Venkataraman, *Chem. Mater.* **2002**, *14*, 962–964.

[14] a) M. Bieri, S. Blankenburg, M. Kivala, C. A. Pignedoli, P. Ruffieux, K. Müllen, R. Fasel, *Chem. Commun.* **2011**, *47*, 10239-10241; b) N. S. Makarov, S. Mukhopadhyay, K. Yesudas, J.-L. Brédas, J. W. Perry, A. Pron, M. Kivala, K. Müllen, *J. Phys. Chem. A* **2012**, *116*, 3781–3793.

[15] a) K. Do, D. Kim, N. Cho, S. Paek, K. Song, J. Ko, *Org. Lett.* **2012**, *14*, 222–225; b) S. Paek, N. Cho, S. Cho, J. K. Lee, J. Ko, *Org. Lett.* **2012**, *14*, 6326–6329; c) C. Liu, Y. Li, Y. Zhang, C. Yang, H. Wu, J. Qin, Y. Cao, *Chem. Eur. J.* **2012**, *22*, 6928-6934; d) Z. Fang, V. Chellappan, R. D. Webster, L. Ke, T. Zhang, B. Liu, Y.-H. Lai, *J. Mater. Chem.* **2012**, *22*, 15397-15404.

[16] H. Zhang, S. Wang, Y. Li, B. Zhang, C. Du, X. Wan, Y. Chen, *Tetrahedron* **2009**, *65*, 4455–4463.

[17] D. L. Reger, A. Debreczeni, B. Reinecke, V. Rassolov, M. D. Smith, R. F. Semeniuc, *Inorg. Chem.* **2009**, *48*, 8911–8924.

[18] Z. Fang, T.-L. Teo, L. Cai, Y.-H. Lai, A. Samoc, M. Samoc, *Org. Lett.* **2009**, *11*, 1–4.

[19] M. S. Alexiou, V. Tychopoulos, S. Ghorbanian, J. H. P. Tyman, R. G. Brown, P. I. Brittain, *J. Chem. Soc, Perkin Trans. 2* **1990**, 837-842.

[20] It is common practice to associate the potential for formation of the anion (cation) with the energy of the LUMO (HOMO), *i.e.* the one-electron molecular orbitals of the neutral species. However it is worth to note that LUMO and HOMO are theoretical constructs and their energies cannot be observed by any experimental method.

Experimentally accessible is the optical gap which corresponds to the energy difference between the electronic S_0 and S_1 states of the neutral compound.

Supporting Information to

Synthesis and Photophysical Properties of Multichromophoric Carbonyl Bridged Triarylamines

Andreas T. Haedler,[#1] Sebastian R. Beyer,[#2] Richard Hildner,[2]* Natalie Hammer,[3] Milan Kivala,[3]* Jürgen Köhler,[2] and Hans-Werner Schmidt[1]*

[1] Macromolecular Chemistry I and Bayreuther Institut für Makromolekülforschung (BIMF) and Bayreuth Zentrum für Kolloide und Grenzflächen (BZKG) University of Bayreuth, 95440 Bayreuth (Germany)

[2] Experimental Physics IV and Bayreuther Institut für Makromolekülforschung (BIMF) University of Bayreuth, 95440 Bayreuth (Germany)

[3] Chair of Organic Chemistry I, Department of Chemistry and Pharmacy University of Erlangen-Nürnberg, 91054 Erlangen (Germany)

[#] These authors contributed equally

Table of Content

^{1}H-^{1}H COSY NMR Spectra of Compounds **1** and **2**

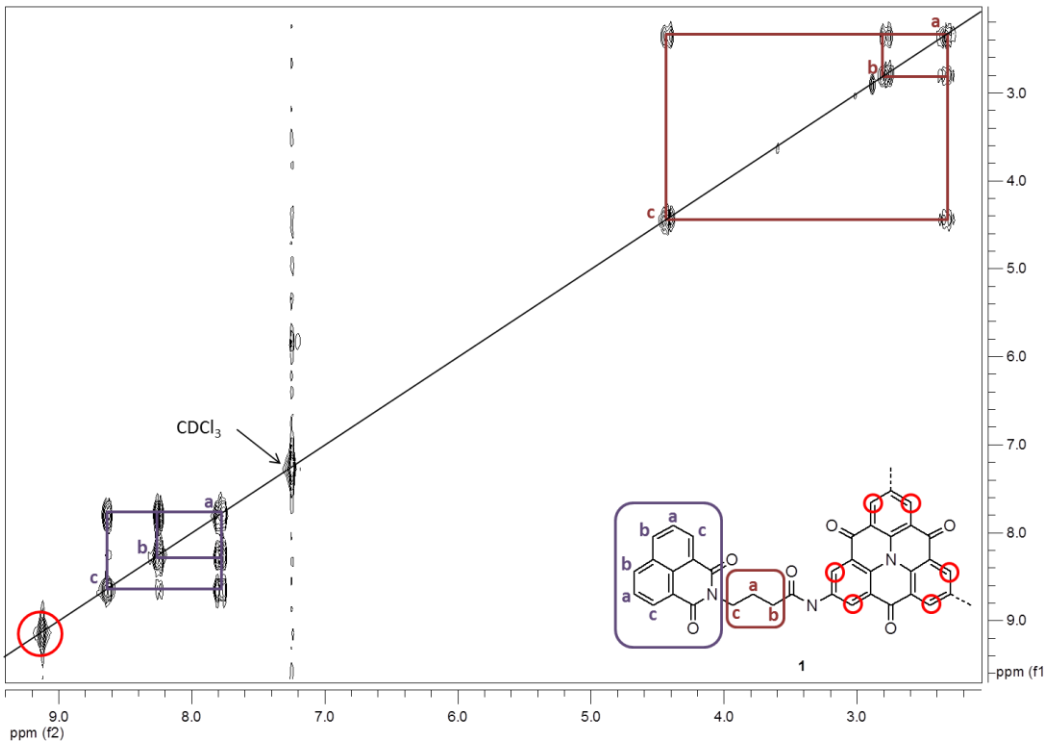

Figure S1 ^{1}H-^{1}H COSY spectra of compound **1** in $CDCl_3$/TFA-d_1.

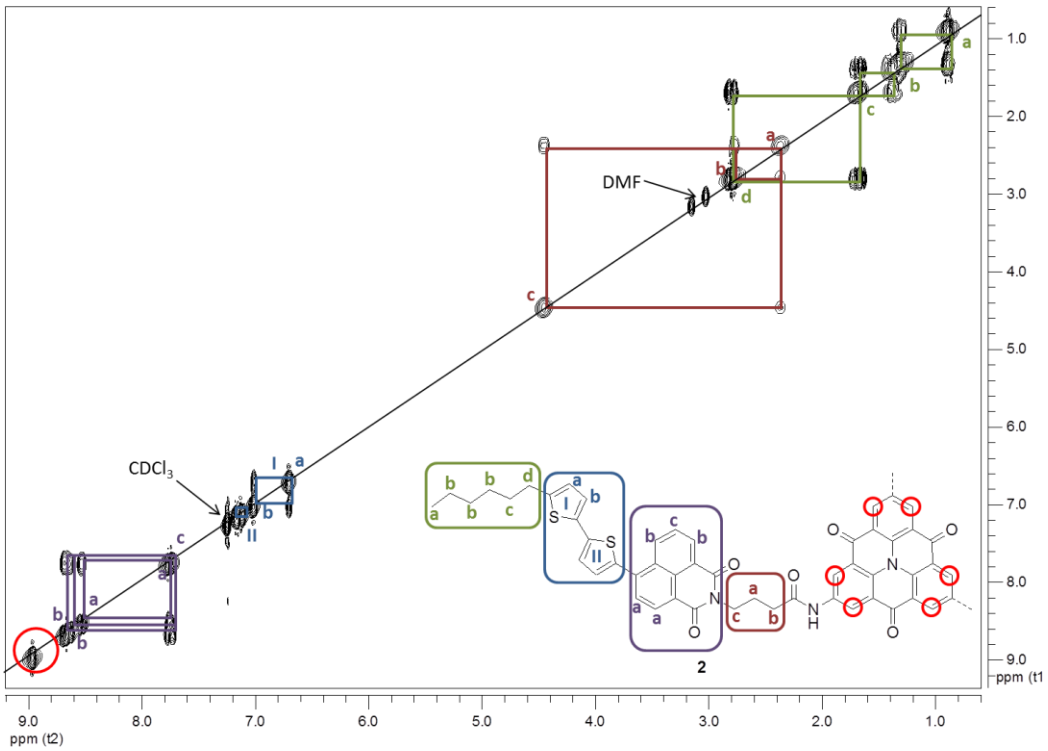

Figure S2 ^{1}H-^{1}H COSY spectra of compound **2** in $CDCl_3$ and DMF-d_7.

Photoluminescence (PL) Spectroscopy

Fig. S**3** shows the photoluminescence emission maps of all seven solutions discussed in the main text. The data shown supports our hypothesis of a highly efficient energy transfer from periphery to core in compound **1** and vice versa in compound **2**. The emission maps of compounds **3**-**5** are shown in Fig. S**3 A-C** and highlight the characteristic emission band of the respective reference substance: 340-450 nm / 450-530 nm / 530-800 nm for NI / CBT / NIBT. To qualitatively assess these spectral fingerprints we extracted the PL-excitation spectra between 372-392 nm / 480-500 nm / 600-620 nm with the respective curve being drawn next to the PL emission maps in blue / green /orange (labeled i / ii / iii) in Fig. S**3**.

For the mixtures of the carbonyl-bridged triarylamine (CBT) **3** with the unbound NI **4**/NIBT **5** all characteristic spectral features of the single reference compounds are fully contained (see Fig. S**3 D** & **E**). Neither an analysis of the emission intensities nor of the PL-excitation spectra delivers any hint towards an energy transfer between the species in these solutions.

For the solutions containing compounds **1** and **2** though (where we have a covalent bond between core and periphery), the case is different. In the PL emission map of compound **1** (Fig. S**3 F**) we can only find the spectral signature of the CBT dye **3** (green box). The characteristic emission of NI vanishes completely and independently of the excitation wavelength (blue box). Moreover, we observe an enhancement of the core's fluorescence throughout the whole area of the NI's absorption around 340 nm. That means that we do not only see a quenching of the periphery's emission by the presence of the core, but an effective energy transfer to the emitting state of the core. These observations are supported by the corresponding PL-excitation spectra. In contrast to the PL-exctitation spectra of the mixture of compounds **3**+**4** (Fig. S**3 D**), in Fig S**3 F** the spectrum from region i) matches the background level while the spectrum in region ii) shows an additional feature around 340 nm. This peak corresponds to the additional absorptive channel opened by the NI-periphery.

For the solution containing compound **2** (Fig. S**3 G**) we see the complementary case: While the spectral fingerprint of the CBT dye **3** is fully present in the mixture of compounds **3** and **5** (Fig. S**3 E**, green box) it completely vanishes in the emission map of **2**. The emission band of **5**, though, is enhanced in the regions of the absorption of compound **3** (mainly between 280 and 310 nm, orange box). Consequently in this case, we have a quenching of the CBT core emission with efficient energy transfer to the NIBT periphery's emitting state. Here as well the PL-excitation spectra support our observation. In Fig S**3 E** (the mixture of compounds **3**+**5**) the PL-excitation spectra from regions ii) and iii) do not differ from those observed for the respective individual compounds. However, in Fig. S**3 G** the spectrum from region ii) completely vanishes, while the spectrum from region iii) shows additional features in the absorptive region of the CBT dye (mainly between 280 and 310 nm). These features arise from absorption by the core and subsequent energy transfer from the core to the periphery.

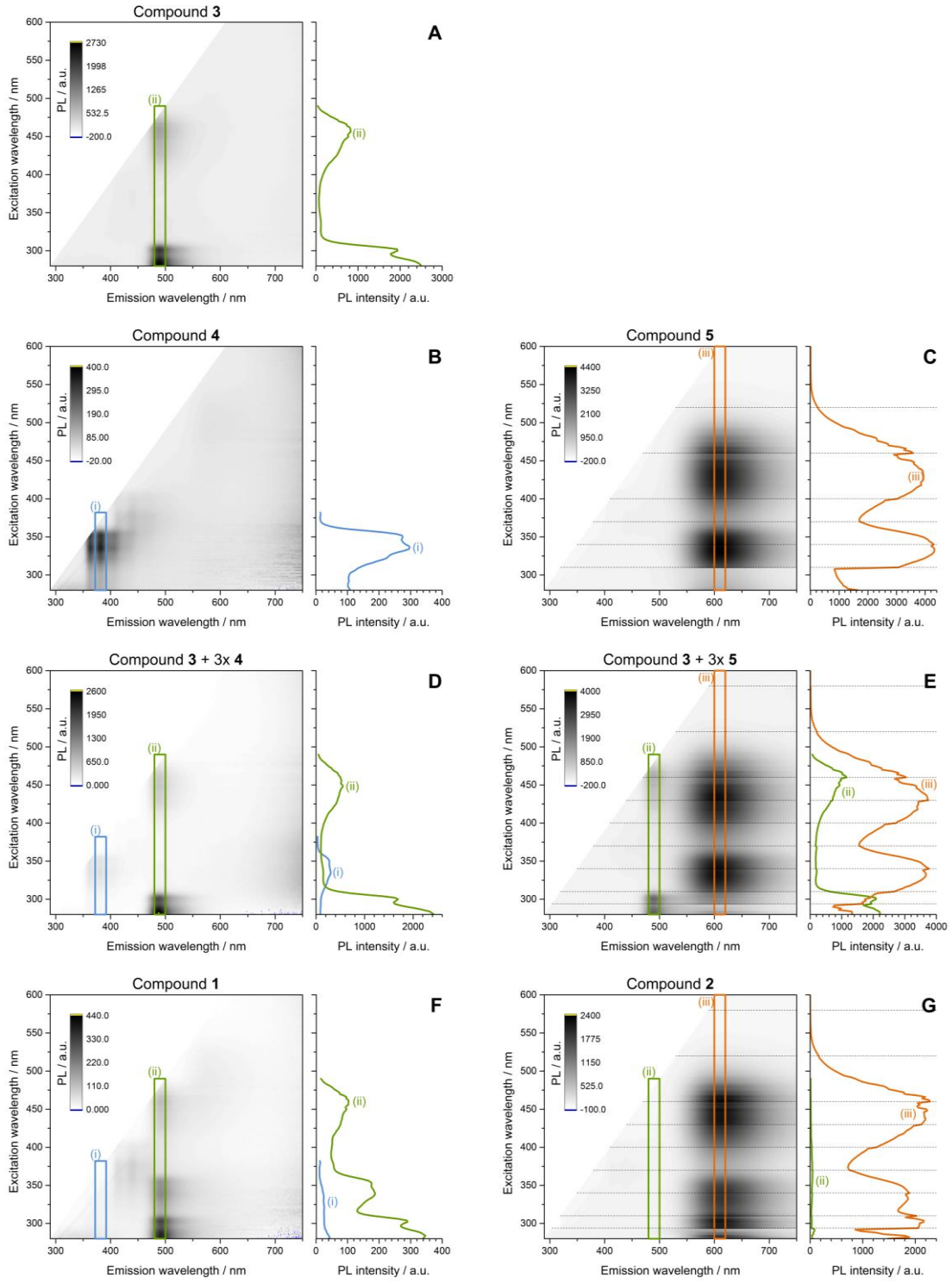

Fig. S3 PL emission maps of solutions of the reference compounds **3**-**5** (A-C), the mixtures of **3**+**4**/**3**+**5** (D/E) and compounds **1**/**2** (F/G). The concentrations were 1 µM for compounds **1**-**3** and 3 µM for compounds **4** and **5** in TCE. The spectral signatures of the reference compounds are highlighted with colored boxes. The PL excitation spectra (on the right) are also extracted from these areas. The dotted, horizontal lines give the excitation wavelengths

at which the solutions containing NIBTs were changed to minimize the influence of photo-bleaching.

Time-Resolved Photoluminescence Spectroscopy

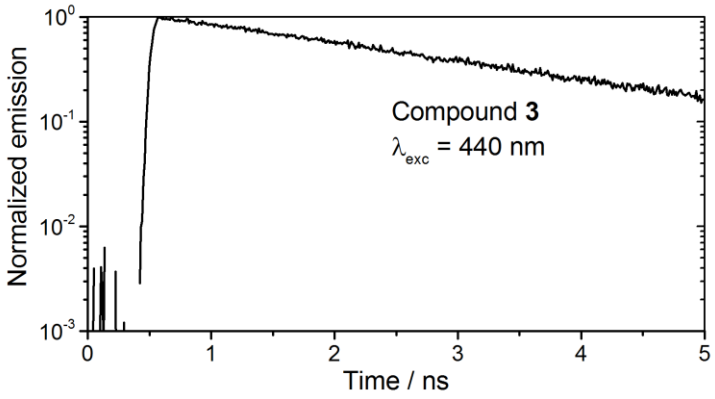

Figure S4 Time-resolved PL emission of compound **3** at c = 1 µM in 1,1,2,2-tetrachloroethane (TCE) after excitation at 440 nm revealing a monoexponential decay with a time constant of 2.5 ns.

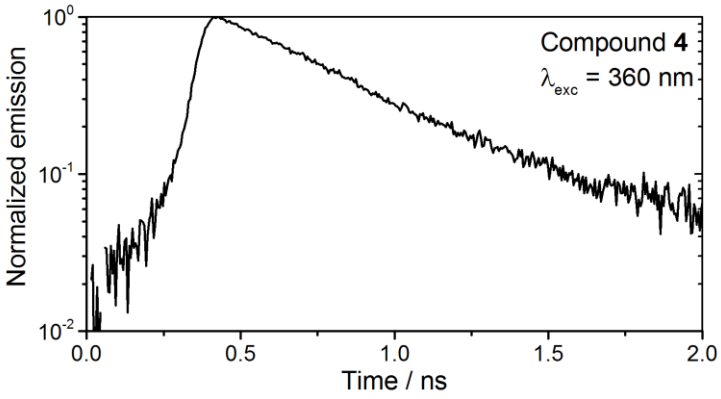

Figure S5 Time-resolved PL emission of compound **4** at c = 3 µM in 1,1,2,2-tetrachloroethane (TCE) after excitation at 360 nm revealing a monoexponential decay with a time constant of 495 ps.

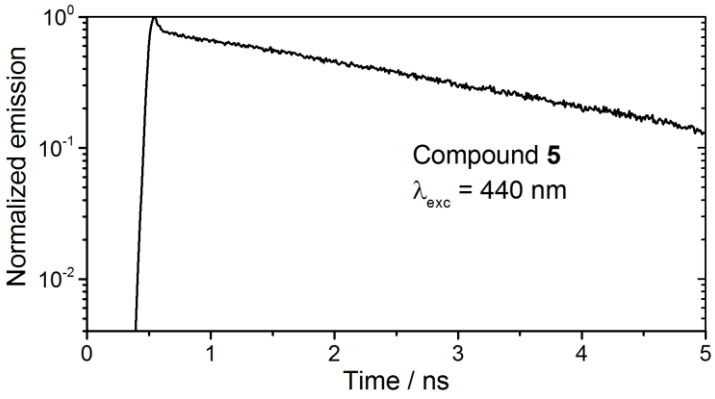

Figure S6 Time-resolved PL emission of compound **5** at c = 3 µM in 1,1,2,2-tetrachloroethane (TCE) after excitation at 440 nm revealing a bi-exponential decay with time constants $\tau_1 = 17\ ps$ and $\tau_2 = 2.5\ ns$ and an amplitude ratio of $A_1/A_2 = 1.57$.

Kinetic Model for Time-Resolved Data

To describe the time-resolved data of compounds **1** and **2** we used a standard donor-acceptor model as depicted in Fig. **S7**.

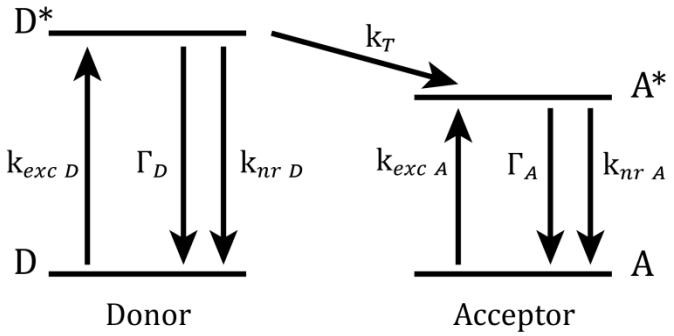

Figure S7 Sketch of the energy level scheme used in the model for fitting the time resolved decays of compounds **1** and **2**. See text for details.

In this scheme, the electronic ground (excited) states of the donor and the acceptor are named D (D*) and A (A*). An excitation from the ground to the excited state of the donor (acceptor) occurs via the rate of excitation $k_{exc\ D}$ ($k_{exc\ A}$), while a deexcitation can either occur by emitting a photon with the radiative rate Γ_D (Γ_A) or by nonradiative processes described by the rate $k_{nr\ D}$ ($k_{nr\ A}$). Energy transfer from the excited donor state D* to the excited acceptor state A* can occur with the transfer rate k_T. The time dependent population probabilities of the ground [excited] states of the donor and the acceptor are denoted as· $n_D(t)$ [$n_{D^*}(t)$] and $n_A(t)$ [$n_{A^*}(t)$].

Assuming that coherent effects do not play a role, the temporal evolution of the populations can be described by the following set of differential equations:

$$\frac{d}{dt}n_{D^*}(t) = -(\Gamma_D + k_{nr\,D} + k_T) \cdot n_{D^*}(t) + k_{exc\,D} \cdot n_D(t)$$

$$\frac{d}{dt}n_{A^*}(t) = -(\Gamma_A + k_{nr\,A}) \cdot n_{A^*}(t) + k_T \cdot n_{D^*}(t) + k_{exc\,A} \cdot n_A(t)$$

These equations can be simplified by omitting the last term in both equations because we use a pulsed excitation source with a pulse duration that is much shorter than any decay time in our systems. Hence, the initial population probability of the donor and acceptor is set to $n_{D^*}(t=0) = N_{0D^*}$ and $n_{A^*}(t=0) = N_{0A^*}$ (with $N_{0D^*} + N_{0A^*} = 1$), respectively, depending on whether the excitation is resonant with the donor and/or acceptor. Then the solution for the differential equation for $n_{D^*}(t)$ becomes:

$$n_{D^*}(t) = N_{0D^*} \cdot e^{-(\Gamma_D + k_{nr\,D} + k_T)\cdot t} = N_{0D^*} \cdot e^{-k_{obs\,D}\cdot t},$$

with $k_{obs\,D} = \Gamma_D + k_{nr\,D} + k_T$ being the effective rate that depopulates the donor D*. With the knowledge of $n_{D^*}(t)$ and defining the effective rate that depopulates the acceptor A* as $k_{obs\,A} = \Gamma_A + k_{nr\,A}$, we find for the time dependence of the A* population:

$$n_{A^*}(t) = \left\{N_{0A^*} + N_{0D^*} \cdot \frac{k_T}{k_{obs\,D} + k_{obs\,A}}\right\} \cdot e^{-k_{obs\,A}\cdot t} - N_{0D^*} \cdot \frac{k_T}{k_{obs\,D} + k_{obs\,A}} \cdot e^{-k_{obs\,D}\cdot t}.$$

This reflects a biexponential behavior with the first term describing the decay and the second term the rise of the population of the acceptor excited state.

As we only observe the photoluminescence of the acceptor we limit the following discussion to $n_{A^*}(t)$. We will first consider the situation that we only excite the donor chromophore as for compound **1**, i.e. $n_{D^*}(t=0) = N_{0D^*} = 1$ and $n_{A^*}(t=0) = N_{0A^*} = 0$. Then $n_{A^*}(t)$ simplifies to:

$$n_{A^*}(t) = \frac{k_T}{k_{obs\,D} + k_{obs\,A}} \cdot \{e^{-k_{obs\,A}\cdot t} - e^{-k_{obs\,D}\cdot t}\}.$$

Importantly, the rate constant obtained for the rise component is $k_{obs\,D} = \Gamma_D + k_{nr\,D} + k_T$, and therefore does not only contain the transfer rate k_T from D* to A*, but all rates that lead to a depopulation of D*. Given that the pure donor lifetime $\Gamma_D + k_{nr\,D}$ is known (e.g. by measurements of reference compounds) and does not change in the presence of the acceptor, the pure transfer rate can be obtained from $k_{obs\,D}$. Notably, the amplitudes of the decaying and rising components are equal.

Second, in the case where the donor as well as the acceptor are excited simultaneously, as for compound **2**, we will accordingly have to apply different initial conditions for N_{0D^*} and N_{0A^*}. Specifically, for compound **2**, where according to the excitation conditions and the absorption cross sections of compounds **3** and **5**, we have a situation with $N_{0D^*} = 0.155$ and $N_{0A^*} = 0.845$. Then it follows for the population of A*:

$$n_{A^*}(t) = \left\{0.845 + 0.155 \cdot \frac{k_T}{k_{obs\,D} + k_{obs\,A}}\right\} \cdot e^{-k_{obs\,A} \cdot t} - 0.155 \cdot \frac{k_T}{k_{obs\,D} + k_{obs\,A}} \cdot e^{-k_{obs\,D} \cdot t}.$$

As the donor in compound **2** distributes its energy to three equivalent molecules, each with a rate k_T, we get for the rate constant of the rise component $k_{obs\,D} = \Gamma_D + k_{nr\,D} + 3k_T$. In this case the rising component possesses a high rate due to excess of acceptors. Moreover, the amplitude of the rising component is much smaller than that of the decay component. Hence, resolving the rising component is difficult, if not impossible.

Cyclic Voltammetry (CV), LUMO Values, and Optical Gaps

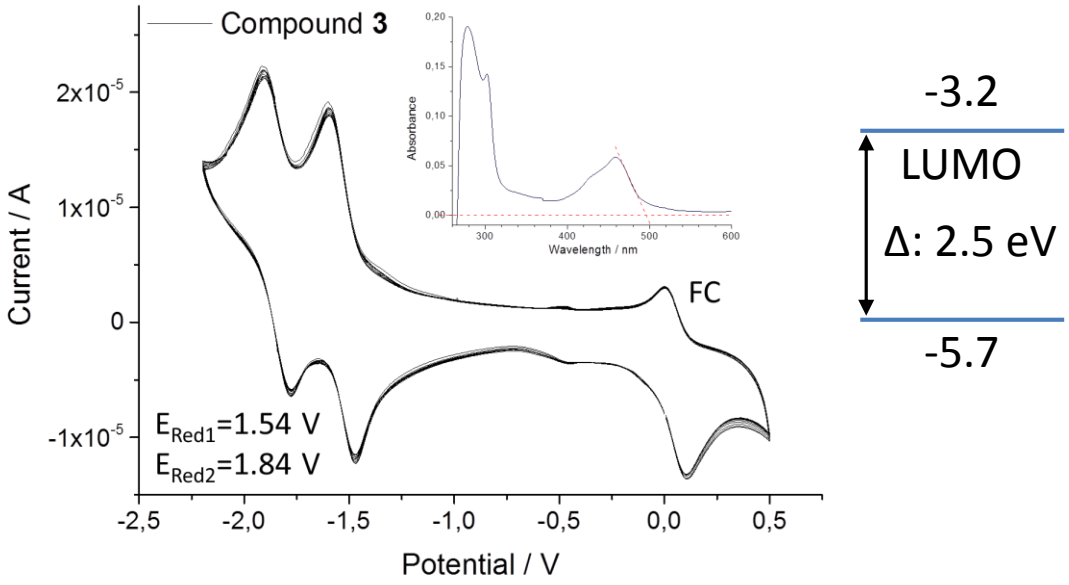

Figure S8 Cyclic voltammetry (10 repeating cycles) of compound **3** and ferrocene as reference substance in NMP. Inlay: UV/vis absorption spectrum of compound **3** in TCE (c = 1 µM) depicting the absorption onset. Right: LUMO level and optical gap of compound **3** determined from first reduction peak of the cyclic voltammetry and from the UV/vis absorption onset, respectively.

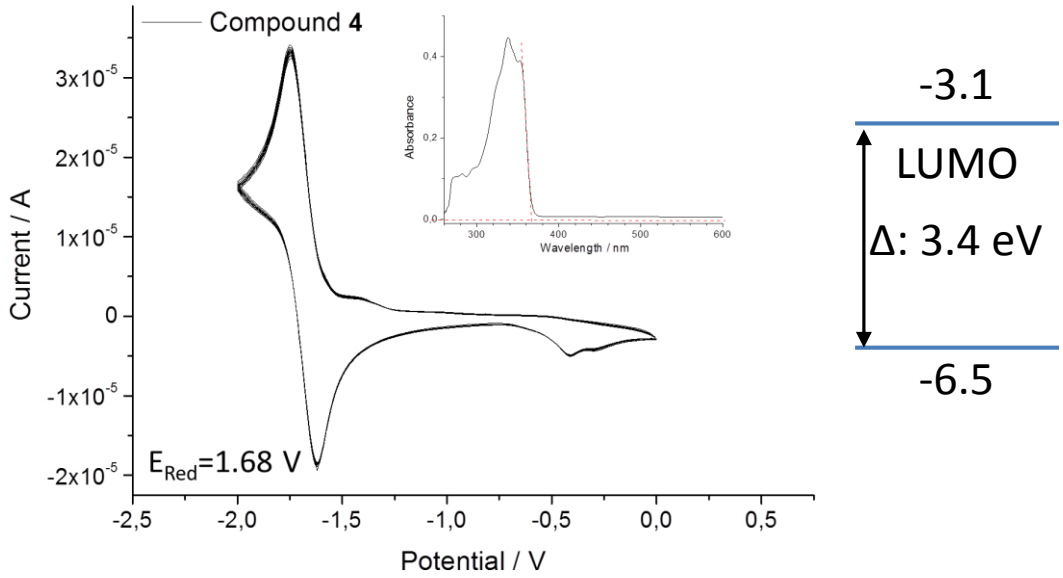

Figure S9 Cyclic voltammetry (10 repeating cycles) of compound **4** in NMP. Inlay: UV/vis absorption spectrum of compound **4** in TCE (c = 3 µM) depicting the absorption onset. Right: LUMO level and optical gap of compound **4** determined from first reduction peak of the cyclic voltammetry and from the UV/vis absorption onset, respectively.

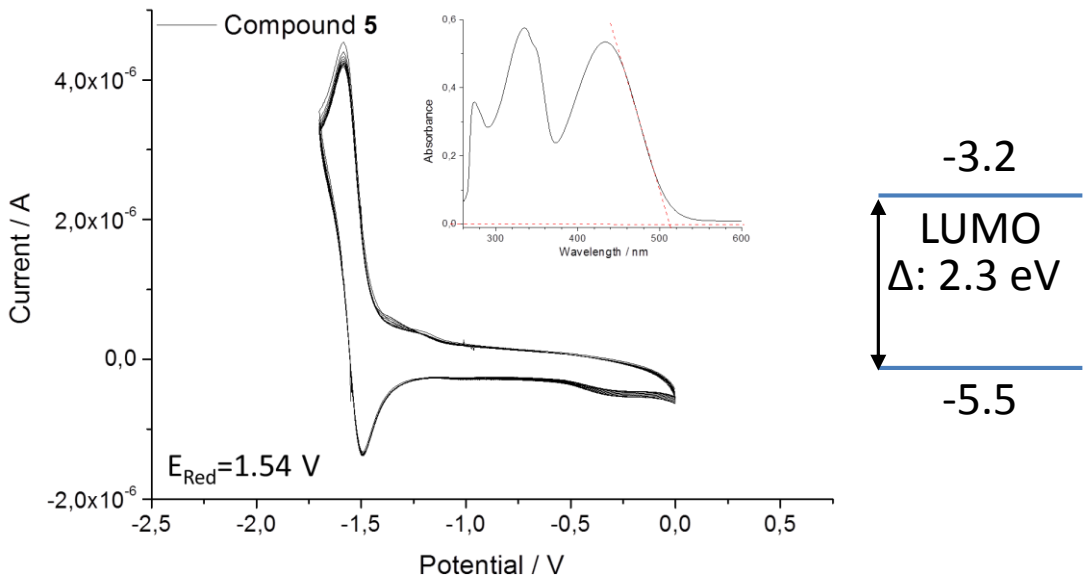

Figure S10 Cyclic voltammetry (10 repeating cycles) of compound **5** in NMP. Inlay: UV/vis absorption spectrum of compound **5** in TCE (c = 3 µM) depicting the absorption onset. Right: LUMO level and optical gap of compound **5** determined from first reduction peak of the cyclic voltammetry and from the UV/vis absorption onset, respectively.

Photoluminescence Emission Map of a Gelled Sample of Compound **1** in o-DCB

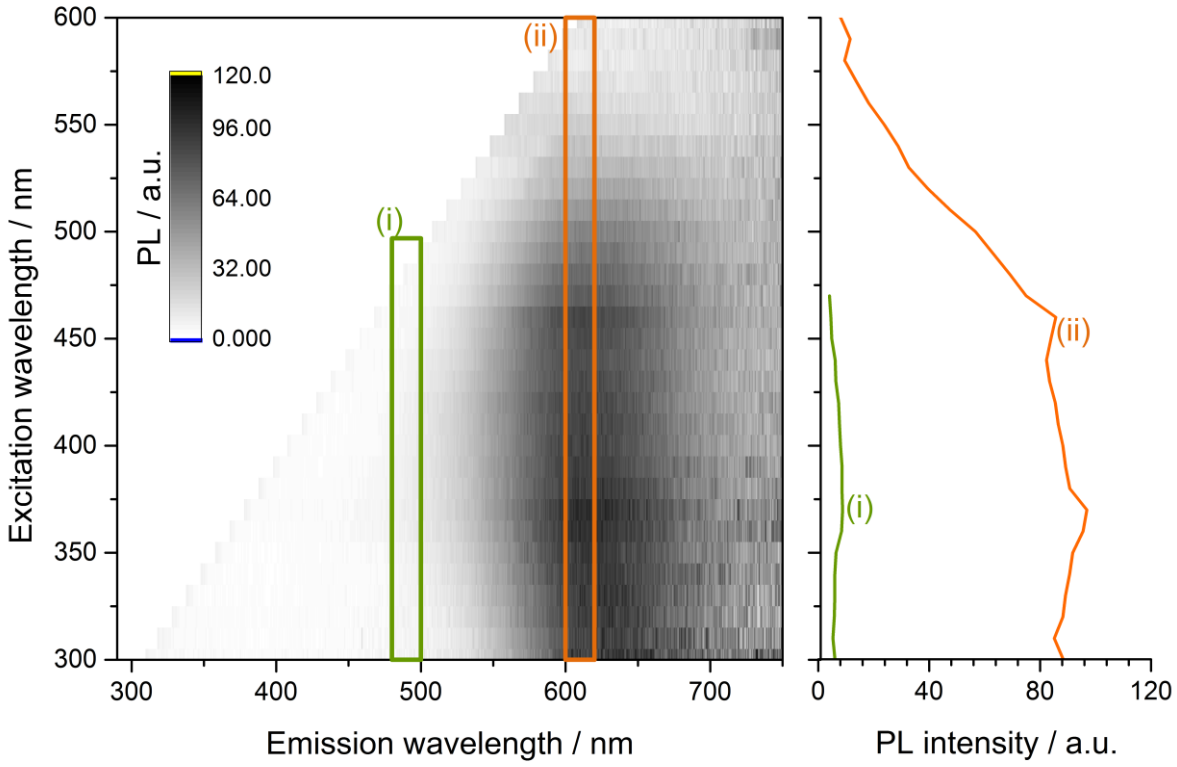

Figure S11 PL emission map of a gelled sample of compound **2** in *o*-DCB (0.7 mM). The spectral signatures of the CBT core (green) and the NIBT (orange) are highlighted with colored boxes. The PL excitation spectra (on the right) are also extracted from these areas.

5. Long-Range Energy Transport in Single Supramolecular Nanofibres at Room Temperature

Andreas T. Haedler[1], Klaus Kreger[1], Abey Issac[2†], Bernd Wittmann[2], Milan Kivala[3], Jürgen Köhler[2], Hans-Werner Schmidt[1]*, and Richard Hildner[2]*

[1] Makromolekulare Chemie I, Bayreuther Institut für Makromolekülforschung (BIMF), and Bayreuther Zentrum für Kolloide und Grenzflächen (BZKG), Universität Bayreuth, 95440 Bayreuth (Germany)

[2] Experimentalphysik IV and Bayreuther Institut für Makromolekülforschung (BIMF), Universität Bayreuth, 95440 Bayreuth (Germany)

[3] Lehrstuhl für Organische Chemie I, Department für Chemie und Pharmazie, Universität Erlangen-Nürnberg, 91054 Erlangen (Germany)

[†] Current address: Department of Physics, Sultan Qaboos University, Muscat (Oman)

* Corresponding authors: richard.hildner@uni-bayreuth.de
hans-werner.schmidt@uni-bayreuth.de

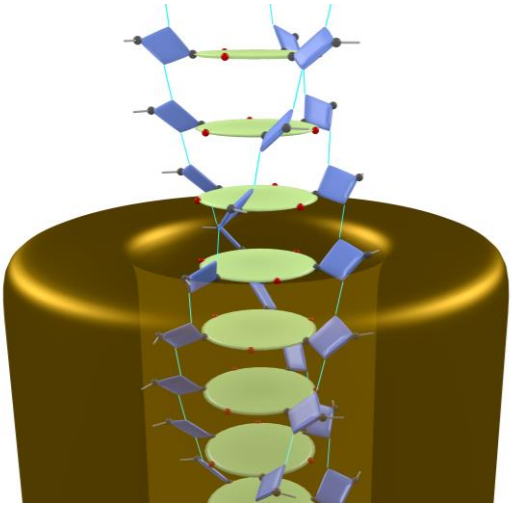

Accepted in *Nature*

Abstract and Introduction

Efficient transport of excitation energy over long distances is a key process in light-harvesting systems as well as in molecular electronics.[1–3] However, in disordered organic materials the exciton diffusion length is typically in the order of ~ 10 nm,[4,5] in exceptional cases up to ~ 50 nm,[6,7] largely determined by the probability laws of incoherent hopping. Only for highly ordered organic systems transport of excitation energy over macroscopic distances was reported, e.g. for triplet excitons in anthracene single crystals at room temperature[8] as well as coherent transport along single polydiacetylene chains embedded in their monomer crystalline matrix at cryogenic temperatures.[9] In contrast, for supramolecular nanostructures uniaxial, long-range transport has not been demonstrated at room temperature. Here we show that individual self-assembled nanofibres with molecular diameter efficiently transport singlet excitons at ambient conditions over more than 4 μm, only limited by the fibre length. Our data suggest that this remarkable long-range transport is predominantly coherent, which is achieved by one-dimensional self-assembly of supramolecular building blocks, based on carbonyl-bridged triarylamines,[10] to well-defined H-aggregates with substantial electronic interactions. These findings are highly relevant for developments towards novel organic nanophotonic devices and for quantum information technology.

Supramolecular chemistry utilises directed non-covalent interactions to construct welldefined architectures in a bottom-up approach that provide functionalities beyond those of the constituent building blocks.[11–16] For example, supramolecular nanostructures were identified as potential components to transport excitation energy in light-harvesting applications.[17–22] Those nanostructures feature a controlled and spatially well-defined arrangement of their building blocks with substantial intermolecular electronic coupling, which is a requirement for efficient energy transport. The observed migration lengths of ~ 100 nm were attributed to incoherent hopping with some contribution of coherent motion, i.e. a delocalisation of electronic excitations over several building blocks. In those nanostructures, however, J-type aggregates are formed,[17–20,22] and the oscillator strength is redistributed into the lowest-energy exciton level forming a super-radiant state.[23] Consequently, the competition between radiative decay and energy transport strongly

constrains the distance that electronic excitations can migrate. In contrast, in ideal H-aggregates, with cofacially stacked building blocks, the lowest-energy transition is dipole forbidden.[23] This results in a strongly increased radiative lifetime of the relaxed excited state, which should be beneficial for efficient energy transport over macroscopic distances.[8,24]

Here, we demonstrate at room temperature long-range energy transport along individual Haggregated nanofibres with molecular diameter. We utilise a specifically designed supramolecular building block (compound **1**, Fig. 1**a**) based on a carbonyl-bridged triarylamine (CBT) as core, that is functionalised at 2, 6, and 10 positions *via* amide linkers with 4-(5-hexyl-2,2'-bithiophene)-naphthalimides (NIBT).[10] The combination of the planar, aromatic heterotriangulene core[25] and the three hydrogen-bonding amide groups is the structure-defining element that enforces columnar self-assembly (Fig. 1**b**). The peripheral NIBT units exhibit a bright orange photoluminescence (PL) either upon direct photoexcitation or after energy transfer from CBT.

Self-assembly into nanofibres with molecular diameter

The pronounced self-assembly behaviour of compound **1** is demonstrated by gelation in *ortho*-dichlorobenzene (*o*-DCB) at a concentration of 700 µM (1,000 ppm).[10] A dense network of nanofibres is visualised by transmission electron microscopy (TEM) on a solvent-free sample, directly prepared from the gel (Fig. 2**a**). Some fibres align next to each other resulting in structures with widths of multiples of 5 nm (Fig. S1). The mean diameter of single fibres of 5 nm ± 1 nm matches well with the calculated diameter of 6 nm for compound **1** (Fig. 2**b,c**), which shows the presence of one-dimensional nanofibres with molecular diameter. This is confirmed by uniform fibre heights of 2 – 2.5 nm observed with atomic force microscopy (AFM) on samples spin-coated from a dispersion of self-assembled compound **1** in *o*-DCB (7 µM, 10 ppm, Fig. S2).

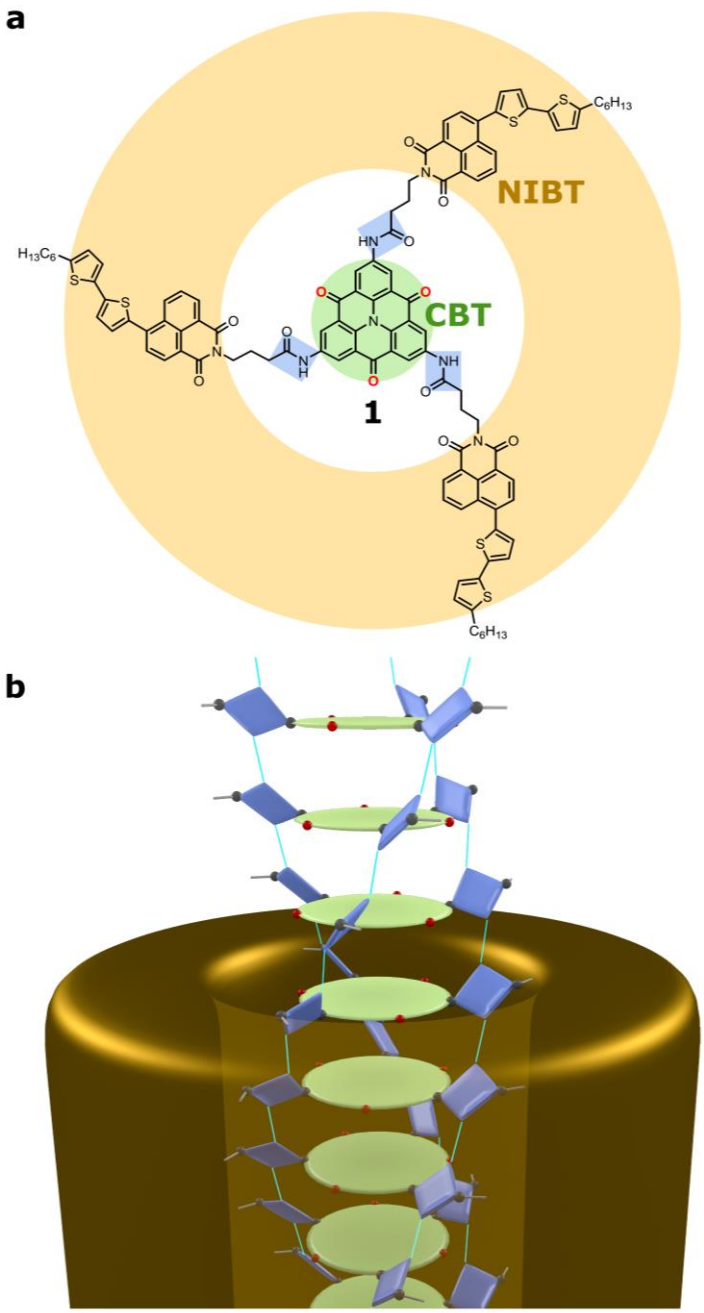

Figure 1 | Self-assembly of compound 1. a, Chemical structure of compound **1**: carbonyl-bridged triarylamine (CBT) core (green); amide moieties (blue); 4-(5-hexyl-2,2'-bithiophene)-naphthalimide (NIBT) periphery (orange). **b,** Illustration of the self-assembly into nanofibres with an ordered H-aggregated core, driven by π-stacking of CBT and stabilised by three chains of hydrogen bonds between the amide groups.

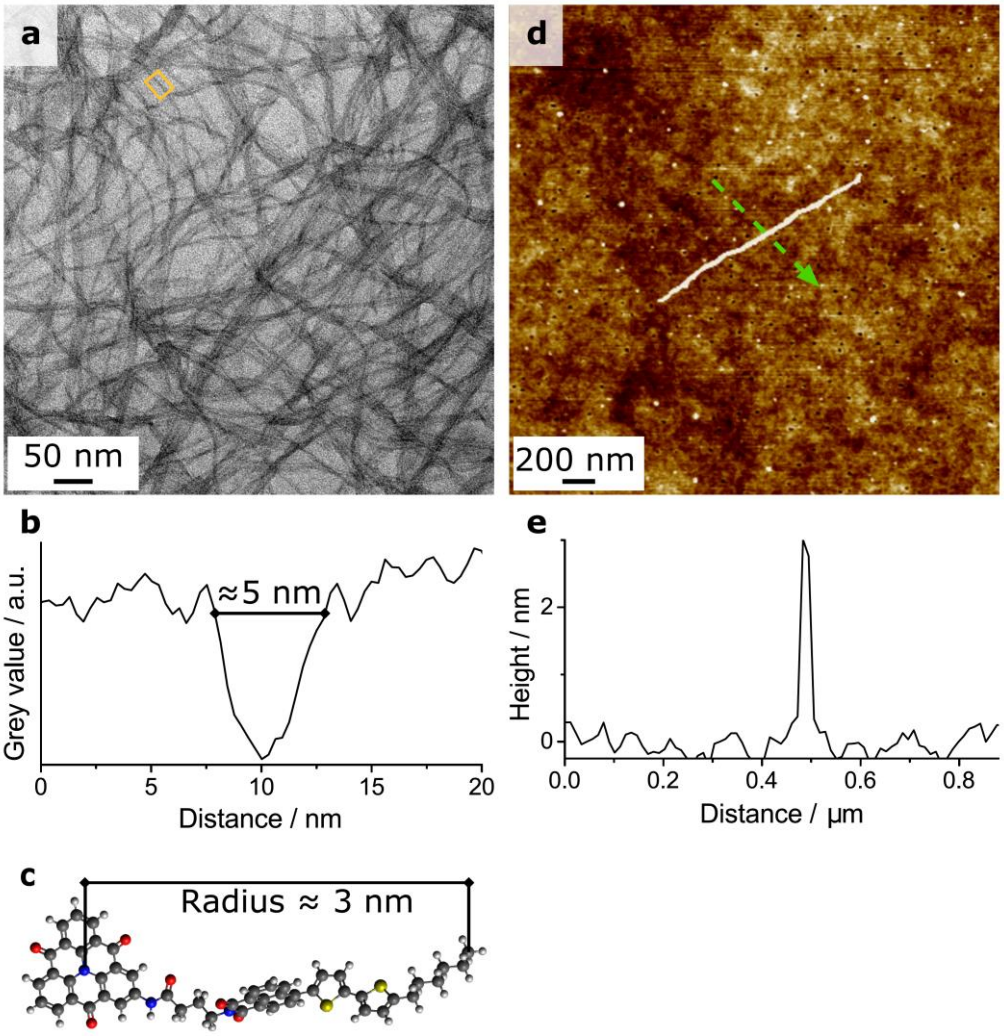

Figure 2 | Characterisation of self-assembled nanofibres. **a**, Transmission electron microscopy image of a sample prepared from a gel of compound **1** in *ortho*-dichlorobenzene (*o*-DCB) at 700 µM (1,000 ppm). **b**, Cross section of the nanofibre in the yellow boxed area in **a**. Grey value is a measure for the intensity of the transmitted electron beam. **c**, Energy minimised structure of compound **1** in its extended form. **d**, Atomic force microscopy image (topographical scan) of a spatially isolated single nanofibre, prepared by spin-coating selfassembled compound **1** (0.07 µM, 0.1 ppm, in *o*-DCB). **e**, Height profile along the dashed green arrow in **d**.

The self-assembly into nanofibres is driven by π-stacking of the aromatic CBT units, as shown by changes of the optical spectra (Fig. S3). In the absorption spectra, a strongly blueshifted band rises at about 380 nm (ca. 26,300 cm^{-1}) upon self-assembly in *o*-DCB, indicating the formation of H-aggregates. However, it is not clear which chromophore(s) are involved in this process, because the absorptions of CBT and NIBT overlap.[10] In contrast, the PL of self-

assembled compound **1** stems exclusively from the NIBT chromophores (Fig. S3). The PL spectra do not feature new and strongly shifted bands that can be associated with aggregation. Hence, the NIBT units are not stacked in an ordered fashion. Only the CBT units within the supramolecular nanofibres form well-defined π-stacked assemblies. These one-dimensional H-aggregates are stabilised by intermolecular hydrogen bonds between the amide groups of compound **1**, which is evidenced by changes of the N-H stretch vibration in Fourier-transform infra-red spectra (Fig. S4). It is noteworthy, that carbonyl-bridged triarylamines without amide groups are stacked with a clear offset.[25,26] In compound **1**, however, the three chains of hydrogen bonds enforce the cofacial arrangement of the CBT units, as illustrated in Fig. 1**b**, and thus the formation of supramolecular nanofibres with molecular diameter.

Long-range excitation energy transport

An important factor for efficient energy transport along the nanofibres is the electronic coupling between neighbouring CBT units. To determine this parameter, we resort to a reference compound **2**, which features the identical supramolecular motif as compound **1**; however, the NIBT chromophores are replaced by octyl chains (Fig. S5). The spectra of self-assembled compound **2** demonstrate the presence of H-aggregates. From those data we obtain a nearest-neighbour electronic coupling of $W \geq 44$ meV (350 cm^{-1}, Fig. S5), employing a theoretical framework developed by Spano.[27] For compound **1** we expect a similar value for W owing to the same supramolecular motif. The magnitude of this electronic coupling between the CBT units is close to the strongest intermolecular coupling strengths in other self-assembled nanostructures, such as J-aggregates based on small molecules[17,28] and photosynthetic light-harvesting antenna systems.[29,30]

In order to study energy transport along single nanofibres, we diluted self-assembled compound **1** to a concentration of 0.07 µM (0.1 ppm, in *o*-DCB) and subsequently spincoated this dispersion on microscopy cover slips. Well-isolated µm-long nanofibres are revealed by AFM (Fig. 2**d,e**, Fig. S7). Owing to this large spatial separation, single nanofibres can be resolved and addressed with a confocal microscope. We first operate the microscope in imaging mode using widefield illumination and a charge-coupled device (CCD) camera to

detect the nanofibres' PL. Fig. 3**a** depicts a representative PL image with several individual nanofibres in agreement with AFM data (Fig. S7). Having identified an isolated fibre (Fig. 3**a**, orange box), the microscope is switched to confocal illumination while the PL is still imaged onto the CCD-camera. We then position the nanofibre such that one of its ends coincides with the laser focus with a radius of ~ 300 nm (green spot, Fig. 3**b**). Intriguingly, PL from the entire structure with a length of ~ 4 µm is observed. We rule out a waveguide effect, because of the molecular diameter (5 nm) of the nanofibres, as well as direct photoexcitation more than ~ 500 nm away from the centre of the laser focus (section 7, SI). Consequently, this PL signal results from efficient transport of excitation energy over 4 µm. Given the typical π-stacking distance of 0.35 nm,[14,15] this involves more than 10,000 molecules.

We investigated in total 97 individual fibres, in order to proof the robustness of this long-range energy transport. In most cases the transport distance is only limited by the nanofibre length, which is demonstrated in Figs. 3**c** and S9: Their lengths, determined from PL images upon widefield illumination, range from 1.9 to 6.4 µm (average: 3.3 µm). This histogram strongly overlaps with the distribution of transport distances between 1.6 and 4.4 µm (average: 2.9 µm), retrieved from PL images upon confocal excitation at one fibre end (Fig. S8 shows an example with interrupted energy transport).

To elucidate the transport mechanism, we recorded PL spectra from single nanofibres (Fig. S10). These data confirm that the photoluminescent NIBT periphery does not form structurally defined assemblies and therefore does not support transport over macroscopic distances.[4,5] Hence, the efficient long-range transport occurs along the ordered nanofibres' core, promoted by substantial electronic coupling between the H-aggregated CBT units. The electronic coupling gives rise to the formation of vibronic singlet excitons with a small transition dipole moment for the lowest-energy transition (section 4, SI). This strongly reduces the rate of the main loss mechanism for electronic excitations on the CBT units of compound **1**, i.e. energy transfer to the NIBT periphery,[10] which can thus no longer compete with transport along the core. However, excitation energy can be trapped at small defects within the core. Then, energy transfer to the periphery becomes more likely and PL from

NIBT is observed. In this sense, the NIBT emission reports on the transport distance along

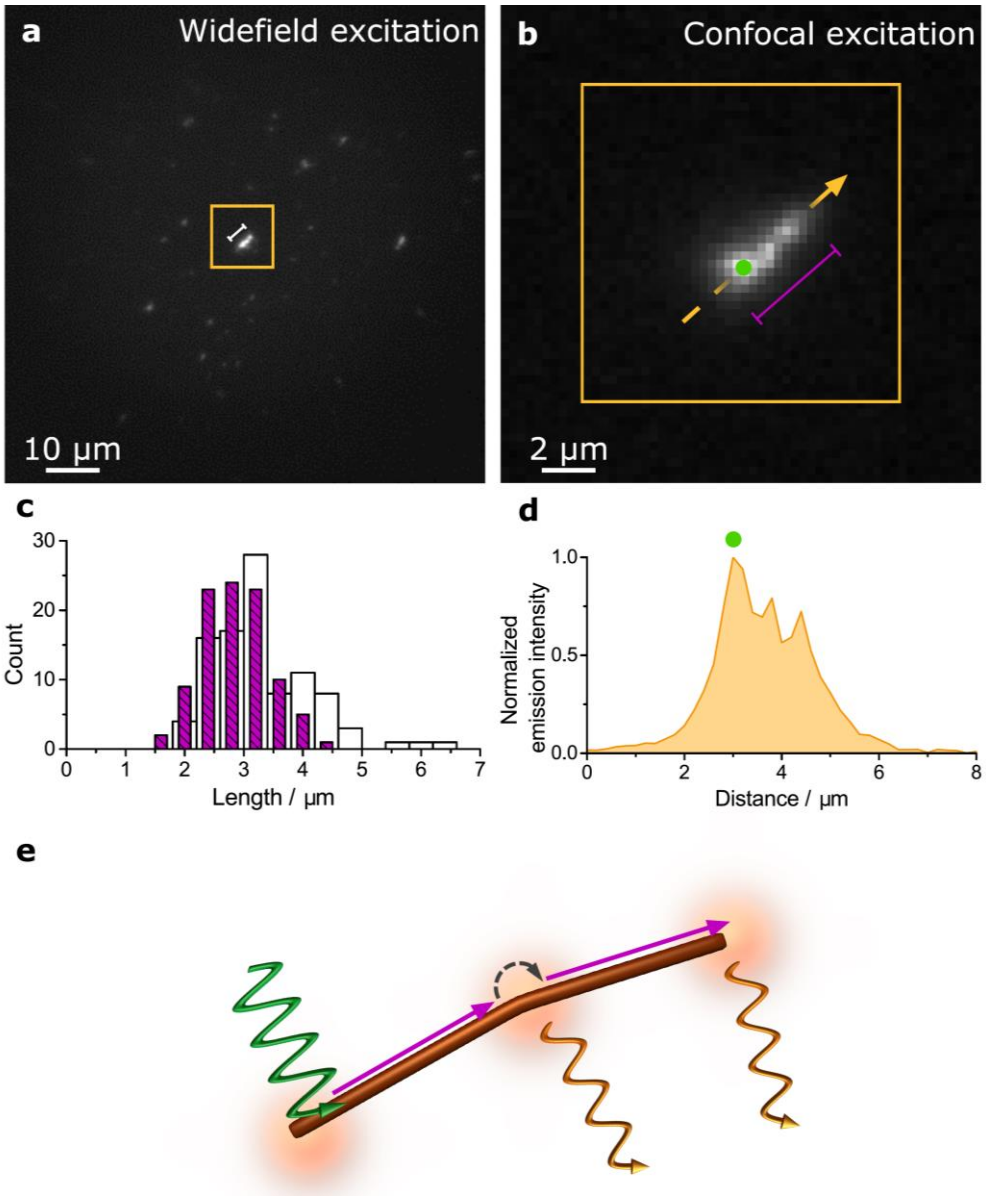

Figure 3 | Long-range energy transport along single supramolecular nanofibres. a, Widefield photoluminescence (PL) image of a spin-coated sample of self-assembled compound **1** (0.07 µM, 0.1 ppm, in *o*-DCB). The nanofibre in the boxed region appears slightly brighter than the other structures due to a non-perfectly uniform widefield illumination. **b**, PL image of the nanofibre in the orange boxed region in **a** upon confocal excitation at its bottom left end (filled green circle), demonstrating highly efficient energy transport over ~ 4 µm. **c**, Open bars: distribution of fibre lengths determined from PL images upon widefield illumination; violet bars: distribution of transport distances along single nanofibres retrieved upon confocal illumination of the same set of 97 nanofibres. **d**, Intensity profile along the orange dashed arrow in **b**. **e**, Schematic illustration of the transport mechanism along the nanofibre in **b**. Local illumination at one end (green arrow) gives rise to coherent energy transport along an ordered domain of the nanofibre's core (violet arrow). At small defects, here symbolised by a kink, incoherent energy transfer occurs either to the

NIBT periphery with subsequent PL (orange arrow), or to the next ordered domain of the core (black dashed arrow), where coherent transport takes place to the nanofibre's end.

the nanofibres as well as on the structural order of the core. This interpretation is evidenced by the spatially non-uniform PL intensity along the nanofibre upon confocal illumination (Fig. 3**b**,**d**). The PL maxima are attributed to small defects within the fibre core, where excitation energy leaks to the photoluminescent periphery. The smaller PL signal stems from those parts of the nanofibre where energy transfer to the periphery is less efficient due to a highly ordered core (Fig. 3**e**).

The remarkable transport distances of up to 4.4 µm along single nanofibres at room temperature demonstrate a high mobility of electronic excitations. Based on the electronic coupling between CBT units (44 meV) and the excited state lifetime of self-assembled reference compound **2** (2.3 ns), we estimate transport distances between some 100 nm for diffusive (Forster-type) hopping and ~ 8 µm for entirely coherent motion (section 6, SI). Exclusively incoherent hopping can not account for our observations; yet, fully coherent transport is also unlikely at room temperature.[17,28] We therefore suggest a combined coherent - incoherent motion with a predominant coherent contribution. The electronic coupling promotes delocalisation of electronic excitations over ordered domains along the core,[22] i.e. a coherent sharing by many CBT units (coherent transport), while between these domains incoherent hopping occurs (Fig. 3**e**). This largely coherent long-range transport makes this system a promising candidate to develop new concepts for quantum information technologies and for efficient solar energy conversion based on functional supramolecular architectures. For instance, H-type nanofibres are useful for efficient and directed energy transport from an antenna system for light-harvesting to a transducer for conversion into charge carriers. In addition, the strongly reduced transition dipole moment of the lowest-energy transition in H-aggregates may be beneficial for achieving a stable charge-separated state, because there is no competition with (super-radiant) emission.

References

1. Scholes, G. D., Mirkovic, T., Turner, D. B., Fassioli, F. & Buchleitner, A. Solar light harvesting by energy transfer: from ecology to coherence. *Energy Environ. Sci.* **5,** 9374–9393 (2012).
2. Laquai, F., Park, Y.-S., Kim, J.-J. & Basche, T. Excitation energy transfer in organic materials: from fundamentals to optoelectronic devices. *Macromol. Rapid Commun.* **30,** 1203–1231 (2009).
3. Siebbeles, L. D. A. & Grozema, F. C. (eds.) *Charge and exciton transport through molecular wires*. (Wiley-VCH, Weinheim, 2011).
4. Menke, S. M. & Holmes, R. J. Exciton diffusion in organic photovoltaic cells. *Energy Environ. Sci.* **7,** 499–512 (2014).
5. Lin, J. D. A. *et al.* Systematic study of exciton diffusion length in organic semiconductors by six experimental methods. *Mater. Horiz.* **1,** 280–285 (2014).
6. Bolinger, J. C., Traub, M. C., Adachi, T. & Barbara, P. F. Ultralong-Range Polaron-Induced Quenching of Excitons in Isolated Conjugated Polymers. *Science* **331,** 565–567 (2011).
7. Vogelsang, J., Adachi, T., Brazard, J., Vanden Bout, D. A. & Barbara, P. F. Self-assembly of highly ordered conjugated polymer aggregates with long-range energy transfer. *Nat. Mater.* **10,** 942–946 (2011).
8. Avakian, P. & Merrifield, R. E. Experimental Determination of the Diffusion Length of Triplet Exciton in Anthracene Crystals. *Phys. Rev. Lett.* **13,** 541–543 (1964).
9. Dubin, F. *et al.* Macroscopic coherence of a single exciton state in an organic quantum wire. *Nat. Phys.* **2,** 32–35 (2006).
10. Haedler, A. T. *et al.* Synthesis and photophysical properties of multichromophoric carbonylbridged triarylamines. *Chem. Eur. J.* **20,** 11708–11718 (2014).
11. Aida, T., Meijer, E. W. & Stupp, S. I. Functional Supramolecular Polymers. *Science* **335,** 813–817 (2012).
12. Seki, S., Saeki, A., Sakurai, T. & Sakamaki, D. Charge carrier mobility in organic molecular materials probed by electromagnetic waves. *Phys. Chem. Chem. Phys.* **16,** 11093–11113 (2014).
13. Sengupta, S. & Wurthner, F. Chlorophyll J-Aggregates: From Bioinspired Dye Stacks to Nanotubes, Liquid Crystals, and Biosupramolecular Electronics. *Acc. Chem. Res.* **46,** 2498–2512 (2013).
14. Cantekin, S., de Greef, T. F. A. & Palmans, A. R. A. Benzene-1,3,5-tricarboxamide: a versatile ordering moiety for supramolecular chemistry. *Chem. Soc. Rev.* **41,** 6125–6137 (2012).
15. Dou, X., Pisula, W., Wu, J., Bodwell, G. J. & Mullen, K. Reinforced self-assembly of hexa-perihexabenzocoronenes by hydrogen bonds: from microscopic aggregates to macroscopic fluorescent organogels. *Chem. Eur. J.* **14,** 240–249 (2008).

16. Scheibe, G., Schontag, A. & Katheder, F. Fluoreszenz und Energiefortleitung bei reversibel polymerisierten Farbstoffen. *Naturwiss.* **29,** 499–501 (1939).

17. Eisele, D. M., Knoester, J., Kirstein, S., Rabe, J. P. & Vanden Bout, D. A. Uniform exciton fluorescence from individual molecular nanotubes immobilized on solid substrates. *Nat. Nanotech.* **4,** 658–663 (2009).

18. Clark, K. A., Krueger, E. L. & Vanden Bout, D. A. Direct Measurement of Energy Migration in Supramolecular Carbocyanine Dye Nanotubes. *J. Phys. Chem. Lett.* **5,** 2274–2282 (2014).

19. Lin, H. *et al.* Collective fluorescence blinking in linear J-aggregates assisted by long-distance exciton migration. *Nano Lett.* **10,** 620–626 (2010).

20. Zhang, W. *et al.* Supramolecular Linear Heterojunction Composed of Graphite-Like Semiconducting Nanotubular Segments. *Science* **334,** 340–343 (2011).

21. Winiger, C. B., Li, S., Kumar, G. R., Langenegger, S. M. & Haner, R. Long-Distance Electronic Energy Transfer in Light-Harvesting Supramolecular Polymers. *Angew. Chem. Int. Ed.* **53,** 13609–13613 (2014).

22. Eisele, D. M. *et al.* Robust excitons inhabit soft supramolecular nanotubes. *Proc. Natl. Acad. Sci. U.S.A.* **111,** E3367–3375 (2014).

23. Kasha, M., Rawls, H. R. & Ashraf El-Bayoumi, M. The Exciton Model in Molecular Spectroscopy. *Pure Appl. Chem.* **11,** 371–392 (1965).

24. Chaudhuri, D. *et al.* Enhancing long-range exciton guiding in molecular nanowires by H-aggregation lifetime engineering. *Nano Lett.* **11,** 488–492 (2011).

25. Field, J. E. & Venkataraman, D. Heterotriangulenes - Structure and Properties. *Chem. Mater.* **14,** 962–964 (2002).

26. Kivala, M. *et al.* Columnar Self-Assembly in Electron-Deficient Heterotriangulenes. *Chem. Eur. J.* **19,** 8117–8128 (2013).

27. Spano, F. C. Modeling disorder in polymer aggregates: the optical spectroscopy of regioregular poly(3-hexylthiophene) thin films. *J. Chem. Phys.* **122,** 234701 (2005).

28. Scheblykin, I. G., Sliusarenko, O. Y., Lepnev, L. S., Vitukhnovsky, A. G. & Van der Auweraer, M. Strong Nonmonotonous Temperature Dependence of Exciton Migration Rate in J Aggregates at Temperatures from 5 to 300 K. *J. Phys. Chem. B* **104,** 10949–10951 (2000).

29. Cogdell, R. J., Gall, A. & Kohler, J. The architecture and function of the light-harvesting apparatus of purple bacteria: from single molecules to in vivo membranes. *Quart. Rev. Biophys.* **39,** 227–324 (2006).

30. Oostergetel, G. T., van Amerongen, H. & Boekema, E. J. The chlorosome: a prototype for efficient light harvesting in photosynthesis. *Photosynth. Res.* **104,** 245–255 (2010).

Acknowledgements

We gratefully acknowledge financial support from the Bavarian State Ministry of Science, Research, and the Arts for the Collaborative Research Network "*Solar Technologies go Hybrid*", Deutsche Forschungsgemeinschaft (DFG) within projects GRK1640 (ATH, AI, BW, JK, HWS, RH), HI1508/2 (RH), and SFB953 "*Synthetic Carbon Allotropes"* (MK, NH). ATH would like to thank the elite study program "*Macromolecular Science*" at the University of Bayreuth and the "*Elite Netzwerk Bayern*" for a fellowship. We are indebted to Andreas Schedl, Markus Hund, and Dr. Markus Drechsler for their support with AFM and TEM.

Author contributions

ATH, KK, and HWS designed and prepared compounds **1** and **2**, and investigated their self-assembly. MK and NH synthesised the functionalised CBT core as building block for the synthesis of **1** and **2**. RH, AI, BW, and JK designed and performed optical experiments on single nanofibres. All authors contributed to the discussion of the data and writing of the manuscript.

Competing financial interest

The authors declare no competing financial interests.

Methods Section

Materials and sample preparation. The synthesis, purification, and characterization of compound **1** and reference compound **2** are described in detail elsewhere.[10] Self-assembled nanofibres of compound **1** were prepared in *ortho*-dichlorobenzene (*o*-DCB). Molecularly dissolved solutions of compound **1** were obtained in 1,1,2,2-tetrachloroethane (TCE, see SI). All solvents were used as received. The following procedures for sample preparation were employed for the various characterisation techniques:

a) Transmission Electron Microscopy (TEM): Compound **1** was heated in *o*-DCB at a concentration of 700 µM (1,000 ppm, 0.1 wt.%) until a clear orange solution was obtained. Stable gels formed upon cooling. Then a carbon-coated copper grid was dipped into the gel and *o*-DCB was removed by a filter paper.

b) Fourier-transform infra-red (FT-IR) spectroscopy: FT-IR measurements were conducted on compound **1** in *o*-DCB at a concentration of 14 mM (20,000 ppm, 2 wt.%).

c) Atomic Force Microscopy (AFM): Compound **1** at a concentration of 7 µM (10 ppm) in *o*-DCB was heated until a clear orange solution was obtained. After cooling to room temperature compound **1** was allowed to self-assemble for 24 h before spin-coating the dispersion on microscopy cover slips (Menzel, see below for details). To prepare samples with well-isolated nanofibres, self-assembled compound **1** at a concentration of 70 µM (100 ppm) in *o*-DCB was diluted to 0.07 µM (0.1 ppm) and immediately spin-coated. Finally, all samples were dried under vacuum.

d) Optical imaging and spectroscopy of single nanofibres: Isolated nanofibres for optical imaging and spectroscopy were prepared by two procedures: (i) Self-assembled compound **1** at 7 µM (10 ppm) in *o*-DCB was further diluted to 0.07 µM (0.1 ppm) in a single step without further heat treatment. This dispersion was immediately spin-coated onto microscopy cover slips (Menzel, borosilicate glass; refractive index n_e = 1.5255 at 546.1 nm; measured thickness 150 µm). (ii) Self-assembled compound **1** at 70 µM (100 ppm) in *o*-DCB was diluted to 0.07 µM (0.1 ppm) and immediately spin-coated. Finally, all samples were dried under vacuum.

Transmission Electron Microscopy (TEM). TEM images were recorded on a LEO 922 Omega electron microscope operated at 200 kV in bright-field mode.

Fourier-transform infra-red (FT-IR) spectroscopy. FT-IR spectroscopy was performed on a Digilab Division FTS-40 spectrometer using a home-built sample cell with ZnS windows and 0.5 mm path length. For the measurement a hot solution of compound **1** in *o*-DCB (14 mM, 20,000 ppm) was injected in the preheated sample cell (160 °C). The heating was turned off and the sample was allowed to slowly cool to room temperature within ~ 60 min. FT-IR measurements were conducted during the cooling process and at room temperature.

UV/vis absorption and photoluminescence (PL) spectroscopy in solution. The UV/vis spectra were recorded on a JASCO V-670 Spectrophotometer. The PL spectra were measured at room temperature on a JASCO FP-8600 Spectrofluorometer, and the PL

quantum efficiency was determined with an integrating sphere ILF-835. Hellma QS quartz-glass was used as cuvettes. Depending on the concentrations, the path length of the cuvette was adapted (10 mm or 1 mm) to avoid optical densities above 2.

Atomic Force Microscopy (AFM). AFM images were recorded on a Dimension 3100 NanoScope V (Veeco Metrology Group). Scanning was performed in tapping mode using silicon nitride cantilevers (OTESPA-R3, Bruker) with a typical spring constant of 26 Nm^{-1} and a typical resonance frequency of 300 kHz. The AFM image in Fig. S2 was taken with a Dimension Icon (Bruker) equipped with a Nano-Scope V controller. Scanning was performed in tapping mode using Si3N4 cantilevers (OMCL-AC160TS, Olympus) with a typical spring constant of 42 Nm^{-1} and a typical resonance frequency of 300 kHz. Image processing and analysis was conducted with NanoScope Analysis V1.40 software. We note that the discrepancy between the heights and the diameters of the nanofibres, as determined by AFM (2 – 2.5 nm) and TEM (5 nm), respectively, is a known phenomenon, see Refs. [17,20].

Optical imaging and spectroscopy of single nanofibres. Optical imaging and spectroscopy was performed using a home-built microscope.[31,32] The excitation source was a pulsed diode laser (LDH-P-C-450B, Picoquant; 20 MHz repetition rate, 70 ps pulse duration) that operates at a wavelength of 450 nm, where both self-assembled CBT as well as the NIBT chromophores absorb. The laser light was spatially filtered and directed to the microscope that is equipped with an infinity-corrected high-NA oil-immersion objective (PlanApo, 60x, numerical aperture NA = 1.45; Olympus). The sample was placed in the focal plane of the objective, and the sample position was controlled by a piezo-stage (Tritor 102 SG, piezosystem jena). The PL was collected by the same objective and passed a set of dielectric filters (dichroic beam splitter z460RDC, long pass filter LP467; AHF) to suppress scattered or reflected laser light.

In *imaging mode* the PL signal was imaged onto a charge-coupled device (CCD) camera (Orca-ER, Hamamatsu) by an objective lens. In this mode we employed two illumination methods: First, for widefield illumination we flipped an additional lens (widefield lens) into the excitation beam path to focus the laser light into the back focal plane of the microscope objective. This allowed for a nearly uniform illumination of a large area with ~ 70 µm

diameter in the sample plane; yet, the excitation intensity is slightly higher in the centre of the image. Thus, overview PL images of our samples can be acquired to identify single nanofibres (Fig. 3**a**). Second, for confocal illumination the widefield lens was removed and the laser light was tightly focussed to a spot with a radius of ~ 300 nm in the sample plane (section 7, SI). As the PL was still imaged onto the CCD-camera, this allowed us to visualise the spatial distribution of the PL signal from single nanofibres under local excitation conditions (Fig. 3**b**). We note that we did not investigate single nanofibres with lengths shorter than 1.5 µm in order to reduce the influence of the spatial extend of our confocal spot on the measured transport distances as much as possible.

In *spectroscopy mod*e we measured simultaneously the PL spectrum and the PL lifetime of single nanofibres using only confocal illumination. Importantly, in this mode the detected PL stems exclusively from the illuminated area on a nanofibre. This PL signal was directed to a 70/30 beam splitter cube. To record emission spectra, 70 % of the signal was focussed onto the entrance slit of a spectrograph (250IS, Bruker; 150 grooves/mm, blaze wavelength 500 nm) equipped with a back-illuminated electron-multiplying CCD-camera (iXon DV887-BI, Andor Technology). For lifetime measurements, the remaining 30 % of the PL signal were focussed onto a single-photon counting avalanche photodiode (MPD, Picoquant). The electrical signal of this detector was fed into a time-correlated single-photon counting module (TimeHarp 200, Picoquant).

For all measurements the excitation intensities were 24 W/cm2 for confocal and 0.2 W/cm2 for widefield illumination. All experiments were carried out at room temperature under ambient conditions.

Molecular modelling. The energy minimised structure of compound **1** in Fig. 2**c** was calculated using a free copy of Avogadro Version 1.1.0 with an MMFF94s force field.

References:

31. Issac, A. *et al.* Single molecule studies of calix[4]arene-linked perylene bisimide dimers: relationship between blinking, lifetime and/or spectral fluctuations. *Phys. Chem. Chem. Phys.* **14,** 10789–10798 (2012).

32. Issac, A., Hildner, R., Hippius, C., Wurthner, F. & Kohler, J. Stepwise Decrease of Fluorescence versus Sequential Photobleaching in a Single Multichromophoric System. *ACS Nano* **8,** 1708–1717 (2014).

Supporting Information to

Long-Range Energy Transport in Single Supramolecular Nanofibres at Room Temperature

Andreas T. Haedler[1], Klaus Kreger[1], Abey Issac[2†], Bernd Wittmann[2], Milan Kivala[3], Jürgen Köhler[2], Hans-Werner Schmidt[1]*, and Richard Hildner[2]*

[1] Makromolekulare Chemie I, Bayreuther Institut für Makromolekülforschung (BIMF), and Bayreuther Zentrum für Kolloide und Grenzflächen (BZKG), Universität Bayreuth, 95440 Bayreuth (Germany)

[2] Experimentalphysik IV and Bayreuther Institut für Makromolekülforschung (BIMF), Universität Bayreuth, 95440 Bayreuth (Germany)

[3] Lehrstuhl für Organische Chemie I, Department für Chemie und Pharmazie, Universität Erlangen-Nürnberg, 91054 Erlangen (Germany)

[†] Current address: Department of Physics, Sultan Qaboos University, Muscat (Oman)

Table of Content

1. TEM images and bundle size distribution of nanofibres from compound 1

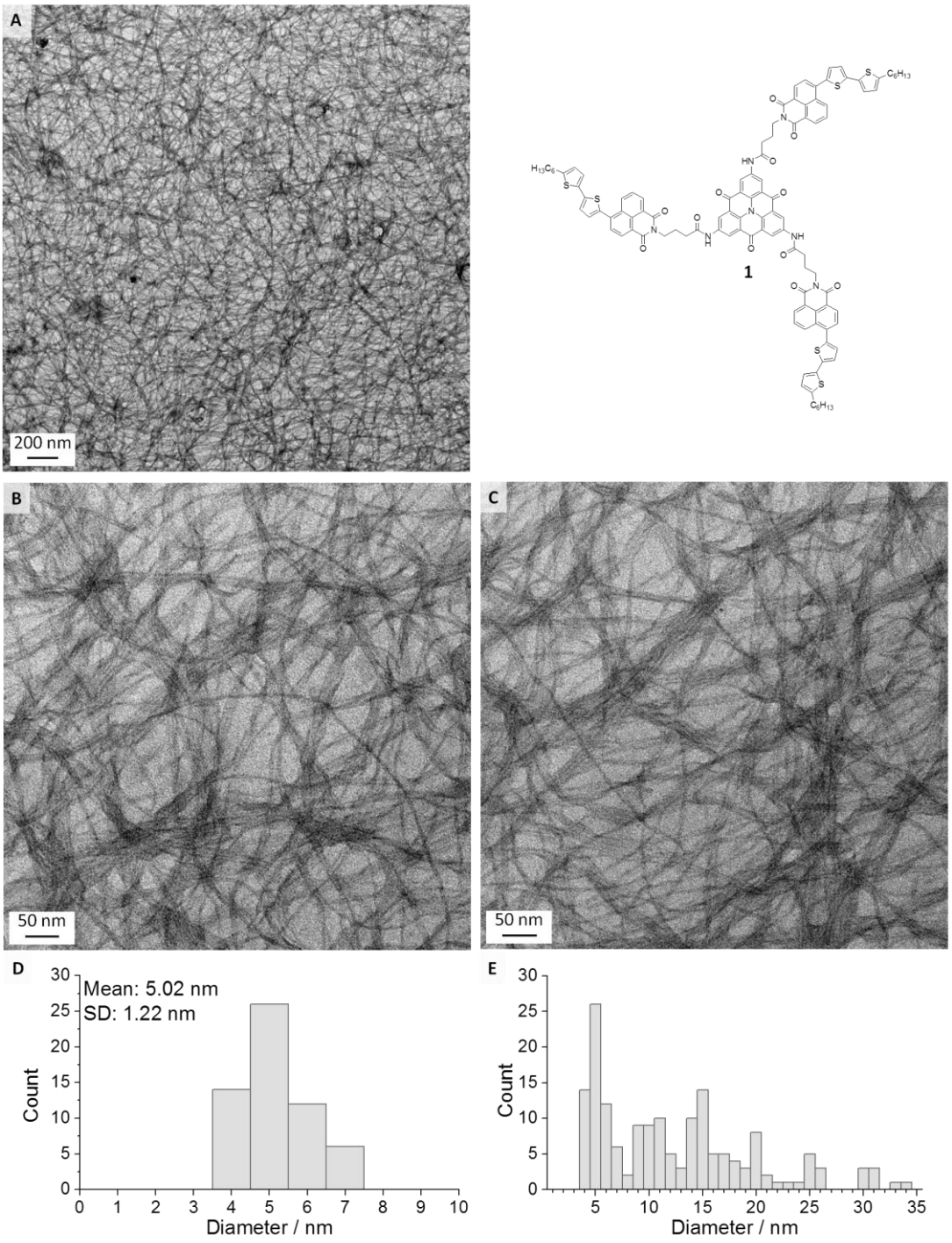

Figure S1. TEM characterisation of self-assembled nanofibres. A - C: TEM images of samples prepared from a gel of compound **1** (**A**, right) in *o*-DCB (700 µM, 1,000 ppm); **D**: Distribution of fibre widths retrieved from the narrowest structures in the TEM images (**B**,**C**), showing that the fibres possess molecular diameter. **E**: Distribution of widths determined from all structures in the TEM images (**B**,**C**), demonstrating that the widths of the structures are distributed around multiples of 5 nm.

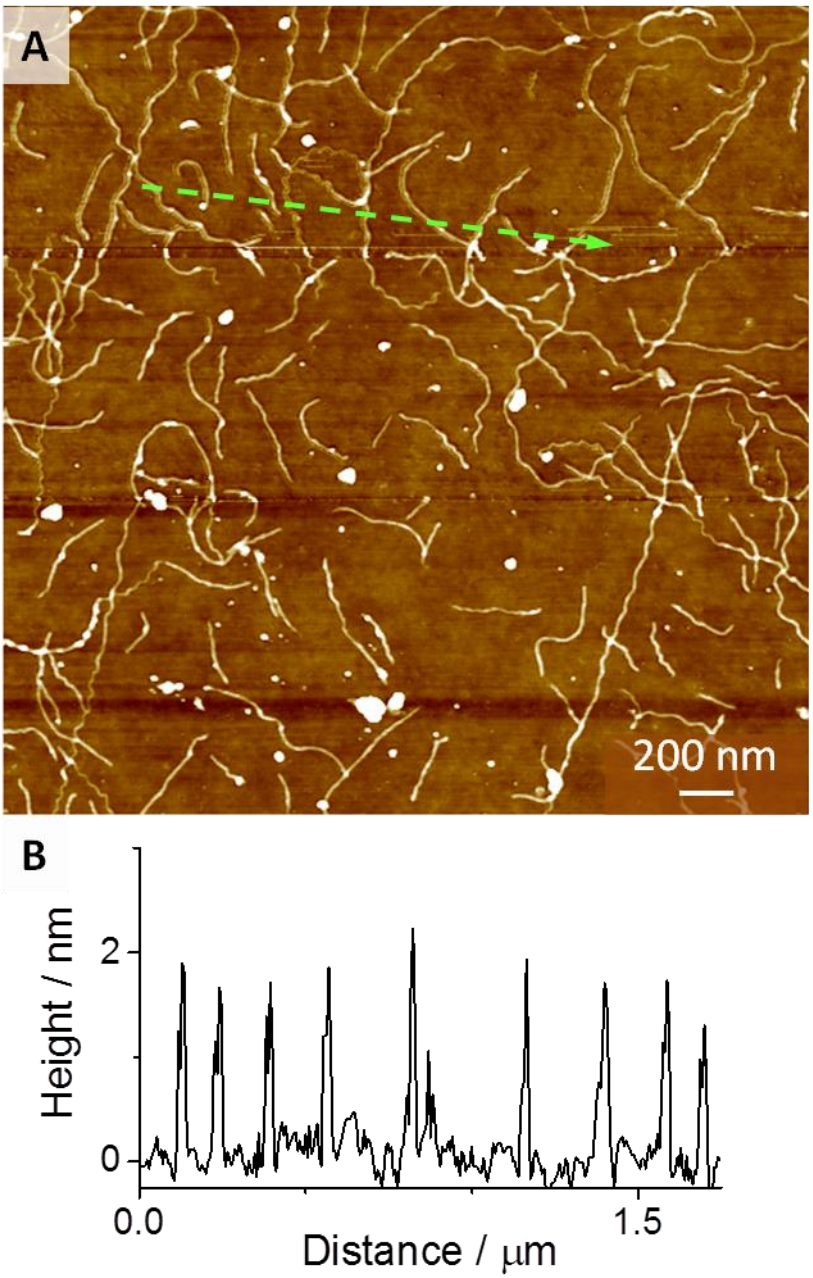

Figure S2. AFM characterisation of self-assembled nanofibres. A: AFM image (topological scan) of a self-assembled, spin-coated sample of compound **1** (7 μM, 10 ppm, in *o*-DCB). **B:** Height profile along the green dashed arrow in the AFM image, demonstrating the very uniform height distribution of individual nanofibres. The discrepancy between the diameters and heights of the nanofibres, as determined by TEM (5 nm, Fig. S1**D**) and AFM (~ 2 nm, Fig. S2**B**), is a known phenomenon.[1,2]

2. UV/vis absorption and photoluminescence spectroscopy

In order to study the π-stacking behaviour of compound **1** we recorded the optical spectra upon selfassembly in *o*-DCB (7 µM, 10 ppm). The absorption spectrum shows pronounced changes as a function of time (Fig. S3**A**). Particularly the rising band at around 380 nm (ca. 26,300 cm-1), that is strongly blue-shifted with respect to the main absorption at 450 nm, hints at the formation of H-aggregates. However, it is difficult to identify the chromophore(s) involved in the self-assembly process from these data, because the absorptions of the CBT units and the NIBT periphery overlap.[3]

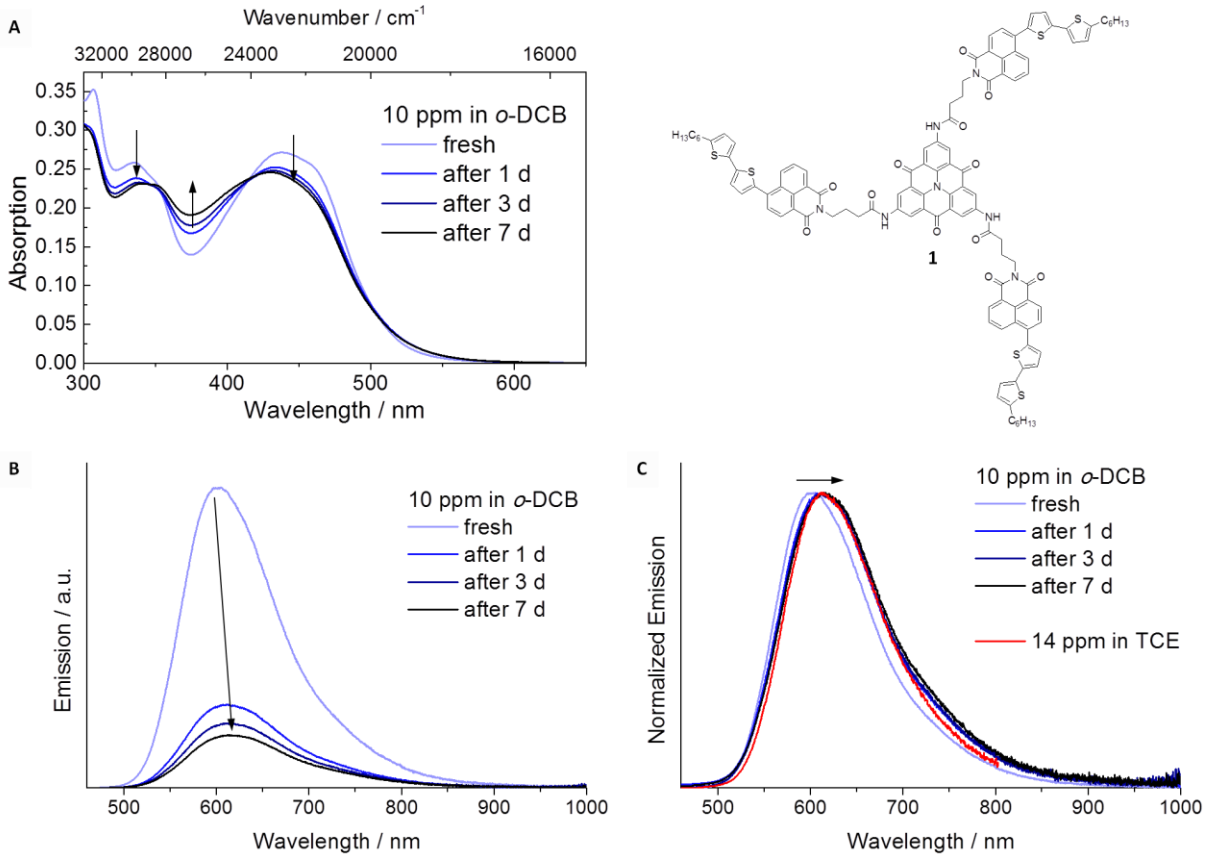

Figure S3. UV/vis absorption and photoluminescence (PL) spectra of compound 1 after ageing at room temperature. A: UV/vis absorption spectra (left) and chemical structure of compound **1** (right). **B**: PL spectra; **C**: Normalized PL spectra. The concentration of compound **1** in *o*-DCB was 7 µM (10 ppm). For comparison the PL spectrum of molecularly dissolved, non-aggregated compound **1** in 1,1,2,2-tetrachloroethane (TCE) is also shown (red line). In all spectra the main changes occur within the first 24 hours, as indicated by arrows (d: day).

The photoluminescence (PL) of self-assembled compound **1** dispersed in *o*-DCB was excited at 450 nm. The PL spectra exhibit a red-shift of ~ 20 nm and a reduction of the PL intensity as a function of time (Fig. S3**B**,**C**); yet, the spectral width and shape does not change. These spectra closely resemble those of molecularly dissolved, non-aggregated compound **1** in TCE (Fig. S3**C**, red curve). For the latter we have shown that the PL stems exclusively from the peripheral NIBT chromophores independent of the excitation wavelength, while the CBT emission is efficiently quenched by energy transfer to the NIBT units.[3] Consequently, the PL of self-assembled compound **1** dispersed in *o*-DCB originates from the periphery as well. Moreover, we do not observe new and strongly shifted emission bands in the PL spectra, indicating that the NIBT chromophores are not stacked in an ordered fashion and do not form H-aggregates. The observed time-dependent changes in the PL spectra rather result from the increased density of the NIBT chromophores upon self-assembly in *o*-DCB (i.e. from different electrostatic environments and concentration quenching). In summary, the UV/vis and PL spectra of compound **1** provide strong evidence that exclusively the CBT units form well-defined H-type aggregates in *o*-DCB, whereas the NIBT periphery is disordered. For a quantitative analysis of the H-aggregation behaviour of the CBT units, we resort to a reference compound **2**, as will be discussed below in section 4 (Fig. S5).

3. Temperature-dependent FT-IR spectroscopy

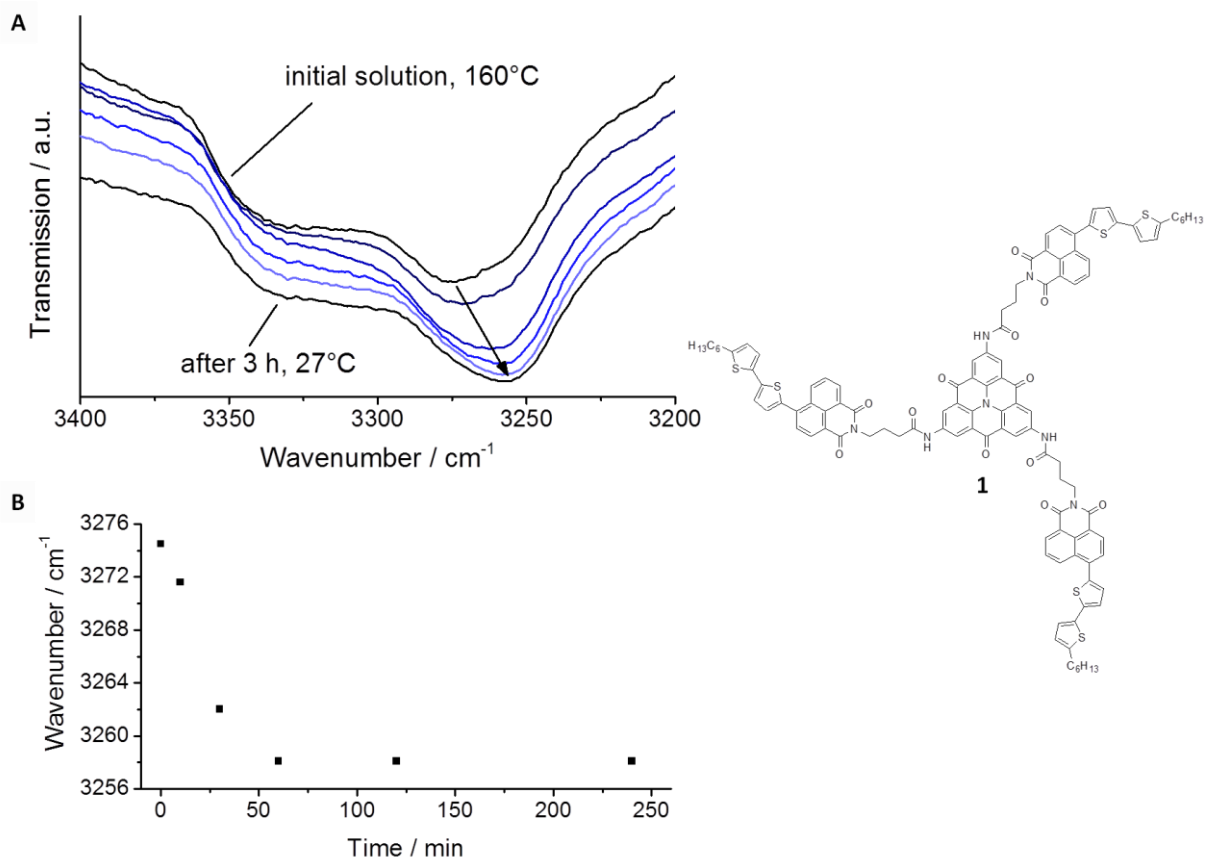

Figure S4. A: Fourier-transform infra-red (FT-IR) spectra of compound **1** dispersed in *o*-DCB (14 mM, 20,000 ppm, 2 wt.%) during cooling from 160 °C to room temperature. The N-H stretching mode shifts to smaller energies and its absorption increases as marked with an arrow. **B**: Spectral shift of the N-H stretching vibration extracted from the data in **A**. This demonstrates the formation of hydrogen bonds during self-assembly and gelation of compound **1** in *o*-DCB.

4. Excitonic coupling and radiative rate of H-aggregates of reference compound 2

Excitonic Coupling: The aggregation of aromatic π-conjugated systems gives rise to strong resonant electronic coupling between the transition dipole moments of the molecules.[4–6] In the simplest approach we can approximate the electronic structure of the non-interacting molecules by only two energy levels, the electronic ground and one excited state (Kasha-model). The interaction between such "two-level" molecules leads to a delocalisation of the excitation energy over many molecules and to the formation of exciton states, i.e. a splitting of the energies of the initially degenerate electronically excited levels over a bandwidth of $4 \cdot W$ for linear aggregates ("free exciton bandwidth", if only nearest-neighbour electronic coupling W is considered). Moreover, the transition dipole moment is redistributed among the exciton states, which is reflected by band shifts in the optical spectra of aggregates as compared to the spectra of isolated, non-interacting molecules depending on the magnitude and sign of the electronic coupling. In ideal H-aggregates the molecular building blocks are stacked cofacially, and thus their transition dipole moments are oriented parallel with respect to each other (Fig. S5**A**, top). In this arrangement only the highest-energy exciton state carries oscillator strength (i.e. is optically accessible), whereas the lower-energy exciton states are optically forbidden (Fig. S5**A**, left).[4] Consequently, for H-aggregates the absorption is blue-shifted with respect to the absorption of the non-interacting building blocks. After photoexcitation into the optically allowed highest-energy state, rapid relaxation within the exciton manifold populates the lowest-energy level. As this relaxation process is much faster than the decay into electronic ground state and as the transition from lowest-energy exciton state to the electronic ground level is dipole-forbidden, structurally perfect H-aggregates are entirely non-emissive.

However, often Kasha's two-level approximation does not hold for organic molecules because their optical spectra usually exhibit a pronounced vibronic progression due to electron-phonon coupling, i.e. coupling of electronic transitions to intra-molecular vibrations (typically carbon-bond stretch modes with energies ω_0 ~ 1,400 – 1,600 cm^{-1}), see the energy level scheme in Fig. S5**A**, right. The electron-phonon coupling strength is characterised by the Huang-Rhys parameter S. To account for the influence of electron-phonon coupling on

the excited state structure of molecular aggregates, Spano extended the exciton model and developed an approach based on one- and two-particle states (Spano-model):[7,8] A one-particle state $|n,v\rangle$ describes a vibronic excitation at molecule n, i.e. molecule n is in its electronically excited state with $v \geq 0$ vibrational quanta, and all other molecules of the aggregate are in their vibrationless electronic ground state. A two-particle state $|n,v;\ n',v'\rangle$ reflects a vibronic excitation at molecule n as above, but includes a vibrational excitation with v' (≥ 1) quanta of molecule n' ($\neq n$) in its electronic ground state.

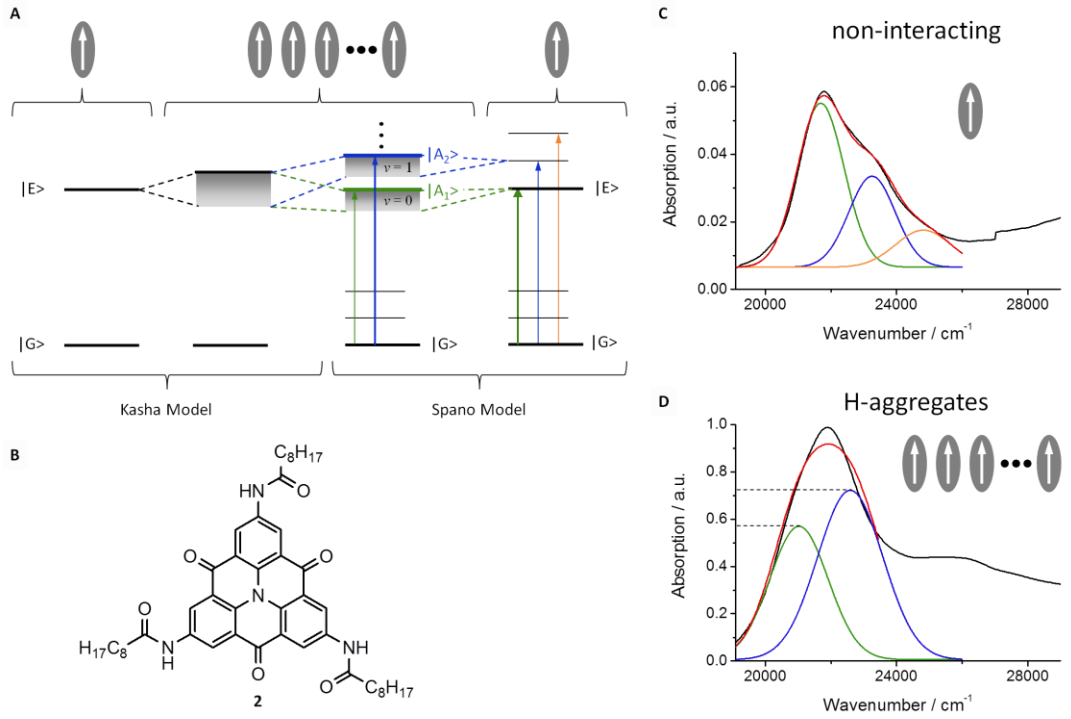

Figure S5. H-aggregates of reference compound 2. A: Energy level scheme for non-interacting molecules with two states only, the electronic ground $|G\rangle$ and electronically excited state $|E\rangle$ (left), and for a molecule with intra-molecular vibrational modes coupling to the electronic states (right). Switching on electronic interaction between the molecules, exciton bands are formed that lift the initial degeneracy of the energy levels. In the twolevel approximation (Kasha-model), only a single exciton band arises (grey box, second from left) with the optically allowed exciton state (solid line) being at the top of this band in case of an H-aggregate. Including vibrational modes in the electronically excited state (Spano-model), a progression of vibronic exciton bands is formed, separated in energy by the vibrational energy and characterised by the vibrational quantum number v. In this situation the optically accessible vibronic exciton states, labelled $|A_1\rangle$ and $|A_2\rangle$, are located at the top of each band for H-aggregates (green and blue solid line, second from right). The allowed optical transitions are indicated by coloured arrows. **B:** Chemical structure of reference compound **2**. **C:** UV/vis absorption spectrum of the non-aggregated compound **2** dissolved in TCE (3.5 µM, 5 ppm, black curve). The 0-0, 0-1, and 0-2 transitions in the spectrum are fitted by Gaussian functions (green, blue, and orange curves, see the corresponding arrows in **A**). The red curve is the sum of these Gaussian functions. **D**: UV/vis absorption spectrum of self-assembled H-aggregated compound **2** dispersed in *o*-DCB (70 µM, 100 ppm, black curve). The transitions into the $|A_1\rangle$ and $|A_2\rangle$ exciton states are fitted by Gaussian functions (green and blue curves, see the corresponding arrows in **A**), and the red curve is the sum of both Gaussian functions.

In the regime of strong electron-phonon coupling (with nearest-neighbour electronic coupling W < 1,000 cm-1 and relaxation energies $S \cdot \omega_0$ of about 1,600 cm^{-1}) a series of manifolds of so called *vibronic excitons* is formed,[7] i.e. manifolds of exciton states that are dressed by intra-molecular vibrations and separated by the vibrational energy ω_0 (Fig. S5**A**, right). In other words, the single exciton manifold for purely electronic two-level molecules splits into several manifolds of vibronic excitons, each with N states (N: number of chromophores in the aggregate) and each characterized by its vibrational quantum number v. The vibronic exciton bandwidths are strongly reduced as compared to the free exciton bandwidth of $4 \cdot W$ due to electron-phonon coupling. In the absence of disorder the vibronic excitons are delocalised over the entire aggregate. For such molecular H-aggregates the transition into the lowest-energy vibronic exciton state of *each* manifold is optically forbidden, whereas that into the highest-energy exciton states is dipole-allowed. These optically accessible excitons at the top of each manifold are labelled $|A_{i+1}>$ (i = 0, 1, …), and correlate to the 0 – i transitions of the isolated non-interacting molecules (Fig. S5**A**, right). As a consequence, the optically accessible vibronic exciton states typically show up as a progression of peaks with an energy difference of ω_0 in the absorption spectrum.

According to Spano the nearest-neighbour electronic coupling W can be determined from the intensity ratio I_1/I_2 between the two lowest-energy absorptions, corresponding to the transitions from the vibrationless electronic ground state $|G>$ into the $|A_1>$ and $|A_2>$ exciton states. This ratio decreases for increasing W, and, in that sense, the transition into the $|A_1>$ exciton state becomes optically forbidden for increasing electronic coupling. For self-assembled compound **1**, however, this approach to determine the nearest-neighbour interaction strength W between the CBT units in the fibre core is not possible, because for this compound the CBT absorption is superimposed by that of the NIBT periphery. We therefore studied the behaviour of a reference compound **2**, in which the NIBT periphery is replaced by octyl chains (Fig. S5**B**). To illustrate the effect of self-assembly of compound **2** we depict the absorption spectra in both the non-aggregated (dissolved in TCE at 3.5 µM, 5 ppm, Fig. S5**C**) and in the self-assembled state (dispersed in *o*-DCB at 70 µM, 100 ppm, Fig. S5**D**). For non-interacting molecules the spectrum exhibits a maximum at ~ 21,800 cm^{-1}, that is attributed to the transition from the singlet ground state into the the lowest excited

singlet state of CBT,[9,10] and a clearly resolved vibronic progression with a vibrational energy of about 1,500 cm^{-1}. In contrast, in the self-assembled state the absorption features a broad band centred at 22,000 cm^{-1} with a weak shoulder in the low-energy tail at ~ 21.000 cm^{-1}. The shoulder is attributed to the transition into the singlet exciton state $|A_1\rangle$ of the lowest-energy v = 0 manifold, which is weaker than the transition into the $|A_2\rangle$ singlet exciton in the v = 1 manifold at ~ 22,500 cm^{-1}, providing evidence for the formation of H-aggregates with a substantial electronic coupling between the CBTunits in reference compound **2**. Finally, an additional absorption appears in the spectrum around 26,000 cm^{-1} that is not present in the non-aggregated state. Notably, this band can also be identified at about 26,300 cm^{-1} (corresponding to ~ 380 nm) in the absorption spectrum of self-assembled compound **1** in Fig. S3**A**.

Quantitatively, the excitonic coupling W between nearest neighbours in H-aggregates can be determined from the absorption spectrum from the peak intensity ratio I_1/I_2 for the transitions into the singlet exciton states $|A_1\rangle$ and $|A_2\rangle$ according to equation (1):[8]

$$\frac{I_1}{I_2} = \frac{n_1}{n_2} \cdot \frac{\left(1 - \frac{2W}{\omega_0} e^{-S} \sum_{v>0} \frac{S^v}{v!\, v}\right)^2}{S \cdot \left(1 - \frac{2W}{\omega_0} e^{-S} \sum_{v\neq 1} \frac{S^v}{v!\, (v-1)}\right)^2} \qquad (1)$$

Here, S denotes the Huang-Rhys parameter, ω_0 the energy of the vibrational mode coupling to the electronic transition, and v the vibrational quantum number. The refractive indices n_1 and n_2 of the solvent at the spectral positions of the transitions into the exciton states $|A_1\rangle$ and $|A_2\rangle$, respectively, are neglected in the following, which is justified because their ratio is of the order of 1. Note that S and ω_0 have to be determined from the absorption spectra of the non-aggregated reference compound **2**. These parameters represent effective values, because the vibronic absorption peaks of organic molecules typically involve several closely-spaced, and thus unresolved, vibrational modes.

To retrieve S and ω_0, we fitted the sum of three Gaussian functions to the spectrum of the non-interacting reference compound **2** (Fig. S5**C**; green, blue, orange curves). We find S = 0.6 and ω_0 = 1,563 cm^{-1}, which is in the range of aromatic C=C bond stretch vibrations. Subsequently, the absorption spectrum of the H-aggregated reference compound in *o*-DCB

was fitted with the sum of two Gaussian functions keeping ω_0 = 1,563 cm^{-1} fixed (Fig. S5**D**; green, blue curves). The best fit yielded I_1/I_2 = 0.79, and with equation (1) the nearest-neighbour electronic coupling between CBT units is then calculated to W = 350 cm^{-1} (corresponding to 44 meV).

The CBT units of both the reference compound **2** and compound **1** are structurally identical, and hence their cofacial stacking behaviour into H-aggregates and the nearest-neighbour electronic coupling W should be essentially identical as well. The value W = 350 cm^{-1} for the electronic interaction represents a lower boundary only. Owing to the small intermolecular distances between adjacent CBT units (~ 0.35 nm) in an aggregate, also next-nearest neighbour interactions are likely to contribute substantially to the total coupling.

Finally, we note that the electronic coupling of ~ 350 cm^{-1} between the H-aggregated CBT units puts our nanofibres into the limit of "weakly coupled H-aggregates" according to Spano's notation, because W is smaller than the relaxation energy $S\cdot\omega_0$.[7,8] On the other hand, our value for W is, within a factor of the order unity, essentially identical to the magnitudes of the *strongest* electronic couplings in natural and artificial supramolecular structures. For instance, in photosynthetic lightharvesting systems those values vary between ~ 300 and 800 cm^{-1},[11,12] and similar numbers were reported for J-aggregates based on small organic molecules.[1,13] In this sense, the electronic coupling between the CBT units in the nanofibres' H-aggregated core is substantial, i.e. 'strong enough' to allow for delocalisation of electronic excitations and thus coherent transport (see section 6, below).

Radiative Rates: A change of the radiative rate of the lowest-energy excited state of the H-aggregated CBT units in the nanofibres is related to a change of the corresponding transition dipole moment. In order to provide an estimate for these changes, we measured the PL quantum efficiency (PL-QE) as well as the excited state lifetime of the H-aggregated reference compound **2** dispersed in *o*-DCB at a concentration of 70 µM (100 ppm). The PL-QE was determined to be below 1 % using an integrating sphere. The PL decay was recorded by time-correlated single photon counting and features a non-exponential behaviour, Fig. S6, with time constants t_i (relative amplitudes F_i) of t_1 = 3.1 ns (F_1 = 0.45) and t_2 = 0.7 ns (F_2 = 1).

The radiative rate $k_{r,agg}$ of self-assembled compound **2** is given by the ratio between the PL-QE and the amplitude average lifetime[14,15]

$$t_{av} = \frac{\sum F_i t_i}{\sum F_i} = 1.44\ ns \qquad (2)$$

which yields $k_{r,agg}$ = 6.9·10^6 s^{-1}. For the non-aggregated (molecularly dissolved) compound **2** in TCE we recently reported a PL-QE of 15 % and an excited state lifetime of 2.5 ns,[3] which translates into a radiative rate $k_{r,iso}$ = 6·10^7 s^{-1}. Thus, upon formation of H-aggregates the radiative rate of compound **2** decreases by about one order of magnitude, which is associated mainly with the "forbidden" purely electronic transition from the lowest-energy excited state into the vibrationless electronic ground state.[7,8] This purely electronic transition is entirely forbidden for ideal H-aggregates, but becomes weakly allowed in the presence of disorder. Transitions into vibrational levels of the ground state remain allowed, because the momentum conservation required for these vibronic transitions is satisfied by the simultaneous excitation of one or more vibrational quanta in the electronic ground state.

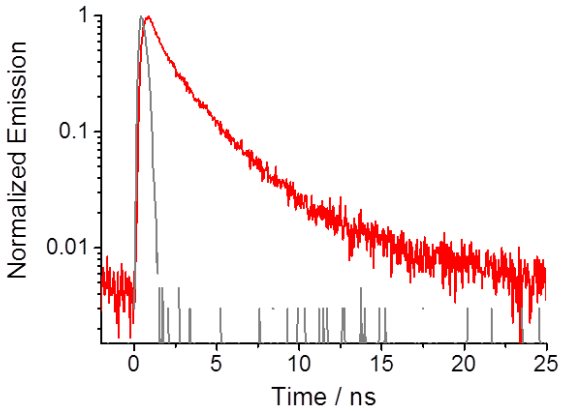

Figure S6. PL lifetime of self-assembled reference compound 2: Red: PL decay curve of reference compound **2** dispersed in *o*-DCB at a concentration of 70 µM (100 ppm). Grey: Instrument response function (IRF).

To conclude, we note that reference compound **2** is an ideal system to investigate the π-stacking behaviour of the CBT units with three amide groups at 2, 6, and 10 positions by photophysical methods. However, for this compound **2** we were so far not able to obtain extended and isolated nanofibres with molecular diameter. For the µm-long nanofibres based on compound **1** we expect the radiative rate of the core to decrease by more than one order of magnitude, because the number of monomers in the H-aggregates is an important factor for the radiative rate as well.[8]

5. Single nanofibres: Structural, optical, and spectroscopic characterisation

AFM images of single nanofibres: Fig. S7 shows AFM images of samples that were prepared by spin-coating self-assembled compound **1** dispersed in *o*-DCB at a concentration of 0.07 µM (0.1 ppm) on microscopy cover slips. The large 40x40 μm^2 image in Fig. S7**A** demonstrates the presence of several nanofibres (within the red ellipses) with different lengths and spatial separations of some µm, which is in very good agreement with the optical PL images upon widefield illumination (see Figs. 3**a**, S8**A**, S8**D**). We note that the larger and randomly distributed circular structures in Fig. S7**A** are artefacts on the surface of the microscopy cover slips, as verified by measurements on a microscopy cover slip without spin-coated nanofibres in Fig. S7**B**.

Fig. S7**C** depicts an AFM image of a different sample (prepared under the same conditions described above) with two neighbouring nanofibres in the red boxed area. Repeated AFM scans of this area with higher resolution (Figs. S7**D-F**) clearly demonstrate the robustness of our nanofibres. The corresponding height profiles (Fig. S7**E**,**F**) provide evidence for the presence of single, spatially isolated nanofibres with molecular diameter on such samples.

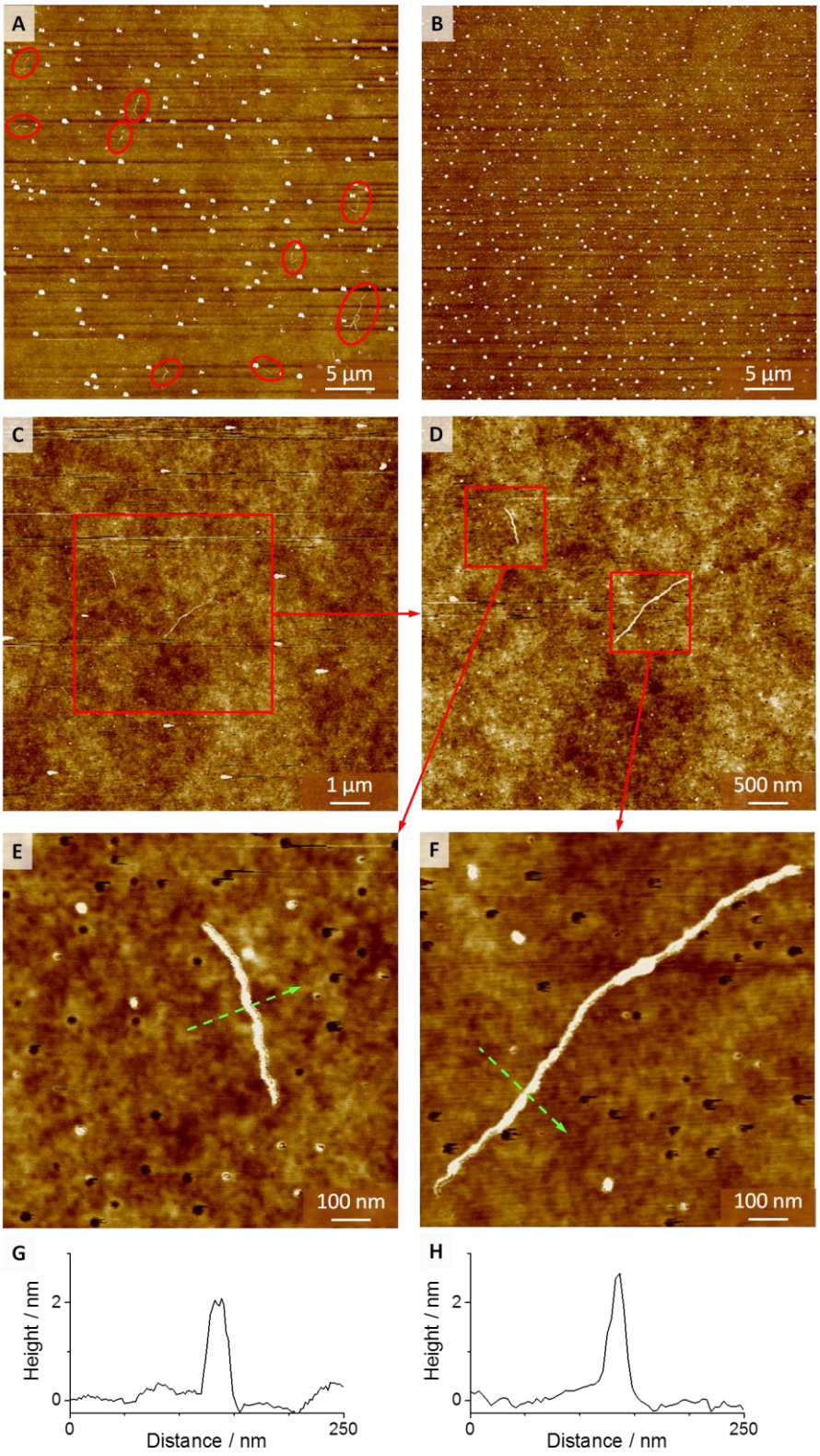

Figure S7. AFM characterisation of individual nanofibres. A: AFM image (topological scan) of a sample prepared by spin-coating self-assembled compound **1** dispersed in *o*-DCB (0.07 µM, 0.1 ppm**)**. The red circled areas enclose individual nanofibres. **B:** AFM image of a microscopy cover slip without nanofibres. **C-F:** Higher-resolution AFM images demonstrating the presence of single, spatially well-separated nanofibres (red boxes). **G,H:** Height profiles across the dashed green arrows in **E** and **F**, respectively. We note that the AFM images in **A** and **C-F** have been measured on different samples.

Optical imaging of single nanofibres: Figs. S8**A**-**C** display a nanofibre that exhibits energy transport over its entire length of 3.5 µm. Figs. S8**D**-**F** depict an example for a nanofibre, where the energy transport does not occur along the entire structure: Whereas in the PL image upon widefield illumination the fibre appears with a length of 5.8 µm (Fig. S8**E**), upon local (confocal) illumination at the bottom right end energy is transported only up to 3.6 µm (Fig. S8**F**). We suggest that the energy transport is interrupted due to a larger structural defect of the fibre core (likely introduced by the rather harsh spin-coating process during sample preparation). For instance, a small gap of a few nm between two adjacent CBT units strongly reduces the electronic coupling across the gap, which is sufficient to prevent further energy transport along the fibre. Using widefield illumination, however, such a nm-sized gap is too small to be optically resolved.

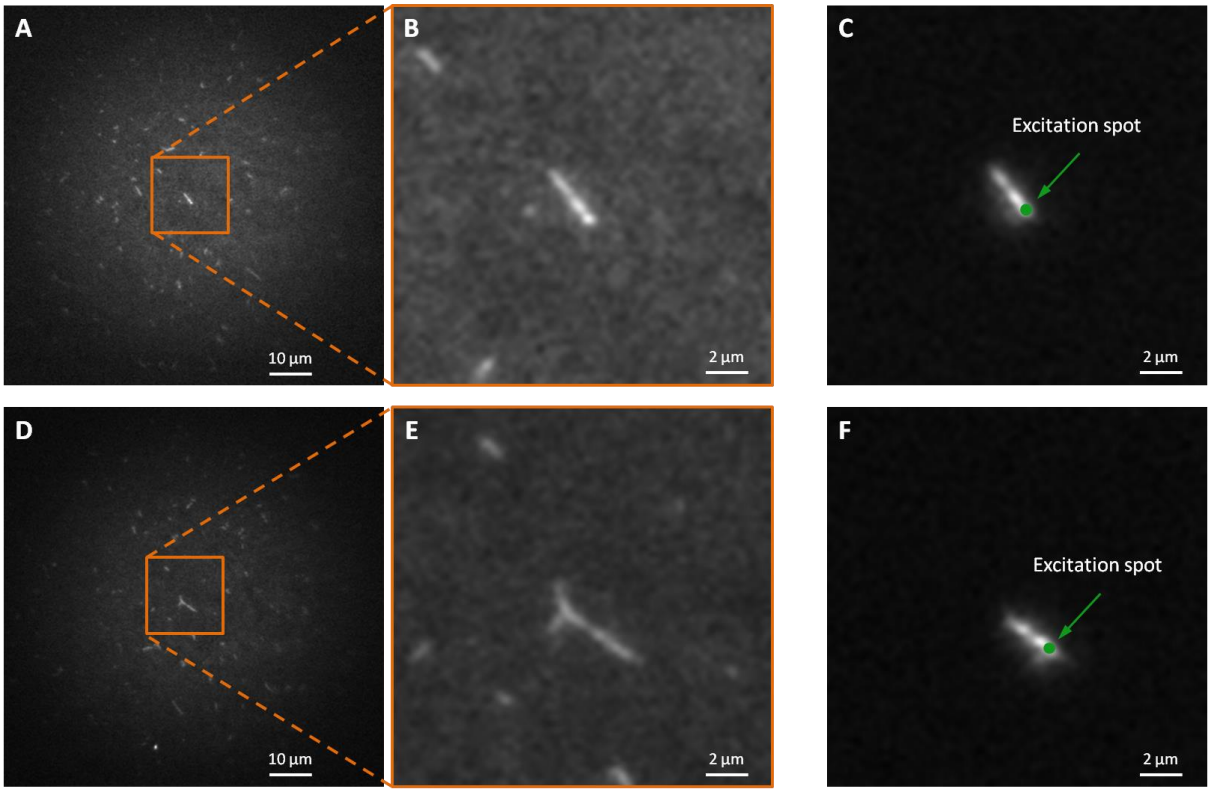

Figure S8. Optical imaging of single nanofibres. A,D: PL images upon widefield illumination of a sample prepared by spin-coating self-assembled compound **1** dispersed in *o*-DCB (0.07 µM, 0.1 ppm). **B,E**: Expanded views of the orange-boxed areas in **A** and **D**, respectively. **C,F**: PL images of the fibres shown in **B,E** upon confocal illumination at the bottom right end (green circle), demonstrating energy transport over macroscopic (µm) distances. The example shown in **D**-**F** represents a situation where energy transport does not occur along the entire fibre but is interrupted due to (probably structural) defects on the fibre that are not visible in the widefield PL image.

In order to prepare isolated single nanofibres for optical imaging we used two methods (see Methods section for details): Self-assembled compound **1** at a concentration of either 70 µM (100 ppm) or 7 µM (10 ppm) in *o*-DCB was diluted to 0.07 µM (0.1 ppm) before spin-coating. For these preparation methods we separately analysed the fibre lengths, determined from PL images upon widefield illumination, and the transport distances, retrieved from PL images upon local illumination, see Fig. S9. These histograms demonstrate that there is essentially no difference in fibre lengths and transport distances between nanofibres prepared initially from a 7 µM (10 ppm) solution (Fig. S9**A**) and from a 70 µM (100 ppm) solution (Fig. S9**B**). Consequently, we have merged the histograms in Fig. S9 to obtain the distributions of fibre lengths and transport distances in Fig. 3**c** of the main manuscript. We note that the accuracy for the determination of the fibre lengths and transport distances is about 0.3 µm, corresponding to the pixel size of the CCD camera (6.45 µm) divided by the magnification of the microscope (23.5).

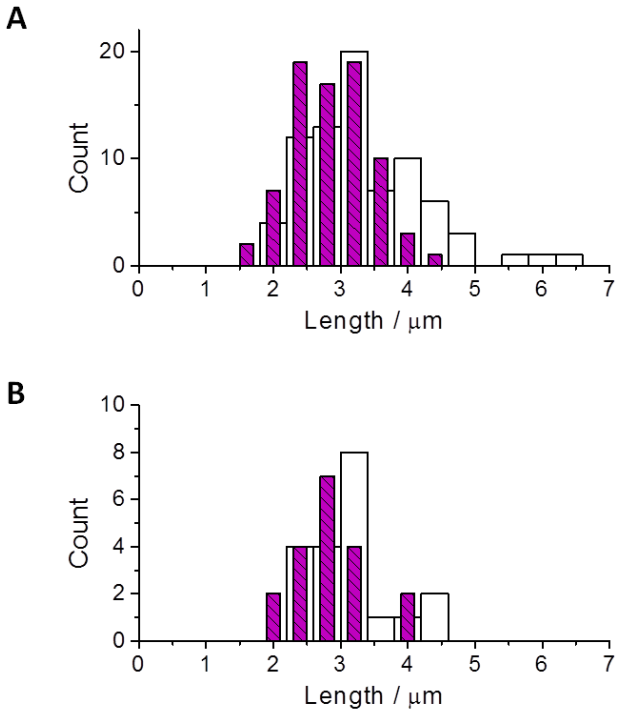

Figure S9. Nanofibre lengths and transport distances. Open bars: distributions of fibre lengths determined from PL images upon widefield illumination; violet bars: distribution of transport distances along single nanofibres retrieved from PL images upon confocal illumination. **A**: Single nanofibres prepared by diluting selfassembled compound **1** at 7 µM (10 ppm) in *o*-DCB to 0.07 µM (0.1 ppm) before spin-coating. **B:** Single nanofibres prepared by diluting self-assembled compound **1** at 70 µM (100 ppm) *o*-DCB to 0.07 µM (0.1 ppm) before spin-coating.

Steady-state and time-resolved spectroscopy of single nanofibres: PL spectra of two different single nanofibres are presented in Fig. S10**A** together with the PL spectrum of compound **1** dispersed in *o*-DCB (7 µM, 10 ppm, red curve). For the acquisition of these spectra we used an excitation wavelength of 450 nm, where both self-assembled CBT and NIBT absorb. As discussed above in section 2 of this SI, the PL of compound **1** in *o*-DCB stems exclusively from the peripheral NIBT chromophores, that are either directly excited or populated by energy transfer from the core upon photoexcitation of CBT.[3] As the spectra of the nanofibres are very similar in width and shape to that of compound **1** in *o*-DCB solution, we ascribe the emission of single nanofibres to PL from the NIBT periphery as well. The blue-shift of about 20 nm of the nanofibre spectra with respect to the solution spectrum is attributed to the different dielectric environment for the NIBT units in nanofibres (measured at a glass-air interface) and in *o*-DCB, respectively.

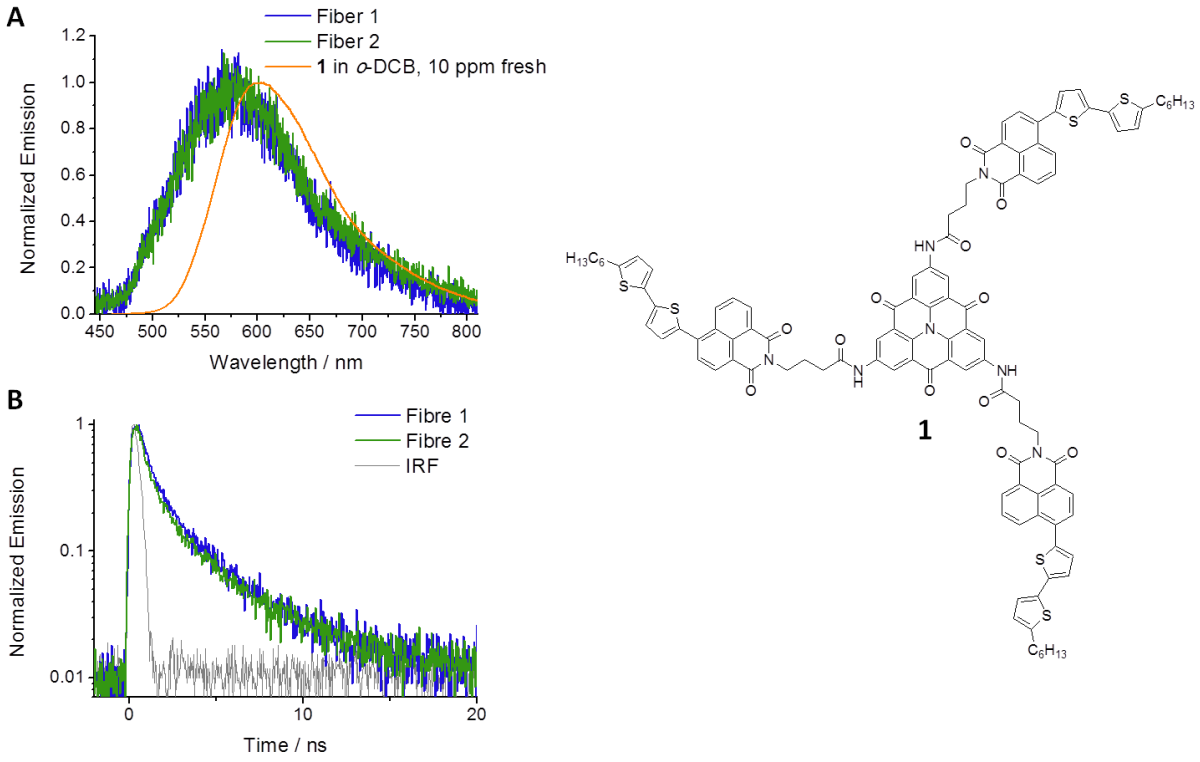

Figure S10. Steady-state and time-resolved spectroscopy of individual nanofibres. A: PL spectra of single nanofibres (green and blue curves) and of self-assembled compound **1** in *o*-DCB (7 µM, 10 ppm, red curve). **B**: PL decay curves of the same individual nanofibres as in **A**. IRF: instrument response function.

Moreover, these data demonstrate that the NIBT periphery is not well ordered and does not form structurally defined aggregates in the nanofibres, because new spectral bands are not observed (see also section 2, SI). This interpretation is further corroborated by excited state lifetime measurements of individual nanofibres (Fig. S10**B**). The PL decay curves are clearly not mono-exponential and can only be fitted by a sum of 2 or 3 exponential functions with good accuracy. This nonexponential behaviour is probably related to structural relaxation in the excited state of the NIBT chromophores prior to photon emission. To quantify the excited state lifetime we use the intensity average lifetime defined below in section 6, which yields about 2.4 ns. This number is in good agreement with the value of 2.3 ns for non-interacting compound **1** in TCE.[3]

We note that in our PL decay curves we do not observe a rising component that may be associated with energy transport along the core and with (incoherent) energy transfer from CBT to the NIBT periphery. This can be attributed to experimental limitations: Our setup requires that we record the PL decay curves of single nanofibres from the same spatial position where we illuminate them. Hence, in these measurements we will be only sensitive to transport distances of ~ 300 nm along the core, which corresponds to the radius of our confocal spot, see Fig. S11**A**. For coherent transport over 300 nm a time scale of some 10 ps can be estimated (see below section 6 for details). In this context we note that Dubin *et al.* provided an even shorter time scale of a few ps for coherent transport on > 10 µm long polydiacetylene single chains in their own monomer matrix at cryogenic temperatures.[16] Moreover, the incoherent transfer step from the core of the nanofibres to the NIBT periphery is likely to take place within 1 – 10 ps, because we were not able to resolve this transfer time in recent experiments on molecularly dissolved, non-aggregated compound **1**.[3] Given these short time constants and the limited time resolution of our setup of some 100 ps (the full width at half maximum of the instrument response function, IRF see Fig. S10**B** grey curve, is ~ 500 ps), a rising component can not be resolved in our experiments on single nanofibres.

6. Coherent versus incoherent exciton transport along single nanofibres

In order to elucidate the nature of the transport of electronic excitations (singlet excitons) along the H-aggregated core of single nanofibres, we consider the limiting cases of entirely coherent and fully incoherent (diffusive) motion.

For coherent transport along the core we assume that the CBT units possess identical transition energies. The time constant for a full population oscillation between adjacent CBT units is then determined by the inverse magnitude of the electronic coupling *W* (see Ref. [17])

$$\tau_{coh} = \frac{1}{W[cm^{-1}] \cdot 3 \cdot 10^{10}} s \tag{3}$$

With *W* = 350 cm^{-1} we obtain τ_{coh} ~ 100 fs. In order to translate this number into an unidirectional 'coherent' transport distance L_{coh} we use the π-stacking distance of 0.35 nm and the intensity average lifetime[15] of self-assembled reference compound **2** (only CBT) of $\tau_{av} = \frac{\sum F_i t_i^2}{\sum F_i} = 2.3\ ns$ (see Fig. S6: the time constants t_i and relative amplitudes F_i of the non-exponential decay of self-assembled compound **2** are t_1 = 3.1 ns, F_1 = 0.45, t_2 = 0.7 ns, F_2 = 1). Hence, about 23,000 'coherent jumps' between CBT units are possible, which corresponds to L_{coh} = 8 µm. We note that the values for the electronic coupling *W* and the excited state lifetime τ_{av} are lower limits only (see section 4, SI), i.e. the number for τ_{coh} is an upper bound and that for L_{coh} is a lower bound.

Entirely incoherent motion is described by a one-dimensional diffusive process with a diffusion constant *D* and a transport length[18]

$$L_{inc} = \sqrt{2D\tau_{av}} \tag{4}$$

Diffusion constants between 0.1 cm^2/s and 1.2 cm^2/s have been reported for molecular J-aggregates at room temperature.[1,19] Using those numbers together with τ_{av} = 2.3 ns of self-assembled reference compound **2** we obtain L_{inc} ~ 215 – 740 nm. We note that the diffusion constants for the J-aggregates are rather high, because even in the purest molecular crystals at cryogenic temperatures *D* was found to be at most ~ 0.1 cm^2/s,[18,20–22] i.e. the values for L_{inc} are very likely to represent upper limits.

These estimates clearly illustrate that the transport of electronic excitations along the nanofibres' core cannot be described by incoherent hopping processes alone. Yet, entirely coherent transport is unlikely as well, because in a real system disorder is unavoidably present and will limit the maximum coherent transport distances. We therefore suggest a combined coherent – incoherent transport mechanism along the nanofibres: Owing to the substantial electronic coupling between the CBT units, the excitation energy is largely delocalised over domains along the core, i.e. coherently shared by many CBT units (up to many hundred[23]), which is termed coherent transport. Between these domains incoherent hopping of electronic excitations occurs. We propose that the boundaries of the domains are defined by small structural imperfections of the fibre core, as detailed in the manuscript (see Fig. 3**e**, at those positions excitation energy can probably also leak from the core to the periphery, giving rise to the observed PL from single nanofibres). The mismatch between the measured transport distances (> 1.6 µm, Fig. 3**c**) and the incoherent transport distances estimated above (< 740 nm) strongly indicates that the coherent contribution to the transport dominates.

A more thorough theoretical description of combined coherent and incoherent motion of excitons was developed by Haken and Reineker,[21] Grover and Silbey,[24] and Kenkre and Knox[25] to model the transport in highly ordered molecular crystals. Here we use the framework of Haken and Reineker mainly for two reasons: First, their approach allows to determine the nature of the transport from spectroscopic and structural data that are available from our work. Second, it was explicitly modelled for a linear chain in the presence of diagonal and off-diagonal disorder. According to Haken and Reineker the criterion for predominantly coherent motion along a linear chain is[21]

$$\frac{W^2}{\gamma_0 + 3\gamma_1} > 2\gamma_1 \tag{5}$$

where γ_0 and γ_1 are measures for the fluctuations in the site energies and the electronic coupling, respectively. For the derivation of this expression only nearest-neighbour electronic coupling *W* between the building blocks as well as uncorrelated fluctuations in the molecules' site energies and electronic couplings was assumed. The left-hand side of

equation (5) describes coherent (band-like) motion of excitons, while the right-hand side represents the incoherent (Forster-type hopping) contribution to the exciton transport.

The parameter γ_0 can be estimated by the half width at half maximum of the purely electronic (0-0) transition of the absorption spectrum of reference compound **2** (only CBT) dissolved in TCE. From the fits in section 4 of this SI we obtained a line width of ~ 1200 cm^{-1} (full width at half maximum), thus γ_0 ~ 600 cm^{-1}. The parameter γ_1, i.e. the fluctuations in the electronic coupling, is determined by deviations from the ideal geometry of the aggregate. Here only small effects are to be expected, because the π-stacking and the three-fold symmetric hydrogen-bonding between adjacent CBT units yield a rather rigid structure. To provide an estimate for γ_1, we use the point-dipole approximation, in which the electronic coupling between two neighbouring CBT units is given by

$$W = \frac{1}{4\pi\varepsilon_0} \cdot \left[\frac{\overrightarrow{\mu_m} \cdot \overrightarrow{\mu_n}}{\left|\overrightarrow{R_{mn}}\right|^3} - \frac{3 \cdot \left(\overrightarrow{\mu_m} \cdot \overrightarrow{R_{mn}}\right) \cdot \left(\overrightarrow{\mu_n} \cdot \overrightarrow{R_{mn}}\right)}{\left|\overrightarrow{R_{mn}}\right|^5} \right] \tag{6}$$

with $\overrightarrow{\mu_i}$ being the transition dipole moment of the ith CBT unit and $\overrightarrow{R_{mn}}$ the centre-to-centre connecting vector with $\left|\overrightarrow{R_{mn}}\right|$ = 0.35 nm the π-stacking distance. There are essentially two possible deviations from the ideal geometry of the fibre core: First, the molecular planes of neighbouring CBT units, and thus their transition dipole moments, are not parallel with respect to each other but are slightly tilted. However, the three-fold symmetric hydrogen bonding between neighbouring CBT units provides a rigid frame and allows only for very small tilt angles. We neglect this contribution, because the cosine of this angle entering in equation (6) is a rather flat function for small angles. Second, there can be a variation in the distance between the CBT units. For a similar supramolecular building block, a benzenetrisamide with a planar aromatic core and three hydrogenbonding amide groups, the π-stacking distance was found to vary within ± 0.05 Å.[26] For our system, we conservatively estimate this variation to ± 0.1 Å. The cubic dependence of *W* on the distance in equation (6) gives rise to a change in *W* by about ± 10 %, yielding γ_1 ~ 35 cm^{-1}.

Using *W* = 350 cm^{-1} together with the values for γ_0 and γ_1 we find that the criterion in equation (5) is met, with the coherent (left) term being larger than the incoherent (right)

term (170 cm^{-1} *vs.* 70 cm^{-1}). In other words, coherent transport along the nanofibres dominates, yet, with some contribution of incoherent motion, in agreement with the picture detailed above.

In this context, it is important to realise that the incoherent transport steps between the domains of the nanofibres' core (as well as from the core to the periphery) cannot be described by a simple dipole-dipole picture. The large delocalisation of electronic excitations along the core gives rise to a substantial contribution of transitions, that are optically forbidden or that possess a reduced transition dipole moment, to the transport within supramolecular aggregates. This is illustrated for instance in the photosynthetic light-harvesting antenna proteins LH2 of purple bacteria, in which dark exciton states contribute to the transport within these complexes.[11,27]

Finally, we emphasise that a direct evidence for partially coherent transport, i.e. delocalisation of electronic excitations, along the core of the nanofibres is provided by the change of the absorption spectra of reference compound **2** upon self-assembly (see Fig. S5). As shown in section 4, these changes reflect the formation of vibronic singlet excitons, i.e. delocalised electronic excitations that are dressed with intra-molecular vibrations. Our interpretation of a combined coherent – incoherent transport is in agreement with literature data on other self-assembled nanostructures, in which transport distances of up to 150 nm have been interpreted to arise from some coherent contribution.[1,13,19,28,29] Other experimental approaches to distinguish between coherent and incoherent transport, such as temperature-dependent measurements,[13] are not useful for our system, because for most fibres the transport distances are already determined by their lengths at room temperature. Hence, working at lower temperature, which will probably strengthen the coherent contribution, will not improve transport distances. Another alternative are interferometric PL measurements,[16] which are unfortunately not feasible for our nanofibres. As discussed above, incoherent motion between coherent domains along the core and from the core to the periphery is involved in the transport along the nanofibres. These incoherent steps randomise phase information and thus wash out interference patterns in the photoluminescence of the peripheral NIBT units.

7. Control Experiments

We have performed several control experiments in order to verify that upon confocal excitation of single nanofibres their elongated PL signal stems from long-range energy transport and not from direct illumination of the entire fibre. We note that we used excitation intensities between 14 and 24 W/cm^2 for the control experiments shown below, i.e. intensities very close to those used for the measurements on isolated nanofibres.

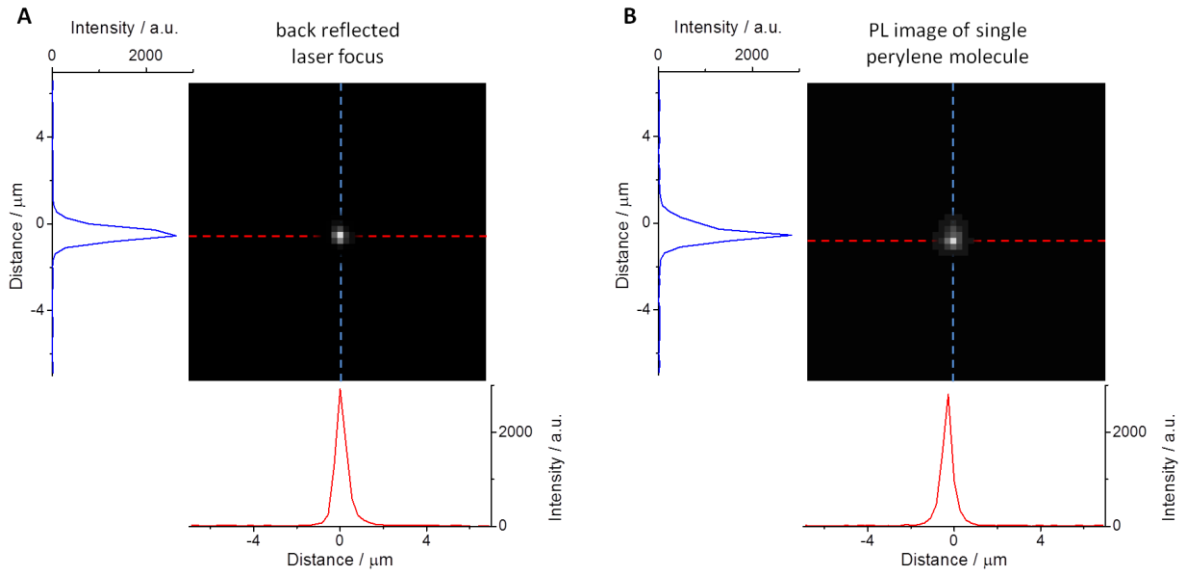

Figure S11. Control experiment I. A: PL image of the laser focus back-reflected from a microscopy cover slip and imaged onto the CCD camera. **B**: PL image of a single perylene molecule upon confocal excitation. From both images lateral profiles (red and blue curves) were retrieved along the dashed lines in the CCD-images.

Fig. S11**A** shows an image of the laser light (wavelength: 450 nm) that was focussed by our high-NA objective onto a microscopy cover slip, back-reflected at the glass – air interface, and imaged onto the CCD camera (see Methods Section for details). Fig. S11**B** depicts a PL image of a single dye molecule (perylene bisimide) upon confocal excitation. We retrieved intensity profiles along the dashed lines from both images. Gaussian fits to the profiles reveal that both the back-reflected laser focus and the single-molecule PL exhibit a radius of < 350 nm (half width at half maximum, HWHM; both images are slightly asymmetric, we have given the larger value for the radius). This radius is about a factor of two larger than theoretically predicted, $r = 0.51 \cdot \lambda / \mathrm{NA} \sim 160$ nm,[30] which is mainly due to aberrations introduced by the cover slip thickness (the measured thickness is ~ 150 µm, whereas the

objective is corrected for 170 µm).[31] However, this radius is still substantially smaller than the shortest nanofibres measured, see Fig. 3**c**.

In order to exclude direct excitation of a photoluminescent object, that is located substantially off the centre of the confocal excitation spot, we moved a single perylene molecule within the focal plane of the objective laterally across the laser focus in steps of 100 nm by means of the piezo stage of our microscope. For each position we recorded the PL image of the single molecule with the CCD camera. The peak PL signal of the single molecule in each image is displayed in Fig. S12. These data demonstrate that the PL signal drops to ~ 10 % of the maximum value upon moving the molecule by 200 nm away from the centre of the excitation spot.

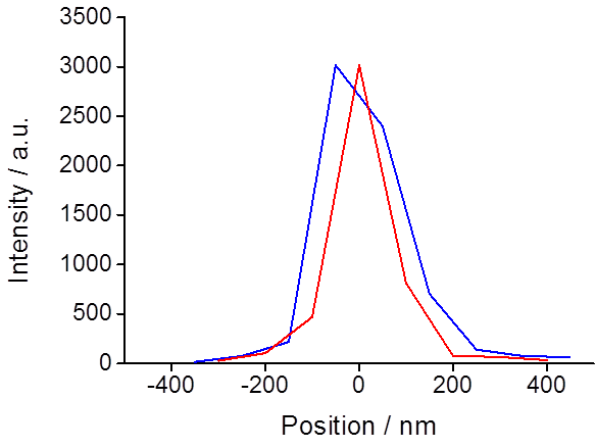

Figure S12. Control experiment II. Peak PL signal of a single perylene molecule in CCD-images while the molecule is moved through the confocal excitation spot along the two perpendicular directions (red and blue curve) in the focal plane of the objective.

We stress that we did not investigate transport along single nanofibres that are shorter than 1.5 µm (see the histogram in Fig. 3**c**) in order to reduce the influence of the spatial extend of the excitation spot as much as possible.

8. References

1. Eisele, D. M., Knoester, J., Kirstein, S., Rabe, J. P. & Vanden Bout, D. A. Uniform exciton fluorescence from individual molecular nanotubes immobilized on solid substrates. *Nat. Nanotech.* **4,** 658–663 (2009).
2. Zhang, W. *et al.* Supramolecular Linear Heterojunction Composed of Graphite-Like Semiconducting Nanotubular Segments. *Science* **334,** 340–343 (2011).
3. Haedler, A. T. *et al.* Synthesis and photophysical properties of multichromophoric carbonylbridged triarylamines. *Chem. Eur. J.* **20,** 11708–11718 (2014).
4. Kasha, M., Rawls, H. R. & Ashraf El-Bayoumi, M. The Exciton Model in Molecular Spectroscopy. *Pure Appl. Chem.* **11,** 371–392 (1965).
5. Pope, M. & Swenberg, C. E. *Electronic Processes in Organic Crystals and Polymers*. (Oxford University Press, Oxford, New York, 1999).
6. Davydov, A. S. & Dresner, S. B. *Theory of Molecular Excitons*. (Plenum Press, New York, 1971).
7. Spano, F. C. The Spectral Signatures of Frenkel Polarons in H- and J-Aggregates. *Acc. Chem. Res.* **43,** 429–439 (2010).
8. Spano, F. C. Modeling disorder in polymer aggregates: the optical spectroscopy of regioregular poly(3-hexylthiophene) thin films. *J. Chem. Phys.* **122,** 234701 (2005).
9. Kivala, M. *et al.* Columnar Self-Assembly in Electron-Deficient Heterotriangulenes. *Chem. Eur. J.* **19,** 8117–8128 (2013).
10. Makarov, N. S. *et al.* Impact of electronic coupling, symmetry, and planarization on one-and two-photon properties of triarylamines with one, two, or three diarylboryl acceptors. *J. Phys. Chem. A* **116,** 3781–3793 (2012).
11. Cogdell, R. J., Gall, A. & Kohler, J. The architecture and function of the light-harvesting apparatus of purple bacteria: from single molecules to in vivo membranes. *Quart. Rev. Biophys.* **39,** 227–324 (2006).
12. Oostergetel, G. T., van Amerongen, H. & Boekema, E. J. The chlorosome: a prototype for efficient light harvesting in photosynthesis. *Photosynth. Res.* **104,** 245–255 (2010).
13. Scheblykin, I. G., Sliusarenko, O. Y., Lepnev, L. S., Vitukhnovsky, A. G. & Van der Auweraer, M. Strong Nonmonotonous Temperature Dependence of Exciton Migration Rate in J Aggregates at Temperatures from 5 to 300 K. *J. Phys. Chem. B* **104,** 10949–10951 (2000).
14. Lakowicz, J. R. *Principles of fluorescence spectroscopy*. (Springer, New York, 2006).
15. Sillen, A. & Engelborghs, Y. The Correct Use of 'Average' Fluorescence Parameters. *Photochem. Photobiol.* **67,** 475–486 (1998).
16. Dubin, F. *et al.* Macroscopic coherence of a single exciton state in an organic quantum wire. *Nat. Phys.* **2,** 32–35 (2006).

17. Parson, W. W. *Modern Optical Spectrocopy*. (Springer, Dordrecht, Heidelberg, London, New York, 2009).

18. Schwoerer, M. & Wolf, H. C. *Organische Molekulare Festkorper*. (Wiley-VCH, Weinheim, 2005).

19. Clark, K. A., Krueger, E. L. & Vanden Bout, D. A. Direct Measurement of Energy Migration in Supramolecular Carbocyanine Dye Nanotubes. *J. Phys. Chem. Lett.* **5,** 2274–2282 (2014).

20. Wolf, H. C. Energy Transfer in Organic Molecular Crystals: A Survey of Experiments. *Adv. At. Mol. Phys.* **3,** 119–142 (1968).

21. Haken, H. & Reineker, P. The Coupled Coherent and Incoherent Motion of Excitons and its Influence on the Line Shape of Optical Absorption. *Z. Phys.* **249,** 253–268 (1972).

22. Huijser, A., Savenije, T. J., Meskers, S. C. J., Vermeulen, M. J. W. & Siebbeles, L. D. A. The Mechanism of Long-Range Exciton Diffusion in a Nematically Organized Porphyrin Layer. *J. Am. Chem. Soc.* **130,** 12496–12500 (2008).

23. Eisele, D. M. *et al.* Robust excitons inhabit soft supramolecular nanotubes. *Proc. Natl. Acad. Sci. U.S.A.* **111,** E3367–3375 (2014).

24. Grover, M. & Silbey, R. Exciton Migration in Molecular Crystals. *J. Chem. Phys.* **54,** 4843–4851 (1971).

25. Kenkre, V. M. & Knox, R. S. Generalized-master-equation theory of excitation transfer. *Phys. Rev. B* **9,** 5279–5290 (1974).

26. Schmidt, M. *et al.* Crystal Structure of a Highly Efficient Clarifying Agent for Isotactic Polypropylene. *Cryst. Growth Des.* **12,** 2543–2551 (2012).

27. Sumi, H. Bacterial photosynthesis begins with quantum-mechanical coherence. *Chem. Rec.* **1,** 480–493 (2001).

28. Lin, H. *et al.* Collective fluorescence blinking in linear J-aggregates assisted by long-distance exciton migration. *Nano Lett.* **10,** 620–626 (2010).

29. Winiger, C. B., Li, S., Kumar, G. R., Langenegger, S. M. & Haner, R. Long-Distance Electronic Energy Transfer in Light-Harvesting Supramolecular Polymers. *Angew. Chem. Int. Ed.* **53,** 13609–13613 (2014).

30. Corle, T. R. & Kino, G. S. *Confocal scanning optical microscopy and related imaging systems*. (Academic Press, San Diego, London, 1996).

31. Pawley, J. B. (ed.) *Handbook of biological confocal microscopy*. (Plenum Press, New York, London, 1995).

6. List of Publications

1. A. T. Haedler, H. Misslitz, C. Buehlmeyer, R. Q. Albuquerque, A. Köhler, H.-W. Schmidt, “Controlling the p-Stacking Behavior of Pyrene Derivatives: Influence of H-Bonding and Steric Effects in Different States of Aggregation”, *ChemPhysChem*, **2013,** *14,* 1818-1829**,** DOI: 10.1002/cphc.201300242.

2. A. T. Haedler, S. R. Beyer, N. Hammer, R. Hildner, M. Kivala, J. Köhler, H.-W. Schmidt, “Synthesis and Photophysical Properties of Multichromophoric Carbonyl-Bridged Triarylamines”, *Chem. Eur. J,.* **2014**, *20*, 11708-11718, DOI: 10.1002/chem.201403667

3. A. T. Haedler, K. Kreger, A. Issac, Bernd Wittmann, M. Kivala, J. Köhler, H.-W. Schmidt, R. H, “Long-Range Energy Transport in Single Supramolecular Nanofibres at Room Temperature”, accepted in *Nature*.

Danksagung / Acknowledgement

Die vorliegende Arbeit wurde im Zeitraum von Oktober 2009 bis März 2014 unter der Anleitung von Herrn Prof. Dr. Hans-Werner Schmidt am Lehrstuhl für Makromolekulare Chemie I an der Universität Bayreuth angefertigt.

Ihm möchte ich ganz besonders danken, für die interessante wissenschaftliche Themenstellung und der Möglichkeit diese mit eigenen Ideen weiterzuentwickeln und zu gestallten, dem äußerst gut ausgestattetem Arbeitsplatz sowie den gewinnbringenden wissenschaftlichen Diskussionen.

Besonderer Danke gilt auch Dr. Klaus Kreger, der mir immer hilfsbereit mit Rat und Tat zur Seite stand und ein wertvoller Ansprechpartner während meiner Doktorarbeit war. Die vielen äußerst hilfreichen Diskussionen wissenschaftlicher Problemstellungen, das Einbringen von anderen Sichtweisen auf anstehende wissenschaftliche Fragestellungen und die immerwährende Hilfsbereitschaft habe ich sehr geschätzt.

Des Weiteren möchte ich mich bei meinen Kooperationspartnern im Rahmen des Graduierten Kollegs 1640 aus den physikalischen Lehrstühlen der Uni Bayreuth für die gute Zusammenarbeit und die tieferen Einblicke in die Photophysik bedanken: Prof. Dr. Anna Köhler, Prof. Dr. Jürgen Köhler, Dr. Richard Hildner, Prof. Dr. Rodrigo Albuquerque, Sebastian Beyer und Christina Scharsich. Auch für die stets sehr motivierende und fruchtbare Zusammenarbeit mit Dr. Milan Kivala von der Universität Erlangen-Nürnberg möchte ich mich an dieser Stelle bedanken.

Herzlich danken möchte ich auch allen meinen Kolleginnen und Kollegen vom Lehrstuhl Makromolekulare Chemie I, die mit zahlreichen wissenschaftlichen Diskussionen und der freundschaftlichen Atmosphäre zum Gelingen dieser Arbeit beigetragen haben. In diesem Rahmen möchte ich auch den Technikerinnen und Technikern der MCI, allen voran Doris Hanft danken. Ein großer Dank gilt auch den akademischen Räten und den Sekretärinnen: Dr. Reiner Giesa, Dr. Christian Neuber, Christina Wunderlich und ganz besonders Petra Weiss die uns mit ihrer unermüdlichen Arbeit immer den Rücken frei halten.

Weiterhin möchte ich mich bei Martina Heider, Dr. Markus Drechsler und Dr. Markus Hund für ihre Unterstützung am REM, TEM und AFM bedanken.

Für die finanzielle Unterstützung, die gute Atmosphäre und den Austausch mit Doktoranden, Habilitanden und Professoren aus anderen Fachgebieten möchte ich mich beim Graduiertenkolleg 1640 für „Fotophysik synthetischer und biologischer multichromophorer Systeme“ der DFG bedanken. Weiterhin möchte ich mich bei der Universität Bayern e.V. bedanken, die mich über 2 Jahre mit einem Stipendium nach dem Bayerischen Eliteförderungsgesetz unterstützt haben.

Zu guter Letzt danke ich meiner Familie und meinen Freunden für die immerwährende Unterstützung, dem Verständnis in stressigen Phasen und den vielen motivierenden Worten.

Vielen herzlichen Dank!

(Eidesstattliche) Versicherungen und Erklärungen

nach der Promotionsordnung der BayNAT in der Fassung vom 20. März 2014

(§ 8 S. 2 Nr. 6 PromO)

Hiermit erkläre ich mich damit einverstanden, dass die elektronische Fassung meiner Dissertation unter Wahrung meiner Urheberrechte und des Datenschutzes einer gesonderten Überprüfung hinsichtlich der eigenständigen Anfertigung der Dissertation unterzogen werden kann.

(§ 8 S. 2 Nr. 8 PromO)

Hiermit erkläre ich eidesstattlich, dass ich die Dissertation selbständig verfasst und keine anderen als die von mir angegebenen Quellen und Hilfsmittel benutzt habe.

(§ 8 S. 2 Nr. 9 PromO)

Ich habe die Dissertation nicht bereits zur Erlangung eines akademischen Grades anderweitig eingereicht und habe auch nicht bereits diese oder eine gleichartige Doktorprüfung endgültig nicht bestanden.

(§ 8 S. 2 Nr. 10 PromO)

Hiermit erkläre ich, dass ich keine Hilfe von gewerbliche Promotionsberatern bzw. -vermittlern in Anspruch genommen habe und auch künftig nicht nehmen werde.

……

Ort, Datum, Unterschrift